Hydrocarbon Dynamics in Microporous Catalysts

Alexander James O'Malley

Department of Chemistry, University College London (UCL)

Supervisor: Professor C. R. A. Catlow

Second Supervisor: Dr D. W. Lewis

Thesis submitted for the degree of Doctor of Engineering

2015

I, Alexander James O'Malley, confirm that the work presented in this thesis is my own. Where information has been derived from other sources, I confirm that this has been indicated in the thesis.

I wish to dedicate this thesis to Sylvia Patricia O'Malley, Matthew 'Romeo' Rodrigues and Nelson Rodrigues, who are always in my thoughts.

Also, to the parents and politicians who believe selective schools are necessary for academic children to flourish, you are incorrect.

Abstract

The dynamics of hydrocarbons inside microporous zeolite catalysts are studied using neutron scattering methods and complementary molecular simulations, to investigate quantitatively a crucial component of industrial zeolite catalysis.

The diffusion of longer *n*-alkanes in the siliceous analogue of ZSM-5, silicalite is modelled using state-of-the-art molecular dynamics (MD) simulations. The measured diffusivities show far improved agreement with quasielastic neutron scattering (QENS) experiments. Isobutane diffusion in silicalite is also modelled, giving good agreement with diffusion coefficients and jump diffusion parameters obtained by neutron spin-echo experiments. The simulations give interesting insights into preferred siting locations, contradicting previous studies of isobutane dynamics in the MFI structure due to the use of a more accurate framework model.

Tandem QENS and MD studies of octane isomer diffusion in zeolite HY show a counterintuitive increase in diffusion with branching, due to alkane clustering in the faujasite supercage. The difference in intermolecular forces (dictated by molecular shape) slow the diffusion of *n*-octane significantly more than 2,5-dimethyhexane in the faujasite structure. The behaviour contrasts with that in the MFI structure where branching is known to hinder alkane diffusion.

Methanol diffusion in commercial HY and H-ZSM-5 samples was studied using QENS, showing free methanol diffusion in HY, but not in H-ZSM-5 due to room temperature methoxylation as confirmed by inelastic neutron scattering (INS) spectroscopy and quantum mechanical calculations of vibrational spectra. QM/MM embedded cluster calculations were also performed to compare the acidity and methanol adsorption energy of HY, and at three locations in the H-ZSM-5 structure.

The diffusion component of the recently patented SAPO-37 catalysed Beckmann rearrangement is also studied using QENS to measure cyclohexanone oxime mobility in zeolites HY and SAPO-37, highlighting diffusion differences correlatable to catalytic activity despite sharing the same faujasite structure.

This thesis illustrates the power of complementary neutron scattering and computational studies of sorbate dynamics in zeolites, future work aims to incorporate these studies into the design of new microporous catalytic processes.

Acknowledgements

I would first and foremost like to thank my supervisor Prof. Richard Catlow for the opportunities he has given me, and his invaluable guidance and support throughout my EngD. I also thank my second supervisor Dr Dewi Lewis for his advice, and for being the catalyst for my undertaking a doctorate in the first place.

I am extremely grateful to my industrial (or facilities) supervisor Dr Stewart F. Parker for his assistance in planning, and performing all the neutron experiments which took place at the ISIS facility. I also thank Dr Victoria Garcia-Sakai, Dr Ian Silverwood and Dr Sanghamitra Mukhopadhyay for their expertise and assistance in preparing for and performing the neutron experiments.

This EngD was funded by the Engineering and Physical Sciences Research Council, the UCL Centre for Doctoral Training, the ISIS Neutron and Muon Source and the STFC at Harwell. I am extremely grateful for their financial support. I would like to acknowledge the ISIS Neutron and Muon Source for access to beamline facilities, those who maintain the UCL Legion cluster, and thank Dr Jörg Sassmannshausen for maintenance of the UCL Faraday Cluster.

I would like to thank Dr Andrew Logsdail, Dr Nikolaos Dimitratos, Dr Peter Wells, Dr Arun Chutia, Dr Paul Collier, Dr Matthew Potter, Prof. Robert Raja and Prof. Herve Jobic for their collaboration, advice both broad and technical, stimulating discussion and for helping me to settle into the UK Catalysis Hub. I am extremely grateful to have had such fantastic work colleagues throughout my time based here. I thank Antonis Vamvakeros, Scott Rogers, Wilm Jones, Anna Gould, Catherine Brookes, Donato Decarolis, Miren Agote and Stephanie Chapman for making this experience far more than simply completing a qualification.

Huge thanks goes to my close friends Ben Robinson, Joe Manzi, Hazel Kitching and Isaac Sugden for their support during my time at UCL. Thank you to Milly, Jo and Ollie for being themselves. I also thank Silvana and Stefania Arias, whose significance does not need explaining to those who know me.

Finally I would like to thank my mother and father for their unconditional love, encouragement, tolerance, support and belief in me over the last four years. Thank you for everything.

Publications

Work carried out during this EngD program has been published, or is under review for publication in the following papers:

O'Malley, A. J.; Catlow, C. R. A. Molecular dynamics simulations of longer n-alkanes in silicalite: a comparison of framework and hydrocarbon models. *Physical Chemistry Chemical Physics* **2013**, *15* (43), 19024-19030.

O'Malley, A. J.; Catlow, C.R.A. Molecular dynamics simulations of longer n-alkanes in silicalite: state-of-the-art models achieving close agreement with experiment. *Physical Chemistry Chemical Physics* **2015**, *17* (3), 1943-1948.

O'Malley, A. J.; Catlow, C. R. A.; Monkenbusch, M.; Jobic, H. Diffusion of Isobutane in Silicalite: A Neutron Spin-Echo and Molecular Dynamics Simulation Study. *The Journal of Physical Chemistry C* **2015**, *119* (48), 26999-27006.

O'Malley, A. J.; Parker, S.F.; Chutia, A.; Farrow, M.R.; Silverwood, I.P.; Garcia-Sakai, V.G.; Catlow, C. R. A. Room Temperature Methoxylation in Zeolites: Insight into the Methanol-to-Hydrocarbons Process. *Chemical Communications* **2016**, *52,* 2897-2900.

O'Malley A. J.; Logsdail A. J.; Sokol A. A.; Catlow C. R. A. Modelling Metal Centres, Acid Sites and Reaction Mechanisms in Microporous Catalysts. *Faraday Discussions **2016***, DOI: 10.1039/C6FD00010J.

O'Malley, A. J.; Garcia-Sakai, V. G.; Silverwood, I.P.; Dimitratos, N.; Parker, S.F.; Catlow, C. R. A. Methanol Diffusion in Zeolite HY: A Combined Quasielastic Neutron Scattering and Molecular Dynamics Simulation Study. *Physical Chemistry Chemical Physics* **2016** – Accepted.

O'Malley, A. J.; Hitchcock. I.; Sarwar, M.; Silverwood, I.P.; Hindocha, S.; Catlow C. R. A.; York, A. P. E.; Collier, P. J. Ammonia Mobility in Chabazite: Insight into the Diffusion Component of the NH_3-SCR Process*. Physical Chemistry Chemical Physics* **2016** – Accepted.

Potter, M. E.; O'Malley, A. J.; Kezina, J.; Newland, S. H.; Chapman, S.; Silverwood, I. P.; Mukhopadhyay, S.; Carravetta, M.; Mezza, T. M.; Parker, S. F.; Catlow C. R. A.; Raja, R. Unravelling the Crucial Interplay between Active Site Design and Molecular Diffusion *Journal of the American Chemical Society* **2016** – Under Review

Contents

Chapter 1

Introduction to Zeolites, Catalysis and Dynamics

Zeolites and zeotype materials are well established in the field of catalytic science. Particularly notable is their commercial use in hydrocarbon cracking, and shape-selective, acid-catalysed conversions of simple hydrocarbons to alcohols, olefins and aromatics. The need to optimise such catalytic processes in a period where fossil fuels are limited has led to large volumes of research both experimental and theoretical, into the dynamics of hydrocarbons within zeolite frameworks. Microscopic studies into these dynamics combining theory and experiment can give a unique insight into these systems on a molecular level. This approach forms the basis of this thesis. In this chapter we introduce zeolites and their applications to industrial catalytic processes, namely fluid catalytic cracking (FCC) and the methanol-to-hydrocarbons/methanol-to-olefins (MTH/MTO) processes. We then outline dynamic processes of interest in zeolites based on molecular diffusion, and the advances in experiment and computational study which have formed the basis of the work in this thesis.

The first zeolite was discovered by Swedish mineralogist Axel Fredrik Cronstedt in 1756 as a constituent in volcanic rocks. Now known as stilbite, Cronstedt observed that large amounts of steam were released from the rock sample after rapid heating, as water had been absorbed from the atmosphere through trapping in the pores and cavities of the mineral. The name 'zeolite' derives from the ancient Greek words 'zeo' meaning 'to boil', and 'lithos' meaning 'a stone'. Research was limited to natural zeolites for roughly the following 200 years, however the pioneering work of Barrer in the mid-1930s expanded the field significantly, including the first synthesis of a zeolite, mordenite.[1] Before the work of Barrer, zeolites already had exhibited many useful observed properties such as adsorption, molecular sieving capabilities and ion exchange.[2]

1.1 Zeolite Structure and Functionality

Zeolites are crystalline aluminosilicate materials containing pores, channels and cavities of molecular dimensions, typically 3–15 Å.[3] The chemical composition of zeolites is generally limited to the elements Si, Al and O, however these elements combine in a vast number of ways giving way to the observed wide range of topologies. The primary structural unit of a zeolite is the tetrahedron (TO_4), where the T-site is a silicon or aluminium atom. The $[SiO_4]^{4-}$ and $[AlO_4]^{5-}$ tetrahedra (shown in figure 1.1) are linked at the corners to create the observed structures. Other tetrahedrally orientated classes of microporous solids are aluminophosphates (ALPOs) and silicoaluminophosphates (SAPOs).

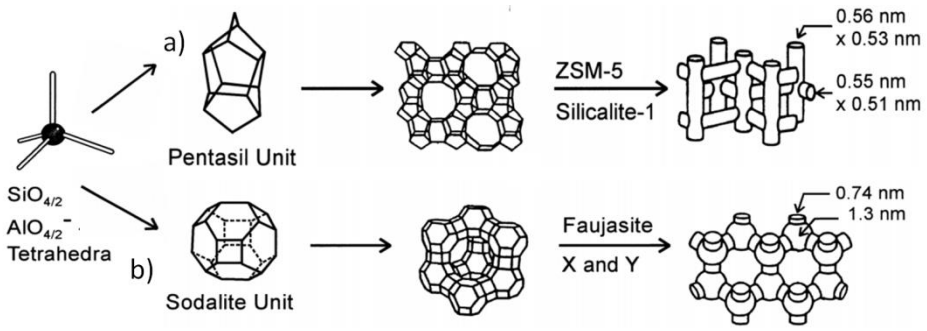

Fig. 1.1. Schematics of the framework structures of a) ZSM-5 (MFI) and b) zeolite Y (FAU) and their composite building units formed from the TO_4 tetrahedron. Figure adapted from reference 6.

Zeolite framework structures are classified by a three letter code, there are currently 229 framework structures approved by the International Zeolite Association Structural Commission.[4] The two structures relevant to this thesis are the MFI (mordenite framework inverted) and FAU (faujasite) frameworks shown in figures 1.1 (a) and (b) respectively. The MFI framework has channels of ~ 5.5 Å width, which are straight in the 010 direction however, in the 100 direction the channels have a sinusoidal (or 'zig-zag') structure. The channels meet at intersections as shown schematically in figure 1.1 (a). The faujasite structure is composed of sodalite cages connected by their hexagonal faces to create the tetrahedrally connected supercages shown in figure 1.1 (b). These supercages are 13 Å in diameter, connected by windows with a diameter of 7.5 Å.

Fig. 1.2. Alumination of the siliceous framework and resultant protonation of the adjacent O atom forming the Brønsted acid hydroxyl site. Figure reproduced from reference 5.

When the siliceous framework has a silicon T-site replaced with aluminium, a negative charge is induced on the adjacent oxygen atom. In order to maintain a neutral framework structure, a cation is necessary to compensate for the induced charge. These cations may be alkali metals, alkali earth metals, transition metals or lanthanides located within the channel/cage region of the zeolite. The charge may also be compensated by a proton which is bonded to the framework oxygen. These protons are weakly bound and thus very acidic, the Brønsted acid sites form the basis of the acidic catalysis integral to the petrochemical industry, and relevant to the work carried out in this thesis.

1.2 Shape-selective Acidic Zeolite Catalysis [6,7]

Acidity in a zeolite sample may come in the form of Brønsted or Lewis acidity (or both). The former is caused by the aforementioned framework hydroxyls, and the latter is caused by extra-framework ions. Though there are some very notable Lewis acid applications of zeolites,[8] the work in this thesis is concerned with Brønsted acid catalysed conversions, which will form the focus of this section.

The industrial use of synthetic faujasites in the early 1960s for the fluid catalytic cracking (FCC) of larger hydrocarbons in crude oil fractions[9] signalled the beginning of the routine use of acidic zeolites in the petrochemical industry. Catalytic cracking is the largest single application of zeolites in terms of financial market size, but other important industrial applications include hydrocarbon synthesis, and isomerisation reactions.

Additional to the higher activity of zeolite catalysts, the shape-selective nature of the catalysis is another defining feature of zeolite catalysed conversions. The selectivity arises from the zeolite pores having molecular dimensions, so the pore size or shape has a direct influence on the observed products of the reaction. Shape-selectivity may manifest itself in three ways: Reactant shape-selectivity, product shape-selectivity and transition state shape-selectivity. Reactant shape-selectivity involves the diffusion of one reactant being hindered perhaps due to its size or shape preventing it from reaching the active site. Product selectivity involves the hindered diffusion of a bulkier product molecule, so the smaller products are formed and recovered preferentially. Transition state shape-selectivity involves suppression of the reaction pathway involving formation of a bulky transition state which the zeolite framework cannot accommodate, so the product achieved by this pathway is not formed. Detailed discussions on understanding and influencing this shape selectivity can be found in references 10 and 11.

We now outline two very significant processes for the petrochemical industry based on acidic zeolite catalysed conversions: The fluid catalytic cracking (FCC) reaction, converting heavy crude oil fractions to hydrocarbons appropriate for gasoline, and

the synthesis of hydrocarbons from methanol, termed the methanol-to-hydrocarbons (MTH) process.

1.2.1 Fluid Catalytic Cracking Processes [12]

The cracking of hydrocarbons involves the breaking down of longer chain hydrocarbons to smaller, simpler hydrocarbons through the scission of carbon-carbon bonds, usually by a high silica faujasite zeolite catalyst at temperatures ~ 500˚C. The process has been under intensive research for over 60 years due to the necessity of efficient fuel production from crude oil. An understanding of the exact mechanisms is very desirable so has received much attention.[13,14] The two distinguished mechanisms in catalytic cracking are bimolecular cracking via carbenium ions, and monomolecular cracking via carbonium ions (proposed by Haag and Dessau[15]).

The reaction itself is a chain reaction with initiation, propagation and termination steps. An accepted mechanism in the case of alkene cracking would involve the attacking of a double bond by a Brønsted acid site to form a carbenium ion (figure 1.3 (a)), the hydrocarbon may then undergo β-scission to produce a smaller alkene and a further carbenium ion (figure 1.3 (b)). The catalyst is regenerated through deprotonation of the second carbenium ion (often after intramolecular rearrangement through a hydrogen shift) to form another alkene (figure 1.3 c)).

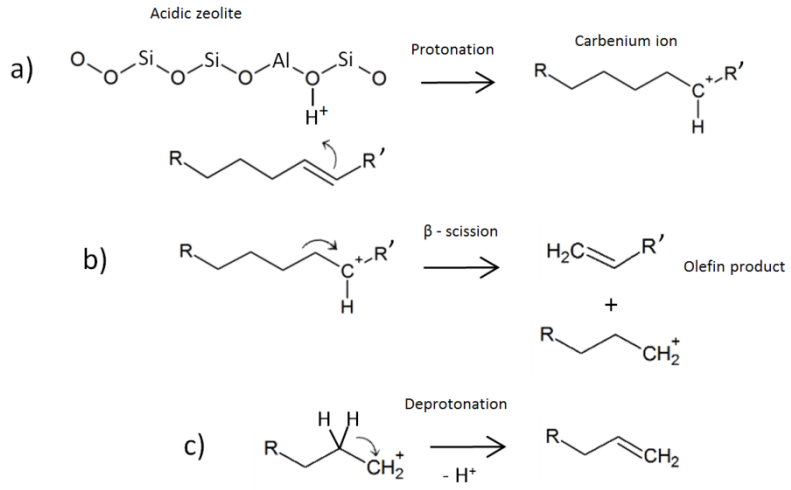

Fig. 1.3. An example of a carbenium ion pathway associated with the zeolite catalysed FCC process.

The process takes place as the preheated feedstock of long chain hydrocarbons is vapourised and mixed with the catalyst powder at 535˚C and 1.72 bar pressure. The catalyst is regenerated by burning off the coke at around 715˚C. Zeolite Y (faujasite) based cracking catalysts were introduced commercially in 1964.[16] However ZSM-5 additives have been intensively studied by the likes of Mobil.[17]

1.2.2 Methanol-to-Hydrocarbons Processes [18]

The term 'methanol-to-hydrocarbons' (MTH) signifies a broad set of reactions including methanol-to-olefins (MTO) and methanol-to-gasoline (MTG) processes. Industrial interest in these processes stems from a number of drivers, such the monetisation of natural gas and the demand for light olefins such as ethene and propene. Most ethene is produced from the steam cracking of naptha and natural gas liquids, which is also the case with propene. The second largest source of propene is as an FCC coproduct. The cost of these feedstocks is related to the price of crude oil which is expected to remain high in the future, thus the olefin and derivatives industry has a significant interest in lower cost feed stocks such as natural gas, where the MTO process is a crucial step in this gas to olefins process.

The formation of C-C bonds from methanol upon heating with acidic reagents was known before the mid-1970s. However, very little research took place until this time, when Chang and Silvestri found that H-ZSM-5 could transform methanol to C_1-C_{10} range hydrocarbons at 300-500 ˚C [19] leading to intensive research efforts. [20-23] The process was commercialised by Mobil Oil in New Zealand due to high crude oil prices, however this plant was shut down as prices lowered again.

Industrial MTH reactions all take place in zeotype systems, with the original paper in reference 19 taking place in H-ZSM-5, where lower feed rates gave the desired hydrocarbon mixture (higher rates gave only dimethyl ether and water). However, other zeotype materials such as SAPO-34 are also capable of MTH catalysis.[24] The product range of the reaction depends on the zeolite pore structure, for example, smaller pores (8 membered ring or less) would not allow entrance of aromatic rings into the framework, so only C_1-C_5 hydrocarbons are formed. H-ZSM-5, with 10

membered ring channels, allows for diffusion of dimethylbenzenes, and even tetramethylbenzene, while the smaller components are still formed.

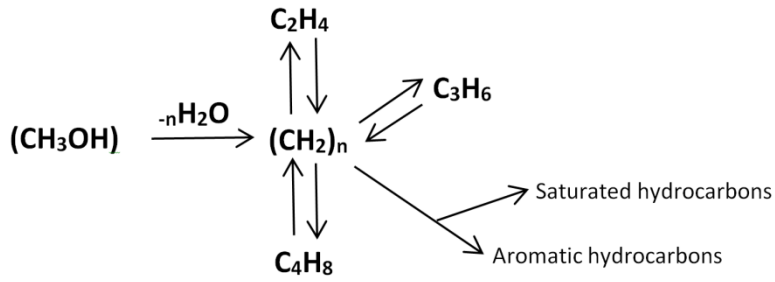

Fig. 1.4. The hydrocarbon pool reaction scheme.

A large number of mechanistic pathways have been proposed which can be broadly grouped into carbene-carbenoid mechanisms,[25] carbocationic mechanisms,[26] and mechanisms involving trimethyloxonium intermediates.[27] However, presently the mechanism receiving the most interest is that of the hydrocarbon pool, brought to attention by Dahl and Kolboe[28-30] who performed experiments involving isotopic labelling of ^{13}C methanol co-fed with ^{12}C ethanol/propanol. They found that only a small proportion of products contained ^{12}C and that it was mixed thoroughly within all the products, suggesting the MTH process involves a pool of adsorbed hydrocarbons constantly adding methanol and splitting off ethene, propene and higher hydrocarbons. The direct C-C bond formation mechanisms are now considered less significant compared to the hydrocarbon pool mechanism, with further evidence of aromatics such as methylbenzenes also playing an important role in the total mechanism.[31,32]

1.3 Studying Dynamics in Zeolites

The study of the dynamic processes governing the industrial applications of zeolites is difficult, as the majority take place inside the zeolite channels. The importance of understanding such dynamics can be illustrated by considering the heterogeneous catalytic process. Rate limiting steps to the reaction progress can be found in either

the diffusion of the reactants towards the active site, adsorption onto the active site, conversion at the active site, or the diffusion of the products away. The diffusion of sorbates inside the zeolite channels is not only crucial to reaction efficiency, but also selectivity, as separation processes depend on a significant difference in the diffusivity of the components involved.

There are two main approaches to studying the diffusion of sorbates in microporous solids, based on either macroscopic or microscopic methods. Macroscopic methods usually involve measuring mass transfer in the presence of a concentration gradient, or concentration differences as a function of length. Techniques include gravimetry, zero-length column (ZLC) chromatography and membrane permeation methods. Macroscopic studies of diffusion in zeolites and the principles governing such methods are outside the scope of this thesis and we refer the reader to an extensive review given by Kärger.[33] Microscopic methods differ in that they are concerned with the stochastic motions of molecules, and can probe molecular diffusion without the limit of a concentration gradient. These methods include pulsed field gradient (PFG) NMR and quasielastic neutron scattering (QENS), the latter is outlined further in section 2.5. Unfortunately a discussion of all the experimental techniques capable of measuring sorbate diffusion in zeolites is not feasible in this thesis, however an attempt to summarise some key characteristics of the more prominent methods is given in table 1.1.

An important advantage of microscopic methods is that they are directly comparable with computational simulations of diffusivity, based on the molecular dynamics (MD) method outlined in section 3.3. The majority of the work in this thesis exploits this comparability. A large number of microscopic studies into hydrocarbon diffusion have taken place using these techniques, and a review of the work relevant to the exact studies in this thesis is given at the beginning of each chapter. For this reason, discussion in this introduction will be limited to the more unusual phenomena observed historically, which formed the original inspiration for the current studies.

Technique	Description	Advantages/Limitations (+/-)
Gravimetric methods	The sample is subjected to a step in the pressure of the surrounding atmosphere, the time dependence of changes in the amount adsorbed is monitored.	**+** Accessible experimentally. **+** Can study large systems accessing both macro- , meso and micropore diffusion. **-** Affected by external heat and mass transfer resistances. **-** Unreliable for faster diffusion processes due to the response time of the measurement.
Frequency response methods	Pressure of the sorbate is varied sinusoidally, the phase angle and amplitude of the weight changes are measured. Alternatively, the pressure response of a sorbate system to sinusoidal volume variation may be measured.	**+** Accessible experimentally. **+** Can study large systems accessing both macro- , meso and micropore diffusion. **+** Sensitive to a wide range of diffusivities. **-** Also affected by heat and mass transfer resistances.
Zero-length column	The zeolite is equilibrated with the sorbate under controlled conditions. The desorption curve is measured when the carrier is switched to a non-adsorbing stream and the effluent concentration is monitored.	**+** Not affected by heat and mass transfer phenomena. **-** Limited by the system response time. **-** The resistance of an external sorbate film around crystals may also affect the accuracy requiring a high flow rate to remove it. Sample size is also very small.
Single crystal membrane permeation	A single crystal is embedded in a substance such as epoxy resin, the 'inflow' side is exposed to the diffusant gas and the pressure increase is measured in constant volume on the 'outflow' side of the membrane.	**+** Not affected by external heat transfer and mass-transfer phenomena. **-** Difficult experimentally as large crystals are needed (>100 μm). **-** Technique is limited to certain samples which can produce larger crystals and heterogeneities will cause inconsistencies in measurement. **-** Diffusant gas may bypass the embedded crystal.

Pulsed field gradient-NMR	Radiofrequencies are applied to the sample to generate a spin echo NMR signal. Pairs of magnetic field gradients from the sample are superimposed to label spin positions. The spin echo amplitude is recorded as a function of pulsed gradients and spin echo attenuation is analysed to deduce the diffusivity.	**+** Can measure self-diffusivity on the micro-miliscale. **+** Non destructive method with fast data collection. **-** Range of diffusivity measureable is limited by spin relaxation time **-** Larger zeolite crystals are needed to prevent the sorbate from reaching the crystallite boundary on the time scale of the experiment. **-** Presence of paramagnetic species eg. Cu^{2+} restricts the experiment to shorter observation times.
Quasielastic neutron scattering	Small differences in the energy of incident and scattered neutrons (μeV-meV) are evaluated as a function of neutron momentum transfer and fit to models describing diffusivity and translational diffusion mechanisms.	**+** Allows self-diffusivity (> 1x 10^{-10} m^2s^{-1}) measurements and diffusion mechanism elucidation on the nanoscale. **-** Instrumental access is severely limited and time length of a single measurement is on the order of hours.
Neutron spin- echo	Energy differences between incident and scattered polarised neutrons are determined from spin vector differences, similar to quasielastic neutron scattering the neutron energy transfer is evaluated as a function of momentum transfer to obtain diffusivity.	**+** Allows self and transport diffusivity (> 1x10^{-11} m^2s^{-1}) measurements and diffusion mechanism elucidation on the nanoscale. **-** Instrumental access is even more limited than QENS, and time length of a single measurement is longer than a QENS experiment.

Table 1.1. Summary of prominent experimental methods for diffusion measurement both macroscopic (Gravimetry[34], frequency response[35], zero-length column[36] and single crystal membrane permeation[37]) and microscopic (pulsed fiend gradient NMR[38], quasielastic neutron scattering[39] and neutron spin echo[40]). Table is adapted, edited and added to from reference 34.

1.3.1 Hydrocarbon Diffusion in Zeolites: Unusual Observations

As mentioned, understanding diffusion within zeolites is of paramount importance for separation and catalysis processes. The separation processes often rely on a significant difference in the diffusion coefficients of the components, whereas in catalytic processes the rate limiting step may be in the diffusion of the reactant or product to or from the active site. Classically, the diffusion coefficient is defined as a factor of proportionality between the flux density and the concentration gradient of the species under study, as described by Ficks' 1st law:

$$J(c) = -D_t(c)\nabla c \tag{1.1}$$

J is the macroscopic flux of particles, D is the diffusion coefficient and c is the concentration gradient (measured in molecules per unit volume). Types of diffusion studied are transport-diffusivity (D_t) (in equation 1.1) which is the average diffusion coefficient of a substance in the presence of a concentration gradient, and the self-diffusivity (D_s) where the diffusion coefficient is measured under equilibrium and without the influence of a concentration gradient (usually achieved using microscopic measurements). Each microscopic method used to measure the self-diffusivity has its own specific formula for calculating this value based on stochastic molecular motion (as discussed for QENS in section 2.5.1.1).

Computational methods such as molecular dynamics (MD) simulations may also be used to measure diffusion coefficients by directly tracking the time resolved movement of molecules through space as detailed in chapters 4 and 5. In terms of self-diffusion coefficient measurements, it is common for simulations to yield higher values of the diffusion coefficient than experimental methods such as PFG-NMR and QENS[39], as illustrated for *n*-alkanes in figure 1.5 from reference 34. This observation is attributed first to the historical modelling of the zeolite lattice as a perfect siliceous crystal, when defects, extra-framework ions and Brønsted acid sites are inevitable in real zeolite samples and are known to inhibit diffusion. Also, many MD simulations are conducted in the limit of infinite dilution, removing all the

sorbate-sorbate interactions (rarely possible experimentally), these interactions often slow the diffusion of sorbates through the channels, thus lowering the diffusion coefficient. It is also observed that the diffusion coefficients of *n*-alkanes in zeolites decrease monotonically with chain length, attributed to the fact that the longer the alkane, the higher the diffusion barrier because more atoms have to be moved from their position, necessitating more energy (such a trend is also illustrated in figure 1.5).

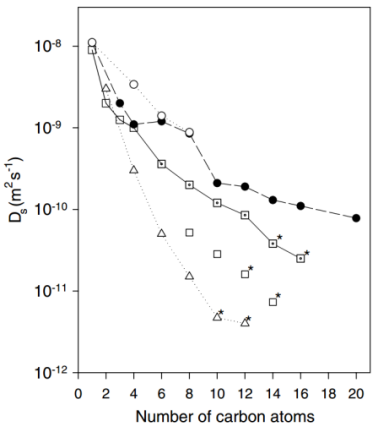

Fig. 1.5. Self-diffusivities obtained at 300 K from MD simulations (○), hierarchical simulations (●), QENS in Na-ZSM-5 (□), QENS in silicalite-1(▪) and PFG-NMR (Δ). * = extrapolation to 300K. Figure taken from reference 46.

This assumption was brought into question by the selective uptake experiments of Gorring in 1973,[41] who found a minimum in the diffusion coefficient for octane in synthetic erionite, while finding maxima in diffusivity for butane and dodecane as shown in figure 1.6 (a). The observation was interpreted by considering that the length of an octane molecule matches the free length of an erionite cage (c. 13 Å).

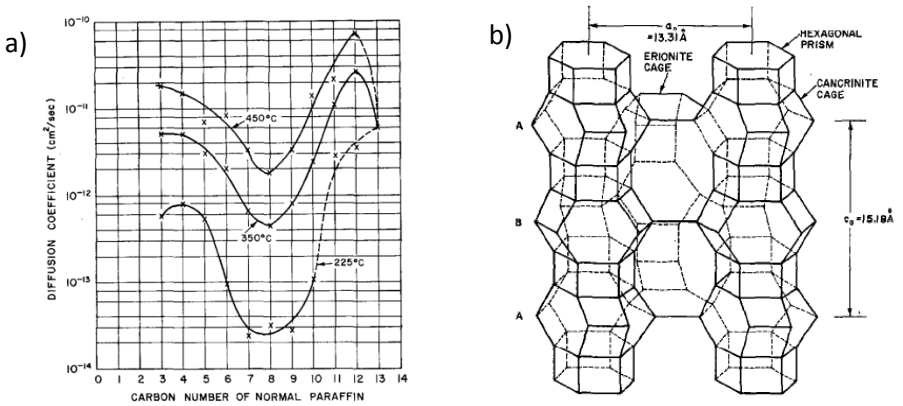

Fig. 1.6. a) The plot of diffusion coefficients against carbon chain length in synthetic erionite. b) the erionite cage structure. Figure taken from reference 41.

The octane molecule then fits perfectly into the cavity, which acts as a low energy trap, with the entrance and exit to the cage forming diffusion barriers. These low energy traps then lead to lower diffusion coefficients for 'just-fitting' molecules, as more energy is needed for movement.

This 'window-effect' (so named because the molecule preferentially stays in the cage rather than diffusing through the windows) has however been called into question by groups such as Ruthven,[42] who suggest the results could be accounted for by considering the effect of isotherm non-linearity and the finite rate of heat dissipation.

The window effect was studied by Runnebaum and Maginn[43] using classical molecular dynamics, (referred to in this case as 'resonant diffusion') studying *n*-alkane diffusion in silicalite at chain lengths ranging from C_4 to C_{20}, at temperatures ranging from 300 to 400 K. The diffusion coefficients were measured along the [010] direction (straight channels), and the 100 direction (sinusoidal channels). In the [100] direction a typical monotonic decrease in the self-diffusivity with chain length was observed at all temperatures (figure 1.7 (b)) however in the [010] direction the diffusivity showed a periodic fluctuation with chain length, with maxima at C_8 and C_{16}, and minima at C_6 and C_{14} as shown in figure 1.7 a), attributed to structural energy trapping. This was observed at temperatures of 300 and 350 K, however not 400 K. This was found to be because at the lower temperatures, silicalite acts as a one-dimensional zeolite, as interchange between the two channel systems is very slow at lower temperatures.

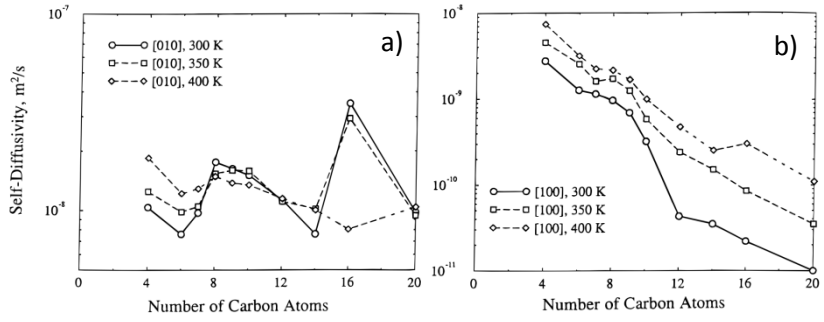

Fig. 1.7. a) The periodic dependence of diffusivity on chain length through the straight channels of silicalite, b) the standard monotonic dependence of diffusivity on chain length through the sinusoidal channels of silicalite. Figure adapted from reference 43.

A comparative review by Jobic et al [44] studied this structural energy trapping phenomenon, comparing self-diffusivities of *n*-alkanes in NaX, ZSM-5 and zeolite 5A using QENS, PFG-NMR and neutron spin-echo (NSE). The NSE technique was necessary for zeolite 5A due to the low diffusivity in such narrow pores (the technique is outlined in section 2.5.3). The diffusivities were found to decrease monotonically with chain length in ZSM-5 and NaX. However, for zeolite 5A, composed of cages connected by windows with a diameter of 4.1 Å (smaller than that of NaX, at 7.4 Å) a drop to a minimum in diffusivity was found at C_8 , with a maximum at C_{12}, followed by a decrease at C_{14}. The diffusion activation energies also supported the slowing of C_8, with a larger activation energy than C_{12} (41 kJ mol^{-1} compared to 35 kJ mol^{-1}). The interpretation in figure 1.8 postulates that a C_8 molecule fits tightly inside the zeolite 5A cavity, residing in a potential energy well, unlike C_{12} which can extend through the window, causing the (largely entropic) energy barrier of diffusion to drop. The decrease in diffusivity after this length was attributed to molecular weight, with the possibility of another maximum in the C_{16}-C_{18} range.

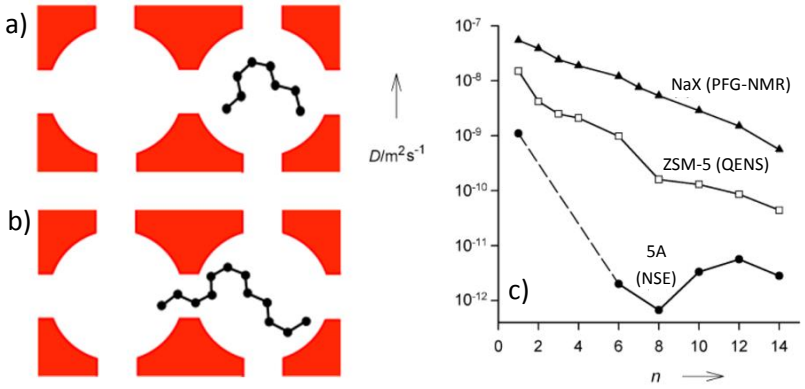

Fig. 1.8. Schematic representation of *n*-alkane configurations in zeolite 5A: *n*-octane fits neatly into a cavity (a), but one end of *n*-dodecane reaches into the window between cages (b). The dependence of diffusivity on chain length of n-alkanes in 3 different zeolites, non-monotonic dependence is exhibited for zeolite 5A. Figure from reference 44.

Simulations supporting the window effect and other structural energy trapping phenomena have been called into question due to the nature of the models used, not least because differences of up to 3 orders of magnitude in the absolute values of experimental and calculated diffusion coefficients being commonplace. The next

section will outline the computational models used in simulations of zeolite dynamics, and how differences in these models can have a significant impact on conclusions drawn when studying dynamical phenomena.

1.3.2 Modelling Hydrocarbon Diffusion in Zeolites

The large length and time scales associated with diffusion require force-field based simulations (outlined in section 3.1). Though these are of a lower level of theory than quantum mechanical simulations (outlined in section 3.3), detailed qualitative and quantitative information may be obtained about the diffusing sorbate. We note that extensive reviews of classical (and quantum mechanical) simulations of adsorption, diffusion and reaction processes in zeolites are given by Smit and Maesen[45] and more recently by Van Speybroeck et al.[7] Given that a detailed review of the relevant theoretical literature also takes place at the beginning of each chapter, we will centre this discussion on a point of particular significance and motivation for this work. These include the approximations necessary historically for modelling these systems, and their potential shortcomings for quantitative (and indeed qualitative) study of hydrocarbon diffusion in zeolites.

Though computational methods have long been established in zeolite science as highlighted by the aforementioned reviews, growth in computational power has allowed for increasingly realistic simulations. In earlier work a common approximation made to reduce computational expense was the use of a rigid framework to represent the zeolite structure.[45] Given that in any zeolite simulation, the vast majority of the atoms belong to the zeolite framework itself, fixing the zeolite atoms in their crystallographic positions will cut the cost of these simulations significantly. This approximation however, may have been at least partially responsible for the sizeable discrepancies between QENS measurements[46,47] and MD simulations of *n*-alkane diffusion in silicalite.[43]

The role of framework flexibility on the diffusivity of shorter alkanes in silicalite was systematically studied by Leroy and co-workers.[48] It was found that diffusion was enhanced by framework flexibility for the shorter alkanes (methane and butane) at the lowest loadings, as sorbate–sorbate interactions dominated at higher loadings rendering the effect of framework flexibility negligible. The dependence of self-diffusivity on chain length however, remained unchanged with the framework model. Other examples include higher diffusion coefficients for *n*- and isobutane in MFI using a flexible framework,[49] along with studies showing faster diffusion for methane in a flexible MFI lattice (at low loadings) with little influence in LTA frameworks.[50]

It is often argued that for molecules which do not fit tightly in the zeolite pores, this approximation is reasonable, as with tighter fitting molecules pore-breathing is more likely to facilitate potential barrier crossing. It is also important to remember that crucial features of the framework are the interactions between the framework species; only with an accurate description of these is the required accuracy achieved. It is important to note that the above simulations were all carried out using a united-atom hydrocarbon model as opposed to an all-atom hydrocarbon model. The details of these hydrocarbon models will now be outlined.

When simulating hydrocarbons, there are a number of models available. The most realistic of course is the all-atom (AA) model, where all carbon and hydrogen atoms are explicitly represented with their associated potentials. The united-atom (UA) approach is however a very popular choice. CH_3, CH_2 and CH groups are represented by single atoms, reducing considerably the computational cost. However, in the present context it has severe limitations; reducing barriers to diffusion as the potential is too 'smooth' and it may not represent properly the larger surface area for intermolecular interactions between the chain and the channel walls. Indeed, the united-atom model is known to give higher local mobilities of *n*-tridecane melts,[51] perhaps due to the aforementioned factors combining to decrease the energy barriers to mobility and allowing the molecule to move more freely. Another representation used in diffusion studies is the anisotropic united-atom model (AUA)

proposed by Toxvaerd for *n*-alkanes.[52] While each force centre is located on the carbon in the conventional united-atom potentials, the force centre is shifted in the AUA potential and is placed between the carbon and hydrogen atoms of the related group. A further issue is that the majority of force-fields for hydrocarbons were originally developed for biological applications, which give very accurate descriptions of behaviour at ambient conditions. However, many simulations of diffusion within zeolites are carried out at much higher temperatures to mimic industrial conditions. Thus, it is critical that the force field gives an accurate description across a range of temperatures and pressures. Examples are force fields that have been shown to replicate the liquid–vapour coexistence curve over a wide range of conditions, such as the TraPPE-UA force-field.[53]

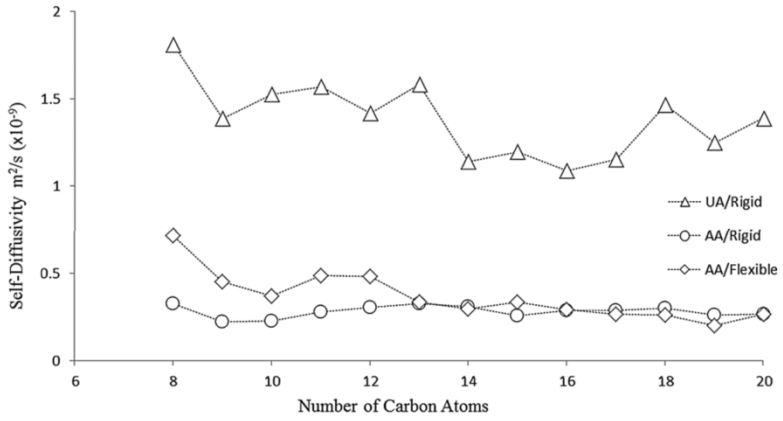

Fig. 1.9. The dependence of diffusivity on chain length for n-alkanes in silicalite using three different model systems, comparing the united-atom/rigid framework simulation, all-atom/rigid framework simulation and all-atom/flexible framework simulation. Figure from reference 54.

O'Malley and Catlow[54] aimed to systematically assess the role of framework flexibility and hydrocarbon models over a range of longer *n*-alkanes in the silicalite framework. The study performed simulations using a united-atom model with a rigid zeolite cage, an all-atom hydrocarbon model with a rigid zeolite cage, and an all-atom model with a flexible zeolite cage. It was found that the use of a rigid cage gave the formerly observed window effect with a periodic dependence of diffusivity on chain length as shown in figure 1.9. The use of a united-atom hydrocarbon model give diffusion coefficients up to an order of magnitude higher than those obtained using an all atom-hydrocarbon model. All diffusion coefficients obtained

using a flexible framework and all-atom hydrocarbon model not only gave the same trend as QENS studies of the same systems[46] (a monotonic decrease in diffusivity with chain length), but the absolute values of the self-diffusion coefficient were all within 1 order of magnitude of these QENS studies. The conclusion was that the potential of the united-atom hydrocarbon model is indeed too smooth, allowing more free mobility and increased diffusivity. Also, the study suggests the structural energy trapping phenomena observed in previous simulations are merely a product of the rigid framework zeolite model. Upon use of a flexible zeolite model, these energy traps dissipate too quickly during the framework breathing process to significantly affect sorbate diffusion. The remaining sources of discrepancy when using the up-to-date models were attributed to the use of a perfect silicalite crystal in the simulations, and the condition of infinite dilution eliminating sorbate-sorbate interactions which, if modelled at experimental alkane loadings would lower the diffusion coefficients, bringing them closer to values obtained experimentally. We address this discrepancy directly in chapter 4.1.

1.4 The Current Study

Our study in reference 54 illustrates that the approximations chiefly responsible for discrepancies between experimental and theoretical diffusivities, and for the erroneous behaviours in these systems are no longer necessary. Such a demonstration highlights the opportunity for tandem microscopic experiments and complementary simulations, with the potential for accurate comparison and detailed insight into the diffusion behaviour of the species relevant to the catalytic systems discussed in this introduction. The focus of this thesis is exactly that, with chapter 4 presenting molecular dynamics simulations of longer *n*-alkanes and isobutane in the silicalite (MFI) framework, directly compared with previous QENS and neutron spin-echo (NSE) experiments. Chapter 5 studies the effect of molecular shape on the diffusion of octane isomers in a commercial HY catalyst using QENS and MD simulations, of direct relevance to FCC catalysis. Chapter 6 is concerned

with experimental and theoretical study of methanol behaviour in H-ZSM-5 and HY, the former giving insight into key steps of the methanol-to-hydrocarbons process through a combination of QENS, vibrational spectroscopy, and quantum mechanical calculations. The study of methanol in HY obtains the first microscopic measurement of methanol diffusion in an acidic HY catalyst. Finally, chapter 7 details the first quantitative microscopic diffusion measurements to be incorporated into the design of a novel microporous catalytic process. QENS is used to study the diffusion component of the SAPO-37 catalysed Beckmann rearrangement of cyclohexanone oxime to ε-caprolactam. Before presenting these studies, we introduce the neutron scattering techniques relevant to the experimental component of this thesis in chapter 2, and the computational methods used for the complementary theoretical calculations for each study in chapter 3.

References

(1) Barrer, R. *Journal of the Chemical Society (Resumed)* **1948**, 2158.
(2) Jacobs, P.; Flanigen, E.; Jansen, J.; van Bekkum, H. *Introduction to Zeolite Science and Practice*; Elsevier, 2001.
(3) Auerbach, S. M.; Carrado, K. A.; Dutta, P. K. *Handbook of Zeolite Science and Technology*; CRC press, 2003.
(4) http://izasc.ethz.ch/fmi/xsl/IZA-SC/ft.xsl.
(5) http://www.cchem.berkeley.edu/molsim/teaching/fall2009/mto/cat.html.
(6) Weitkamp, J. *Solid State Ionics* **2000**, *131*, 175.
(7) Van Speybroeck, V.; Hemelsoet, K.; Joos, L.; Waroquier, M.; Bell, R. G.; Catlow, C. R. A. *Chemical Society Reviews* **2015**.
(8) De Vos, D. E.; Dams, M.; Sels, B. F.; Jacobs, P. A. *Chemical Reviews* **2002**, *102*, 3615.
(9) Venuto, P. B.; Habib Jr, E. T. **1979**.
(10) Weitkamp, J.; Ernst, S.; Puppe, L. In *Catalysis and Zeolites*; Springer: 1999, p 327.
(11) Smit, B.; Maesen, T. L. *Nature* **2008**, *451*, 671.
(12) Corma, A.; Orchilles, A. *Microporous and Mesoporous Materials* **2000**, *35*, 21.
(13) Jentoft, F. C.; Gates, B. C. *Topics in Catalysis* **1997**, *4*, 1.
(14) Weitkamp, J. *ChemCatChem* **2012**, *4*, 292.
(15) Haag, W.; Dessau, R. *Berlin (West), Vol. Ⅱ* **1984**, 305.
(16) Plank, C. J. In *Heterogeneous Catalysis—Selected American Histories* 1983, p 253.

(17) Degnan, T.; Chitnis, G.; Schipper, P. *Microporous and Mesoporous Materials* **2000**, *35*, 245.
(18) Kvisle, S.; Fuglerud, T.; Kolboe, S.; Olsbye, U.; Lillerud, K. P.; Vora, B. V. *Handbook of Heterogeneous Catalysis* **2008**.
(19) Chang, C. D.; Silvestri, A. J. *Journal of Catalysis* **1977**, *47*, 249.
(20) Chang, C. D. *Catalysis Reviews Science and Engineering* **1984**, *26*, 323.
(21) Froment, G.; Dehertog, W.; Marchi, A. *Catalysis-Vol. 9, Royal Society of Chemistry, Londen, pp. 1-64, 10 figg., 15 tabb* **1992**.
(22) Stöcker, M. *Microporous and Mesoporous Materials* **1999**, *29*, 3.
(23) Haw, J. F.; Song, W.; Marcus, D. M.; Nicholas, J. B. *Accounts of Chemical Research* **2003**, *36*, 317.
(24) Kaiser, S. *Arabian Journal for Science and Engineering* **1985**, *10*, 361.
(25) Venuto, P. B.; Landis, P. *Organic Catalysis over Crystalline Aluminosilicates*; Academic Press, 1968.
(26) Ono, Y.; Mori, T. *Journal of the Chemical Society, Faraday Transactions 1: Physical Chemistry in Condensed Phases* **1981**, *77*, 2209.
(27) Munson, E. J.; Haw, J. F. *Journal of the American Chemical Society* **1991**, *113*, 6303.
(28) Dahl, I. M.; Kolboe, S. *Catalysis Letters* **1993**, *20*, 329.
(29) Dahl, I. M.; Kolboe, S. *Journal of Catalysis* **1994**, *149*, 458.
(30) Dahl, I. M.; Kolboe, S. *Journal of Catalysis* **1996**, *161*, 304.
(31) Arstad, B.; Kolboe, S. *Catalysis letters* **2001**, *71*, 209.
(32) Arstad, B.; Kolboe, S. *Journal of the American Chemical Society* **2001**, *123*, 8137.
(33) Kärger, J.; Ruthven, D. *Handbook of Zeolite Science and Technology* **1992**, 341.
(34) Karger, J.; Ruthven, D. M. *Zeolites* **1989**, *9*, 267.
(35) Yasuda, Y. *The Journal of Physical Chemistry* **1982**, *86*, 1913.
(36) Eic, M.; Ruthven, D. M. *Zeolites* **1988**, *8*, 40.
(37) Hayhurst, D. T.; Paravar, A. R. *Zeolites* **1988**, *8*, 27.
(38) https://www.uni-leipzig.de/~pore/files/Stallmach_PFG_NMR_01.pdf.
(39) Jobic, H.; Theodorou, D. N. *Microporous and Mesoporous Materials* **2007**, *102*, 21.
(40) Mezei, F. *The Principles of Neutron Spin Echo*; Springer, 1980.
(41) Gorring, R. *Journal of Catalysis* **1973**, *31*, 13.
(42) Ruthven, D. M. *Microporous and Mesoporous Materials* **2006**, *96*, 262.
(43) Runnebaum, R. C.; Maginn, E. J. *The Journal of Physical Chemistry B* **1997**, *101*, 6394.
(44) Jobic, H.; Méthivier, A.; Ehlers, G.; Farago, B.; Haeussler, W. *Angewandte Chemie International Edition* **2004**, *43*, 364.
(45) Smit, B.; Maesen, T. L. *Chemical Reviews* **2008**, *108*, 4125.
(46) Jobic, H.; Theodorou, D. N. *The Journal of Physical Chemistry B* **2006**, *110*, 1964.
(47) Jobic, H. *Journal of Molecular Catalysis A: Chemical* **2000**, *158*, 135.
(48) Leroy, F.; Rousseau, B.; Fuchs, A. *Physical Chemistry Chemical Physics* **2004**, *6*, 775.
(49) Bouyermaouen, A.; Bellemans, A. *Journal of Chemical Physics* **1998**, *108*, 2170.
(50) Kar, S.; Chakravarty, C. *Chemical Physics Letters* **2002**, *352*, 294.
(51) Paul, W.; Yoon, D. Y.; Smith, G. D. *The Journal of chemical physics* **1995**, *103*, 1702.

(52) Toxvaerd, S. *The Journal of Chemical Physics* **1997**, *107*, 5197.
(53) Martin, M. G.; Siepmann, J. I. *The Journal of Physical Chemistry B* **1998**, *102*, 2569.
(54) O'Malley, A. J.; Catlow, C. R. A. *Physical Chemistry Chemical Physics* **2013**, *15*, 19024.

Chapter 2

Neutron Scattering Methods

Neutron scattering is a uniquely sensitive probe for studying the structure and dynamics of materials at an atomic and molecular level. Access is granted to the timescales of fast vibrational modes of molecules, frameworks and lattices, down to slow molecular diffusion. The increase in the use of neutron scattering in chemistry and materials science is illustrated by the commissioning of a new pulsed neutron source in Sweden (ESS). The following chapter will outline the basics of neutron scattering theory, focusing on inelastic scattering and thus the probing of dynamical properties (along with advantages and limitations compared to more conventional spectroscopic methods), followed by an introduction to the neutron sources available and their respective advantages and limitations (with particular emphasis on the ISIS spallation source). A discussion of inelastic vibrational neutron spectroscopy, quasielastic neutron scattering (including the neutron spin-echo method) and the methods used to derive diffusion characteristics will be discussed, along with information on the instrumentation associated with work in this thesis.

2.1 Introduction to Neutron Scattering [1]

Discovered in 1932 by J. Chadwick from bombardment of beryllium with α particles, the neutron (^1_0n) has zero charge, a rest mass close to that of a proton (1.674928 x 10^{27} kg), a spin of ½, and a magnetic moment. The zero charge means that interactions are confined to short range nuclear (or magnetic) interactions. For this reason the interaction probability is small, resulting in often deep penetration into the bulk of condensed matter.

The neutron may display both wave and particle like behaviour; the de Broglie wavelength of a thermal neutron is ~1-5 Å, comparable to interatomic and intermolecular distances, while its energy is in the range of 30-700 cm^{-1}, comparable to molecular vibrational energies. Low-energy neutrons (< 0.025 eV) have an energy distribution spectrum upon scattering which corresponds to very small energy transfers, down to sub-micro-eV (~0.1 cm^{-1}) in some quasielastic studies. These energy transfers correspond to molecular diffusion or rotation over time scales on the order of 10^{-10} – 10^{-12} s. Hence neutron scattering can yield detailed structural and dynamic information of the system under study.

The scattering of neutrons differs from other spectroscopic methods in that neutrons are scattered by nuclei, whereas photons (X-Rays, UV-Vis IR etc.) and electrons interact with the electron cloud, which leads to some of the advantages to be discussed. Briefly, some important distinctions to make are those between *elastic* and *inelastic* scattering, and between *coherent* and *incoherent* scattering (discussed in detail in section 2.2). Scattering is referred to as elastic when the neutron is scattered without a change in energy, as opposed to inelastic scattering where the neutron exchanges energy with the sample. Scattering is referred to as coherent when the scattered waves from different nuclei undergo interference, while incoherent scattering arises when interference between scattered waves is reduced by the natural isotopic and spin mixture of the sample, destroying the local order in the scattering (a consequence of the neutron interacting solely with the atomic nucleus). Coherent elastic scattering is measured in diffraction experiments, investigating structures and telling us about the relative positions of atoms in a

sample. Inelastic scattering in incoherent systems is the subject of this thesis, forming the basis of inelastic vibrational neutron scattering spectroscopy and quasielastic neutron scattering. Accordingly it will form the bulk of this chapter. Advantages of using inelastic/quasielastic neutron scattering (INS/QENS) to study dynamic processes in systems can be summarised as follows:

- INS spectra are not subject to the rules of optical selection. Due to the mass of the neutron, upon scattering the neutron transfers momentum to the nuclei in the sample. Observation is not limited to the Brillouin zone centre as with photon techniques (X-ray, infrared, Raman spectroscopy etc.). Moreover, unlike IR or Raman techniques, neutrons are able to interact with all vibrational modes of a molecule or adsorbed species.
- Neutron scattering is uniquely sensitive to ^{1}H hydrogen: the large incoherent scattering cross section of ^{1}H makes it far more visible than other elements, as opposed to photon techniques which are more sensitive to dynamics of heavy atoms due to the higher electron number. Significantly, the scattering cross section of deuterium is 1/40 that of hydrogen. Thus the signal of certain species/modes may be removed through deuteration of the compound.
- Neutrons can penetrate very deeply into the sample as mentioned above, often on the order of centimetres, which allows for measurement of bulk processes in solids, rather than limitation to processes taking place on the surface. The neutrons are also easily able to pass through sample containment vessels made of aluminium.
- The energy spectrum range of neutrons is very wide and the lower range of the vibrational spectrum < 300 cm^{-1} is routinely accessible unlike in infrared or Raman spectroscopy. Extremely low energy processes such as translational or rotational movements are accessible and quantifiable with very high resolution using quasielastic neutron scattering (QENS).
- INS data is straightforwardly and accurately comparable with computational simulations. INS vibrational intensities are related simply

to the atomic displacements of the scatterer and quantity thereof (modelled easily by classical dynamics as complications due to electro-optic parameters are not present). Absorption bands/intensities are calculated accurately by quantum mechanical calculations. While with QENS, the time and length scales of motion probed are in the remit of classical molecular dynamics simulations.

2.2 Principles of Neutron Scattering [2,3]

Basic principles governing the neutron scattering process will now be outlined followed by those of inelastic neutron scattering as a vibrational spectroscopy technique, and quasielastic neutron scattering for the study of molecular motions.

The energy of a neutron is equal to its kinetic energy

$$E = \frac{1}{2}mv^2 \tag{2.1}$$

Though as previously mentioned, it may also be considered as a plane wave with a wave vector k and wavelength λ:

$$k = \frac{m}{\hbar}v \qquad \lambda = \frac{2\pi}{|k|} = \frac{h}{mv} \tag{2.2}$$

Therefore the neutron kinetic energy may be written as

$$E = \frac{\hbar^2 k^2}{2m} = \frac{h^2}{2m\lambda^2} \tag{2.3}$$

After the neutrons are generated, their energy is determined upon passing through a hydrogenous moderator (consisting of hydrogenous substances such as water, H_2 or methane) at a temperature T to control the energy of the neutrons reaching a

sample. At thermal equilibrium, the distribution of velocities is dictated by a Maxwell distribution around an average velocity $\bar{v}$ so the energy distribution is

$$\bar{E} = \frac{1}{2}\, m\bar{v}^2 = \frac{3}{2} k_B T \tag{2.4}$$

Neutrons passing through a moderator at 300 K will have energies of $\bar{E} \approx 25$ meV corresponding to a wavelength of $\lambda \approx 1.8$ Å. The energies are therefore of the same magnitude as molecular energies, and the wavelengths of the same order of magnitude as molecular dimensions and *d*-spacings in lattices.

Two quantities are measured in a scattering experiment, the energy transfer $\hbar\omega$ and the momentum transfer vector Q also known as the wave vector transfer, or scattering vector

$$\hbar\omega = E - E_0 = \frac{\hbar^2}{2m}\,(k^2 - k_0^2) \quad , \tag{2.5}$$

E_0 and E are the initial and post scattering energies of the neutron. In this equation $k = 2\pi/\lambda$ and is the wave vector. Thus, the wave vector transfer is:

$$\vec{Q} = \vec{k} - \vec{k}_0 \tag{2.6}$$

The momentum transfer is

$$\overrightarrow{\hbar Q} = \overrightarrow{mv} - \overrightarrow{mv_0} \quad , \tag{2.7}$$

as the neutron is transferring momentum to the sample by virtue of any change in its direction or energy. The magnitude of Q increases with scattering angle 2θ.

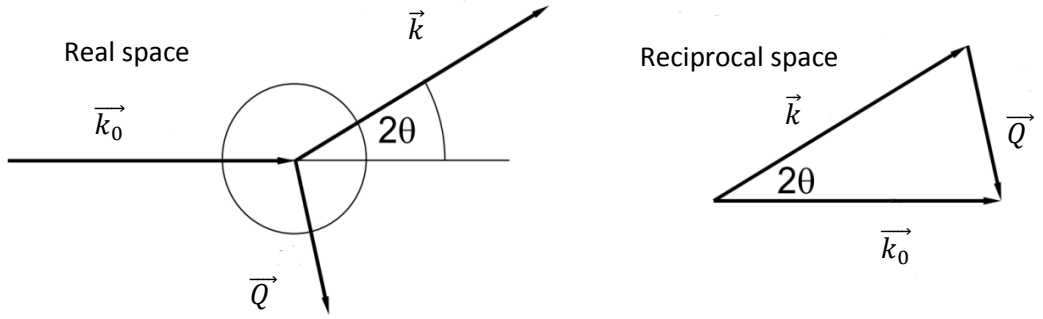

Fig. 2.1. The scattering triangle for an elastic scattering event where the neutron is scattered with no energy change ($k = k_0$). The scattering vector is given by the vector relationship $\overrightarrow{Q} = \vec{k} - \vec{k}_0$. Figure adapted from reference 4.

This scattering process may be treated classically, resulting in a vector triangle with two sides being the incident and scattered wave vectors (and thus momenta), therefore the momentum transfer vector Q completes the scattering triangle. In the case of elastic scattering in figure 2.1, Q may be calculated as follows:

$$Q = 2k_0 sin\theta \tag{2.8}$$

In the case of inelastic scattering, at a fixed angle 2θ, the magnitude and direction of Q varies with the energy transfer. Q therefore may not be kept constant with a varying energy transfer.

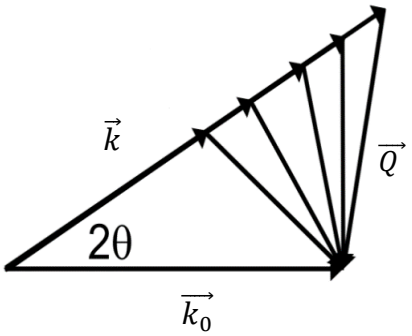

Fig. 2.2. The scattering triangle for an inelastic scattering event, where the neutron is scattered with an energy change. Upon gaining energy $k > k_0$ and upon losing energy $k < k_0$. The scattering vector is still given by the vector relationship $\overrightarrow{Q} = \vec{k} - \vec{k}_0$. Figure adapted from reference 4.

This leads to a reciprocal scattering triangle as in figure 2.2, and Q may be solved using the cosine rule for triangles as below.

$$Q^2 = k_0^2 + k^2 - 2k_0 k \cos 2\theta \tag{2.9}$$

An important point to make is that optical techniques usually ignore momentum as the mass of a photon is so small that no significant momentum transfer takes place (unless at energies close to the ionisation potential). So only the zero-momentum transfer region can be explored.

2.2.1 Neutron Scattering Cross Sections

There are two possibilities when a neutron reaches a nucleus in a sample. The neutron may be absorbed; creating a compound nucleus which decays either through γ radiation or α particle/triton emission; nuclear fission is also a possibility. However, the alternative, scattering may involve a change in direction and also in the energy of the neutron, which causes the small energies associated with atomic motions to be transferred to the neutron in the scattering process. Put simply, the scattering cross section is a measure of how strongly neutrons will scatter from a particular nucleus, or how 'large' the nucleus appears to the incident neutron.

One may define the number of scattering events occurring each second, assuming an incident current of neutrons per second per square centimetre I_0. A scattering cross section σ_s from the current of scattered neutrons I_s can be calculated.

$$I_s = I_0 \sigma_s \tag{2.10}$$

Here, σ_s has the dimension of a surface in the unit of barns, where 1 barn = 10^{-24} cm^2.

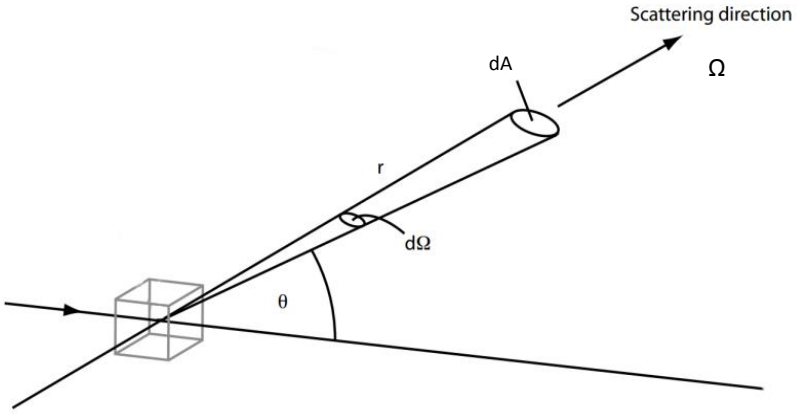

Fig. 2.3. The geometry of a scattering experiment. Some of the incident neutrons are scattered from the sample by an angle θ, in direction Ω into the detector area d*A*, a distance *r* from the sample. Figure adapted from reference 5

We consider a scattering measurement where an incident neutron is scattered by a sample in an angle θ onto an area of the detector d*A*, a distance *r* from the sample. Two quantities are measured by the experiment, the differential and double differential cross section. The differential cross section (eq. 2.11) in one direction gives the probability a neutron will be scattered in a solid angle element $d\Omega$ about the direction Ω as shown in figure 2.3.

$$\frac{\partial\sigma}{\partial\Omega} \tag{2.11}$$

The double differential cross section gives the probability that a neutron is scattered onto a solid angle element $d\,\Omega$ with an energy transfer $E = \hbar\omega$ and is also measured in Barns.

$$\frac{\partial^2\sigma}{\partial\Omega\partial E} = \frac{1}{\hbar}\frac{\partial^2\sigma}{\partial\Omega\partial\omega} \tag{2.12}$$

The relationship of this measurement to the scattering function used for deriving dynamical properties will be discussed in section 2.5. The scattering cross section is

split into coherent and incoherent contributions, affecting their visibility as the technique changes. The proportions of these contributions differ between elements and isotopes of each element. The theory behind, and consequences of these contributions will be discussed next.

2.2.2 Coherent and Incoherent Scattering Cross Sections

As previously mentioned, coherent and incoherent characteristics are dependent on the way that the neutron interacts with the sample both as a wave and as a particle. Viewed as a wave, the neutron may be seen to interact with multiple atomic centres. These new wavefronts will spread spherically from each new source and remain in phase. In an ordered lattice, the coherence (the fixed nature of the phase relationship between waves) of the incident wave is conserved. Constructive interference between the new wavefronts leads to well defined beams in certain directions and no intensity in other directions, causing the diffraction patterns characteristic of coherent scattering. The particle model of the neutron involves interaction with a single nucleus. There is no possibility of interference between wavefronts from many sources. This scattering is incoherent (the phase relationship of the waves is not consistent) and may be characterised by an even intensity distribution in all directions, the scattering in any one direction is weak.

We mentioned in the previous section that the total scattering cross section is measured by integrating over energies and solid angles. The neutron interacts with the sample by nuclear and magnetic forces, the nuclear part is very short range compared to the wavelength of the neutron. The nuclear scattering at the nucleus is isotropic and characterised by the scattering length b, independent of neutron energy. b has a complex part, related to the neutron absorption, and may be positive or negative depending on the attractive or repulsive nature of the interaction.

The amount of coherent/incoherent scattering of a sample depends on its composition. The coherent component will be more significant in a sample with

translational symmetry and long range order. Coherent scattering is reduced in a sample where the short range order varies, producing an incoherent background. Elemental solids should have long and short range order, however may not necessarily be purely coherent scatterers due to isotopic content.

The total cross section of a sample is the sum of the coherent and incoherent part

$$\sigma_{tot} = \sigma_{coh} + \sigma_{inc} \tag{2.13}$$

The two components are related to the mean and variance of the scattering length b as

$$\sigma_{coh} = 4\pi < b >^2 , \tag{2.14}$$

and

$$\sigma_{inc} = 4\pi(< b^2 > - < b >^2) \tag{2.15}$$

Again, this incoherent part is due to isotopic and spin effects (detailed comprehensively in reference 3), and the average cross section over all stable isotopes is detected experimentally

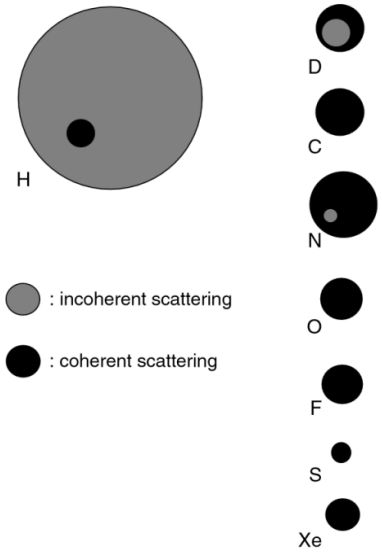

Fig. 2.4. Neutron scattering cross sections for certain elements, comparing their incoherent and coherent scattering cross sections. Figure adapted from reference 6.

Hydrogen has the largest total cross-section (82 barns). Furthermore, this cross-section is essentially incoherent because the non-zero nuclear spin of ^{1}H (1/2) gives rise to two scattering lengths of opposite sign with a weighted average close to zero. With incoherent scattering, the motions of individual protons or hydrogenous molecules can be investigated relatively unaffected by the presence of other elements. Other elements of note are aluminium which absorbs very weakly and is frequently used to build sample containers and cryostat windows; and vanadium, an almost purely incoherent scatterer but with a minimal cross section. It is therefore used as a standard material to calibrate instruments.

When using optical techniques, deuteration of hydrogenated compounds causes shifting in vibrational spectra due to changing the mass of the oscillator. This may expose modes involving the deuterated hydrogen atoms, however may not be so clear if the spectrum is densely populated by many modes. This band shift is the same in vibrational neutron spectroscopy; however the modes which have their hydrogen atoms replaced by deuterium have their scattering cross section reduced from 82 Barns to 7.6 Barns. Usually, this causes bands to be less visible and in many cases disappear from the spectrum allowing for a clearer interpretation.

2.3 Neutron Sources and Transportation [1]

Crucial to any neutron experiment is a source of neutrons and a means of neutron transport, before they may be detected and have their energy/momentum characteristics analysed after interactions with the sample. The production and transportation steps will be outlined in this section. Current sources of neutrons are either fission reactors or spallation sources. This section will discuss both, however with much more detail on spallation sources, as the ISIS neutron spallation source has provided the neutrons used for the work in this thesis.

2.3.1 Reactor Sources

Nuclear reactor sources produce fast neutrons (with energies of 1 - 20 MeV) by using thermal neutrons (0.025 eV), to induce fission in a critical mass of ^{235}U. For each fission event roughly 2.5 neutrons are produced. ~0.5 are lost to absorption while 1 leaves the reactor to be used experimentally, 1 is then used to perpetuate the reaction. In research reactors heat is an undesirable by-product and the size of the reactor must be limited in order to assist this heat removal which results in the limiting of neutron flux produced and available to the experimental stations.

A schematic of a reactor source is shown in figure 2.5. The reactor core sits in a large water tank which has both coolant and neutron moderator properties (moderators as briefly mentioned in section 2.2 are used to reduce the energies of neutrons usually from very high (MeV) energies, through inelastic collisions with hydrogenous material). The size of the tank also allows for specialised moderators and guide tubes for neutron transport. For safety reasons, reactors are usually triple contained to prevent release of fission products. The fuel is first cladded, surrounded by the water pool lined with concrete and stainless steel, and the

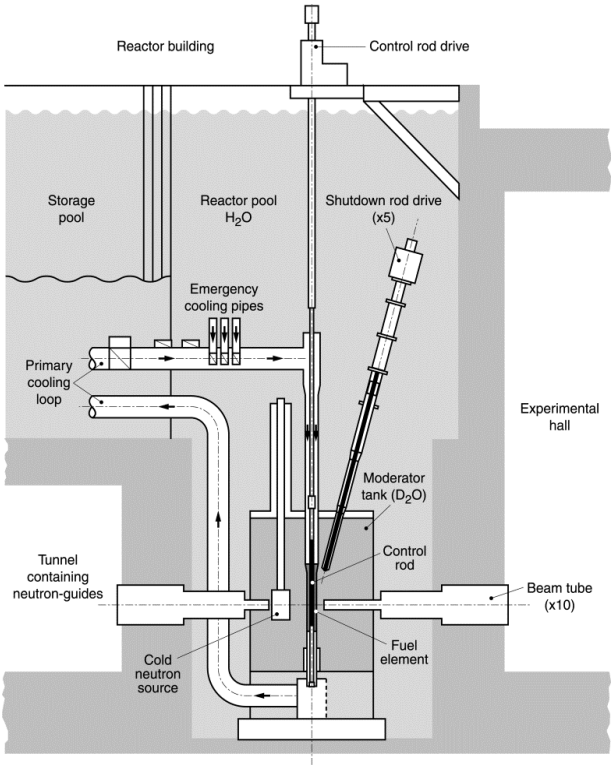

Fig. 2.5. Schematic of the FRM –II reactor, Münich, Germany. Figure reproduced from reference 7.

whole reactor is housed in a reinforced building accessed by an air lock.

Moderators are used to bring the fast neutrons (~1 MeV) to experiment appropriate energies. At reactor sources this is carried out by inelastic collisions with the D_2O coolant, achieving approximate thermal equilibrium at ambient temperature. At this temperature moderators produce neutrons with a mean energy of ~208 cm^{-1}, distributed in a Maxwell-Boltzmann distribution about this value (those outside this distribution are known as 'epithermal' neutrons). Thermal neutrons are not useful for many experiments, so must be moderated further using specialised moderators, such as liquid D_2 at 25 K to provide cold neutrons (peak flux at ~ 40 cm^{-1}).

Reactor sources are more common than the spallation sources described in the next section. They provide large numbers of cold and thermal neutrons with a constant flux. However, they are less able to produce epithermal neutrons (0.025 – 0.4 eV) necessary for neutron vibrational spectra. The energy spectrum of the neutrons from these sources is also narrower. For this reason along with safety, political and environmental concerns, it is less likely that reactor sources will play a significant role in the future of neutron scattering research.

2.3.2 Spallation Sources - ISIS

Spallation sources are based on the process depicted in figure 2.6. A heavy metal target is bombarded with high energy protons (800 MeV), triggering an intranuclear cascade of the target atoms releasing energy, and giving off neutrons. Some of these leave the target to be used in experiments; other nuclei propagate the cascade. Each proton which hits the target results in roughly 1.5 neutrons, and each pulse of protons hitting the target results in a very intense neutron pulse. The ISIS neutron spallation source (Didcot, Oxfordshire, UK) will be discussed in detail now.

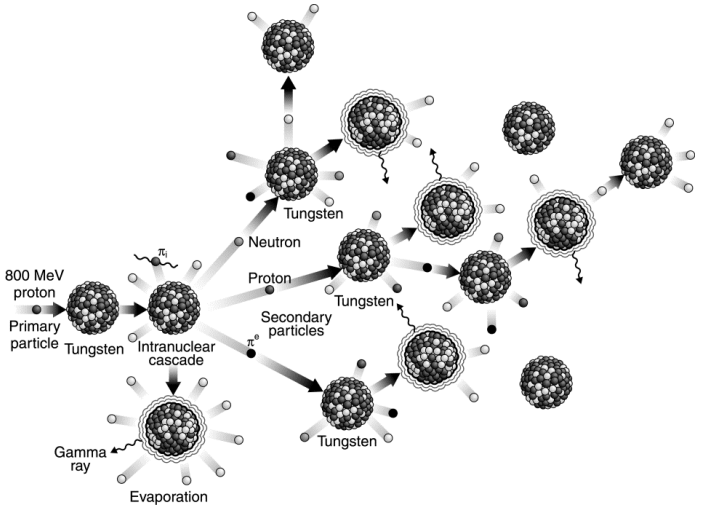

Fig. 2.6. Schematic of the spallation process using a tungsten target. Figure reproduces from reference 1.

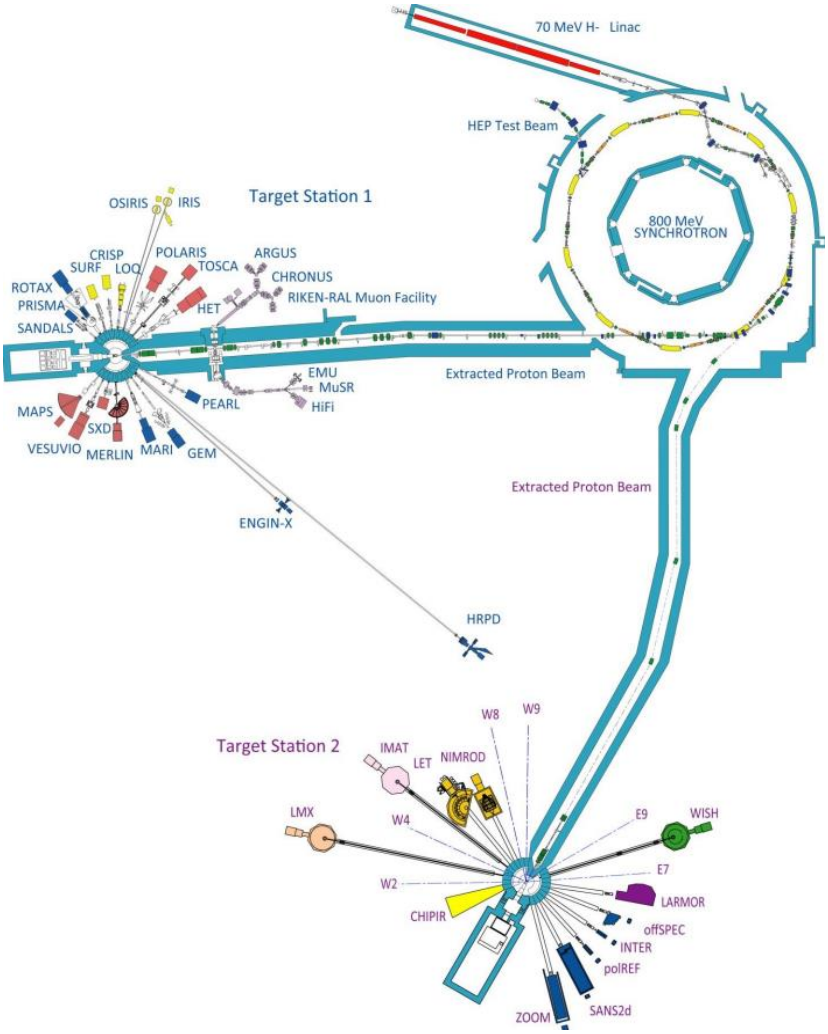

Fig. 2.7. The ISIS Facility, Oxfordshire, UK. The accelerator, synchrotron, and extracted proton beamlines are shown, leading to the high power target station 1 and lower energy target station 2. Figure reproduced from reference 21.

The layout of the ISIS facility is depicted in figure 2.7 and the method with which neutrons are generated is as follows:

H_2 gas is dissociated to form H^- ions after electron transfer from a caesium coated cathode.

- The H^- ions are extracted from the ion source by an electric field into a quadrupole accelerator. Upon acceleration they are then injected into a linear accelerator (linac) with energy of 665 keV.
- The linac accelerates the beam to 70 MeV, resulting in a 200 μs long H^- pulse of current 22 mA.
- The pulse then enters a synchrotron, after passing through a stripping foil (0.3 μm thick aluminium oxide) which removes the electrons from the H^- beam to create protons. The proton beam is injected at intervals into the synchrotron approximately 130 times until 4.2 x 10^{13} protons accumulate.
- The protons are trapped into two bunches, then accelerated to 800 MeV (84% of the speed of light) by ferrite-tuned radio frequency cavities.
- The proton pulses are 100 ns long (separated by 230 ns) upon transferral into an extracted proton beamline (EPB) through a deflection by a 'kicker' magnet.
- The target (tungsten plates surrounded by flowing D_2O coolant, sitting in a beryllium reflector with moderators above and below) is at the end of the 200 m EPB. The proton beam hits the target causing the spallation process shown in figure 2.6. Neutrons produced through spallation enter a moderator to lose energy.
- The neutrons which happened to travel in the direction of the neutron port are used for experiments. Some travelling in other directions may be reflected back into the moderators.

Neutrons are transported from the source along beam tubes arranged tangentially from the target, to avoid primary radiation such as fast neutrons or gamma rays. It is important to note that neutrons hit the sample and other important components by chance. Being neutral, it is very difficult to influence their trajectory. For the distance between the moderator and sample (d_i) the flux decays as $(1/d_i^2)$, thus flight paths must be kept short. Beam tubes are evacuated to avoid attenuation by air scattering. For neutrons of long wavelength, neutron guides may be used, which are square or rectangular section tubes made from metal (nickel is preferred)

coated flat glass. Long wavelength neutrons undergo total external reflection from the metal surface and are kept in the guide.

2.4 Inelastic Neutron Scattering Spectroscopy [8]

Vibrational spectroscopy may be performed either through absorption of a photon which is of the correct energy to excite a vibrational transition, or through scattering of a particle inelastically by an atom involved in the vibration – the latter is the basis of INS. INS encompasses a wide range of energies. However, this section is restricted to the 'infrared region' applied to studying the frequencies of bond vibration in a molecule (0 – 4000 cm^{-1}). As the neutron has mass, the transfer event involves both energy transfer (E, cm^{-1}) and momentum transfer (Q, $Å^{-1}$). As outlined in section 2.1, Q is the difference in incident and outgoing wavevector k, where $k = \frac{2\pi}{\lambda}$. INS has the advantage noted earlier, of not being bound to the same electro-optical parameters governing IR or Raman scattering (transition dipole moment and polarisation coupling parameters respectively). The degree of scattering is dependent on the aforementioned scattering cross section of the nucleus, the largest incoherent cross section being ^{1}H hydrogen (80.3 Barn), almost an order of magnitude larger than that of other elements. For this reason INS is used predominantly for investigating vibrations within hydrogenous molecules. The intensity of an INS band, the scattering function (S) is described by:

$$S(Q, n\omega_i) \propto \frac{(QU_i)^{2n}}{n!} \exp[(-QU_{Tot})^2]\sigma \qquad (2.16)$$

Here, ω_i is the i^{th} mode at frequency ω_i, n is the order of the oscillation (n = 1 for a fundamental oscillation, 2 for a first overtone/binary combination, 3 for a secondary overtone/tertiary combination etc.) U_i is the root mean squared displacement of the atoms associated with the oscillation. U_{Tot} is the total mean square displacement of all atoms in all modes. σ is the inelastic neutron scattering cross section. The exponential term is known as the Debye-Waller factor, the magnitude of which is determined by thermal motions of the molecule. This may

lead to a low signal to noise ratio, but can be minimised by performing the measurements at low temperature, typically < 30 K.

2.4.1 Direct Geometry Instruments

INS spectroscopy aims to measure the scattering intensity $S(Q, \omega)$ at a particular energy transfer $\hbar\omega$ and momentum transfer Q. The instruments relevant to this thesis are those which fix the incident energy of the neutrons, while measuring a range in energy of scattered neutrons. These are known as direct geometry instruments. Direct geometry instruments use choppers to fix the energy of the incident neutron beam, choppers interrupt the white beam by allowing the beam to pass through only during the time it is open. The phasing of the chopper opening to the beginning of the beam determines the frequency (and thus the energy) of the beam transmitted, due to the chopper being a fixed distance from the moderator.

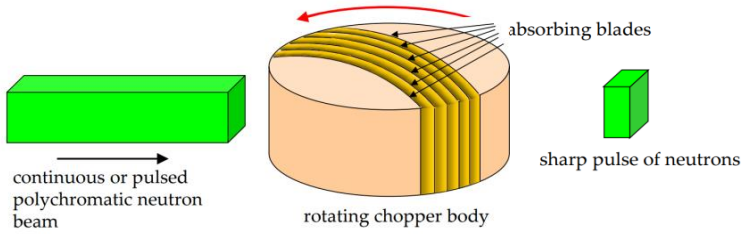

Fig. 2.8. Schematic of a Fermi chopper used to monochromate a beam of neutrons. Figure reproduced from reference 9.

Figure 2.8 gives an example of a Fermi chopper, relevant to work carried out in this thesis for its use on the MAPS spectrometer. The MAPS Fermi Chopper is comprised of an aluminium rotor approximately 15 cm in diameter, suspended magnetically in a vacuum, rotated at up to 600 Hz. The beam is intersected by vertical thin sheets of absorbing material such as boron carbide interleaved with aluminium (transparent with regard to neutrons), which acts as a series of parallel slits. The incident neutron energy is then selected by phasing the opening time of the slit package to the travelling of the neutron pulse.

After scattering from the sample, the final energy is determined from the flight time of the neutron through knowing the sample to detector distances. Direct geometry instruments are able to measure Q and ω independently. Detectors are positioned at different angles allowing measurement of Q at a given energy transfer, since neutrons may be scattered with the same energy transfer but in different directions, and Q is different for each scattering angle.

When using a direct geometry instrument, the resolution of the machine is a fraction of incident energy (typically 1-5%), the drawback of which is that to obtain a well resolved spectrum across the entire energy range, one must use multiple incident energies. The resolution also depends inversely on the sample to detector distance.

2.4.2 The MAPS Spectrometer [8,10]

The work carried out in chapter 5 used direct geometry instrument MAPS at the ISIS Neutron Spallation Source. A schematic of the instrument is shown in figure 2.9. The pulsed beam from the target passes through a water moderator at 300 K; the flux distribution as a function of energy is measured by Monitor 1. The pulse then passes through a Nimonic chopper, which is a bar of strongly scattering metal which blocks the beam when the proton pulse hits the target, thus blocking gamma rays and unmoderated neutrons which may saturate the detectors. The beam then hits a Fermi chopper. The incident energy is then chosen by phasing the Fermi chopper to within 0.1 ms of the chopper opening time with the pulse leaving the target station. The energy range may be between 70 – 8000 cm^{-1}. The flight path between the moderator and the sample is 12 metres (the primary flight path). The sample is then 6 metres from the detector bank (the secondary flight path). The detector bank consists of ~16 m^2 of position sensitive ^{3}He tube detectors. Upon absorption of a neutron by the ^{3}He isotopes in the detector, the nuclear decay produces charged hydrogen ions detected by an anode as in equation 2.17.

$$^{1}_{0}n + {}^{3}_{2}He \rightarrow {}^{3}_{1}H + {}^{1}_{1}H + 0.77\ MeV \qquad (2.17)$$

The low angle detector bank covers ± 30°, and the high angle bank covers 20° to 60°. At small angles in the forward scattering direction, one may measure in small Q. The consequence of which is that by selecting only low Q data, modes at higher energies are clearly visible due to the phenomena represented in equation 2.16.

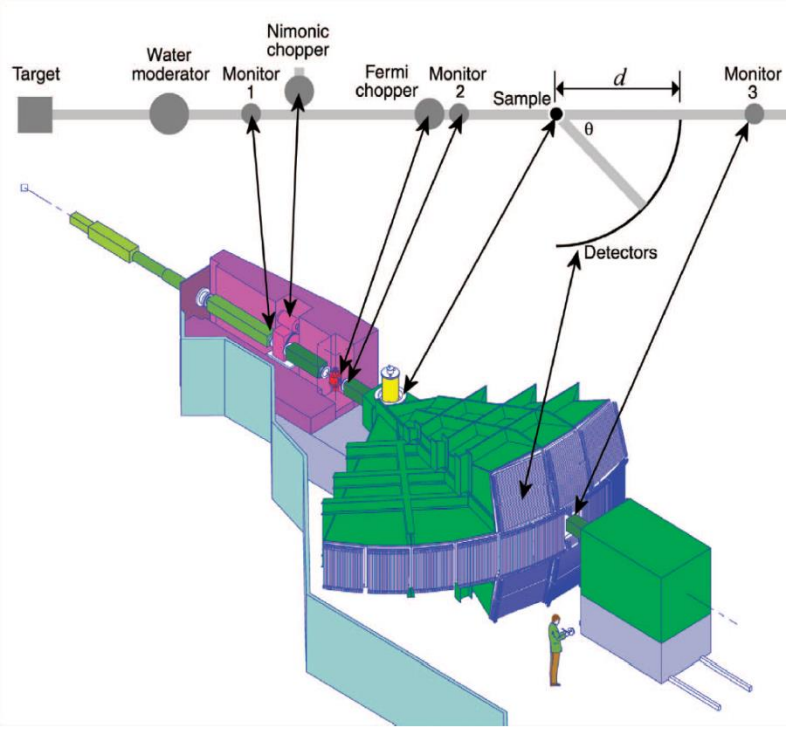

Fig. 2.9. of the MAPS spectrometer at the ISIS neutron source. Figure reproduced from reference 10.

2.5 Quasielastic Neutron Scattering [3,6]

The use of low energy neutrons in the study of molecular transport is based on the neutron energy being close to that of rotational energy levels and energies associated with the translation of molecules. Quasielastic scattering focuses on the scattered energy range of ±2 meV to sub μeV levels, consistent with particles moving on the timescales of pico- to nanoseconds. These motions produce a

broadening in the elastic line as in figure 2.10 representing neutrons scattered with zero energy transfer.

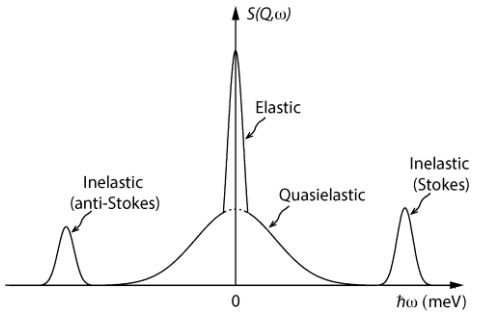

Fig. 2.10. Schematic representation of a neutron scattering spectrum with elastic, inelastic and quasielastic components. As shown, the quasielastic scattering constitutes the broadening of the elastic line, which itself also has a width, due to instrumental resolution factors. Figure reproduced from reference 11.

Sources able to produce large fluxes of low energy neutrons are conducive to the design of spectrometers with high resolution. Exact line shapes may then be examined and fit to numerous theoretical models which yield information of the dynamics of molecules. This section will outline the relationship between this quasielastic broadening and molecular motion, the basis of this technique. This account will be followed by a discussion of how these observables are interpreted by various models of diffusivity, such as free Fickian diffusion, jump diffusion and diffusion within a confined volume. Finally the characteristics of the time-of-flight spectrometer OSIRIS used for the work in this thesis will be outlined, and the neutron spin echo (NSE) technique will be briefly discussed.

2.5.1 The QENS Method

As mentioned in section 2.1, experimentally one measures the double-differential cross-section $\frac{\partial^2\sigma}{\partial\Omega\partial E}$ of scattered neutrons. The measured intensity can be split into coherent and incoherent contributions, as in the case of the scattering cross-sections:

$$\frac{\partial^2\sigma}{\partial\Omega\partial E} = \frac{k}{k_0}\frac{1}{4\pi\hbar}\left[\sigma_{coh}S_{coh}(Q,\omega) + \sigma_{inc}S_{inc}(Q,\omega)\right] \qquad (2.18)$$

Here, $S_{inc}(Q,\omega)$, the incoherent scattering function (or dynamical structure factor) decays smoothly with Q for incoherent scattering due to the Debye-Waller factor (energy transfer due to thermal vibrations of the scatterer). The scattering functions are four dimensional Fourier transforms of the self-part of the van Hove correlation function $G_{s,i}(r,t)$

$$G_{s,i}(r,t) = \langle\delta[r - r_{li}(t) + r_{li}(0)]\rangle = \frac{1}{N_i}\left\langle\sum_{l=1}^{N_i}\delta[r - r_{li}(t) + r_{li}(0)]\right\rangle \qquad (2.19)$$

This is a probability density, in three-dimensional space, that a molecule of species *i* will be displaced by a vector *r* within time *t* at equilibrium. The Fourier transform has this form:

$$S_{inc}(Q,\omega) = \frac{1}{2\pi}\int dt\exp(-i\omega t)\int dr\exp(iQ\cdot r)G_s(r,t) \qquad (2.20)$$

Q and ω are Fourier transformed variables of *r* and *t*, with Q having the dimension of reciprocal distance and ω having the dimension of angular frequency ($\frac{2\pi}{T_{seconds}}$). For this reason, small Q involves average values over long distances and slow motions taking place over long times in $G_s(r,t)$, will correspond to small ω. When the characteristic time of the motion is shorter than the inverse of the instrumental resolution, a broadening of the scattering function will be observed as in figure 2.11. However, when the timescale of movement is larger than the inverse of the instrumental resolution (slower than the machine can measure), the shape of the peak is given by the instrumental resolution function, either a Gaussian or a delta function, and an instrument of higher energy resolution must be used. The

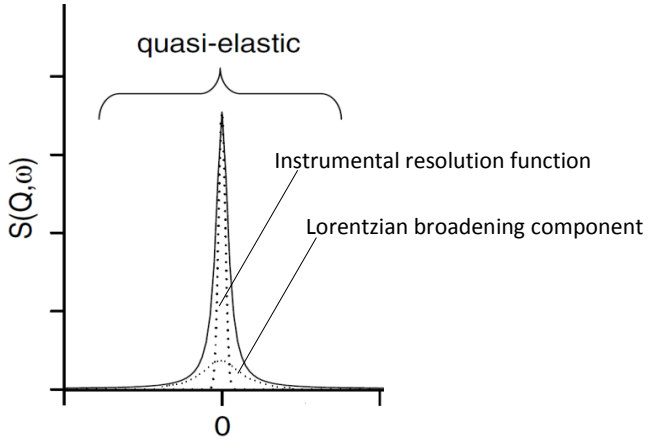

Fig. 2.11. Schematic of a quasielastic spectrum, with the convolution of the instrumental resolution function and the broadening component. Figure adapted from reference 6.

broadening of the scattering function must be convoluted with the instrumental resolution function in order to be quantified. For this reason the scattering function is fitted by a linear combination of the instrumental resolution function, and a Lorentzian function to describe the broadening.

Crucially, the spectrum is measured over a range of Q values and in the case of translational motions the Lorentzian characteristics will vary as a function of Q as shown in figure 2.12. The dependence of this Lorentzian broadening, more specifically the half-width at half-maximum (HWHM) $\Delta\omega$ of the is measured as a function of Q, and this dependence may be fitted to theoretical models which may characterise the diffusion behaviour.

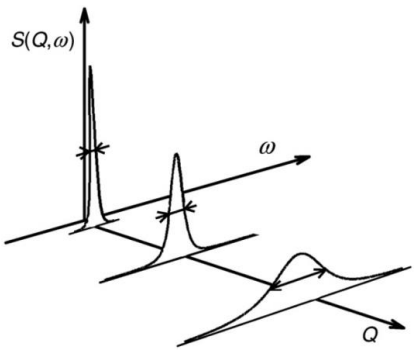

Fig. 2.12. Schematic of quasielastic broadening as a function of Q. Figure reproduced from reference 6.

These models may be based on free diffusion with liquid like character (Fickian diffusion), movement where a molecule may remain stationary for a given period on a site before translating very quickly to the next site (jump diffusion), or movement of a molecule confined to a sphere of a given diameter. In each case, the diffusion coefficient may be calculated along with other parameters associated with these models. These models will now be outlined in the following sections.

2.5.1.1 Deriving Fickian Self-Diffusion Coefficients

Motions of hydrogen atoms in a sample over long enough times and distances are described by Fick's second law:

$$\frac{\partial p(\boldsymbol{r},t)}{\partial t} = D_s \nabla^2 p(\boldsymbol{r},t) \tag{2.21}$$

With $p(\boldsymbol{r},t)$ being the probability of finding an atom at position $\boldsymbol{r}$ at time t. The self part of the van Hove correlation function $G_s(r,t)$ in equation 2.19 is the solution for this. Performing a spatial Fourier transform of equation 2.20 (the obtained spectral profile) leads to the intermediate self-scattering function

$$I_s(Q,t) = \exp(-D_s Q^2 t) \tag{2.22}$$

After which the incoherent scattering function $S(Q,\omega)$ may be obtained by the time Fourier transform of this intermediate scattering function, showing the incoherent scattering function changes with mobility as

$$S(Q,\omega) = \frac{1}{\pi}\frac{D_s Q^2}{\omega^2 + (D_s Q^2)}\ , \tag{2.23}$$

corresponding to a Lorentzian energy profile in the case for isotropic diffusion. As mentioned earlier, the scattering functions (as a function of energy) are measured at differing scattering vector (Q) values, experimentally achieved by using position sensitive detectors at different angles corresponding to different Q. In the case of

Fickian diffusion the half-width at half-maximum ($\Delta\omega$) of this Lorentzian profile has the following dependence on Q:

$$\Delta\omega(Q) = D_s Q^2 \tag{2.24}$$

Therefore a plot of the Lorentzian HWHM as a function of Q^2 will yield a linear dependence, the gradient of which is the self-diffusion coefficient upon conversion of energy to time, illustrated in figure 2.13.

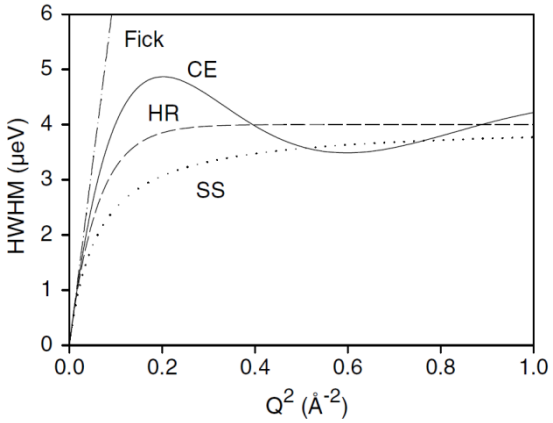

Fig. 2.13. Q dependences of the HWHM observed when molecules exhibit Fickian behaviour, jump diffusion consistent with the Chudley and Elliot (CE), Hall and Ross (HR), and Singwi and Sjölander (SS) models. Figure reproduced from reference 6.

2.5.1.2 Characterising Jump Diffusion

At smaller distances (measured at larger Q values) in confined systems, often there is a deviation from the linear dependence of $\Delta\omega$ with Q. Though for isotropic systems the scattering function will be Lorentzian in form, the width of the energy spectrum will differ from the DQ^2 dependence when we reach higher Q. The model of Chudley and Elliot [12] was originally developed describing liquid systems with local order but is widely used for systems such as ion diffusion in lattices through to diffusion of sorbates in microporous solids. It proposes that for an average time interval τ an atom remains on a given site vibrating about a centre of equilibrium. After this time the atom moves rapidly to another site in a negligible jump time

compared to the time spent at the residence site. The Chudley and Elliott model assumes a constant jump length *d,* with the HWHM dependence on Q being

$$\Delta\omega(Q) = \frac{1}{\tau}\left(1 - \frac{\sin(Qd)}{(Qd)}\right) \tag{2.25}$$

Other models exist such as the Hall and Ross[13] and the Singwi and Sjölander[14] models, which incorporate a jump length distribution around a mean square jump length. Importantly all the current jump diffusion models available make the same assumption that the time taken for the jump along the distance *d* is negligible and is not considered in the broadening. The Q dependencies of the broadenings associated with these models are depicted in figure 2.13, along with a Q^2 dependence associated with Fickian diffusion for a given diffusion coefficient (1 x 10^{-9} m^2s^{-1}). It is shown that at small Q values, the Q dependence matches that of Fickian diffusion behaviour for all jump models, thus sufficient resolution at small Q may yield a Fickian diffusion coefficient measureable even in the presence of jump diffusion.

2.5.1.3 Diffusion in a Confined Volume

A variety of physical systems where diffusion of molecules confined in media or restricted to movements in certain dimensions are of interest, such as lamellar structures, polymers, clay minerals and of course diffusion of sorbates in zeolites. In terms of QENS spectra, there is a change due to the suppression of trajectories over dimensions outside of the confinement volumes. Volino and co-workers[15] developed a model to describe a scattering molecule undergoing translational motions in a confined spherical volume of diameter d_{conf}. This scattering model is based on the general problem of a particle diffusing in a potential field of spherical symmetry, where the potential is low inside the sphere's volume but infinite outside of it, and how the van Hove correlation function behaves under these conditions. Detailed derivation of this model may be found in reference 17 and has

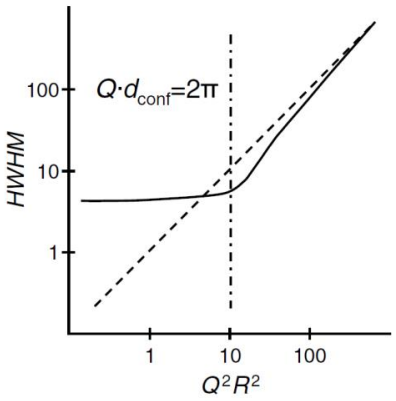

Fig. 2.14. Q dependence of the HWHM for a molecule diffusing inside a sphere. Where the dashed line is the Q dependence of the corresponding unconfined Fickian behaviour. Figure reproduced from reference 18.

been used in systems of confined water in Nafion membranes [16] and Vycor glass.[17] As the trajectory is terminated at low Q values corresponding to larger distances, one observes a large and dominant elastic mode (adherence to the instrumental resolution function) at low Q values. Indeed, at $Q = 2\pi/d_{conf}$, the intensity of the quasielastic component is close to negligible, and the width of the Lorentzian describing that component will stay constant at all Q values below this threshold, and equal to 4.33 D/r_{conf}^2. This is illustrated in figure 2.14 where a plateauing in the Q dependence of the Lorentzian HWHM is observed due to the confinement to these spherical dimensions. After this Q value, a normal DQ^2 dependence is observed, showing that the motion inside this sphere is Fickian in nature inside this volume, allowing the confined diffusion coefficient to be calculated. If the Q dependence after $Q = 2\pi/d_{conf}$ deviates from linearity, one may be observing jump diffusion within the confined volume and fit an appropriate model, previously shown for water diffusion in lignite coal pores.[17]

2.5.2 Quasielastic Neutron Scattering Techniques and Instrumentation

Instruments for measuring quasielastic neutron scattering are based on the time-of-flight (TOF) and back-scattering (BS) technique. Broadening of the elastic peak will be observed if the molecules diffuse over a time scale ranging from 10 ns to 1ps.

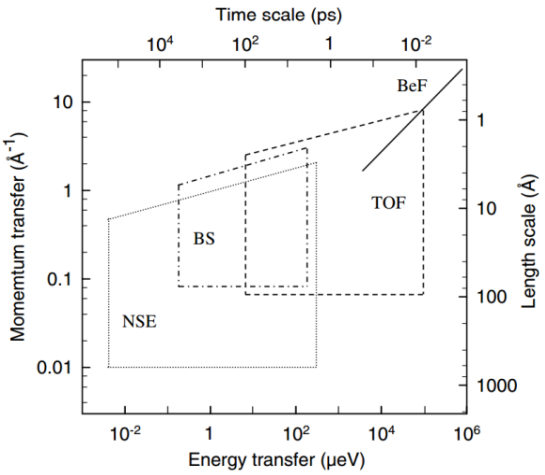

Fig. 2.15. Time, length, energy and momentum transfer ranges available to the types of QENS spectrometers at the Institut Laue-Langevin: Neutron spin-echo (NSE), back-scattering (BS), time-of-flight (TOF), and beryllium-filter (BeF) methods. Figure reproduced from reference 6.

The window of observation is dependent on the energy resolution of the machine, where a typical TOF instrument ranges in resolution between 10 and 100 μeV (~1 – 100 ps), while a BS machine may have resolution on the order of 1 μeV (~1 ns). Depending on the timescales involved; vibrational, rotational and translational motions may be characterised on TOF and BS instruments. Figure 2.15 shows the typical energy, time and Q ranges associated with such instruments, illustrating that TOF instruments may probe time scales on the order of 10 femtoseconds to hundreds of picoseconds, and BS spectrometers may extend this range to up to 10 nanoseconds. The principles governing TOF and BS spectrometers will first be outlined, followed by a discussion of the OSIRIS spectrometer at the ISIS neutron spallation source.

2.5.2.1 Time-of-flight Instruments

Time-of-flight spectrometers allow the simultaneous recording of scattered neutrons over a large Q and ω range. The sample is surrounded by an array of detectors covering the selected Q range shown in figure 2.16. The energy is related to the flight time of the scattered neutrons. The start time is defined by a chopper in the incident beam and from the time it takes a neutron to arrive at the detector; its velocity and finally its energy transfer can be calculated. Monochromatisation of

the incoming neutron beam is achieved by a sequence of choppers phased to transmit a single wavelength only (partly outlined in section 2.4.1). For pulsed sources such as at ISIS, one may use the pulsed nature of the primary beam either to use the time-of-flight from the source to the chopper to define the incident energy (direct geometry instruments) or use all incident energies and select a single energy from the scattered neutrons through the use of analyser crystals (indirect geometry instruments).

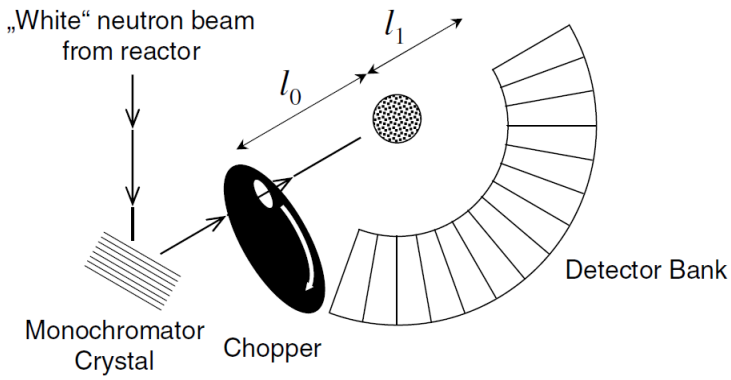

Fig. 2.16. Schematic setup of a time-of-flight spectrometer. Figure reproduced from reference 18.

2.5.2.2 Backscattering Instruments - OSIRIS[19]

Energy resolution of current TOF spectrometers is limited to about 0.01meV, corresponding to an upper limit of sampling ~ 200 ps. This is a sufficient time range for study of processes in larger pore zeolites or of smaller molecules. However, systems with bulky molecules in smaller pore zeolites, which may undergo jump diffusion with residence times on the order of nanoseconds are not within this resolution range. This resolution may be increased by use of the backscattering technique. One form of instrument which employs this is the inverted-geometry instrument. A schematic of the inverted geometry back scattering process is shown in figure 2.17.

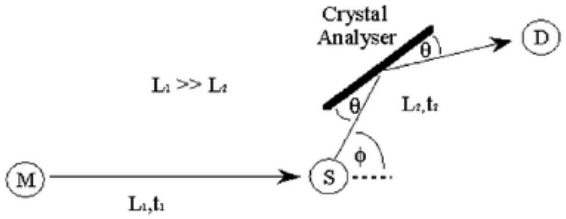

Fig. 2.17. Schematic of an inverted geometry instrument, where M is the moderator, S is the sample position and D is the detector. θ is the Bragg angle of scattering from the analyser crystal and ϕ is the scattering angle from the sample. Figure reproduced from reference 19.

The energy resolution of the spectrometer is limited by the analyser crystal selectivity. The spread of wavelengths is determined by angular divergence upon Bragg scattering. Referring to figure 2.17, the time taken, (t_1), for each neutron to travel distance L_1, is recorded. A single wavelength (and thus energy) is selected for detection from the scattered energy profile, achieved *via* Bragg diffraction from the analyser crystal so the energy of each detected neutron is known from Bragg's law. Flight time between a neutron from the analyser crystal and the detector (t_2) is readily determined, and the total time of flight (t) is the sum of t_1 and t_2. One may set an analyser crystal at a Bragg angle as close to 90° as possible to improve the resolution, which is known as backscattering or near-backscattering geometry.

Neutron energy transfer is related to the TOF measurements, neutron mass and flight paths by the following relationship:

$$\Delta E = E_i - E_{an} = \frac{1}{2}\, m_n \left[\left(\frac{L_1}{t - t_2} \right)^2 - \left(\frac{L_2}{t_2} \right)^2 \right] \qquad (2.25)$$

where E_i is the incident neutron energy, E_{an} is the energy of the neutron leaving the analyser crystal towards the detector, and m_n is the neutron mass. As already mentioned, stochastic or random molecular motions of energy transfers close to the elastic line, lead to this broadening of the elastic line which comprises quasielastic neutron scattering data. This elastic line should be a delta function.

However, experimentally this elastic line has a width due to characteristics of the spectrometer as illustrated in figure 2.11. This resolution is defined by as

$$\frac{\Delta E}{E} = 2\left[\frac{\Delta t_m}{t}\right] \otimes \left[\frac{\Delta d}{d}\right] \otimes \left[cot(\theta)\, \Delta\theta\right], \tag{2.26}$$

where t_m is the energy dependent time width of the neutron pulse, $\Delta\theta$ is the uncertainty in the Bragg angle at the analyser crystal, and Δd is the uncertainty of the analyser crystal lattice spacing. This equation leads to the resolution being highest (uncertainty, ΔE being lowest) when the Bragg angle is close to 90˚ (the beam from the analyser crystal will be scattered back towards the sample position). All these factors contribute to the elastic line width which restricts the time regime that the instrument is able to resolve. Designing a backscattering instrument aims to limit this instrumental broadening, while providing a high flux to the sample with a wide range of energy and momentum transfer, though compromises must be made on each variable.

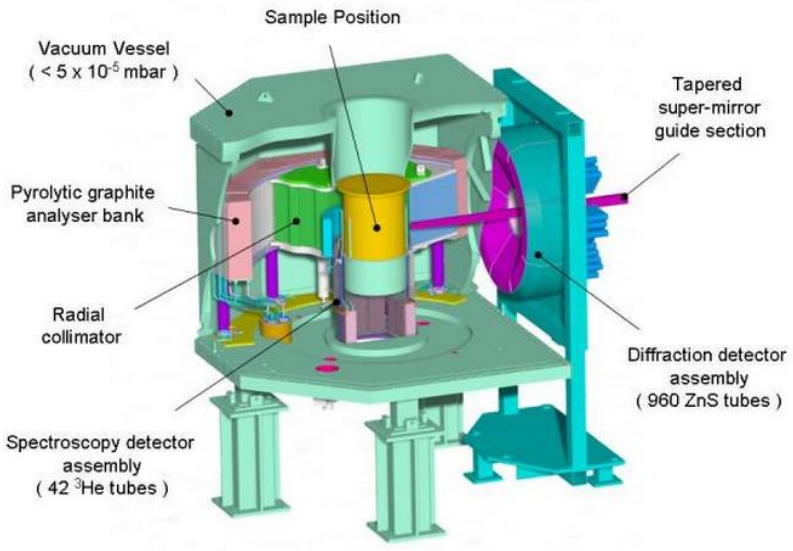

Fig. 2.18. Cutaway diagram of the near-backscattering crystal analyser spectrometer OSIRIS. Figure reproduced from reference 20.

The OSIRIS spectrometer at the ISIS neutron spallation source is separated from the spallation target by a liquid hydrogen moderator cooled at 22 K, allowing access to a large flux of long wavelength cold neutrons. Two counter rotating disk choppers

of 30 cm radius select the neutron velocity at rotation speeds of 50 or 25 Hz. These are located 6.3 and 10 m from the moderator, and the wavelength selection of these determines the wavelength of neutrons reflected from the analyser and in turn the energy resolution/transfer range of the experiment. The neutrons are transported from the moderator using a 34 m curved guide allowing neutrons with wavelength above 1 Å to propagate by reflection from so called 'super-mirrors', made of glass substrates with nickel-titanium coatings.

The spectrometer is inside a 5 m^3 evacuated vessel. The analyser crystals are pyrolytic graphite crystals oriented close to back scattering geometry to energy analyse neutrons from the sample. The analyser itself is comprised of 40 x 226 pyrolytic graphite crystals (10 × 10 × 2 mm thick) mounted on an aluminium backing plate, which is approximately 0.9 m from the sample covering angles from 11 to 155°, intercepting approximately 9% of the total scattered beam. Two analysing reflections are possible: 002 and 004, with analysing energies of 1.845 and 7.375 meV, providing energy resolutions of 24.5 and 99 μeV respectively. The analysed beam is detected using a multi-detector composed of 42 x ^{3}He half-inch diameter detector tubes located approximately 0.67 meters from the analyser which gives a total secondary flight path of 1.582 m. In the 002 reflection used for work in this thesis, an energy range of ± 0.66 meV may be measured, in a Q range of 0.18 to 1.8 $Å^{-1}$.

2.5.3 Neutron Spin-echo Techniques

There are very few neutron spin-echo (NSE) instruments in existence and thus access is very restricted. NSE studies can probe timescales two orders of magnitude longer than conventional TOF/BS instruments as illustrated in figure 2.15. The incident energy does not need to be so accurately defined, as the energy resolution is not determined by the monochromatisation of the incident neutron energy, so a broad incident wavelength distribution may be used ($\Delta\lambda/\lambda$ = 15%).

The velocities of polarized neutrons are compared before and after the scattering event, using the Larmor precession of the neutron spin in a B magnetic field region of length l. The precession angle, φ, of the neutron is given equation 2.27, where γ is the gyromagnetic ratio of the neutron and v is its velocity.

$$\varphi = \frac{\gamma B l}{v} \tag{2.27}$$

The spin vector acts as an internal timer linked to each neutron, connecting it to the velocity measurement. This allows the velocities before and after scattering of the same neutron to be compared so a direct measurement of the velocity difference can be performed.

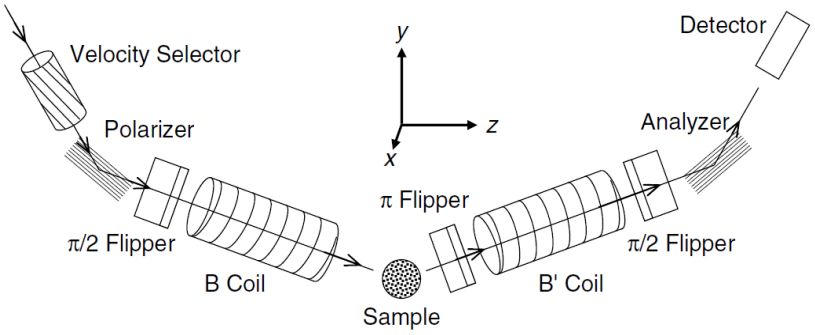

Fig. 2.19. Schematic of a neutron spin-echo spectrometer reproduced from reference 18.

The sample is kept between two identical precession coils. A π flipper close to the sample inverts the sense of precession of the neutron, the spin is turned by 180° so φ becomes -φ. If there is no energy transfer (elastic scattering) the original beam polarisation is obtained. For energy transfers in the quasielastic regime, the total precession angle may be expressed as a function of the energy transfer:

$$\varphi = \omega t \tag{2.28}$$

The proportionality constant t is called the spin echo time (or Fourier time) and is equal to

$$t = \frac{\hbar\gamma Bl}{mv^3} \tag{2.29}$$

Experimentally one measures the beam polarisation, the average cos φ

$$\langle \cos\varphi \rangle = \int S(Q,\omega)\cos(\omega t)\, d\omega = I(Q,t) \tag{2.30}$$

One can see that NSE measures the intermediate scattering function $I(Q,t)$ (an inverse fourier transform of $S(Q,\omega)$ as explained in section 2.5.1)is measured, so data are actually recorded as a function of time rather than a function of ω as with conventional QENS experiments. In the case of quasielastic scattering, one measures the decay of $I(Q,t)$ as a function of time. When the self-part of the van Hove correlation function can be described by a Gaussian, the spatial Fourier transform yields an exponential function

$$I(Q,t) = \exp(-DQ^2 t)\,, \tag{2.31}$$

illustrated in figure 2.20. The diffusion coefficient may then be obtained relatively simply if the diffusion is in the Fickian regime. As mentioned in section 2.5.1, a time Fourier transform of $I(Q,t)$ results in $S(Q,\omega)$; thus broadenings may be obtained and diffusion coefficients and jump parameters may also be derived as in section 2.5.1.

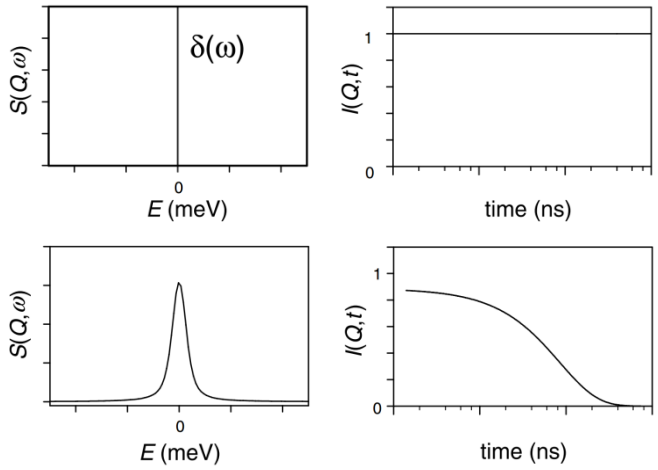

Fig. 2.20. Examples of the scattering function (left) and intermediate scattering function (right) at a single Q value for purely elastic scattering (top) and quasielastic scattering (bottom). Both cases do not account for broadening due to the finite instrumental resolution. Figure reproduced from reference 6.

During the scattering event, the beam polarization can be reduced if the sample contains hydrogen atoms (spin-incoherent scattering inverts the neutron spin with a probability of 2/3. Coherent and isotopic-incoherent scattering involve no spin-flip) for this reason, deuterated molecules or coherent scatterers are preferably studied. With new instruments under construction, increases in flux by one or two orders of magnitude will allow to measure the diffusion of hydrogenated molecules as well.

Chapter 4 of this thesis details the use of conventional TOF-QENS experiments performed at ILL, Grenoble referenced in comparison with molecular dynamics simulations of *n*-alkanes. NSE is also used to quantify the movement of isobutane. Chapter 5 details TOF-QENS measurements on the OSIRIS spectrometer of octane isomers, while chapter 6 includes measurement of the vibrational INS spectra of methanol adsorbed in different zeolites on the MAPS spectrometer, combined with TOF-QENS measurements using the OSIRIS spectrometer. Chapter 7 also details TOF-QENS measurement of cyclohexanone oxime diffusion using the OSIRIS spectrometer.

References

(1) Mitchell, P. C. H. *Vibrational Spectroscopy with Neutrons: with Applications in Chemistry, Biology, Materials Science and Catalysis*; World Scientific, **2005**; Vol. 3.

(2) Bacon, G. E. *Neutron Scattering in Chemistry*; Butterworth-Heinemann Limited, **1977**.

(3) Bee, M. *Quasielastic Neutron Scattering: Principles and Applications in Solid State Chemistry, Biology and Material Science; Adam Hilger, Bristol* **1988**.

(4) https://www.ncnr.nist.gov/summerschool/ss11/pdf/SS2011_Copley_Neutron Scattering.pdf

(5) https://www.ncnr.nist.gov/summerschool/ss10/pdf/SANS_NR_Intro.pdf.

(6) Jobic, H.; Theodorou, D. N. *Microporous and Mesoporous Materials* **2007**, *102*, 21.

(7) http://www.frm2.tum.de/startseite/frm2/index_en.html.

(8) Parker, S. F.; Lennon, D.; Albers, P. W. *Applied Spectroscopy* **2011**, *65*, 1325.

(9) http://www.sonsfpricci.org/wpcontent/uploads/2014/05/Anderson_ Instrumentation_III .pdf

(10) http://www.isis.stfc.ac.uk/instruments/maps/maps4739.html.

(11) Karlsson, M. *Physical Chemistry Chemical Physics* **2015**, *17*, 26.

(12) Chudley, C.; Elliott, R. *Proceedings of the Physical Society* **1961**, *77*, 353.

(13) Hall, P. L.; Ross, D. *Molecular Physics* **1981**, *42*, 673.

(14) Singwi, K.; Sjölander, A. *Physical Review* **1960**, *119*, 863.

(15) Volino, F.; Dianoux, A. *Molecular Physics* **1980**, *41*, 271.

(16) Volino, F.; Pineri, M.; Dianoux, A.; De Geyer, A. *Journal of Polymer Science: Polymer Physics Edition* **1982**, *20*, 481.

(17) Bellissent-Funel, M.-C.; Chen, S.; Zanotti, J.-M. *Physical Review E* **1995**, *51*, 4558.

(18) Zorn, R. *The European Physical Journal Special Topics* **2010**, *189*, 65.

(19) Telling, M. T.; Andersen, K. H. *Physical Chemistry Chemical Physics* **2005**, *7*, 1255.

(20) http://www.isis.stfc.ac.uk/instruments/osiris/

(21) http://www.stfc.ac.uk/stfc/cache/file/24C09892-BF82-4C27-80C9B5567C033C82.jpg

Chapter 3

Computational Methods

Computational techniques have become integral to advancing the fields of zeolite and catalytic science. Development of novel methods and algorithms combined with the steady increase in computational power has led to enormous progress in the field of computational chemistry. Calculations evaluate the energy of a system as a function of atomic coordinates, allowing the derivation of properties both static and dynamic. There are two broad sets of methods for achieving this: Force-field methods (otherwise known as 'classical' methods) and quantum mechanical methods (also termed *ab initio* methods). Force-field methods replace costly electronic structure calculations with empirically/quantum mechanically derived mathematical potential functions, which approximate the interactions of atomic nuclei and electrons. Quantum mechanical methods treat electronic interactions explicitly, calculating approximate solutions to the Schrödinger equation of the system. This chapter will outline the methods used in this thesis.

3.1 Force-field Based Simulations [1]

Force-field methods, unlike more complex quantum mechanical methods bypass the step of calculating the electronic energy of the system, as the electron is not considered as an individual particle. The different interactions between bodies in a system are summed through equations describing the different contributions of the systems energy as a function of particle positions. The Born-Oppenheimer approximation[2] is applied, where the motions of the nuclei are considered slow compared to the motions of the electrons, and only the positions of the nuclei are considered. This approximation allows up to thousands and in the most ambitious calculations, millions of atoms to be simulated.

The force-field energy is written as a sum of terms incorporating bonded and non-bonded terms

$$E_{tot} = E_{bond} + E_{angle} + E_{dihedral} + E_{elec} + E_{vdW} \ , \qquad (3.1)$$

where E_{bond} is the energy function for the stretching of a bond between two atoms, E_{angle} represents the energy for the bending of an angle within the molecule, $E_{dihedral}$ is the torsional energy for rotation around a bond, E_{elec} accounts for the energy contribution of electrostatic interactions, and E_{vdW} is the energy contribution from van der Waals interactions. These energies are calculated from a potential function describing the variance of potential energy as a function of atomic position, which is fitted either to experimental data or to quantum mechanical models. The functional forms of the intra- and intermolecular interactions will now be discussed in greater detail. Though there are many functional forms to describe the energies associated with the total force-field energy, only the ones appropriate to this thesis will be discussed.

3.1.1 Intramolecular Potentials

Intramolecular potentials are concerned with the interactions which keep the molecule consistent with a chemically accurate structure through an energy penalty being applied when deviations from the equilibrium structure take place.

As mentioned above, bond potentials describe explicit chemical bonds between specified atoms. The potential used in this thesis is that of a harmonic potential based on Hooke's law, shown below

$$E_{bond} = \frac{1}{2}\, k\left(r_{ij} - r_0\right)^2 \quad , \tag{3.2}$$

where k is the force constant for the bond between atoms i and j, with r_{ij} being the length of the bond and r_0 being the equilibrium bond length. The energy varies with the square of the displacement from the equilibrium bond length. The harmonic form is the simplest expression, useful for arriving at most equilibrium geometries. A more complex functional form (able to describe wider ranges of behaviour such as dissociation) is the Morse potential

$$E_{bond} = E_0 \left\{1 - \exp\left(-a\left(r_{ij} - r_0\right)\right)\right\}^2 \quad , \tag{3.3}$$

where E_0 is the depth of the potential energy minimum and $a = \omega\sqrt{\frac{\mu}{2E_0}}$, where μ is the reduced mass and ω is the frequency of the bond vibration (related to the force constant (k) of the bond by $\omega = \sqrt{\frac{k}{\mu}}$). r_0 is the equilibrium distance of the bond. This potential can describe the bond over a wider range of distances than the harmonic function but the exponential term in the Morse potential adds computational expense.

Valence angle potentials describe the bond bending terms between specified atoms a, b and c. The potential is usually a Taylor expansion around an equilibrium angle terminated at the second order, giving the harmonic form used in this thesis

$$E_{angle} = \frac{1}{2} k\,(\theta_{abc} - \theta_0) \quad , \tag{3.4}$$

where k is the force constant of the angle θ_{abc}, and θ_0 is the equilibrium bond angle. This harmonic approximation is seen to be accurate to ± 30°. The force constants are smaller than those associated with bonding potentials as less energy is needed to deform an angle.

Dihedral angle potentials describe the energy changes arising from torsional movements in molecules, i.e. the energy change associated with rotating four atoms through a dihedral angle. The dihedral angle is the angle between the *i*-*j* and *k*-*l* bonds in a bond *i*-*j*-*k*-*l*. The dihedral interactions differ from the bonded and angular interactions in that the rotational barrier has contributions from electrostatic and van der Waals forces as well as the torsional energy. The torsional energy function must be periodic, in that if the bond is rotated by 360° the energy must return to the same value.

The dihedral forces in this thesis are represented using the cosine potential form shown below

$$E_{dihedral} = A\,[1 + \cos(m\phi_{ijkl} - \phi_0)]\ , \qquad (3.5)$$

where the constant *A* represents the size of the rotational barrier around the *j*-*k* bond and m represents the divisions of periodicity throughout 360° (m =1 is periodic by 360° m =2 is periodic by 180°, m =3 is periodic by 120° etc)

3.1.2 Intermolecular Potentials

Intermolecular (non-bonding) interactions are usually divided into two categories: electrostatic interactions and short-range (van der Waals) interactions.

Electrostatic interactions are calculated using Coulomb's law:

$$E_{elec} = \sum_{i=1}^{N_A} \sum_{j=1}^{Nb} \frac{q_i q_j}{4\pi\epsilon_0 r_{ij}} \qquad (3.6)$$

They arise due to the difference in electron affinities between components of the system resulting in an uneven charge distribution. One common way to model this is to assign formal or fractional point charges to the different nuclei according to their electronegativity. Of course, in a periodic system of charged atoms, the contribution to total energy by electrostatic interactions converge slowly with distance; while the interaction decreases with *r*, the number of interactions increases in periodic space and therefore, introducing a cut-off radius will often result in an unrealistic sudden jump in energy upon passing the boundary of the cut-off radius. This problem is addressed using the Ewald sum,[3] which works by converting the Coulomb sum into two series. The short range contribution calculated in real space and the long range contribution calculated in reciprocal space, achieving more rapid convergence compared to direct summation. Although this method means that the electrostatic energy can now be computed, the method is still computationally expensive and as such calculating electrostatic forces will be the most time consuming part.

The short-range energy includes both the dispersive forces resulting from instantaneous-induced dipoles leading to attraction, and shorter range repulsive forces arising from the Pauli exclusion principle which results in a repulsive interaction between closed shell atoms. A widely used potential employed extensively in this thesis is the Lennard-Jones 12-6 potential

$$E_{vdw} = 4\epsilon \left[\left(\frac{\sigma}{r}\right)^{12} - \left(\frac{\sigma}{r}\right)^{6}\right] \quad , \tag{3.7}$$

where σ is the minimum energy distance and ε is the depth of the potential energy well. There is an r^{-6} attractive part and a r^{-12} repulsive part. The Lennard-Jones potential is convenient for large systems in terms of computational expense because the r^{-12} component may be calculated by squaring the r^{-6} component. The potential energy is zero at large interatomic distances and is very high at small interatomic distances. At intermediate distances there is a slight attraction due to induced dipole-dipole interactions. This attraction varies as the inverse sixth power of the distance between the two bodies to satisfy the conditions of the short energy being very high at

small distances, slightly negative at intermediate distances and approaching zero at larger distances.

For ionic systems, a widely used model is the Buckingham potential shown below.

$$E_{vdw} = A \exp\left(-\frac{r_{ij}}{\rho}\right) - \frac{C}{r_{ij}^6} \quad (3.8)$$

A, ρ and C are constants, with the right hand term representing the attraction and the left hand term representing the repulsion. Buckingham potentials are commonplace in molecular dynamics. However, the potential 'turns over' as *r* becomes small, since the repulsive exponential term converges to a constant as *r* approaches zero, and the r^{-6} term diverges, bringing difficulties when dealing with short interatomic distances as instability may occur because as the very low potential energy leads to extreme attraction between atom pairs at small distances. Thus it is common to have a cut-off separation below which the Buckingham potential is not active.

3.2 Energy Minimisation Methods [4]

Energy minimisation methods may be used in both classical or quantum mechanical simulations, and are the procedure for finding the lowest energy configuration of a system through exploring the potential energy surface. The potential energy surface represents the energy with respect to the atomic coordinates of a system. For a system with N atoms, the energy is a function of 3N coordinates (or 3N-6 internal coordinates, when it is described by a Z-matrix). An energy minimum is defined as a position on the potential energy surface, where a displacement from these coordinates results in an increase in the potential energy of the system. The position lowest in energy is known as a global minimum; however there is no way to locate this with complete certainty in a complex system.

At a minimum, the first derivative of the energy with respect to position *r* is zero, and the second derivative of the energy will be positive:

$$\frac{\partial E}{\partial r_i} = 0 \, , \frac{\partial^2 E}{\partial r_i^2} > 0 \tag{3.9}$$

The energy functions of interest are very complex and must be found by numerical methods which involve varying the coordinates until conditions for a minimum are met. As computational power improves, and more cost effective methods are developed, full energy landscape exploration (and thus the finding of the global minimum, if so desired) becomes more feasible.

The most common methods for finding a minimum are based on derivatives, using the gradient of the potential energy slope to find the minimum. Methods based on using the first derivative include the steepest descent and the conjugate gradient methods.

The steepest descent method is an iterative process where a lower energy point than the current point x_i is found through

$$x_{i+1} = x_i + \lambda s_i \quad , \tag{3.10}$$

where x_{i+1} is the new position after 1 iteration, the step length is λ (determined by a line search) and s_i is the direction. The minimum of a function f is found by stepping in a direction of a negative gradient $-\Delta f(x_i)$. To begin, the gradient vector $\boldsymbol{g} = \nabla E$ points in the direction of steepest function increase, and is lowered by stepping in the opposite direction (consistent with the force). If the first iteration leads to a reduction in energy then the step size is increased for the next iteration. If the function starts to increase, a new (typically orthogonal) direction of the search is chosen. This method may take many steps to converge if the minimum is in a long narrow valley. As the line search is orthogonal to the previous search, it may undo the progress made by the previous search.

The conjugate gradient method differs from the steepest descent method by performing each line search along a line which is conjugate to the previous search directions. In a purely quadratic surface, this criterion guarantees that each step will not move along previous directions. This gives better performance in long narrow

valleys of the potential energy surface. The first step is equivalent to the steepest descent method; however subsequent line searches are a mixture of the current negative gradient and the previous search direction, with the contribution of both determined by a weighting factor.

It may be advantageous to use second derivative methods. The second derivative provides information about the curvature of a function, giving more information on the potential energy surface and leading to a minimum more efficiently, but with added computational expense. One method is the Newton-Raphson method, which finds the minimum of a function through expanding the gradient function to second order around the current point x_0 as a Taylor series:

$$fx_i \approx f(x_0) + f'(x_0)(x_i - x_0) + \frac{1}{2}f''(x_0)(x - x_0)^2 \qquad (3.11)$$

Gradient Hessian

To find a minimum we require the second order approximation to be zero

$$f'(x_0) + f''(x_0)(x - x_0) = 0 \quad , \qquad (3.12)$$

giving

$$(x - x_0) = -\boldsymbol{H}^{-1}\nabla E \quad , \qquad (3.13)$$

where $\mathbf{H}^{-1}$ is an inverse Hessian matrix (a matrix of the second derivatives of the energy with respect to coordinates, giving the curvature of the potential energy surface) and ∇E is the gradient.

In a coordinate system where the Hessian is diagonalised, the step may be written as

$$\Delta x' = (\Delta x'_1, \Delta x'_2, \ldots \Delta x'_N) \ , \qquad (3.14)$$

where

$$\Delta x'_i = -\frac{f_i}{\varepsilon_i} \ , \qquad (3.15)$$

with f_i being the projection of the gradient along the Hessian eigenvector and ε_i is the Hessien eigenvalue (the gradient component pointing in the direction of the *i*th eigenvector). The formula may be used iteratively for stepping towards a minimum.

Calculating a Hessian (a 3*N*-6 x 3*N*-6 matrix) is not so affordable for systems with more than *N*=100 atoms, and may be simplified by the use of quasi-Newton methods, where the curvature of a non-linear function may be computed without forming the Hessian matrix. The method used in this thesis is that of Broyden,[5] Fletcher,[6] Goldfarb[7] and Shanno[8] which makes an initial guess at an approximate Hessian (a unit matrix being the logical start point) which is updated using an 'update matrix' with each iteration during the minimization process. For each iteration we take a step s_i towards the minimum, with a direction p_i and step size λ_i. At the start of each iteration i , at position x_i there is an approximate Hessian H_k containing curvature information from previous iterations. p_i is found by a Taylor expansion as with the Newton Raphson method:

$$H_i p_i = -\nabla f(x_i) , \tag{3.16}$$

$\nabla f(x_i)$ is the gradient of the function evaluated at x_i; a line search is performed in the direction p_i to find the next point:

$$x_{i+1} = x_i + \lambda_i s \tag{3.17}$$

The approximate Hessian at iteration i is then updated through adding another matrix termed the 'update matrix', resulting in a Hessian taking into account the new curvature information

$$H_{k+1} = H_k + U_i , \tag{3.18}$$

where U_i is the update matrix. This updating procedure has the quasi-Newtonian condition imposed on it:

$$H_{i+1} s_i = \nabla f(x_{i+1}) - \nabla f(x_i) \tag{3.19}$$

The system may be relaxed to its lowest energy state by iteratively minimising the system energy with respect to the atomic positions. The quality of the initial Hessian affects the rate of convergence, though a reasonable starting Hessian may be generated by simple rules connecting bond lengths and force constants. This thesis employs a modified version of this, the Limited-Memory BFGS algorithm (L-BFGS)[9], which restricts the stored history of previous steps to M steps, giving a memory requirement of N × M values, increasing processing speed. This algorithm is employed in section 6.2 of this thesis.

3.3 Classical Molecular Dynamics Simulations [1]

Molecular dynamics simulations aim to predict the real (time-dependant) motion of molecules by using Newtonian equations of motion for a many-body system to calculate trajectories.

The trajectory is obtained by solving the differential equation embodied in Newton's second law

$$m\frac{d^2x(t)}{dt^2} = F(x(t)) \,, \tag{3.20}$$

which describes the motion of a particle with mass m along a coordinate x with F being the force on the particle in that direction.

In a more realistic situation, consisting of a system of N interacting particles, the force acting on a particle will change whenever this particle changes its position, or when any of the particles it interacts with change their position. This leads to a set of *N* coupled Newton's equations:

$$m_i\frac{d^2\vec{x}_i}{dt^2} = F_i\left(\overrightarrow{x_1}, \overrightarrow{x_2}, \ldots, \overrightarrow{x_N}\right), i = 1, N \tag{3.21}$$

The initial configuration may be obtained from experimental data and/or a theoretical model. The initial velocities of each atom are randomly selected from a Maxwell-

Boltzmann distribution at the temperature of interest. This provides a probability density that an atom with mass *m* will have a velocity *v* in direction *i* at a temperature, *T*.

$$f_v v_i = \sqrt{\frac{m}{2\pi kT}} \exp\left[\frac{-mv_i^2}{2kT}\right] \tag{3.22}$$

The initial velocities are adjusted so that the total momentum of the system is zero. Once initial velocities are assigned, the force on each atom must then be calculated by using the derivatives of potentials such as those out lined in section 3.1, and the equations of motion are solved using an integration algorithm based on the finite difference approach, outlined next.

3.3.1 Finite Difference Methods

In molecular dynamics simulations, Newton's equations of motion for a system of interacting bodies are solved, and a trajectory for the components of the system is calculated. Practically, it is difficult to model a system consisting of many bodies under the influence of a continuous potential with all particle motions coupled together. The methods used to solve these ordinary differential equations are based on the finite difference approach. The calculation is broken down into a series of very short time steps, with Δt typically between 10^{-15} and 10^{-14} seconds. At each step the forces on the atoms are computed and combined with the current positions and velocities to generate new positions and velocities a short time ahead. The atoms are then moved to the new positions, and the set of forces is updated. In this way, the MD simulation generates a trajectory describing the time evolution of the dynamic variables of each particle on a time grid:

$$\{\vec{r_i}(t_0), \vec{r_i}(t_0 + \Delta t), \vec{r_i}(t_0 + 2\Delta t), \dots\} \tag{3.23}$$

$$\{\vec{p_i}(t_0), \vec{p_i}(t_0 + \Delta t), \vec{p_i}(t_0 + 2\Delta t), \dots\} \tag{3.24}$$

The timestep (time between evaluating the potentials) should be smaller than the fastest vibration associated with the system, to avoid energy drift associated with larger time steps which can destabilise the system.

All of the algorithms for integrating the equations of motion using finite difference methods assume that the dynamic properties **r**, **v** and **a** can be approximated to Taylor expansions:

$$\mathbf{r}(t+\delta t) = \mathbf{r}(t) + \delta t\mathbf{v}(t) + \tfrac{1}{2}\delta t^2\mathbf{a}(t) + \tfrac{1}{6}\delta t^3\mathbf{b}(t) + \tfrac{1}{24}\delta t^4\mathbf{c}(t) + \ldots \quad (3.25)$$

$$\mathbf{v}(t+\delta t) = \mathbf{v}(t) + \delta t\mathbf{a}(t) + \tfrac{1}{2}\delta t^2\mathbf{b}(t) + \tfrac{1}{6}\delta t^3\mathbf{c}(t) + \ldots \quad (3.26)$$

$$\mathbf{a}(t+\delta t) = \mathbf{a}(t) + \delta t\mathbf{b}(t) + \tfrac{1}{2}\delta t^2\mathbf{c}(t) + \ldots \quad (3.27)$$

v is the velocity (first derivative of the position *r*) with respect to time, **a** is the acceleration (2nd derivative) and b is the third derivative etc. The algorithm employed in this thesis is the Velocity Verlet algorithm,[10] which is a three step process. First the values of the position, velocity and force are required at time *t*, the velocities are advanced to $t + \left(\frac{1}{2}\right)\delta t$ by integration of the force

$$\mathbf{v}\left(t + \tfrac{1}{2}\delta t\right) = \mathbf{v}(t) + \tfrac{1}{2}\delta t\mathbf{a}(t) \ , \quad (3.28)$$

where $\mathbf{a} = \frac{f(t)}{m}$ and the new positions are:

$$\mathbf{r}(t+\delta t) = \mathbf{r}(t) + \delta t\mathbf{v}\,(\mathrm{t} + \tfrac{1}{2}\delta t) \quad (3.29)$$

The forces are then recalculated at $t + \delta t$ using the new positions:

$$f(t+\delta t) \leftarrow f(t) \quad (3.30)$$

The half step velocities are then advanced to a full step using the new force:

$$\mathbf{v}(t+\delta t) = \mathbf{v}\left(t + \tfrac{1}{2}\delta t\right) + \tfrac{1}{2}\delta t\,\mathbf{a}(t+\delta t) \quad (3.31)$$

The velocity Verlet method therefore gives positions, velocities, and accelerations of all particles in the system with each timestep.

Calculating the force is the most expensive part of these calculations, as it involves summing over all pairs of particles, giving scaling of N^2 computational time to N number of molecules. Thus, for practical reasons, the number of particles is restricted to a few thousand, though systems of up to 1 million particles have been simulated. For this reason, and for other reasons such as the avoidance of surface effects, periodic boundary conditions (PBC) are used to simulate bulk systems, outlined next.

3.3.2 Periodic Boundary Conditions

When using periodic boundary conditions (PBC) particles are enclosed in a box, and we can imagine that this box is replicated to infinity in all directions, completely filling the space. Thus, if one of our particles is located at position $\vec{r}$ in the box, we can assume that this particle really represents an infinite set of particles located at

$$\vec{r} + l\vec{a} + m\vec{b} + n\vec{c}\,, (l, m, n = -\infty, +\infty)\ , \qquad (3.32)$$

where *l, m, n* are integer numbers, and $\vec{a}, \vec{b}, \vec{c}$ are the vectors corresponding to the edges of the *a, b, c* box. All of these 'image' particles move in unison, but only one of them is represented in the computer program. The non-faded box in figure 3.1 represents the system we are simulating, while the surrounding boxes are exact copies. [11]

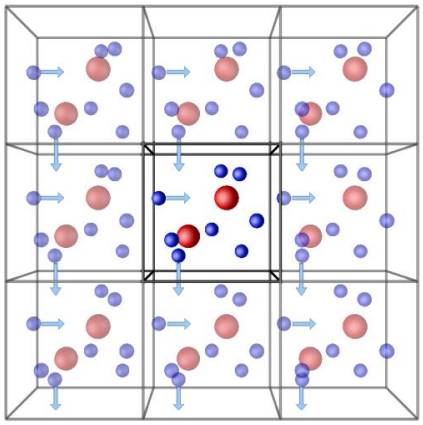

Fig. 3.1. Schematic of a system using periodic boundary conditions. Figure reproduced from reference 11.

So whenever an atom leaves the simulation cell, it is replaced by another entering from the opposite side of the cell with the same velocity, conserving the number of atoms in the cell and removing surface forces. A cut-off radius is applied when calculating the interaction between two atoms. An atom may interact with one in the neighbouring cell (which is an image of one of the atoms in the simulation cell) because it is within the cut-off radius, ignoring the equivalent atom in the simulation cell because it is too far away. Note that the cut-off radius is always chosen so that an atom can interact with only one image of any given atom, which means that the cut-off radius cannot be greater than half the width of the cell.

3.3.3 Constant Temperature Molecular Dynamics

Molecular dynamics is usually performed under the microcanonical (NVE) ensemble. Here, the number of particles, volume and energy are constant. It may be desirable to maintain a constant temperature during the simulation, in which case the canonical (NVT) ensemble is used, where the number of particles, volume and temperature are kept constant. The method used in this thesis to keep the temperature constant is that developed by Berendsen et al, [12] and will be outlined now.

The system temperature is related to the average kinetic energy of the particles in the system

$$\langle K \rangle_{NVT} = \frac{3}{2} N k_B T \quad , \tag{3.33}$$

where $\langle K \rangle_{NVT}$ is the average kinetic energy, N is the number of particles, k_B is the Boltzmann constant and T is the temperature. The simplest way to change the temperature of the system is to multiply the particle velocities by a scaling factor $\chi(t)$. In the Berendsen thermostat the system is coupled to an external heat bath to maintain the system at a stable temperature. This system is regulated through the flow of thermal energy between the system and the bath:

$$\frac{dT(t)}{dt} = \frac{1}{\tau}\left(T_{bath} - T(t)\right) \quad , \tag{3.34}$$

τ is a coupling constant dictating how strongly the bath and the system are coupled. The velocities are scaled so that the change is proportional to the temperature difference between the system and the bath. The particle velocities are scaled by a scaling factor defined as

$$\chi(t) = \sqrt{\left[1 + \frac{\Delta t}{\tau T}\left(\frac{\sigma}{E_{kin}(t)} - 1\right)\right]} \quad , \tag{3.35}$$

where:

$$\sigma = \frac{f}{2} k_B T_{ext} \tag{3.36}$$

Here, T_{ext} is the target temperature, f is the number of degrees of freedom, E_{kin} is the system kinetic energy and τT is the time constant for thermal energy exchange between the system and the heat bath.

3.3.4 Equilibration and Production Runs

The first stage of a molecular dynamics simulation is the equilibration phase, the purpose of which is to bring the system to equilibrium from the starting equilibrium at the target temperature. Equilibration should continue until the values of a set of monitored properties become stable (fluctuating within a reasonable margin with respect to time). The properties that are used to characterise whether the equilibrium has been reached or not, depend to some extent on the simulated system but invariably include the kinetic, potential and total energies, the temperature and pressure. In the microcanonical ensemble the kinetic and potential energies would be expected to fluctuate during a simulation but the total energy should remain constant. The system is then permitted to evolve, (in diffusion studies this is usually in the micro-canonical (NVE) ensemble) and various properties are routinely calculated and stored for subsequent analysis such as coordinates, positions energies and velocities from which other properties such as the diffusion coefficient may be determined post-simulation.

3.4 Electronic Structure Methods

Electronic structure methods (often referred to as *ab initio* meaning 'from the beginning') in contrast to force-field techniques, apply the laws of quantum mechanics to solve the energy of a system as a function of atomic coordinates. These methods attempt to solve the Schrödinger equation of a system, which requires approximations as it may only be solved exactly for the one electron atoms. These calculations are derived from theoretical principles, and are far more computationally expensive than classical methods. Classical methods may scale roughly as N^2, (i.e. increasing the number of particles will increase the time for the calculation to roughly the square). However, *ab initio* methods have a scaling factor between two and eight. For this reason, we are limited to systems with only a few hundred particles. However, the advantage of using *ab initio* methods is their transferability between conditions (something not at all guaranteed using force-field simulations) and also the ability to model bond breaking/formation and electron transfer.

Electronic structure methods calculate the energy and other desired properties of the system by solving the electronic state. The laws of quantum mechanics are applied, in order to solve the Schrödinger equation of the system

$$\hat{\mathrm{H}}\Psi(r,t) = \frac{ih}{2\pi}\frac{\partial\Psi(r,t)}{\partial t} \quad , \tag{3.37}$$

where the system is described in terms of the wavefunction Ψ, and the probability distribution of the wavefunction in the system is given by $|\Psi^2|$. $\hat{\mathrm{H}}$ is the abbreviation of the Hamiltonian operator

$$\hat{\mathrm{H}} = \left\{-\frac{\hbar}{2m}\left(\frac{\partial^2}{\partial x^2} + \frac{\partial^2}{\partial y^2} + \frac{\partial^2}{\partial z^2}\right) + V(r,t)\right\} \quad , \tag{3.38}$$

representing the kinetic and potential energy operators. When the external potential $V(r,t)$ is time independent we may write the more common time independent Schrödinger equation:

$$\hat{\mathrm{H}}\Psi = E\Psi \quad , \tag{3.39}$$

with E being the energy of the system, and the respective eigenvalue of the Hamiltonian. The Hamiltonian of the system can be split into contributions:

$$\hat{\mathrm{H}} = T^{elec}(r) + T^{nuc}(R) + V^{nuc-elec}(R,r) + V^{elec}(r) + V^{nuc}(R) \quad , \qquad (3.40)$$

where the kinetic (T) and potential (V) terms are functions of the electronic coordinates (r) and the nuclei coordinates (R).

The Born-Oppenheimer[2] approximation is made in solving the Schrödinger equation, which assumes that the nuclei are fixed with respect to the electrons due to the mass being much larger. This means that $T^{nuc}(R) = 0$ so only the solution to the electronic wavefunction is solved.

The "Linear Combination of Atomic Orbitals" approximation is also made, where we assume the total wavefunction is a total of smaller functions, known as basis functions.

$$\Psi = \sum_i c_i \phi_i \qquad (3.41)$$

ϕ_i is the atomic orbitals and c_i being the weight of each of their contributions to the molecular orbital (Ψ). In electronic structure calculations, a crucial starting component is the so called 'basis set', which is the choice of basis functions. The form, and number of basis functions used to describe the electrons in the system are considered in this basis set choice, outlined further in section 3.3.1.2.

All electronic structure methods make the following approximations:

- The Schrödinger equation is solved independent of time as the external potential (V) in the Hamiltonian is time independent.
- As mentioned above, the Born-Oppenheimer approximation is employed, thus the kinetic energy operator for the nuclei and the nuclei interaction are removed from the Hamiltonian.
- The particles are treated non-relativistically, so if they approach the speed of light their masses do not increase. This solution is inaccurate for solving

the Schrödinger equation of heavy atoms, where the core electrons may approach this speed. In this case relativistic methods are used.

A discussion of the electronic structure method used in this thesis, density functional theory will now take place.

3.4.1 Density Functional Theory

Density Functional Theory (DFT) is an electronic structure method based on the assumption that the properties of a system, may be determined from the ground-state spatially-dependent electron density $\rho(r)$ (as shown by Hohenberg and Kohn)[13]

This is calculated from non-interacting one electron orbitals:

$$\rho(r) = \sum_i |\Phi_i(\boldsymbol{r})|^2 \tag{3.42}$$

The energy is a function of the electron density $\rho(\boldsymbol{r})$. The DFT energy functional is written as below:

$$E[\rho(r)] = \int V_{ext}(\boldsymbol{r})\rho(\boldsymbol{r})dr + F[\rho(\boldsymbol{r})] \tag{3.43}$$

Here, V_{ext} is the external potential arising from the electron-nuclei interactions, and $F[\rho(\boldsymbol{r})]$ is the kinetic energy of the electrons summed with the interelectronic interactions.

This method is incorporated in chemistry through the introduction of orbitals through the Kohn-Sham method,[14] where $F[\rho(\boldsymbol{r})]$ is approximated to the sum of three terms:

$$F[\rho(r)] = E^T[\rho(r)] + E^J[\rho(r)] + E^{xc}[\rho(r)] \tag{3.44}$$

$E^T[\rho]$ is the electron kinetic energy, $E^J[\rho]$ is the Coulombic potential electron-electron interaction energy and E^{xc} is the exchange correlation energy which requires a chosen functional (discussed later).

$E^J[\rho]$, the electron-electron interaction energy can be calculated as below:

$$E^J[\rho(r)] = \frac{1}{2}\iint \frac{\rho(r_1)\rho(r_2)}{|r_1 - r_2|}\, d\boldsymbol{r}_1 d\boldsymbol{r}_2 \tag{3.45}$$

The electron kinetic energy $E^T[\rho]$ is calculated from one-electron Kohn-Sham orbitals for a system of non-interacting particles

$$E^T\,[\rho(r)] = \sum_{i=1}^{N_{el}} \int \Psi_i(r)\left(-\frac{\nabla^2}{2}\right)\Psi_i(r)dr \tag{3.46}$$

The difference between this and the real kinetic energy is incorporated into $E^{xc}[\rho(r)]$. So the final Kohn-Sham expression of the energy of an N-electron system is:

$$E[\rho(r)] = \sum_{i=1}^{N_{el}} \int \Psi_i(r)\left(-\frac{\nabla^2}{2}\right)\Psi_i(r)dr + \frac{1}{2}\iint \frac{\rho(r_1)\rho(r_2)}{|r_1 - r_2|}\, dr_1 dr_2 + E_{xc}[\rho(r)] + \sum_{A=1}^{N_{at}} \int \frac{-Z_A}{|r - R_A|} \tag{3.47}$$

The second to last term as mentioned before is the exchange-correlation energy, calculated using an exchange-correlation functional, the choice of which is crucial to the properties calculated. The final term is the aforementioned external potential V_{ext}.

The molecular orbitals Φ_i, electron density and then the total energy are solved using the Kohn-Sham equations.

$$\left(-\frac{\hbar^2}{2m}\,\nabla^2 - V^{nuc} + V^{elec} + \mu^{xc}\right)\Phi_i = \varepsilon_i \Phi_i \tag{3.48}$$

Here, ε_i is the orbital energy. These Kohn-Sham equations take the form of Roothan equations

$$HC = \varepsilon SC\,, \tag{3.49}$$

and an iterative procedure is then used to solve these equations as in the Hartree-Fock method, where guesses are made of the Kohn-Sham orbitals, allowing an electron density to be calculated. The Kohn-Sham potential is then calculated building a new set of orbitals, calculating a new density and continuing until the Kohn-Sham densities and the electron densities converge. This process is shown in the schematic in figure 3.2.

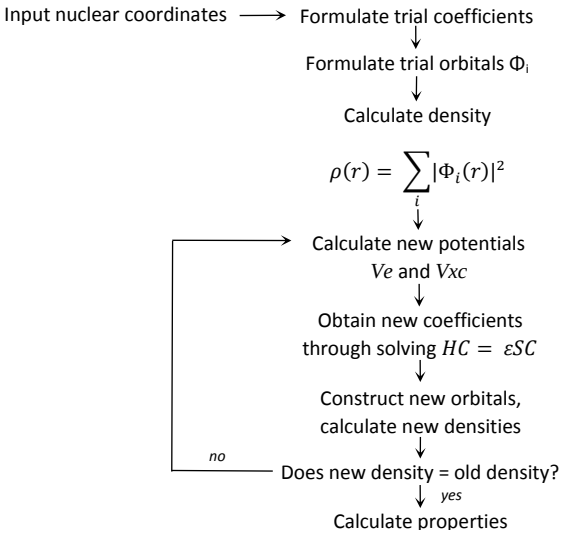

Fig. 3.2. Schematic of the self-consistent field algorithm associated with density functional theory.

3.4.1.1 Exchange Correlation Functionals

The choice of exchange-correlation functional is crucial to the results of any DFT calculation. The exchange correlation energy is an approximation to the difference between the exact energy and the energy calculated from all other contributions. It contains the exchange energy (from the wavefunction anti-symmetry) and the correlation in electron movement, the functional form of which is only exactly known

for a uniform electron gas.[15] Approximations must be made for more complex systems such as the local density approximation (LDA) used by Kohn and Sham.[14] Here, points in the inhomogeneous electron distribution are considered locally homogenous, i.e. the exchange-correlation functional of a uniform electron gas

$$E_{XC}^{LDA}[\rho(r)] = \int \rho(r)\varepsilon_{xc}(\rho)dr\,, \tag{3.50}$$

which may be used as it is known exactly.[16] This approximation has been shown to give correct prediction of trends in structures, bond lengths and vibrational frequencies. However, it fails where the density undergoes rapid changes. LDA favours electron densities which are more diffuse than the physical system, and has been shown to result in overbinding, bond shortening and poor representation of hydrogen bonds.

This approximation is improved upon by the incorporation of gradient corrections, known as the General Gradient Approximation (GGA):

$$E_{XC}^{GGA}[\rho(r)] = \int \rho(r)\varepsilon_{xc}(\rho)dr\ F\big(\rho(r), \nabla(r)\big) \tag{3.51}$$

We consider the gradient and higher derivatives of the density rather than just local density. Experimental data may be used to provide empirical parameters, yielding improved molecular geometries. Functionals include the PW91[17] functional used briefly in this thesis. The Coulombic interaction between different regions of electron density resulting from a single electron however is still not cancelled, which is known as the self-interaction problem and leads to LDA and GGA giving a poor description of localised electronic states. Solutions may involve artificial delocalisation and can give rise to substantial error when calculating properties such as band gaps.

This error may be rectified through the incorporation of exchange obtained from Hartree Fock (HF) methods. The HF method gives an exact exchange contribution unlike DFT.

The general form of the hybrid exchange-correlation function is given by

$$E_{XC}^{Hyb} = (1-a)E_X^{DFT} + aE_X^{HF} + E_C^{DFT} \quad , \tag{3.52}$$

where *a* is the fraction of HF exchange included. These allow for greater accuracy than the aforementioned approximations however are far more expensive computationally (HF scales to from N^4 whereas DFT calculations generally scale to N^2 with the number of electrons.

An example of a hybrid functional employed in this thesis is the very popular B3LYP (Becke, three-parameter, Lee-Yang-Parr) functional,[18] with the following default form:

$$E_{XC}^{B3LYP} = E_X^{LDA} + 0.2\left(E_X^{HF} - E_X^{LDA}\right) + 0.72\left(E_x^{GGA} - E_X^{LDA}\right) + E_C^{LDA} + 0.81(E_C^{GGA} - E_C^{LDA}) \tag{3.53}$$

Combining GGA approximations of the Becke 88 exchange functional[19] and the LYP correlation functional of Lee, Yang and Parr (LYP)[20], E_C^{LDA} is the VWN[21] local density approximation. It is parameterised based to a set of total atomic energies, proton affinities, ionisation potentials and atomization energies.

3.4.1.2 Basis Sets

Basis sets are functions which constitute the wavefunction used to form molecular orbitals through linear combination. There are two types of basis sets, plane wave basis sets, and atom centred basis sets. Only the latter are used in this thesis and are thus discussed.

Atoms centred basis sets comprise of a number of functions which represent the change in electronic population as a function of distance from the atomic nucleus. Common basis sets are those based on Gaussians, known as Gaussian Type Orbitals (GTO's) which have the form

$$\Phi^{Gau}(r) = x^a y^b z^c e^{-\alpha r^2} \quad , \tag{3.54}$$

where r is the distance from the nucleus, α determines the radial extent of the orbital, x, y and z are Cartesian variables and a, b, and c determine the order. If $a + b + c = 0$ then we obtain a zeroth order function comparable to an s orbital, and = 1 obtains a P_x P_y and P_z orbital. More accurate basis functions may be expressed as a linear combination of Gaussian functions, known as a contracted Gaussian functions:

$$\Phi^{Con}(r) = \sum_{i=1}^{L} d_i \Phi^{Gau}(r) \tag{3.55}$$

L is the contraction length, d_i being the contraction coefficient. Contracted gaussians approximate better the exponential function of electron density, with the primitive gaussians having their weighting multiplied by d_i and frozen once the best approximation is obtained. The basis set can be split into two basis functions corresponding to the valence orbitals (known as a double zeta functions), further splitting giving three basis functions (triple zeta).

Another improvement may be the addition of a polarisation function. Accounting for distortion of the orbitals in the presence of other nuclei, e.g. if a hydrogen atom is isolated it has a spherical electron cloud, but this cloud is perturbed when a molecule moves towards other nuclei giving an SP hybrid. Polarisation functions have higher angular quantum numbers corresponding to p-orbitals (in the case of a hydrogen atom).

The TZVP basis set of Ahlrichs and Taylor[22] is used in this thesis: 'TZ' as mentioned above means that the basis set is split into three functions 'V' stands for valence, indicating that this splitting only happens in the case of the valence orbitals, and the P stands for polarized, as polarization functions are included.

3.5 QM/MM Embedding

Also known as the 'embedded cluster' model, QM/MM simulations[23] allow for simulations using electronic structure techniques, in a finite 'quantum region' embedded in a structure modelled with molecular mechanics techniques (the MM region), for realistic modelling of the surrounding environment.[24] This approach has a number of advantages over cluster or periodic simulations, such as the ability to study defects, catalytic active sites, or sorbate adsorption/reaction processes using electronic structure methods. Studying these processes in isolation within a bulk structure, avoids problems encountered in periodic systems such as periodic images of the defect/sorbate interacting with each other. Total relaxation of this bulk structure upon defect/sorbate addition is also possible, although not so in periodic DFT with small unit cells.

The energy of the combined system is calculated in an additive process, summing the energy of the QM and MM regions post optimisation. The QM region of the simulation is influenced by the MM region through electrostatic embedding. This way, the QM region may be polarised due to the influence of charges on MM centres, and also the interatomic potentials. [25]

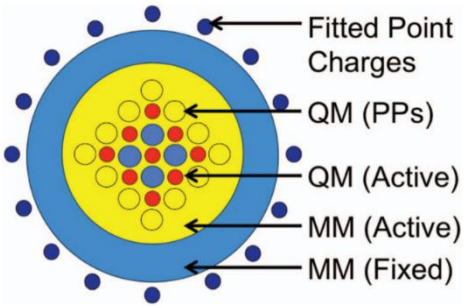

Fig. 3.3. The embedded cluster model used in QM/MM calculations, with the central QM atoms, surrounded by pseudopotentials, surrounded by the active and fixed MM atoms respectively. The point charges are fitted to reproduce the long range electrostatic potential in the active region. Figure reproduced from reference 25.

The interface between the QM/MM regions may be treated differently depending on the nature of the material under study. Ionic materials such as metal oxides[26] have their interfaces treated with large core pseudopotentials placed on the cation sites

surrounding the QM region, whereas covalently bonded materials are interfaced using pseudoatoms, where atom charges near the interface are shifted to prevent unphysical polarisation in the QM region, and forces on the link atoms are transferred to real atoms in a geometry optimisation, or in the case of zeolites[25] by saturating a silica cluster with hydrogen atoms. This is the method used in this work for simulating deprotonation, and methanol adsorption in zeolites.

Constructing the regions begins with the unit cell of the material of interest which is then energy minimised under periodic boundary conditions using molecular mechanics. This structure is then expanded into a supercell, after which an approximately spherical structure is cut with a suitable radius. The electrostatics of the bulk structure are then modelled using a shell of point charges around the total cluster with a bond dipole correction necessary in the molecular mechanics region. A suitable cluster of atoms (for example, a defect and its surrounding nearest neighbours) for the QM region is then generated at the centre of the cluster, which is terminated appropriately. Concentric regions simulated using molecular mechanics are then implemented, the first of which is an active region (allowed to relax in the MM geometry optimisation after the central defect is added) the spacial extent of which is specified by a cut-off distance from the centre of the cluster. This region is surrounded by a second MM region of atoms kept rigid to their lattice positions. To correct for the termination of periodicity, the electrostatic field at the centre of the cluster is sampled and the point charges around the outer edge are tuned to reproduce the electrostatic field of the periodic structure, minimising dipoles in all directions.

In terms of incorporating the effect of the MM regions on the QM optimisation, the energy of the QM region becomes a combination of the QM region Hamiltonian with the potential of the surrounding environment through:

$$E^{QM} = \langle \Psi \left| \hat{\mathrm{H}}^{QM} + \hat{V}^{MM} \right| \Psi \rangle + E_{nuc}^{QM} + E_{nuc}^{QM-MM} \qquad (3.56)$$

Here, $\hat{V}^{MM}$ is the external potential from the surrounding regions, E_{nuc}^{QM} is the Coulombic interaction between nuclei of the QM region, and E_{nuc}^{QM-MM} is the Coulombic interaction between QM and MM nuclei.

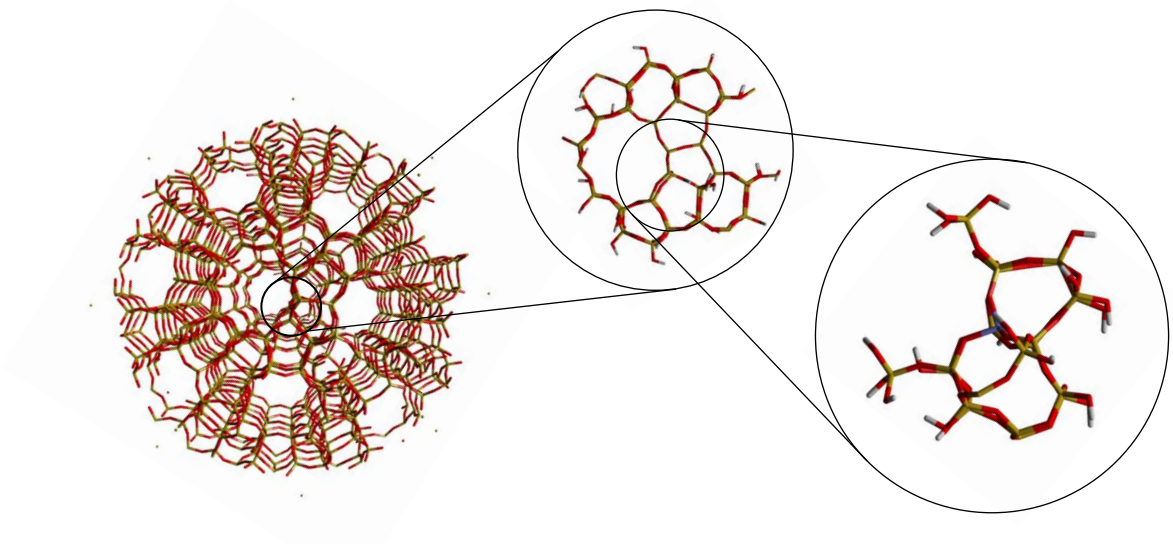

Fig. 3.4. An example of a QM/MM setup for zeolite ZSM-5, with the total cluster including point charges (left), the total QM/MM active region (centre) and the central QM region (right).

Work has taken place with QM/MM methods in zeolite frameworks investigating the reduction potential in Fe-ZSM-5,[25] previously studied using finite fragments to reproduce the active site.[27,28] Given that the structure of the surrounding framework influences the electrostatic potential at the active site,[29,30] QM/MM methods are becoming an increasingly important tool in studying processes in zeolites and catalysts in general.

3.6 Resources

For the QM/MM simulations presented in this thesis, the QM code GAMESS-UK (General Atomic and Molecular Electronic Structure System) [31] and MM codes DL_POLY[34] and DL_FIND[32] were used for optimisation and energy calculations within the ChemShell[33] environment (for summing QM and MM energies). All molecular

dynamics simulations presented in this thesis were performed using the DL_POLY 4 code[34].

The majority of calculations were performed on the UCL Legion High Performance Computing Facility[11] , and the UCL Chemistry Faraday cluster.

References

(1) Leach, A. R. *Molecular Modelling: Principles and Applications*; Pearson Education, 2001.
(2) Born, M.; Oppenheimer, R. *Annalen der Physik* **1927**, *389*, 457.
(3) Ewald, P. P. *Ann. Phys.* **1921**, *64*, 253.
(4) Jensen, F. *Introduction to Computational Chemistry*; John Wiley & Sons, 2013.
(5) Broyden, C. *Mathematics of Computation* **1970**, *24*, 365.
(6) Fletcher, R. *The Computer Journal* **1970**, *13*, 317.
(7) Goldfarb, D. *Mathematics of Computation* **1970**, *24*, 23.
(8) Shanno, D. F. *Mathematics of Computation* **1970**, *24*, 647.
(9) Kittel, C. *Introduction to Solid State Physics*; Wiley, 2005.
(10) Swope, W. C.; Andersen, H. C.; Berens, P. H.; Wilson, K. R. *The Journal of Chemical Physics* **1982**, *76*, 637.
(11) http://isaacs.sourceforge.net/phys/pbc.html
(12) Berendsen, H. J.; Postma, J. P. M.; van Gunsteren, W. F.; DiNola, A.; Haak, J. *The Journal of Chemical Physics* **1984**, *81*, 3684.
(13) Hohenberg, P.; Kohn, W. *Physical Review* **1964**, *136*, B864.
(14) Kohn, W.; Sham, L. J. *Physical Review* **1965**, *140*, A1133.
(15) Martin, R. M. *Electronic Structure: Basic Theory and Practical Methods*; Cambridge University Press, 2004.
(16) Dirac, P. A. In *Mathematical Proceedings of the Cambridge Philosophical Society*; Cambridge Univ Press: 1930; Vol. 26, p 376.
(17) Perdew, J. P.; Wang, Y. *Physical Review B* **1992**, *45*, 13244.
(18) Becke, A. D. *The Journal of Chemical Physics* **1993**, *98*, 1372.
(19) Becke, A. D. *Physical Review A* **1988**, *38*, 3098.
(20) Lee, C.; Yang, W.; Parr, R. G. *Physical Review B* **1988**, *37*, 785.
(21) Vosko, S.; Wilk, L.; Nusair, M. *Canadian Journal of Physics* **1980**, *58*, 1200.
(22) Ahlrichs, R.; Taylor, P. *Journal De Chimie Physique Et De Physico-Chimie Biologique* **1981**, *78*, 315.
(23) Bernstein, N.; Kermode, J. R.; Csanyi, G. *Reports on Progress in Physics* **2009**, *72*, 026501.
(24) Metz, S.; Kästner, J.; Sokol, A. A.; Keal, T. W.; Sherwood, P. *Wiley Interdisciplinary Reviews: Computational Molecular Science* **2014**, *4*, 101.
(25) Berger, D.; Logsdail, A. J.; Oberhofer, H.; Farrow, M. R.; Catlow, C. R. A.; Sherwood, P.; Sokol, A. A.; Blum, V.; Reuter, K. *The Journal of Chemical Physics* **2014**, *141*, 024105.
(26) Downing, C.; Sokol, A.; Catlow, C. *Physical Chemistry Chemical Physics* **2014**, *16*, 184.
(27) Fellah, M. F.; Pidko, E. A.; van Santen, R. A.; Onal, I. *The Journal of Physical Chemistry C* **2011**, *115*, 9668.

(28) Ryder, J. A.; Chakraborty, A. K.; Bell, A. T. *Journal of Catalysis* **2003**, *220*, 84.
(29) de Vries, A. H.; Sherwood, P.; Collins, S. J.; Rigby, A. M.; Rigutto, M.; Kramer, G. J. *The Journal of Physical Chemistry B* **1999**, *103*, 6133.
(30) Sherwood, P.; de Vries, A. H.; Collins, S. J.; Greatbanks, S. P.; Burton, N. A.; Vincent, M. A.; Hillier, I. H. *Faraday Discussions* **1997**, *106*, 79.
(31) Guest, M. F.; Bush, I. J.; Van Dam, H. J.; Sherwood, P.; Thomas, J. M.; Van Lenthe, J. H.; Havenith, R. W.; Kendrick, J. *Molecular Physics* **2005**, *103*, 719.
(32) Kästner, J.; Carr, J. M.; Keal, T. W.; Thiel, W.; Wander, A.; Sherwood, P. *The Journal of Physical Chemistry A* **2009**, *113*, 11856.
(33) Sokol, A. A.; Bromley, S. T.; French, S. A.; Catlow, C. R. A.; Sherwood, P. *International Journal of Quantum Chemistry* **2004**, *99*, 695.
(34) Todorov, I. T.; Smith, W.; Trachenko, K.; Dove, M. T. *Journal of Materials Chemistry* **2006**, *16*, 1911.

Chapter 4

n- and Isoalkane Diffusion in Silicalite

Owing to its relevance to applications in the petrochemical industry and a number of catalytic conversions, a significant amount of work both theoretical and experimental has been carried out studying the diffusion of hydrocarbons in the MFI zeolite structure, the framework type of industrially important ZSM-5 and its siliceous analogue silicalite. Recent implementation of state-of-the-art computational models has yielded diffusivity measurements in close agreement with microscopic experimental techniques. In this chapter, molecular dynamics simulations implementing a flexible zeolite framework and an explicit atom hydrocarbon model are applied first to the study of longer *n*-alkanes (C_8 - C_{16}) and secondly isobutane in silicalite. Self-diffusivities obtained are compared with quasielastic neutron scattering (QENS) and neutron spin echo (NSE) experiments performed by Herve Jobic (IRCELYON). The studies yield a significant improvement in agreement of self-diffusivity and activation energy of diffusion values from previous computational efforts where approximations were necessary. Interesting insight into the preferred siting and channel switching capabilities of sorbates is also obtained.

4.1 Molecular Dynamics Simulations of longer *n*-alkanes in Silicalite: State-of-the-art Models Achieving Close Agreement with Experiment

The work presented in this section covers molecular dynamics simulations of the diffusion of longer *n*-alkanes (*n*-C_8 - *n*-C_{16}) in silicalite at a temperature range of 300 - 400 K, with loadings appropriate for direct comparison with previously carried out quasielastic neutron scattering (QENS) studies. The calculated diffusion coefficients were significantly closer to experimental values than those calculated using more primitive framework and hydrocarbon models. For longer alkanes of the range, closer agreement was found than for MD studies previously performed using the same models, but in the limit of infinite dilution. The calculated activation energies of diffusion agree with experiment to within 1.5 kJ mol^{-1} for the shorter alkanes of the range, but with a larger difference for tetra and hexadecane, due to experimental phenomena which cannot be reproduced using periodic boundary conditions. Channel switching from the straight to the sinusoidal channel system was found for octane at higher temperatures if more than one octane molecule was located in the channel. This observation was attributed to the molecular length of octane, and the additional interactions caused by the presence of the extra octane molecules in the channel system, allowing the potential barrier of channel switching at the junctions to be breached over the timescale of the simulation.

4.1.1 Introduction

As noted in chapter 1, due to its applications in many catalytic conversions, and molecular sieving processes in the petrochemical industry (most notably with the use of ZSM-5, zeolite-X and zeolite-Y),[1] the study of hydrocarbon diffusion in zeolites is of great interest.

A significant amount of work both theoretical and experimental has been carried out studying the diffusion of hydrocarbons in the MFI zeolite structure,[2-14] the framework type of industrially important ZSM-5 and its siliceous analogue silicalite. The diffusion of *n*-alkanes longer than C_8 in this framework is of considerable interest and has been studied by quasielastic neutron scattering (QENS) techniques in both Na-ZSM-5[15] and silicalite.[16] The range of *n*-alkanes C_8 - C_{20} has also been studied with hierarchical simulations,[17] and molecular dynamics (MD) simulations.[18,19] Earlier MD simulations[18] were found to give diffusion coefficients at 300 K too large by 2-3 orders of magnitude, giving also a periodic dependence of diffusivity on chain length, supporting the concepts of the 'window effect'[20-22] and resonant diffusion[23] as mentioned in chapter 1. This was found later to be due to the use of too simplistic a model, in particular the use of rigid frameworks and a united-atom hydrocarbon model. The united-atom hydrocarbon model causes the potential of the molecule to be too smooth, increasing its mobility, while using a rigid framework model allows energy traps to persist within the structure, trapping molecules of a certain length and slowing them down. Our recent study [19] detailed in chapter 1, used an explicit atom hydrocarbon model with a flexible framework to study *n*-alkanes of length C_8 – C_{20} and found that not only was the experimentally observed monotonic dependence of diffusivity on chain length exhibited when the most sophisticated model was used, but the majority of absolute values for the diffusion coefficients were within 1 order of magnitude of QENS studies for these alkanes in silicalite.[16] We note that the simulations were carried out in the limit of infinite dilution, and sorbate-sorbate interactions would be expected to slow diffusion significantly. We also note that the simulations were only carried out at 300 K, and a more suitable test of the accuracy of such simulations would be calculation of the activation energy, in order to gauge the variation of diffusion coefficient with temperature.

We employ the same up-to-date model taking into account framework flexibility and explicit atom hydrocarbons to perform state of the art molecular dynamics simulations of longer *n*-alkanes (C_8, C_{10}, C_{12}, C_{14} and C_{16}) at 300, 350 and 400 K in silicalite for direct comparison with the aforementioned QENS studies by Jobic.[16]

Diffusion coefficients and activation energies are calculated using the experimental loadings of each alkane, to ensure the simulations are as comparable with experiment as possible. Our results show that this model is capable of producing diffusion coefficients within a factor of 5 of those observed experimentally at all temperatures, and that a close agreement in activation energy along with the experimental trend in activation energy with chain length can be obtained.

4.1.2 Computational Methods

It is first worth recapping that the zeolite silicalite has been chosen because it is isostructural to the industrially important zeolite ZSM-5. In the [010] direction the channels are straight; however in the [100] direction the channels have a sinusoidal (or 'zig-zag') structure. The channels both have a diameter of roughly 5.5 Å. These two channel systems meet at junctions which present high energy barriers to the diffusion of sorbates, since the favourable dispersion interactions between the sorbate and the channel walls are reduced.

4.1.2.1 The Silicalite Framework

The structure chosen is the orthorhombic structure with a *Pnma* symmetry.[24] Though silicalite has a reversible structural transition from monoclinic to orthorhombic at around 350 K,[25] and it has been claimed that this can be induced by molecular adsorption,[26] Leroy et al concluded the diffusion of *n*-alkanes is not significantly affected by symmetry of the framework.[3] Periodic boundary conditions were employed to reduce computational expense, and a 2 x 2 x 2 supercell of 2304 atoms was created in order to incorporate the experimental concentration of sorbates.

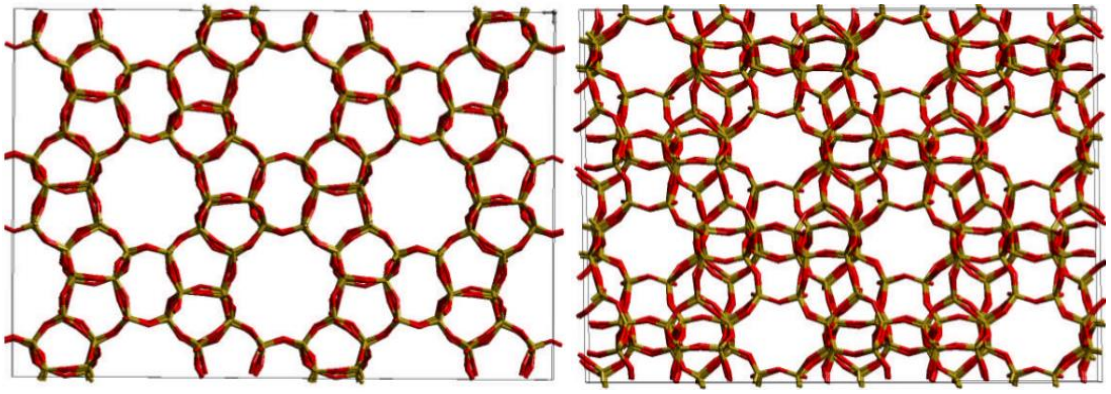

Fig. 4.1. A view of the 2 x 2 x 2 silicalite supercell used in all MD simulations viewed from (left) the [010] direction down the straight channels and (right) the [100] direction down the sinusoidal channels. Note the elliptical appearance of the actually circular channels in the [100] direction, illustrating the tortuousity of this direction.

Full ionic charges were assigned to the framework species for all simulations. The supercell is shown in figure 4.1, with dimensions of 39.67 Å in the [010] direction, 40.18Å in the [100] direction and 26.7 Å in the 001 direction. All experimental visualisations in this study were created using the visualisation software package Aten1.8.[27] The potentials used to describe the framework in the flexible framework simulations were taken from those derived from empirical data of $SiO_{2,}$[28] including the structural, elastic and dielectric properties of α quartz. The potentials include a Buckingham potential to describe Si-O and O-O interactions, along with an harmonic three-body potential to describe the O-Si-O triads. A cut-off distance of 10 Å was used, along with full ionic charges assigned to the Si^{4+} and O^{2-} species. Details of the potential parameters can be found in table 4.1.

Zeolite-Zeolite interactions			
Buckingham potential			
Atoms	*A*(kJ/mol)	*ρ*(Å)	*C*(kJ/mol)Å ^{6}
Si- -O	123878.16	0.149	2690.01
O- -O	2196390	0.32052	1028.53
Three-body potential			
Atoms	*K* (kJ/mol)	θ(°)	
O-Si-O	202.353	109.47	

Table 4.1. Parameters describing intramolecular zeolite framework

4.1.2.2 Hydrocarbon Parameters

The all-atom hydrocarbon model used force-fields derived from vibrational data,[29] which had been applied previously to similar systems studying methane[30] and octane diffusion in silicalite.[31] Each hydrogen atom was assigned a charge of +0.1 au, and the carbon atoms were assigned the appropriate charge to give an overall charge neutral hydrocarbon. The bonds and bond angle vibrations were described by harmonic potentials while the dihedrals were described by a cosine potential. The guest-host interactions were modelled by a Lennard-Jones potential taken from the work of Kiselev et al[32] (empirically derived from Henry constants and adsorption data) as were intramolecular, and sorbate-sorbate interactions between the constituents of each hydrocarbon (described in table 4.2).

Lennard-Jones Parameters		
Interaction	**A (kJ/mol Å^{12})**	**B (kJ/mol Å^6)**
C- -H	270160	563.62
H- -H	37131.41	191.69
C- -C	1899990	1746.32
H- -O	150169.7	537.5872
C- -O	1061340	1703.35

Table 4.2. Potential parameters describing the sorbate-zeolite interactions.

Intramolecular Parameters					
Bonds	***K* (kJ/mol)**	**Length (Å)**	**Angles**	***K* (kJ/mol)**	**θ(°)**
H-C	2990	1.054	C-C-C	327	109.47
C-C	5790	1.405	C-C-H	327	109.47
			H-C-H	327	109.47

Table 4.3. Potential parameters describing the intramolecular hydrocarbon interactions

4.1.2.3 Simulation Procedure

The alkanes of choice were placed in the centre of the straight channel of the supercell, avoiding strong contact with the channel walls. The straight channel was chosen as previous QENS studies have shown that *n*-alkanes generally occupy this channel system, concluded from the observation of one dimensional diffusion.[33] The alkane loadings were kept as close as possible to those used in reference 16 (roughly 28 H atoms per unit cell). These loadings corresponded to 1.56 mol/uc for octane, 1.3 mol/uc for decane, 1.08 mol/uc for dodecane, 0.93 mol/uc for tetradecane and 0.82 mol/uc for hexadecane. An example of the starting configuration for the octane MD runs is shown in figure 4.2.

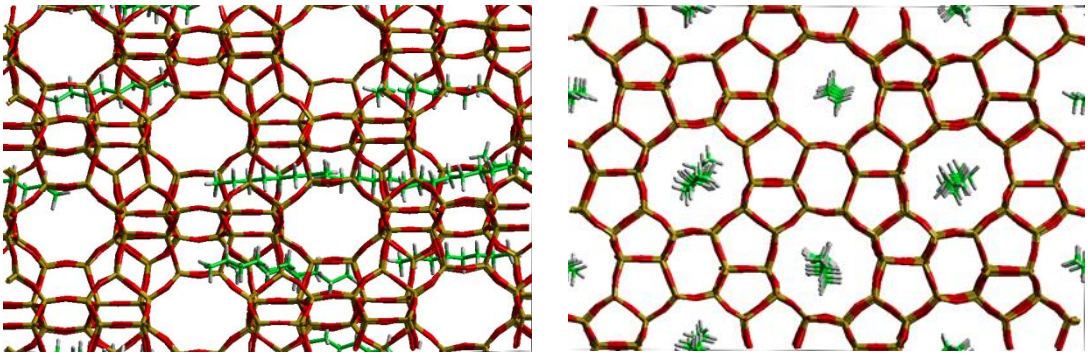

Fig. 4.2. A view of the system for octane pre-production run at 300 K viewed down the (left) [010] direction and (right) [100] direction.

The system was then equilibrated at the desired temperature for 1 ns in the canonical (NVT) ensemble. After the equilibration run, the production run of 10 ns in the microcanonical (NVE) ensemble was carried out for each alkane at 300, 350 and 400 K. A timestep of 0.5 fs was used and the atomic coordinates were saved every picosecond (every 2000 steps). A Berendsen[34] thermostat was used to maintain the temperature near a set point, with a time constant for thermal energy exchange between the system and the heat bath set at 1 ps. All simulations were carried out using the DL_POLY_4 code.[35]

The production time of 10 ns was chosen because it was adequate to obtain true diffusive motion, illustrated by a linear mean-squared displacement (MSD). The central carbon atom of each chain then had its coordinates logged, and the average of the mean-squared displacement for all molecules was then plotted as shown in figure 4.4, enabling the self-diffusion coefficients to be calculated from the Einstein relationship:

$$D_s = \frac{1}{6}\lim_{t\to\infty}\frac{d}{dt}\langle(r(t)-r(0))^2\rangle \qquad (4.1)$$

where the term in braces is the ensemble average of the MSD of the hydrocarbon chain.

4.1.3 Results and Discussion

An important consideration when using the Einstein relationship to calculate a diffusion coefficient is that the simulation time must be long enough to obtain true diffusive motion, i.e. the mean squared displacement must be linear with respect to time over the measured range. As shown for the simulation run of a selected single molecule of *n*-octane in figure 4.3 and the average mean squared displacement of all molecules in figure 4.4, this linearity is well achieved. This linearity was confirmed before calculating the diffusion coefficient for each chain length.

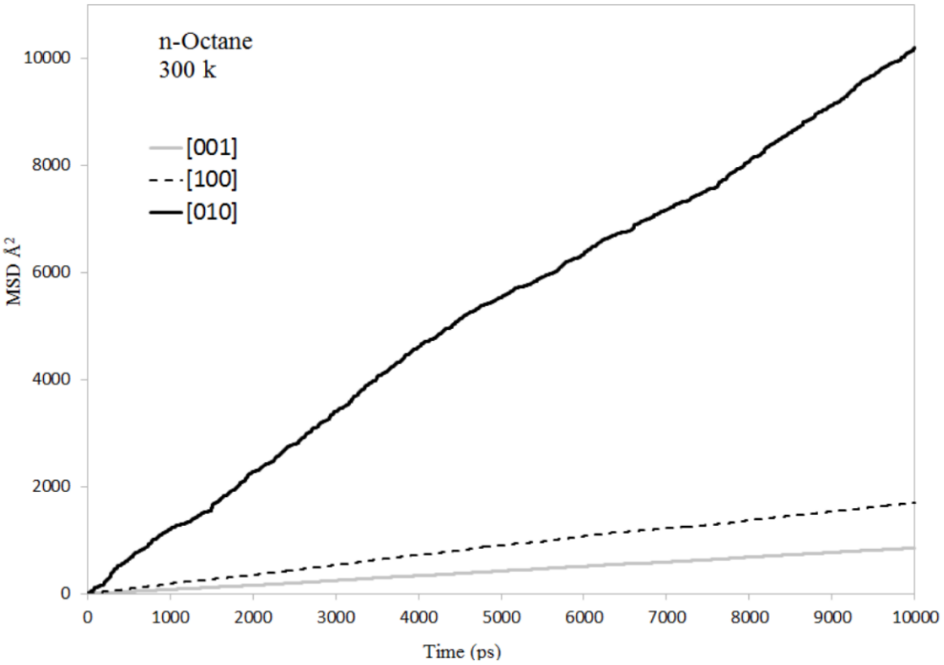

Fig. 4.3. A plot of the mean square displacement as a function of time for a single *n*-octane molecule at 300 K along the three principle axes of silicalite.

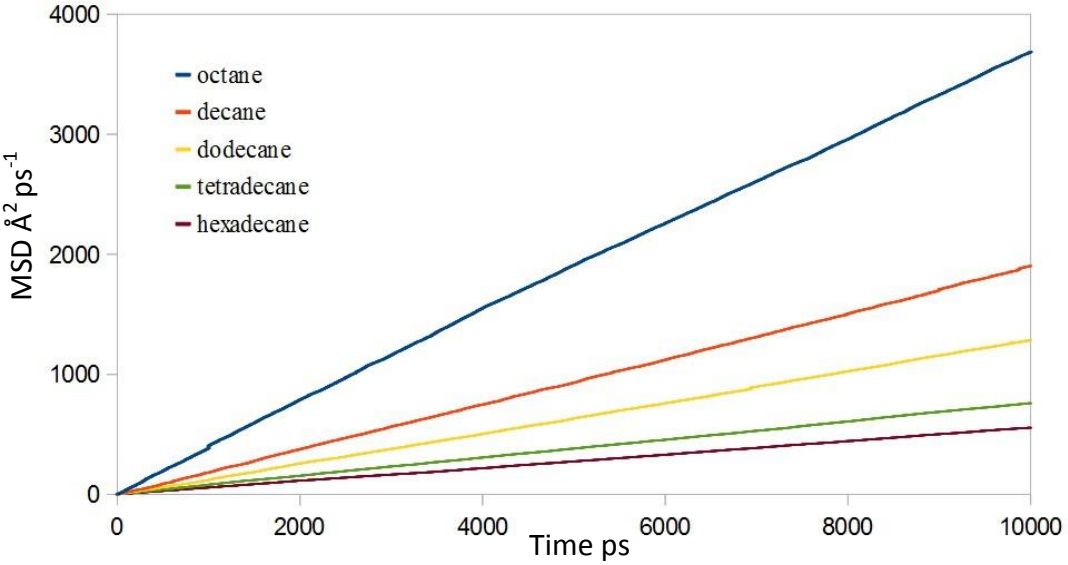

Fig. 4.4**.** A plot of the average mean square displacement as a function of time for all alkanes at 300 K in silicalite.

The diffusion coefficients for all chain lengths, at all temperatures are listed in table 4.4, with those calculated at 300 K plotted in figure 4.5. As expected, the experimentally observed monotonic decrease in diffusion coefficient with chain

length was observed. The trend is contrary to that observed with more primitive models using a rigid zeolite framework and united atom hydrocarbon models, whereby the 'resonant diffusion' or 'window effects' were observed.[18,20,22] As mentioned in reference 19, the difference in trend and the absence of the periodic dependence of diffusivity on chain length can be attributed to the short lifetime of energy traps throughout the silicalite structure, which are maintained when a rigid framework is used and molecules are less mobile when encountering energy traps commensurate to their length.

N	T (K)	Ds (MD)	Ds (QENS)	Ds (HS)	Ds (MD) /Ds (QENS)
8		$6.09\ 10^{-10}$	$2.0\ 10^{-10}$	$8.5\ 10^{-10}$	3.05
10		$3.31\ 10^{-10}$	$1.2\ 10^{-10}$	$2.1\ 10^{-10}$	2.76
12	300	$2.10\ 10^{-10}$	$8.5\ 10^{-11}$	$1.9\ 10^{-10}$	2.47
14		$1.23\ 10^{-10}$	$3.8\ 10^{-11}$	$1.3\ 10^{-10}$	3.23
16		$9.20\ 10^{-11}$	$2.5\ 10^{-11}$	$1.1\ 10^{-10}$	3.68
8		$8.83\ 10^{-10}$	$2.8\ 10^{-10}$		3.15
10		$5.90\ 10^{-10}$	$1.8\ 10^{-10}$		3.27
12	350	$3.91\ 10^{-10}$	$1.4\ 10^{-10}$		2.79
14		$2.38\ 10^{-10}$	$6.7\ 10^{-11}$		3.55
16		$1.81\ 10^{-10}$	$5.1\ 10^{-11}$		3.55
8		$1.09\ 10^{-9}$	$3.9\ 10^{-10}$		2.79
10		$7.20\ 10^{-10}$	2.710^{-10}		2.66
12	400	$5.48\ 10^{-10}$	2.3 10-^{10}		2.38
14		$3.70\ 10^{-10}$	$1.2\ 10^{-10}$		3.08
16		$3.28\ 10^{-10}$	$1.05\ 10^{-10}$		3.12

Table 4.4. A comparison of D_s values in $m^2\ s^{-1}$ obtained by the current MD simulations, hierarchical simulations[17] and QENS studies[16], for all alkanes at all temperatures.

Importantly, all the calculated diffusion coefficients were within a factor of 5 of the QENS measurements. The lowest correlation being with hexadecane at 300 K, differing from QENS studies by a factor of 3.68, which is still a marked improvement

on the biggest discrepancy in our previous study in reference 19 (hexadecane) which differed by a factor of 26, suggesting that the use of experimental loadings can lower the calculated diffusion coefficients bringing them closer to those experimentally observed for these systems. From the plot in figure 4.5 comparing all values between the current study and those obtained at infinite dilution in reference 19, one can see a significant reduction in diffusion coefficient for dodecane, tetradecane and hexadecane which are lower by a factor of 3, 3.8 and 5 respectively (notably this is more due to statistics than sorbate-sorbate interactions, as the molecules stay in their separate channel systems). However, for octane and decane, the diffusion coefficient values are still very similar to those obtained at infinite dilution.

In figure 4.5 the diffusion coefficients obtained at 300 K are also plotted in comparison with previous MD simulations using a united-atom model and rigid zeolite cage[18] and QENS measurements.[16] This plot clearly shows the great improvement in accuracy of MD simulations when a more sophisticated model is used.

When the diffusion coefficients are compared with those obtained from hierarchical simulations,[17] a close agreement is shown, with almost identical values for dodecane and tetradecane, and the only significant difference occurs for dodecane, with a difference of a factor of 2.5. Notably, all the diffusion coefficients obtained by the present study are higher than those obtained experimentally, which can be attributed to the use of a perfect silicalite crystal in the simulations, allowing for faster, less hindered diffusion on the nanometre scale. An experimental sample would have defects such as silanol nests and grain boundaries on the nanometre scale, and also surface effects from each crystallite, not accounted for under periodic boundary conditions.

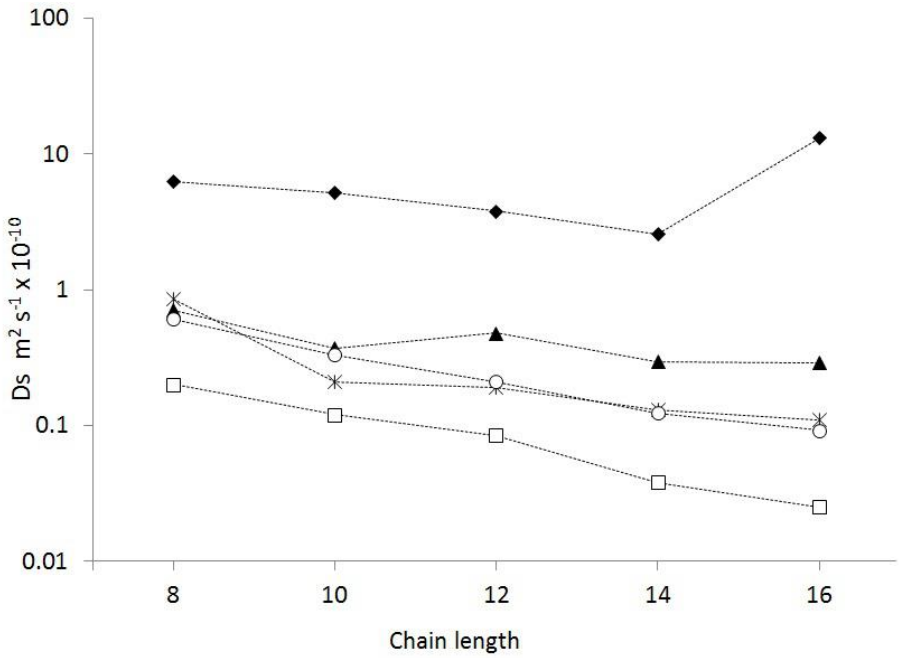

Fig. 4.5. A plot of the calculated diffusion coefficients from the current MD simulations (○), MD simulations at infinite dilution[19] (▲), MD simulations using more primitive models[18] (◆), Hierarchical simulations[17] (*) and QENS studies[16] (□).

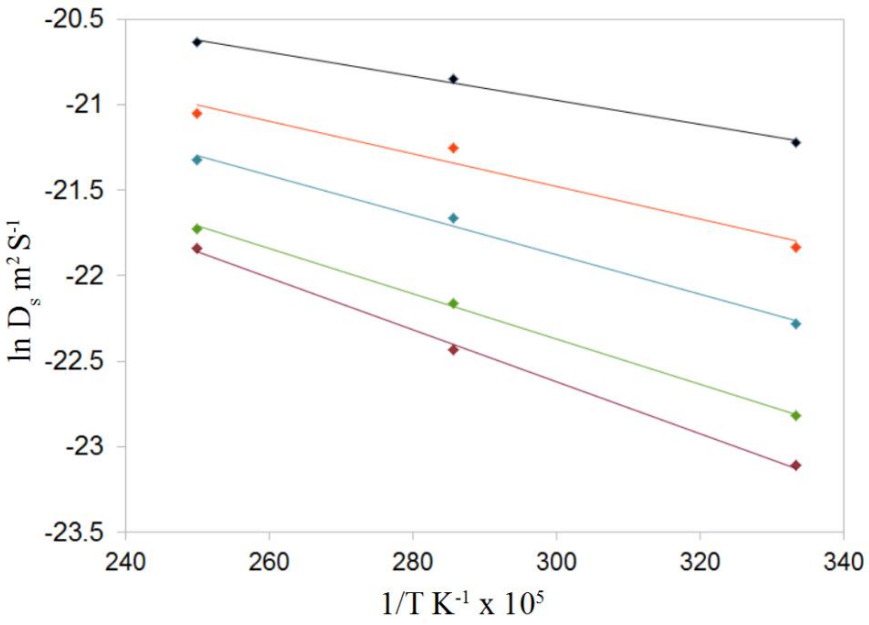

Fig. 4.6. Arrhenius plots for C_8 (◆) C_{10}(◆) C_{12} (◆) C_{14}(◆) C_{16} (◆).

The activation energy of diffusion was calculated for each alkane using Arrhenius plots as shown in figure 4.6. The activation energy values obtained from this study are tabulated and plotted in comparison with values obtained by QENS and hierarchical simulations in table 4.5 and figure 4.7 respectively. One can see that the trend (a roughly monotonic increase) of the calculated activation energies, follows that observed by QENS. The absolute values in activation energy show close agreement with experiment for octane, decane and dodecane (within 1.5 kJ mol^{-1}); the agreement is slightly less so for tetradecane and hexadecane with a difference of 1.9 and 2.6 kJ mol^{-1} respectively. It was noted in neuton spin-echo studies in reference 33 that for longer molecules, redistribution of the molecules throughout the crystal was observed at higher temperatures. For this reason, the activation energy is observed to be higher. As these simulations are carried out using periodic boundary conditions, this behaviour is not possible due to the even distribution of alkanes in the supercell being repeated infinitely. All calculated values of E_a are slightly but consistently below those obtained experimentally, which can be attributed (as with the diffusion coefficients) to the use of a perfect silicalite crystal structure. A perfect structure would have both fewer, and lower energy barriers to diffusion than a real system containing the aforementioned defects, so would cause the variation of diffusion coefficient with temperature to lower in our case.

N	E_a (MD)	E_a (QENS)	E_a (HS)
8	5.83	7.1	4.3
10	7.77	8.6	11.2
12	9.56	10.3	11.6
14	10.40	12.3	13.1
16	12.60	15.2	11.3

Table 4.5. The calculated activation energies in kJ mol^{-1} from the current MD simulations, QENS studies [17] and hierarchical simulations.[18]

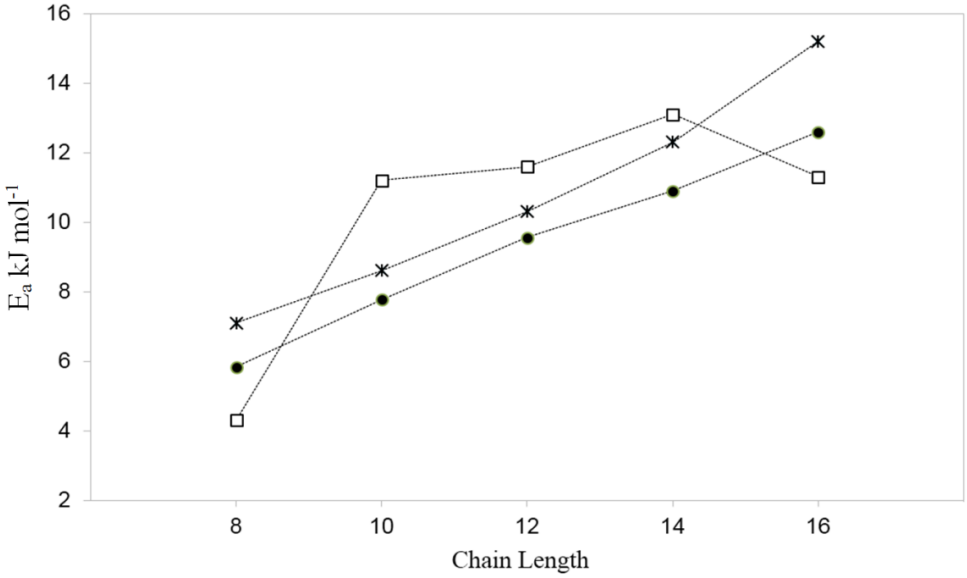

Fig. 4.7. A plot of the activation energy of diffusion with chain length, for the current MD study (•), QENS studies [16] (*) and hierarchical simulations[17] (□).

We note that the trend and agreement in activation energies with experiment is a marked improvement compared to that of the hierarchical simulations, suggesting that although this coarse-grained method is accurate at 300 K, this accuracy is not maintained as a function of temperature.

Particularly interesting behaviour observed for octane at temperatures of 350 K and above involved channel switching from the straight to the sinusoidal channels, which was only observed for octane, as the shorter molecular length allows it to overcome the barrier associated with switching channel systems at the junctions. There are two important factors associated with this behaviour; first, that it only occurs at 350 and 400 K, so the kinetic energy supplied by this temperature increase is enough for the potential barrier at the junction to be breached; second, the channel switch only occurs for molecules which have been placed in a channel with another octane molecule, rather than placed in the channel alone. To replicate successfully experimental loadings, 5 of the 8 available [010] channels in the supercell had 2 octane molecules inserted. It was from 3 of these 5 channels that switching was observed as illustrated in figure 4.8, suggesting that both the increase in temperature and the repulsion caused by sorbate-sorbate interactions in such a confined environment provide enough energy to breach the potential barrier associated with channel switching.

This switching is illustrated also in the MSD plot in figure 4.9 for one particular octane molecule which showed this behaviour. The gradient in the [010] direction decreases markedly before 2 nanoseconds while the MSD gradient in the [100] direction increases, illustrating this change in diffusive direction.

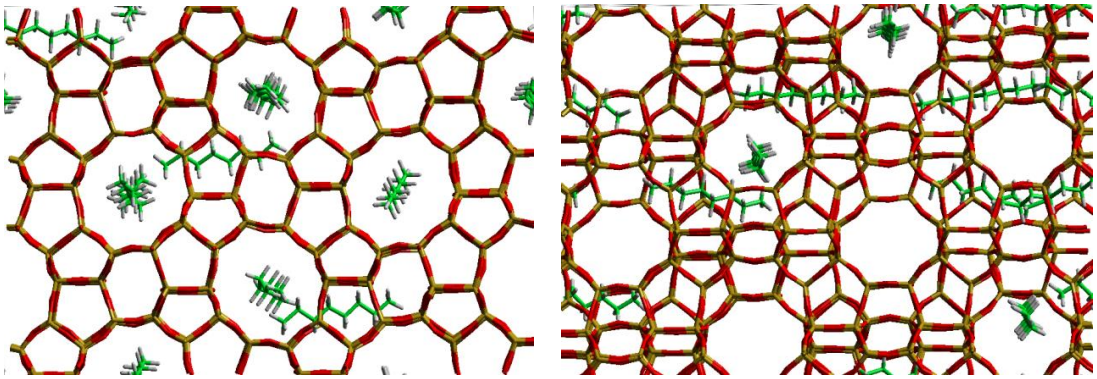

Fig. 4.8. A snapshot of the MD simulation of *n*-octane at 350 K after 4 ns, showing that 3 octane molecules have switched from the [010] channel system to the [100] channel system.

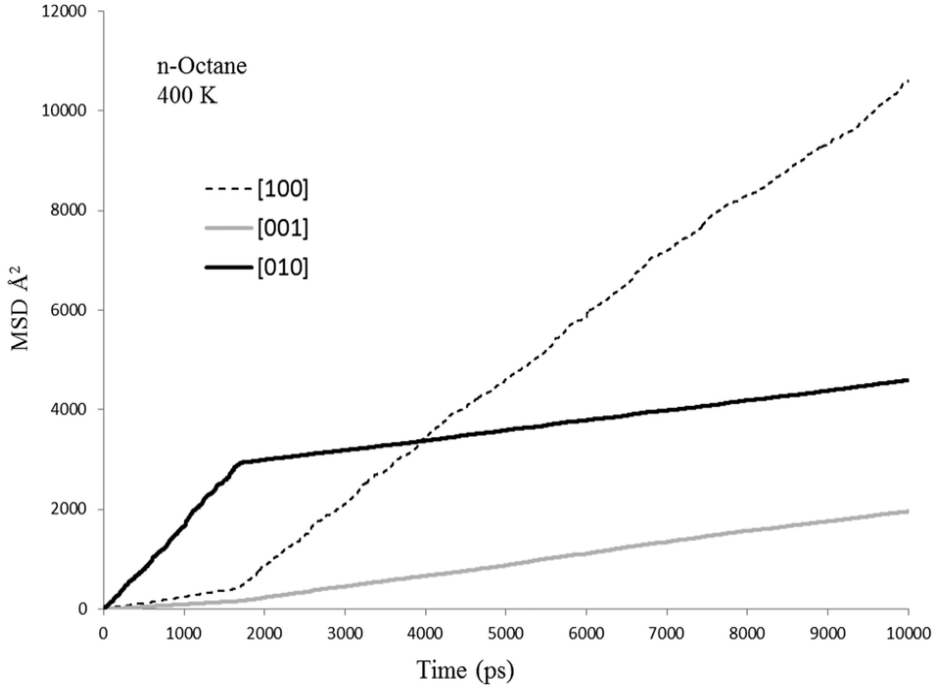

Fig. 4.9. A plot of the mean square displacement as a function of time for a particular channel switching *n*-octane molecule showing the change in MSD gradient in the [010] and [100] direction.

Future developments to this study would involve static calculations of the energetics associated with this channel switching, so that the contributions of both the temperature and sorbate-sorbate interactions could be studied in detail. The magnitude of the free energy change associated with the sorbate-sorbate interactions can then be calculated precisely. An important development would be the introduction of counterions to the framework, so the diffusion measurements can be compared between silicalite, and the industrially important ZSM-5. The introduction of extra-framework ions has been shown to slow the diffusion by roughly a factor of 5 for longer *n*-alkanes due to the potential barrier presented as shown in QENS studies in reference 16 with Na-ZSM-5.

4.2 Diffusion of Isobutane in Silicalite: A Neutron Spin-Echo and Molecular Dynamics Simulation Study

The work presented in this section covers molecular dynamics simulations and neutron spin-echo experiments of isobutane diffusion in silicalite, in the temperature range of 450 - 550 K. The simulations, as in the last section are carried out using an up-to-date flexible zeolite potential and explicit atom hydrocarbon model. Experimentally, the neutron spin echo method is especially appropriate because of its ability to measure diffusion coefficients of very slow moving sorbates in smaller pore zeolites with very high precision, due the high resolution of the instruments as discussed in chapter 2. We find close agreement (within a factor of 7.5) between the measured diffusion coefficients, and in jump diffusion behaviour between both methods. New insight into the preferred sighting of isobutane is obtained, as at lower temperatures the molecules reside in a small section of sinusoidal [100] channel, before rapid 10 Å jumps via the straight [010] channel to the next sinusoidal section. The observation matches the jump distance observed

by experiment, but contradicts the previous assumption that bulky spherical molecules prefer to occupy the intersections between channel systems. These previous observations appear to be a consequence of the approximations used in previous simulations based on a rigid zeolite framework, which for steric reasons would not allow sustained access to, or residence in the small sinusoidal channel section.

4.2.1 Introduction

Though the majority of work studying molecular diffusion in this framework focuses on *n*-alkanes (the majority of which is referenced in section 4.1), branched alkanes are just as prevalent in fluid catalytic cracking and molecular sieving systems under industrial conditions. An understanding of branched alkane diffusion behaviour is crucial to gauge the effect of molecular shape on both catalytic cracking and molecular sieving characteristics. Experimental studies of isobutane in silicalite and ZSM-5 have employed a number of techniques, including the zero-length column method[36,37] showing a strong, inversely proportional dependence on loading. Supported membrane techniques have also been used, comparing straight and branched alkanes[38], showing that self-diffusivity of isobutane is lower by a factor of 8 compared to *n*-butane. Microscopic techniques have rarely been used to study these systems, mainly due to the low resolution of instrumentation leading historically to significant errors in measured diffusion coefficients of slower moving branched sorbates. However, a comparative study of supported membrane and quasielastic neutron scattering (QENS) experiments gave diffusivities of an order of magnitude lower for the QENS measurements, consistent with literature differences between macroscopic and microscopic techniques.[39] This finding was supported by later QENS studies comparing *n*-alkanes with isobutane, [15] though the error on the isobutane diffusion coefficient was a factor of 4 of the measured value due to low instrumental resolution.

Computer simulations have also been used to study these systems, including grand canonical Monte Carlo (μVT) simulations showing preferred adsorption of

isobutane in the straight/sinusoidal channel intersections at lower loadings.[40] Infrequent hopping between intersections was calculated by transition path sampling, giving significantly lower diffusion rates than microscopic experiments.[41] Molecular dynamics (MD) simulations of *n*- and isobutane in a membrane concluded that separation of these isomers is possible as permeation was observed for *n*-butane after 200 ps unlike isobutane.[42] μVT-non equilibrium molecular dynamics also showed preferred intersectional siting of isobutane.[43]

QENS and MD simulations are excellent complementary techniques for study of these systems,[44] due to their measurement over nanosecond and nanometre scales. However it should be noted that due to approximations mentioned in the previous section, such as the use of a rigid zeolite framework, a united-atom hydrocarbon model and short simulated MD times (used in referenced studies of this system), discrepancies of 2-3 orders of magnitude in calculated diffusion coefficients are observed. These approximations can also affect behaviour such as preferred siting and the effect of molecular shape/length on diffusivity; as was reported in our recent comparative study in reference 19 studying longer *n*-alkane diffusion in silicalite as a function of computational model. We recall that greatly improved agreement was achieved between QENS and MD simulations to well within an order of magnitude and close to within experimental error when such models were implemented and loadings matching experiment were used as in section 4.1.[45] The effect of framework flexibility was actually investigated upon studying diffusion of *n*- and isobutane in silicalite (using a united atom hydrocarbon model); [46] however the very short simulated time meant very little behavioural information on the branched alkane diffusion was obtained, especially in terms of experimental comparison.

Though QENS and MD simulations are ideally suited for complementary study of these systems, some sorbates as already mentioned, move too slowly for conventional QENS instruments (time-of-flight and backscattering spectrometers), and a higher energy resolution is obtained using the neutron spin-echo (NSE) technique[47] (discussed in section 2.5.3). We report here the very precise measurement of diffusion coefficients of isobutane in silicalite using the neutron

spin-echo technique and molecular dynamics simulations using contemporary framework and hydrocarbon models. This is the first tandem microscopic experiment/computational study of slow moving branched alkanes in this zeolite. Good agreement between experimental and calculated diffusion coefficients and activation energies is achieved, along with new insight into the preferred sighting of isobutane molecules.

4.2.2 Methodology

4.2.2.1 Neutron Spin-Echo Measurements

The neutron spin-echo experiments were performed by Herve Jobic (IRCELYON), using the NSE spectrometer at the ELLA neutron guide hall at the FRJ-2 reactor in Jülich[48] (which has been transferred to the MLZ in Garching). Data were collected using a neutron wavelength band of 10% FWHM centred at λ = 8 Å over a Fourier-time range from t = 0.1 – 22 ns, at low wave-vector transfer values between Q = 0.08 - 0.3 $Å^{-1}$, and sample temperatures between T = 300 K and 550 K. The incident neutron flux was of ~ 0.6 × 10^6 n cm^{-2} s^{-1} on a sample area of 27 x 27 mm^2. Collection times of 200 s were used for each of the 27 counts to complete an echo, and normalization scan for one (Q, t, T) combination. Sample data were normalized to data from an elastic reference scatterer, i.e. microporous carbon powder. Data evaluation was performed as described in reference 47, without subtraction of background scattering. Data from the full detector area were integrated, which leads to a wave-vector transfer width of about 0.025 $Å^{-1}$ FWHM.

The silicalite sample was activated at 770 K under oxygen flow, then pumped to 10^{-4} Pa at the same temperature. After cooling, the zeolite was loaded with 2 isobutane molecules per unit cell. The sample was transferred, inside a glovebox, into a cylindrical aluminium container. Since a larger intensity is obtained in NSE with coherent scatterers, deuterated isobutane was used. Coherent scattering measures, in principle, the transport diffusivity,[44] but at low loading, which is the case here, the self- and transport diffusion coefficients have the same values.[49]

4.2.2.2 Computational Methods

Our MD simulations employed an identical 2 x 2 x 2 orthorhombic silicalite supercell with Pnma symmetry[24] as in the previous section. Full ionic charges were assigned to the framework species. As mentioned, the potentials used to describe the flexible zeolite framework are widely used for simulations of silicalite but originate from work on SiO_2.[28] The Buckingham potential parameters to describe Si-O and O-O interactions, along with the harmonic three-body potential parameters describing the O-Si-O triads are listed in table 4.1. A cut-off distance of 10 Å was used. Forcefields employed to describe the hydrocarbon were derived from previously referenced vibrational data and listed in table 4.3. Each hydrogen atom was assigned a charge of +0.1, while the primary and tertiary hydrocarbons were given charges of -0.3 and -0.1 respectively to give an overall charge neutral isobutane molecule. The bonds and bond angle vibrations were described by harmonic potentials while the dihedrals were described by a cosine potential listed in table 4.3. The guest-host interactions and intramolecular sorbate interactions were modelled by a Lennard-Jones potential with parameters listed in table 4.2, with a 10 Å cut-off.

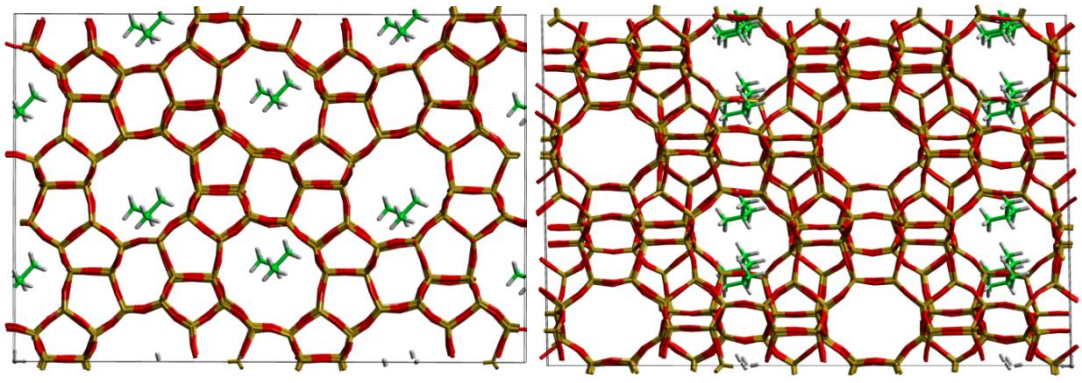

Fig. 4.10. The starting configuration of isobutane in silicalite pre-production run at 450 K viewed down the (left) [010] direction and (right) [100] direction.

For the initial configuration, the isobutane molecules were placed in the intersections of the straight and sinusoidal channels, avoiding strong contact with

the walls. The intersection was used as a starting location as it has been shown for non-linear molecules to be an energetically favourable location. [50,51,52,53,54] This starting configuration for the MD runs is shown in figure 4.10. The loading matched those of the NSE experiment at 2 molecules per unit cell.The system was then equilibrated at the desired temperature for 1 ns in the canonical (NVT) ensemble. After the equilibration run, the production run of 10 ns in the microcanonical (NVE) ensemble was carried out at 440, 500 and 550 K. A timestep of 0.5 fs was used with atomic coordinates saved every picosecond (every 2000 steps). A Berendsen[34] thermostat was used to maintain the temperature near a set point, with a time constant for thermal energy exchange set at 1 ps. All simulations were carried out using the DL_POLY_4 code.[35]

The production time of 10 ns is adequate to obtain a linear mean-square displacement (MSD) plot, indicative of true diffusive motion. The changes in coordinates of the central carbon atom were used in calculating the MSD, and the Einstein relationship was then used to calculate the self-diffusion coefficient.

4.2.3 Results and Discussion

4.2.3.1 Neutron Spin-Echo Experiments

Normalized intermediate scattering functions (I(Q,t)) obtained experimentally for isobutane in silicalite at different temperatures are shown in figure 4.11, at two Q values. The faster decay of the scattering functions observed with increasing temperature at a given Q value, reflects the increase of the diffusivity. The experimental data are well fitted by an isotropic diffusion model.[44] Figure 4.12 shows a comparison with experiment for both 3D and 1D diffusion models, the 3D diffusion model fits better the experimental points than 1D diffusion, which implies that isobutane molecules are able to explore both straight and sinusoidal channels, while previous QENS and NSE measurements showed that linear n-alkanes longer or equal to C_8 diffuse mainly along the straight channels [15,33]

Temporal decays extracted from the curves in figure 4.12 can be expressed as energy broadenings (outlined in section 2.5.3) as depicted in figure 4.13. When plotted as a function of Q^2, one expects a linear variation of the energy broadening in the case of continuous or Fickian diffusion. It appears from figure 4.13 that the experimental points deviate from straight lines, and the trend is characteristic of jump diffusion (as outlined in section 2.5.1.2). The jump model fitted incorporates a fixed jump length of 10 Å, so fits to the Chudley-Eliott model[55] previously used in the case of benzene in ZSM-5.[56] The diffusivities were then extracted from the low-Q range.[44]

The experimental diffusion coefficients are reported in table 4.5 and plotted in figure 4.15. The activation energy obtained from an Arrhenius representation (figure 4.16) is 22.6 kJ mol^{-1}. Previous QENS measurements were performed on a back-scattering spectrometer on the same system, using however ZSM-5 instead of silicalite.[39] The diffusion coefficients were about one order of magnitude lower in ZSM-5, with an estimated activation energy of 17 kJ mol^{-1}. Since the broadenings were small, compared with the instrumental resolution, the errors were much larger than in the present work.

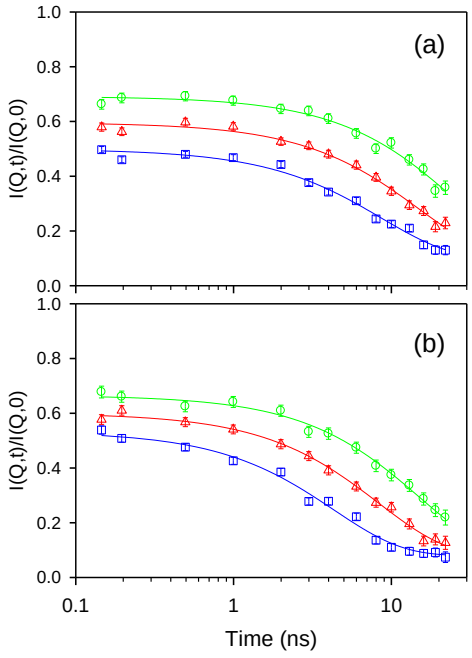

Fig. 4.11. Comparison between experimental and calculated normalized intermediate scattering functions obtained for isobutane in silicalite for Q = 0.2 Å^{-1} (a) and 0.3 Å^{-1} (b), at 444 K (○), 491 K (△), and 550 K (□). The solid lines correspond to a 3D diffusion model.

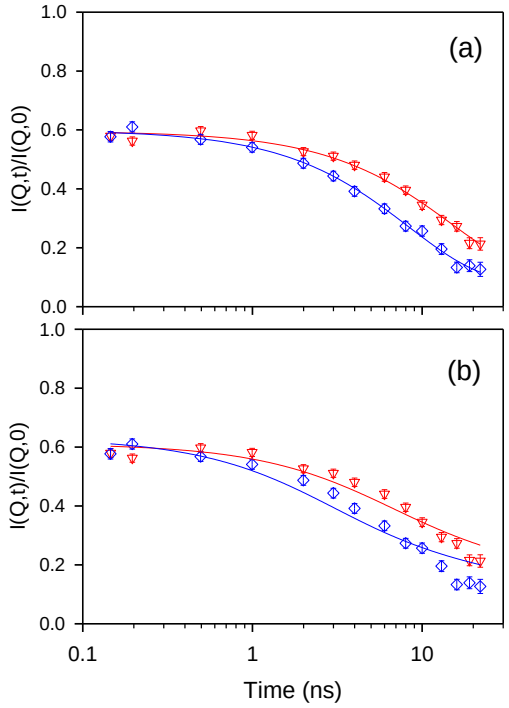

Fig. 4.12. Comparison between experimental and calculated normalized intermediate scattering functions obtained for isobutane in silicalite at 491 K, for Q = 0.2 (▽) and 0.3 Å^{-1} (◇). The solid lines are calculated with: (a) a 3D diffusion model, and (b) a 1D diffusion model.

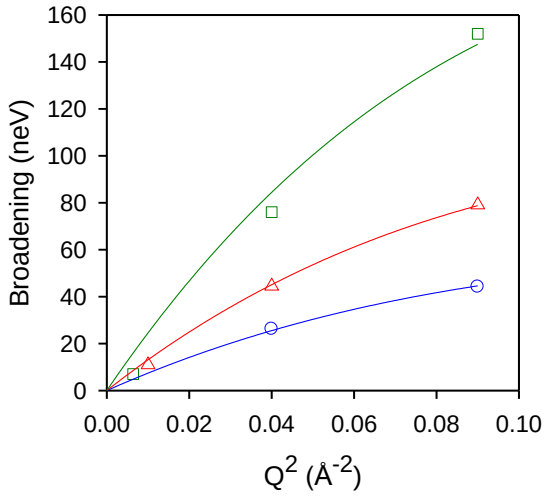

Fig. 4.13 Broadenings obtained for isobutane in silicalite at: 444 K (○), 491 K (△), and 550 K (□). The solid lines correspond to a Chudley-Elliot jump diffusion model.

T K	D_s (NSE)	D_s (MD)
444	1.2×10^{-11}	
450		9.1×10^{-11}
491	2.1×10^{-11}	
500		1.5×10^{-10}
550	3.9×10^{-11}	2.2×10^{-10}
E_a (kJ mol^{-1})	22.6	19.2

Table 4.5. Calculated D_s values in m^2 s^{-1} for isobutane at all temperatures.

4.2.3.2 Molecular Dynamics Simulations

The linearity of the average MSD plot was confirmed before calculating the diffusion coefficients for each system; listed in table 4.5. Simulated diffusion coefficients are all within a factor of 7.5 of experimental results. At 550 K where the temperatures match exactly we obtain agreement to a factor of 5. It is difficult to obtain the statistical errors of these diffusion coefficient values; however the very linear nature of the MSD plots in figure 4.14 suggests that these errors are low (though could potentially be quantified by the blocking method).

All calculated diffusion coefficients are in the upper limit of experimental results, which as in the previous chapter can be attributed to the use of a perfect periodic silicalite crystal structure in these simulations. The experimental sample of silicalite would possess defects within the crystallite, and grain boundaries on the scale of a few nanometres which would lower the average diffusion coefficient. The absence of these defects in the simulation could account for the higher diffusion coefficients measured. The activation energy for the diffusion was calculated from the Arrhenius plots shown in figure 4.16, with a value of 19.2 kJ mol^{-1}, 3.4 kJ mol^{-1} (~15%) lower than that observed by the NSE experiments.

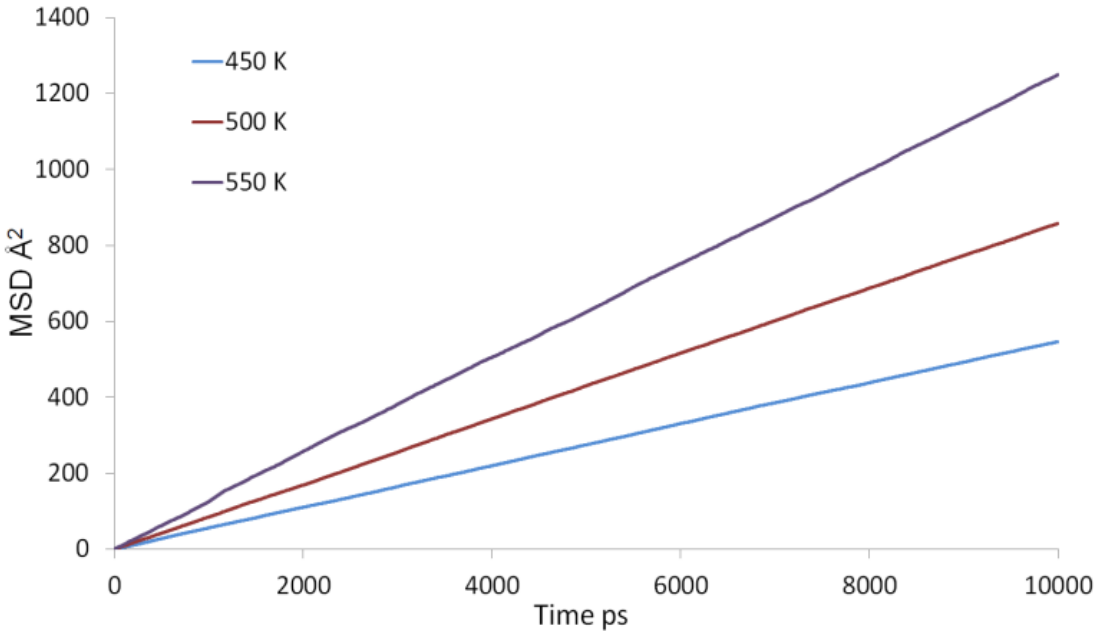

Fig. 4.14. The average mean square displacement as a function of time for isobutane at all 3 temperatures.

It is notable that the diffusion coefficients obtained for isobutane are significantly lower than those obtained for *n*-alkanes in chapter 4.1, and references 19 and 45. The simulated D_s of *n*-octane (also plotted in figure 4.16) at 400 K is higher by a factor of 12 than that of isobutane at 450 K, illustrating the effect of alkane branching on the diffusion in the 5.5 Å silicalite pore, even when framework flexibility is taken into account. This hindrance is also illustrated by the much higher activation energy, compared to that of *n*-octane (5.8 kJ mol^{-1}).

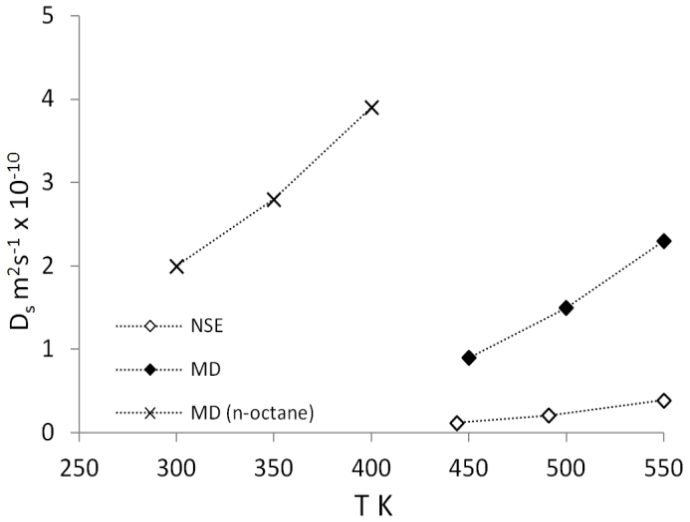

Fig. 4.15. Comparison of diffusion coefficients of isobutane from NSE (◊), MD (♦) compared with previous simulation of *n*-octane diffusion in section 4.1 (x).

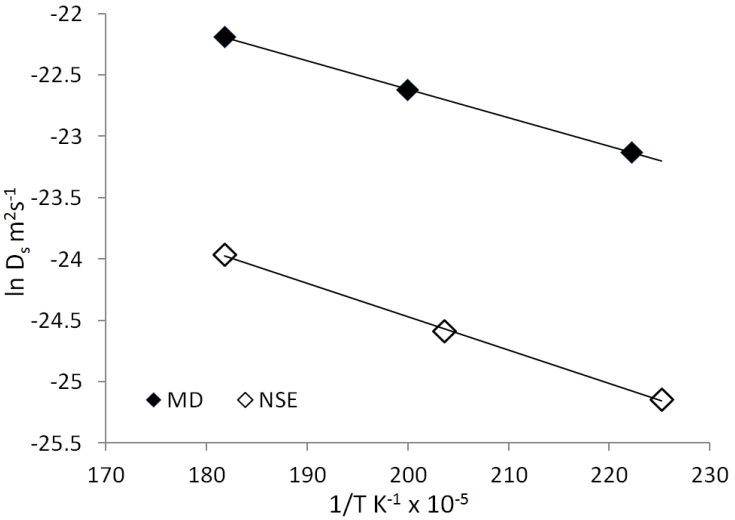

Fig. 4.16. Arrhenius plots from the MD simulations (♦) and NSE experiments (◊).

To gain a greater understanding of the diffusion of isobutane in the silicalite framework, the mean square displacement plot in the possible directions can be examined to observe preference for a specific channel system. These can also be illustrated by the use of a trajectory plot to show specific locations of molecules. The average directional MSD plot of all isobutane molecules at 450 K is shown in figure 4.17(a). The plot shows that the molecules are diffusing in both channel systems, but show preference for the [100] direction (the sinusoidal channels).

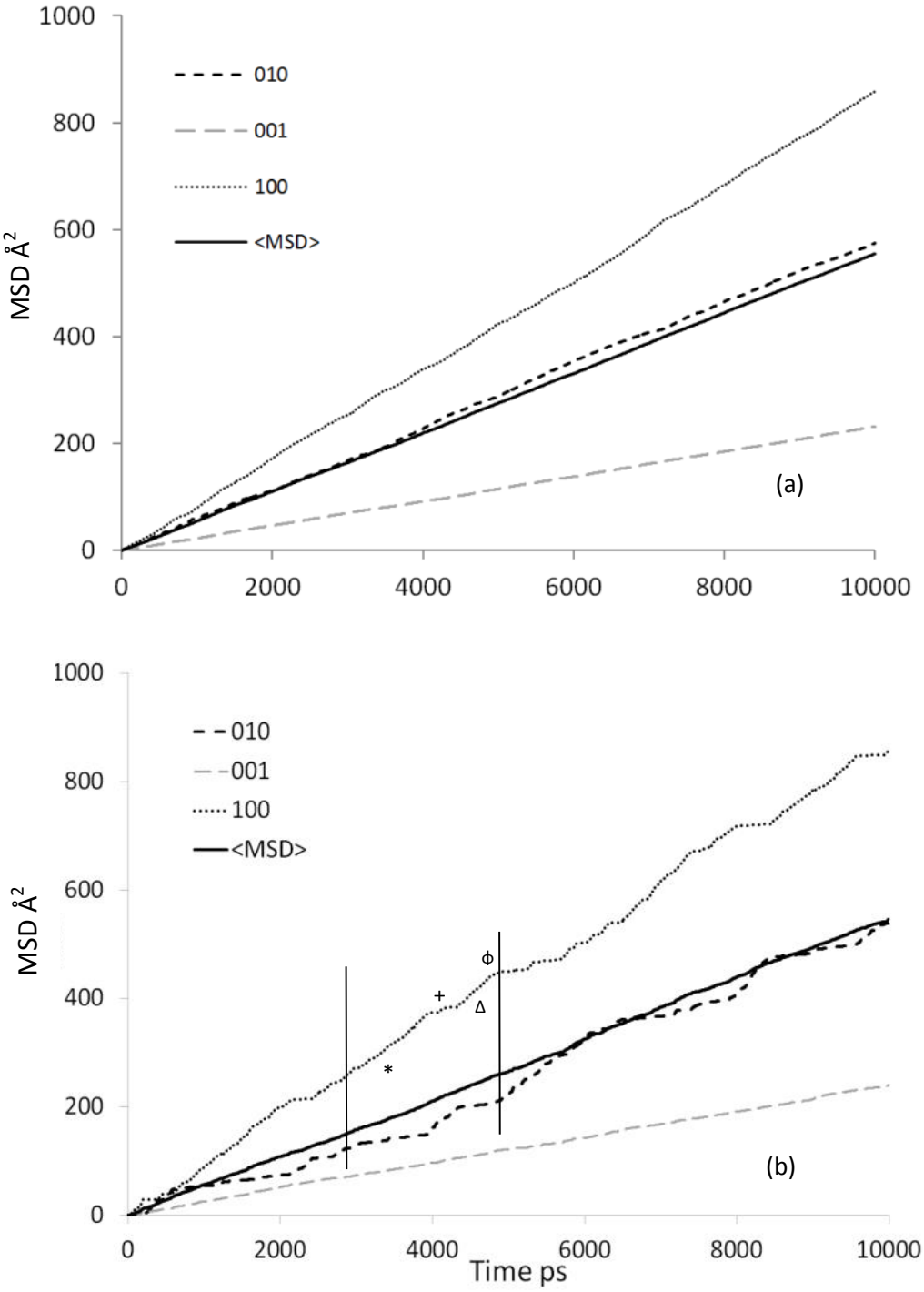

Fig 4.17. Average directional MSD of all isobutane molecules (a) and an individual isobutane molecule (b) in silicalite at 450 K. The symbols represent the appropriate portion of the associated trajectory plot.

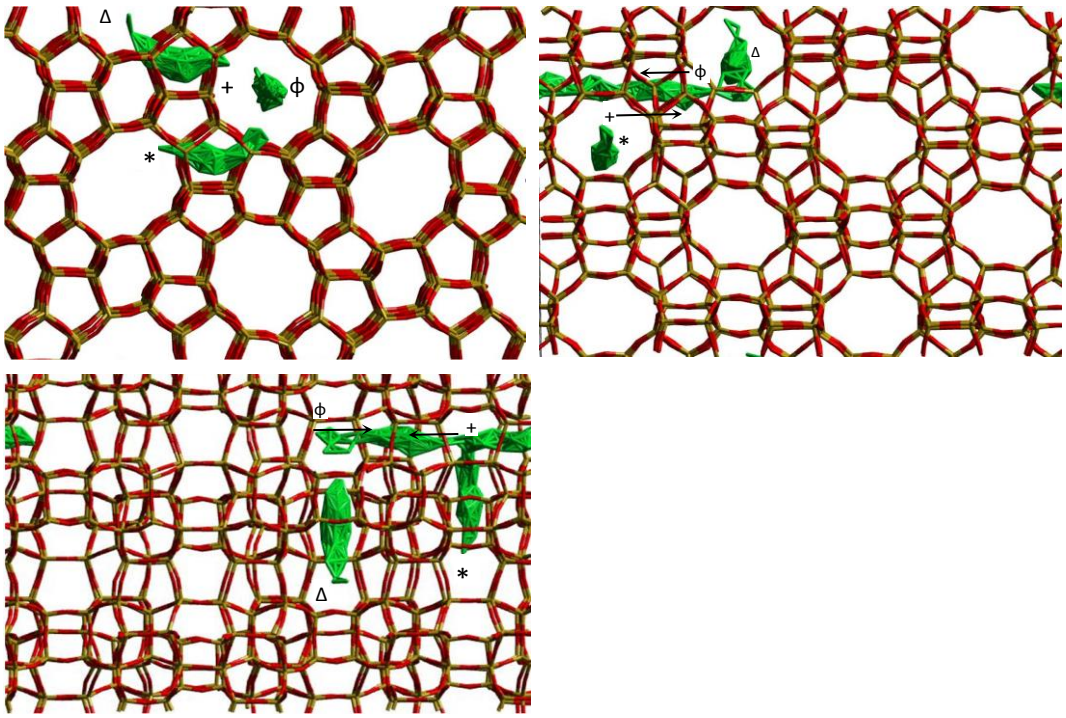

Fig. 4.18. Trajectory plot of isobutane in silicalite at 450 K between 3000 ps and 5000 ps of the MD simulation run. The symbols represent the appropriate portion of the associated MSD plot.

Though this result contrasts with previous studies into *n*-alkane diffusion, where the [010] channel is preferred, the ability to explore both the straight and sinusoidal channels would agree with the 3D diffusion observed by NSE. This behaviour is detailed in the directional MSD of an individual isobutane molecule at 450 K in figure 4.17(b), which particular MSD plot shows that the molecule spends prolonged periods diffusing in the [100] channel system between much shorter periods of time in the [010] channel system. The trajectory plot of this molecule between 3000 and 5000 ps is shown in figure 4.18.

The trajectory plot shows that the molecular diffusion in the [100] direction is actually molecular trapping in the very small section of the sinusoidal channel between intersections (c. 3 Å in length), then movement between two adjacent sinusoidal channel segments via the straight channel segment connecting them. The movement in the [010] direction is rapid as illustrated in the MSD plot in figure 4.17(b), taking place back and forth between the two trapping sinusoidal segments, indicative of a jump diffusion mechanism. The 10 Å jump length between sinusoidal segments matches that observed in the NSE experiments. However, it is not possible from experiment to determine whether the jumps occur between the

intersections or between sinusoidal channels. Previously referenced simulations have all shown that the preferred siting is in the intersections between channels, where it is assumed the molecule would spend the residence time between jumps. This simulation however suggests that the molecule spends the residence time in a 3 Å sinusoidal channel section. This preference can be attributed to the favourable interactions between the molecule and channel walls, enabled by the increased access and geometric freedom offered by the use of a flexible silicalite framework. However, in previous simulations the rigid framework, used due to computational restrictions, would have prevented sustained access to this region due to steric hindrance and associated instability. Thus the lowest potential energy region in the rigid framework would be the intersections. The breathing of the framework in this simulation allows for both sustained access, and framework relaxation around the isobutane accommodating this preferred siting. The isobutane then makes the 10 Å jumps between adjacent sections of sinusoidal channel. Oscillation across the 3 Å channel section and passage via the straight channel segments is sufficient to make the diffusion to appear isotropic in experiment.

We recognise that the trapping of a molecule of a specific shape/length in regular areas of the zeolite framework is evocative of the so-called window effect mentioned in chapter 1. The conclusion of reference 19 was that the use of a flexible framework should decrease the lifetime of these energy traps, so that those commensurate in length to the energy trap have their diffusion slowed. The presence of the window effect may be assessed using another sorbate such as 2,2-dimethylpentane, similar to isobutane but with two extra hydrocarbons on one of the chains. The window effect would predict that the chain of 2,2-dimethylpentane may extend out of the sinusoidal channel section, causing the barrier to mobility to drop and the diffusivity to be higher than isobutane which is more commensurate to the length of the sinusoidal section.

To decipher the dependence of this siting preference on temperature, the average directional MSD plot of all isobutane molecules at 550 K is shown in figure 4.20(a). This behaviour differs from that at 450 K, as the isobutane molecule is preferentially diffusing in the [010] direction (the straight channel system), as opposed to the

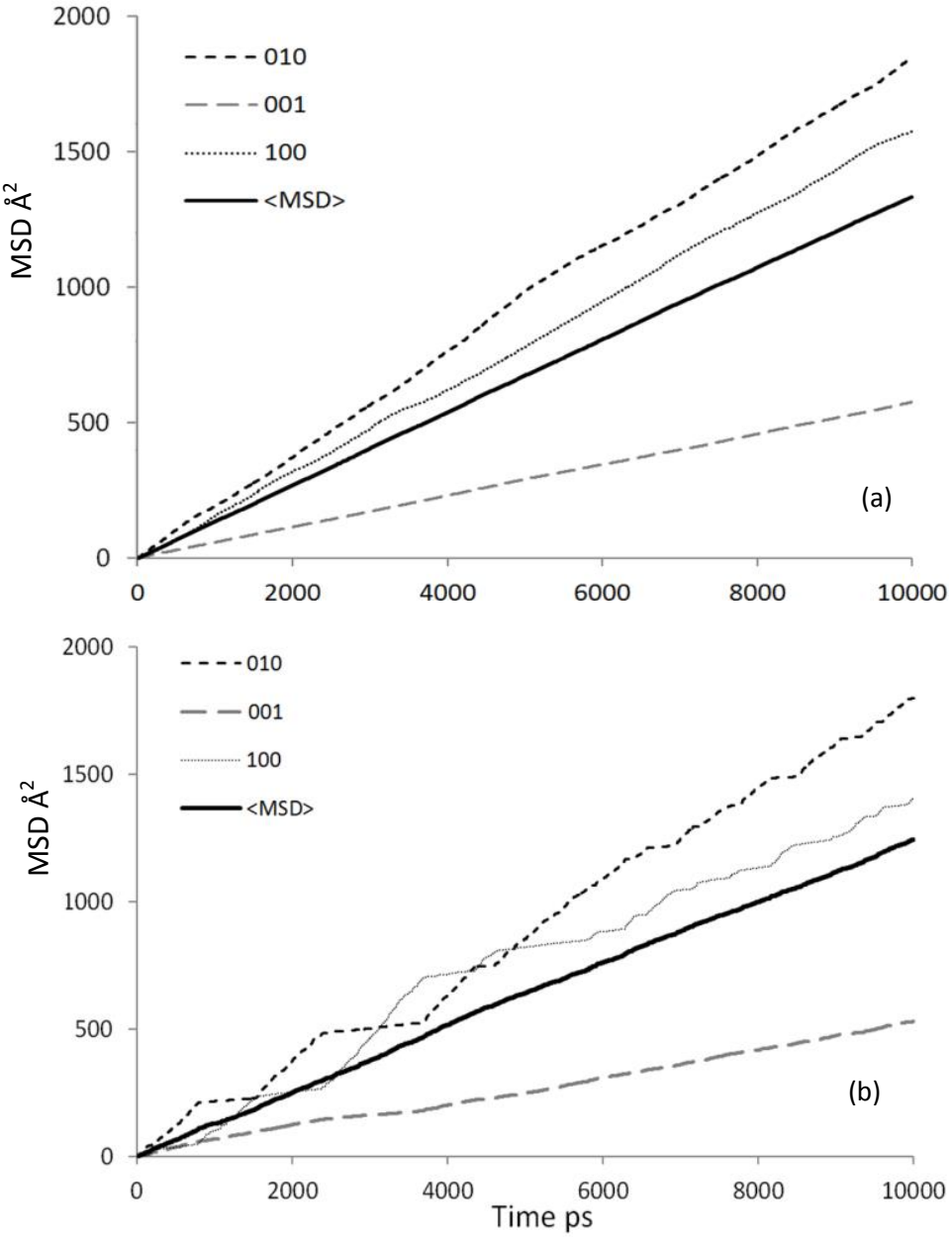

Fig 4.19. Average directional MSD of all isobutane molecules (a) and an individual isobutane molecule (b) in silicalite at 550 K.

[100] direction at 450 K. This observation suggests that less time is spent residing in the small section of sinusoidal channel system, illustrated by the directional MSD plot of an individual molecule in figure 4.20(b). The plot shows two distinct types of behaviour before and after 5000 ps: the first is that of long term residence in either channel, consistent with the experimentally observed 3D diffusion, in that the molecule is prone to translating along either channel system freely. The increased gradient of the diffusive motion in the [100] direction is more indicative of unhindered diffusion along the channel than molecular trapping, which is

consistent with behaviour exhibited by *n*-octane in reference 45, suggesting that the higher temperatures allow behaviour more like an *n*-alkane to take place.

After 5000 ps however, regular and frequent switching between the two channel systems is observed, as illustrated by the trajectory plot in figure 4.20 suggesting that two modes of diffusion are available to isobutane at higher temperatures: That of prolonged, highly mobile diffusion in either channel system, or frequent switching between the two channel systems (both of which would agree with the 3D diffusion observed by NSE). This behaviour is in contrast with that of *n*-alkanes such as octane, which upon switching to another channel system would remain there for extended periods as the molecular length was a hindrance to the channel switching process, which is not the case for the more spherical isobutane. The molecular sinusoidal trapping is diminished in both diffusion modes exhibited at higher temperatures, suggesting that the level of trapping is inversely proportional to temperature, as expected for an activated process such as jump diffusion.

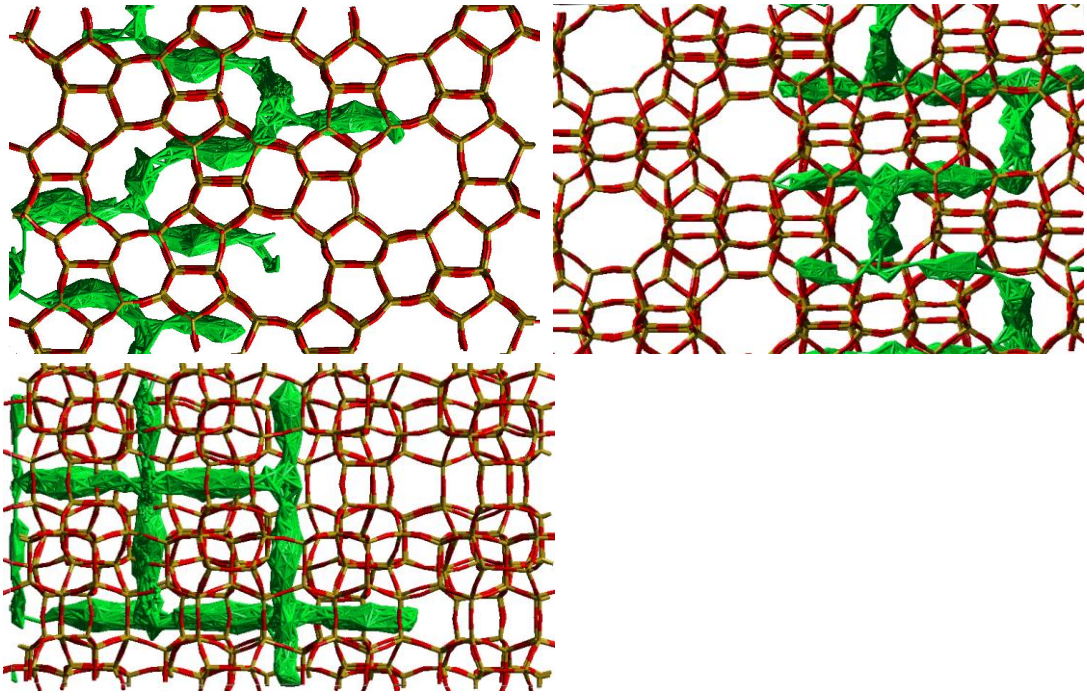

Fig 4.20. Trajectory plot of isobutane in silicalite at 550 K between 7000 ps and 9000 ps of the MD.

The trajectory plot also shows the diffusion is not confined to a specific section of the silicalite structure, with access to much of the supercell during this 2 ns period,

compared to the local restriction showed at 450 K (figure 4.18). This observation supports the proposal that the level of trapping is temperature dependent, and that the increase in average diffusion coefficient is related to the lower level of trapping in small sinusoidal sections. The initial observation of prolonged periods of unidimensional diffusion (though allowed in both [100] and [010] directions) also agree with the decline in this trapping at higher temperatures, despite the confinement of the movement to one channel system for a period.

4.3 Summary and Conclusions

The work in this chapter signifies an advance in the quantitative study of hydrocarbon diffusion in the MFI zeolite framework. Where state-of-the-art molecular dynamics simulations employing a flexible zeolite framework and explicit atom hydrocarbon models provide good agreement in measured diffusion coefficients and activation energy values, close to those measured by precise experimental microscopic methods based on neutron scattering techniques. Our results also provide interesting observations on the channel switching behaviour and preferred siting of the sorbates. The simulations of *n*-alkanes were compared to conventional quasielastic neutron scattering experiments, ideally suited for comparison with molecular dynamics simulations due to their domain over the nanosecond and nanometre regime. The simulations of the slower moving, bulkier isobutane were compared to neutron spin-echo experiments, able to measure diffusion coefficients of slow moving sorbates with very high precision. The emergence of the latter, along with improvement of the conventional QENS techniques allow for comparison of precise microscopic techniques with these advanced computational models to gain a detailed, reliable insight into the dynamics of hydrocarbons in microporous systems.

The diffusion coefficients and activation energies of diffusion were calculated for longer *n*-alkanes (C_8–C_{16}) in silicalite. The measurements were carried out at temperatures of 300, 350 and 400 K at loadings matching those of previous QENS studies. The calculated diffusion coefficients were in good agreement with

experimental values, significantly closer than those calculated using simpler framework and hydrocarbon models. In the case of the longer alkanes, better agreement in diffusion coefficients was obtained than MD studies using the same model, but without using experimental loadings – showing the effect of loading in lowering a diffusion coefficient. The calculated activation energies were found to give the experimentally observed monotonic increase in value with chain length, and agreed with experiment to within 1.5 kJ mol^{-1} for shorter alkanes. However, a larger difference for tetra and hexadecane was observed possibly due to the use of periodic boundary conditions forbidding the experimentally observed redistribution of the alkanes throughout the crystal. The calculated diffusion coefficients and activation energies were found to be in the upper limit and lower limit respectively of the experimental values, attributed to the use of a perfect zeolite crystal for the MD studies and difficulties in extrapolating an Arrhenius relationship in the presence of continuous diffusion (future work would involve use of a defective zeolite structure to assess any difference in Ds obtained). Channel switching between the straight and sinusoidal channels was observed for octane at higher temperatures which was attributed to the molecular size of octane, the kinetic energy supplied by the temperature increase, and the repulsion caused by extra octane molecules in the confined channel system allowing the potential barrier of channel switching at the junctions to be breached. Future work will involve static calculations of the channel switching process, and the introduction of framework aluminium and counterions to the framework, so the diffusion measurements can be compared between silicalite and ZSM-5.

The diffusion of isobutane in silicalite was measured using neutron spin-echo experiments and molecular dynamics simulations between 444 and 550 K. The NSE measurements showed jump diffusion with a jump length of 10 Å, with the intermediate scattering functions showing the isobutane molecules are able to explore both [010] and [100] channel systems, unlike *n*-alkanes in previous studies of silicalite diffusion. The diffusion coefficients measured experimentally were between 1.2 and 3.9 x 10^{-11} m^2s^{-1}, with an activation energy of 22.6 kJ mol^{-1}. Agreement with the molecular dynamics simulations was well within an order of

magnitude (between a factor of 5 and 7.5), with diffusion coefficients ranging from 9.1 – 22 x 10^{-11} m^2s^{-1} and an activation energy of 19.2 kJ mol^{-1}. Discrepancies were attributed to the use of a perfect periodic silicalite crystal structure as with the longer *n*-alkane diffusion. The MD simulations agreed with the 10 Å jump length observed by experiment; however the preferred residence time was spent in small sections of the sinusoidal channel system, rather than the intersections between channels shown to be favourable sites in previous simulations. This difference in preferred siting is attributed to favourable interactions between the molecule and the channel walls, and the access granted by the use of a flexible silicalite framework. However, in previous simulations of isobutane in silicalite the rigid framework would have prevented sustained access of isobutane to this region due to steric hindrance and associated instability. For this reason, the lowest potential energy region in the rigid framework would be the intersections. The breathing of the framework in this simulation allows for both sustained access, and framework relaxation around the isobutane accommodating this preferred siting. At 550 K, isotropic diffusion of isobutane observed in experiment is observed as dominant in the simulations where the sinusoidal trapping diminishes significantly. This reduction in trapping suggests that the diffusion of isobutane in silicalite may be governed by the temperature dependent trapping in small sinusoidal channel sections, becoming increasingly isotropic with temperature, where exploring of both channel systems is allowed.

The study in section 4.1 was published in reference 45. The study in section 4.2 is published in the following paper:

O'Malley, A. J.; Catlow, C. R. A.; Monkenbusch, M.; Jobic, H. *The Journal of Physical Chemistry C* **2015**, *119* (48), 26999-27006.

References

(1) Weitkamp, J.; Puppe, L. *Catalysis and Zeolites: Fundamentals and Applications*; Springer Science & Business Media, 1999.

(2) Jiang, M.; Eic, M.; Miachon, S.; Dalmon, J.-A.; Kocirik, M. *Separation and Purification Technology* **2001**, *25*, 287.

(3) Leroy, F.; Rousseau, B.; Fuchs, A. *Physical Chemistry Chemical Physics* **2004**, *6*, 775.
(4) Krishna, R.; Van Baten, J. *Chemical Engineering Journal* **2008**, *140*, 614.
(5) Koriabkina, A. O.; de Jong, A. M.; Schuring, D.; van Grondelle, J.; van Santen, R. A. *The Journal of Physical Chemistry B* **2002**, *106*, 9559.
(6) Lin, D.; Ducarme, V.; Coudurier, G.; Vedrine, J. *Studies in Surface Science and Catalysis* **1989**, *46*, 615.
(7) Yu, M.; Wyss, J. C.; Noble, R. D.; Falconer, J. L. *Microporous and Mesoporous Materials* **2008**, *111*, 24.
(8) Fried, J.; Weaver, S. *Computational Materials Science* **1998**, *11*, 277.
(9) Jianfen, F.; Van de Graaf, B.; Xiao, H.; Njo, S. *Journal of Molecular Structure: THEOCHEM* **1999**, *492*, 133.
(10) Wu, P.; Debebe, A.; Ma, Y. H. *Zeolites* **1983**, *3*, 118.
(11) Song, L.; Sun, Z.-L.; Rees, L. V. *Microporous and Mesoporous Materials* **2002**, *55*, 31.
(12) Cavalcante, C. L. J.; Ruthven, D. M. *Industrial & Engineering Chemistry Research* **1995**, *34*, 177.
(13) Bing, Z.; Pei, S.; Shishan, S.; Xiexian, G. *J. Chem. Soc., Faraday Trans.* **1990**, *86*, 3145.
(14) Zikanova, A.; Bülow, M.; Schlodder, H. *Zeolites* **1987**, *7*, 115.
(15) Jobic, H. *Journal of Molecular Catalysis A: Chemical* **2000**, *158*, 135.
(16) Jobic, H.; Theodorou, D. N. *The Journal of Physical Chemistry B* **2006**, *110*, 1964.
(17) Maginn, E. J.; Bell, A. T.; Theodorou, D. N. *The Journal of Physical Chemistry* **1996**, *100*, 7155.
(18) Runnebaum, R. C.; Maginn, E. J. *The Journal of Physical Chemistry B* **1997**, *101*, 6394.
(19) O'Malley, A. J.; Catlow, C. R. A. *Physical Chemistry Chemical Physics* **2013**, *15*, 19024.
(20) Gorring, R. *Journal of Catalysis* **1973**, *31*, 13.
(21) Dubbeldam, D.; Calero, S.; Maesen, T. L.; Smit, B. *Physical Review Letters* **2003**, *90*, 245901.
(22) Ruthven, D. M. *Microporous and Mesoporous Materials* **2006**, *96*, 262.
(23) Ruckenstein, E.; Lee, P. *Physics Letters A* **1976**, *56*, 423.
(24) Artioli, G.; Lamberti, C.; Marra, G. *Acta Crystallographica Section B: Structural Science* **2000**, *56*, 2.
(25) Grau-Crespo, R.; Acuay, E.; Ruiz-Salvador, A. R. *Chemical Communications* **2002**, 2544.
(26) Fyfe, C. A.; Kennedy, G. J.; De Schutter, C. T.; Kokotailo, G. T. *Journal of the Chemical Society, Chemical Communications* **1984**, 541.
(27) Youngs, T. *Journal of Computational Chemistry* **2010**, *31*, 639.
(28) Vessal, B.; Amini, M.; Catlow, C. *Journal of Non-Crystalline Solids* **1993**, *159*, 184.
(29) Herzberg, G. *New York: Van Nostrand Reinhold, 1950, 2nd ed.* **1950**, *1*.
(30) Catlow, C.; Freeman, C.; Vessal, B.; Tomlinson, S.; Leslie, M. *Journal of the Chemical Society, Faraday Transactions* **1991**, *87*, 1947.
(31) Raj, N.; Sastre, G.; Catlow, C. R. A. *The Journal of Physical Chemistry B* **1999**, *103*, 11007.
(32) Kiselev, A.; Lopatkin, A.; Shulga, A. *Zeolites* **1985**, *5*, 261.
(33) Jobic, H.; Farago, B. *The Journal of Chemical Physics* **2008**, *129*, 171102.

(34) Berendsen, H. J.; Postma, J. P. M.; van Gunsteren, W. F.; DiNola, A.; Haak, J. *The Journal of Chemical Physics* **1984**, *81*, 3684.
(35) Todorov, I. T.; Smith, W.; Trachenko, K.; Dove, M. T. *Journal of Materials Chemistry* **2006**, *16*, 1911.
(36) Hufton, J. R.; Ruthven, D. M. *Industrial & Engineering Chemistry Research* **1993**, *32*, 2379.
(37) Zhu, W.; Malekian, A.; Eić, M.; Kapteijn, F.; Moulijn, J. *Chemical Engineering Science* **2004**, *59*, 3827.
(38) Millot, B.; Methivier, A.; Jobic, H.; Moueddeb, H.; Dalmon, J. *Microporous and Mesoporous Materials* **2000**, *38*, 85.
(39) Millot, B.; Méthivier, A.; Jobic, H.; Moueddeb, H.; Bée, M. *The Journal of Physical Chemistry B* **1999**, *103*, 1096.
(40) Vlugt, T.; Zhu, W.; Kapteijn, F.; Moulijn, J.; Smit, B.; Krishna, R. *Journal of the American Chemical Society* **1998**, *120*, 5599.
(41) Vlugt, T. J.; Dellago, C.; Smit, B. *The Journal of Chemical Physics* **2000**, *113*, 8791.
(42) Takaba, H.; Koshita, R.; Mizukami, K.; Oumi, Y.; Ito, N.; Kubo, M.; Fahmi, A.; Miyamoto, A. *Journal of Membrane Science* **1997**, *134*, 127.
(43) Furukawa, S.; McCabe, C.; Nitta, T.; Cummings, P. *Fluid Phase Equilibria* **2002**, *194*, 309.
(44) Jobic, H.; Theodorou, D. N. *Microporous and Mesoporous Materials* **2007**, *102*, 21.
(45) O'Malley, A.; Catlow, C. *Physical Chemistry Chemical Physics* **2015**, *17*, 1943.
(46) Bouyermaouen, A.; Bellemans, A. *Journal of Chemical Physics* **1998**, *108*, 2170.
(47) Mezei, F. *The Principles of Neutron Spin Echo*; Springer, 1980.
(48) Monkenbusch, M.; Schätzler, R.; Richter, D. *Nuclear Instruments and Methods in Physics Research Section A: Accelerators, Spectrometers, Detectors and Associated Equipment* **1997**, *399*, 301.
(49) Jobic, H.; Skoulidas, A. I.; Sholl, D. S. *The Journal of Physical Chemistry B* **2004**, *108*, 10613.
(50) Jobic, H.; Bée, M.; Dianoux, A. J. *Journal of the Chemical Society, Faraday Transactions 1: Physical Chemistry in Condensed Phases* **1989**, *85*, 2525.
(51) Jobic, H.; Bée, M.; Caro, J.; Bülow, M.; Kärger, J. *Journal of the Chemical Society, Faraday Transactions 1: Physical Chemistry in Condensed Phases* **1989**, *85*, 4201.
(52) Millot, B.; Méthivier, A.; Jobic, H.; Clemençon, I.; Rebours, B. *Langmuir* **1999**, *15*, 2534.
(53) Gergidis, L. N.; Theodorou, D. N.; Jobic, H. *The Journal of Physical Chemistry B* **2000**, *104*, 5541.
(54) Goyal, R.; Fitch, A.; Jobic, H. *The Journal of Physical Chemistry B* **2000**, *104*, 2878.
(55) Ghorai, P. K.; Yashonath, S.; Demontis, P.; Suffritti, G. B. *Journal of the American Chemical Society* **2003**, *125*, 7116.
(56) Jobic, H.; Bée, M.; Pouget, S. *The Journal of Physical Chemistry B* **2000**, *104*, 7130.

Chapter 5

The Effect of Molecular Shape on the Diffusion of Octane Isomers in Zeolite HY

Zeolites X and Y based on the faujasite structure are routine catalysts for fluid catalytic cracking (FCC) processes in the petrochemical industry. Common species in FCC systems under industrial conditions are C_8 species, where the molecular shape and degree of branching may cause significant differences in the diffusion behaviour of these hydrocarbons. In this chapter, the diffusion of octane isomers *n*-octane and 2,5-dimethylhexane is studied using molecular dynamics simulations and quasielastic neutron scattering (QENS) experiments performed at the ISIS neutron spallation source. Two modes of motion are observed by the QENS experiments, that of jump diffusion, potentially across the window regions between faujasite supercages, and free diffusion within the dimensions of the supercages. Counterintuitively, the branched isomer exhibited faster free diffusion than *n*-octane, emulated by the MD simulations, which was found to be due to aggregation of the hydrocarbons in the large faujasite supercages. Potentially, the presence of greater sorbate-sorbate interactions between the straight chains of *n*-octane decreases mobility over longer time scales, providing an insight into factors affecting hydrocarbon diffusion in a key subset of zeolite catalysts.

5.1 Introduction

The diffusion of hydrocarbons in faujasite (FAU) zeolites X and Y is of great interest due to their applications as fluid catalytic cracking (FCC) catalysts in the petrochemical industry.[1] Zeolite-X is characterised by having a Si/Al ratio between 1-1.5 with zeolite Y having higher Si/Al ratios. FAU zeolites are some of the most widely available and used for these catalytic applications. To recap, the structure is composed of tetrahedrally connected supercages 12.5 Å in diameter, which are connected by windows with a diameter of roughly 7.5 Å as shown in figure 5.1.[2] The open three-dimensional pore system results in diffusion being faster than in other zeolites[3-5] and is useful in separation and reaction processes involving large molecules, leading to its many applications in fluid catalytic cracking (FCC) catalysts.

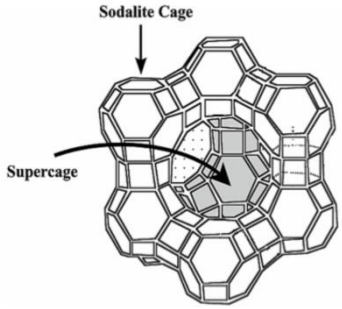

Fig. 5.1. Structure of the faujasite supercage, composed of linked sodalite cages. The cavity within the supercage is 12.5 Å in diameter and the window regions to the supercage are 7.5 Å in diameter. Figure reproduced from reference 6.

Another FAU zeolite used extensively as a cracking catalyst is ultrastable-Y (USY). This is prepared by hydrothermal treatment of zeolite Y and can result in large increases in acidity and cracking activity,[7,8] due in part to dealumination of the framework Al ions,[9-11] and partial destruction of the zeolite framework forming mesopores,[12,13] which may also assist the molecular diffusion component in the cracking process. [14,15]

Historically, experimental measurements of hydrocarbon diffusion coefficients in faujasite structures have given inconsistent results depending on the method used. Early measurements of xylenes and benzene in NaX using zero length column (ZLC) methods[16] agreed with gravimetric experiments[17,18] but disagreed markedly with

PFG-NMR experiments;[19] the same was observed for linear alkanes of length C_4 to C_{14} in NaX.[3, 20]

Though PFG-NMR can give valuable insight into the diffusion behaviour on the millisecond scale, it is limited somewhat by the size of the crystals available, as larger zeolite crystals are necessary (hindering measurement of diffusivity in higher Si/Al ratio zeolites). Consequently, comparison with simulations often carried out in NaY[21,22] for which larger crystals are unavailable is difficult. This problem is not encountered by quasielastic neutron scattering (QENS), where the use of powders (and therefore higher Si/Al ratios) is feasible. QENS has been previously used to investigate the diffusion of benzene[23] in NaX and NaY, giving results in reasonable agreement with PFG-NMR[19] for NaX. The diffusion coefficients of benzene in NaX in reference 23 were measured to be almost two orders of magnitude smaller than those in NaY, highlighting the importance of the cation distribution. This aspect was reiterated by differing translational behaviour of xylene isomers in NaX and BaX, as the Ba^{2+} ion resides in the window region between supercages .[24] The jump diffusion of benzene in NaY was also studied, leading to the conclusion that intracage and intercage jumps occur on the same time scale.[25] Measurements of the diffusion of aliphatic alkanes in faujasites using QENS are less available; however diffusion of *n*-pentane in NaX[26] was measured and showed good agreement with PFG-NMR,[20] indicating jump diffusion behaviour with 7 Å jump lengths independent of temperature. The effect of molecular shape on pentane isomers was also studied using PFG-NMR[27] giving a diffusivity dependence of D_n > D_{iso} > D_{neo}; in agreement with QENS. [28]

Despite the complementary nature of quasielastic neutron scattering and molecular dynamics simulations, studies where they have been used in tandem to probe these systems are rare. However, many studies using this simulation method have modelled hydrocarbon diffusion inside faujasite structures, often focusing on aromatic compounds, such as the localization of benzene[29] and mobility of other aromatics such as meta nitroaniline[30] in both NaY and siliceous faujasite.[31] Smaller alkanes have also been studied in these systems; simulations of methane in NaY[32] suggested that intercage diffusion occurs along pore walls while the use of a probe

molecule[33] found two types of diffusion through the window region: surface mediated diffusion and cage-centre to cage-centre diffusion. The so-called 'levitation effect' was observed upon measuring monoatomic spherical sorbates in NaY[34] (whereby the diffusion coefficient increases, the closer in size the sorbate and the channel). *n*-alkanes of length C_1-C_{14} have also been simulated in siliceous faujasite[35] giving particularly good agreement between predicted self-diffusivities and those obtained by the aforementioned PFG-NMR studies,[20] with discrepancies attributed to the use NaX samples for the experiment. More recently MD has been used to study binary mixtures such as methane/CF_4 and *n*-butane/ethane in siliceous faujasite,[36] simulations have also predicted the nature of the flux of methane and CF_4 mixtures through siliceous faujasite membranes.[37]

As mentioned, few tandem studies have been performed using QENS and MD of hydrocarbons in faujasite zeolites. However, the diffusion[38] and rotational dynamics[39] of propane were investigated in NaY, fitting isotropic rotational behaviour. The rotational constants and translational diffusion coefficients/jump lengths agreed well between the two methods. Diffusion of CH_4 and its binary mixture with CO_2 was also studied,[40] finding a slight decrease of CH_4 diffusivity in the presence of CO_2, and the presence of a maximum in the diffusivity at the loading of 32 mol/uc. Our previous work in chapter 4 and references 41 and 42 have shown that increases in computational power allow for more sophisticated models, giving an improved degree of accuracy compared to more primitive routine models in the MFI structure.[41,42] These developments open up possibilities for transfer to other frameworks and for exploring dynamical behaviour of hydrocarbons in faujasite systems.

In this chapter, quasielastic neutron scattering and molecular dynamics simulations are used in tandem to investigate the diffusion of standard FCC species *n*-octane and 2,5-dimethylhexane in acidic zeolite HY, a significant component in FCC catalysis. We aim to probe the effect of molecular shape and branching on the diffusion behaviour between 300 and 400 K in this industrially essential family of zeolite structures. The effect of alkane branching on diffusion has been studied for *n*- and isobutane in the MFI zeolite structure using QENS[43] where it was found that

the diffusion was slower for the branched isomer to the point where the neutron spin-echo method was necessary to measure such slow diffusion. This issue is not encountered using zeolite HY due to the more open and wider pore structure of the faujasite system. It was found that molecular shape does indeed have an effect on the diffusion coefficient, but due to the process of clustering of both alkanes in the faujasite supercages, rather than the increase in molecular width hindering diffusion through the pores. We find that this effect causes *n*-octane to diffuse more slowly than 2,5-dimethylhexane. This slowing upon clustering is due to stronger sorbate-sorbate interactions between the straight chain alkane than the branched isomer. Our results contrast with the aforementioned studies of isomer diffusion in MFI, where branching hindered diffusion significantly due to increased molecular width.

5.2 Methodology

5.2.1 Quasielastic Neutron Scattering Experiments

All measurements were performed using time-of-flight instrument backscattering neutron spectrometer OSIRIS[44] at the ISIS Pulsed Neutron and Muon Source, Rutherford Appleton Laboratory, Oxfordshire. Graphite 002 analyser crystals were used giving an energy resolution of 24.5 μeV with energy transfers measured in a window of ±0.55 meV.

The zeolite samples were obtained from Zeolyst International (Si/Al = 30) and brought to this composition by steam dealumination. The powder X-ray diffraction pattern can be found in Appendix B. The samples were dried at 150˚C for 4 hours. After cooling, the alkanes were loaded using He as a carrier gas to a loading of 2 molecules per unit cell. The samples (4.5 grams in total) were transferred inside a glovebox under argon to thin walled aluminium containers of annular geometry. The cells were placed in a top-loading closed cycle refrigerator cooled cryostat so that a resolution measurement could be taken at base temperature of 6 K. QENS measurements were then taken at 300, 330, 360 and 400 K in a Q range of 0.2 –

1.55 $Å^{-1}$. The signal taken from the empty zeolite was taken pre-loading and then subtracted from the signal of the loaded zeolite so that only the signal from the alkane was measured.

5.2.2 Molecular Dynamics Simulations

5.2.2.1 The Zeolite HY Structure

The zeolite Y structure has cubic $Fd\bar{3}m$ symmetry.[45] Periodic boundary conditions were employed and a 2 x 2 x 2 supercell of 4609 atoms was used. Aluminium sites and charge compensating protons were added to match the ratio of Si/Al =30 and were located as far from each other as possible in accordance with Dempsey's rule[46] with the hydroxyl group protruding into the supercage. Full ionic charges were assigned to the framework species for all simulations. The supercell with dimensions of 48.49Å in the Cartesian directions is depicted in figure 5.2. The potentials used to describe the flexible, acidic zeolite framework were taken from work studying acidic zeolite frameworks by Schröder *et* al[47] parameterised from Hartree-Fock calculations of IR spectra and phonons. These include a Buckingham potential to describe Si-O, Al-O and O-O interactions, along with a harmonic three-body potential to describe the O-Si-O and O-Al-O triads (listed in table 5.1), and a Morse potential describing the bond between the acidic proton and hydroxyl framework oxygen (O_b). A cut-off distance of 10 Å was used.

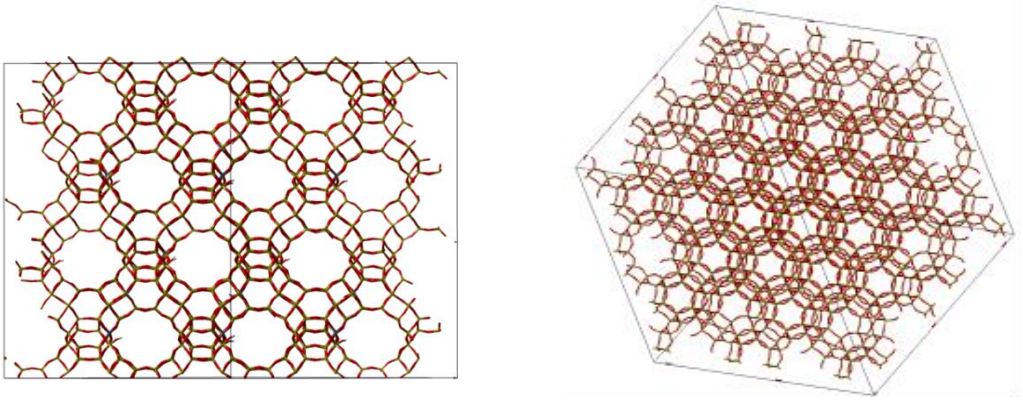

Fig. 5.2. The 2 x 2 x 2 zeolite HY supercell used viewed from (left) the [110] direction and (right) the [111] direction showing the structure of the faujasite cages. All experimental visualisations in this study were created using the visualisation software package Aten1.8.31.[48]

Zeolite-Zeolite Interactions			
Buckingham Potential			
Atoms	*A* (eV)	*ρ* (Å)	*C (eV Å^6)*
Si- -O	1283.907	0.32052	10.66158
Si- -O_b	983.5566	0.32052	10.66158
O- -O	22764.0	0.149	27.88
Al- -O	1460.3	0.29912	0
Al- -O_b	1142.6775	0.29912	0
O_b- -O	22764.0	0.149	27.88
O- -H_b	311.97	0.25	0
Morse Potential			
Atoms	*D* (eV)	α (Å^{-1})	r_0 (Å)
O_b- -H_b	7.0525	2.1986	0.9845
Three-body potential			
Atoms	*K* (eV rad^{-2})		θ(°)
O-Al-O/O_b	2.09724		109.47
O-Si-O/O_b	2.09724		109.47

Table 5.1: Potential parameters describing the zeolite-zeolite interactions, where O_b and H_b are the hydroxyl oxygen and hydrogen respectively.

5.2.2.2 Hydrocarbon Parameters

When modelling the hydrocarbons, each hydrogen atom was assigned a charge of +0.1 au, and the carbon atoms were assigned the appropriate charge to give an overall charge neutral hydrocarbon with intramolecular sorbate interactions taken from the work of Kiselev *et* al listed in chapter 4.1.2.[49] The bonds and bond angle vibrations were described by harmonic potentials; while the dihedrals were described by a cosine potential. The guest-host interactions were modelled by a Lennard-Jones potential empirically derived in the work of Titiloye *et* al[50] and listed in table 5.2, note these potentials are different to those in chapter 4 to accommodate the presence of acidic hydroxyls. Sorbate-sorbate interactions were derived from vibrational data listed in section 4.1.2.[51]

The alkanes were placed in the centre of the faujasite supercages in the supercell, avoiding close contact with the channel walls. The loadings of 2 molecules per unit

Zeolite-Hydrocarbon Interactions		
Lennard-Jones Potentials		
Atoms	*A* (eV Å^{12})	*B* (eV Å^{6})
C- -O/O_b	11825.615	17.661
H- - O/O_b	1557.522	5.574
C- -H_b	2854.571	5.884
H- -H_b	3.553	0.110

Table 5.2: Potential parameters describing the zeolite-sorbate interactions.

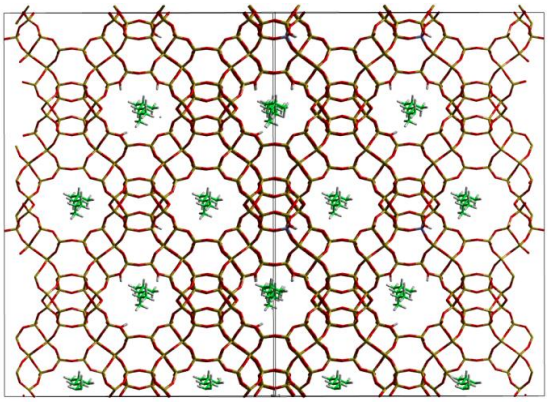

Fig 5.3. A view of the system for dimethylhexane pre-production run at 300 K viewed down the [110] direction.

cell were chosen to match those of the experiment. An example of the starting configuration for the 2,5-dimethylhexane MD runs is shown in Fig. 5.3. The system was then equilibrated at the desired temperature for 1 ns in the canonical (NVT) ensemble. After the equilibration run, the production run of 10 ns in the microcanonical (NVE) ensemble was carried out for each alkane at 300, 330, 360 and 400 K. A timestep of 0.5 fs was used and the atomic coordinates were saved every picosecond (every 2000 steps). A Berendsen[52] thermostat was used to maintain the temperature constant, with a time constant for thermal energy exchange set at 1 ps. All simulations were carried out using the DL_POLY_4 code[53]. The production time of 10 ns was chosen because it was sufficient to obtain true diffusive motion, illustrated by a linear mean square displacement (MSD) plot. The central carbon atom of each chain then had its coordinates logged, allowing self-diffusion coefficients to be calculated from the Einstein relationship.

5.3 Results and Discussion

5.3.1 Quasielastic Neutron Scattering Experiments

For hydrogenous molecules such as alkanes, the incoherent scattering from ^{1}H hydrogen dominates because of the much larger incoherent cross-section of this atom. Self-diffusion coefficients can be obtained from the incoherent translational scattering function, since it gives information on the long-range diffusion of molecules. The incoherent translational scattering function for a molecule following Fick's law or jump diffusion can be described by a Lorentzian function

$$S(Q,\omega) = \frac{1}{\pi}\frac{D_s Q^2}{\omega^2 + (D_s Q^2)} \tag{5.1}$$

As outlined in section 2.5, the total scattering function is a convolution of an elastic component and quasielastic component. The elastic component, representing static protons is a delta function, convoluted with the QENS spectrum of the sample measured at 6 K, which gives it a width representing the instrumental resolution. The quasielastic component of the spectrum is described by one or more of the above Lorentzian functions in equation 5.1. The broadening of these Lorentzian functions with Q is then fit to theoretical models which may represent free Fickian diffusion (outlined in section 2.5.1.1), jump diffusion (2.5.1.2) and diffusion in a confined spherical volume (2.5.1.3). A selection of QENS spectra obtained at 300 K for octane and 2,5-dimethylhexane are shown in figures 5.4 and 5.5 respectively. The spectra comprise of the resolution function convoluted with two Lorentzian functions, one of narrow width (L1) and one of much broader width (L2). L1 for both octane and 2,5-dimethylhexane can be shown to increase in width with wave vector transfer Q indicating translational diffusion. The Q dependence of the half width at half maximum (HWHM) of L2 is far from obvious for both *n*-octane and 2,5-dimethylhexane, though its intensity is insignificant at the lowest Q values. The presence of two Lorentzians suggests two modes of observable motion, the nature of which will now be discussed.

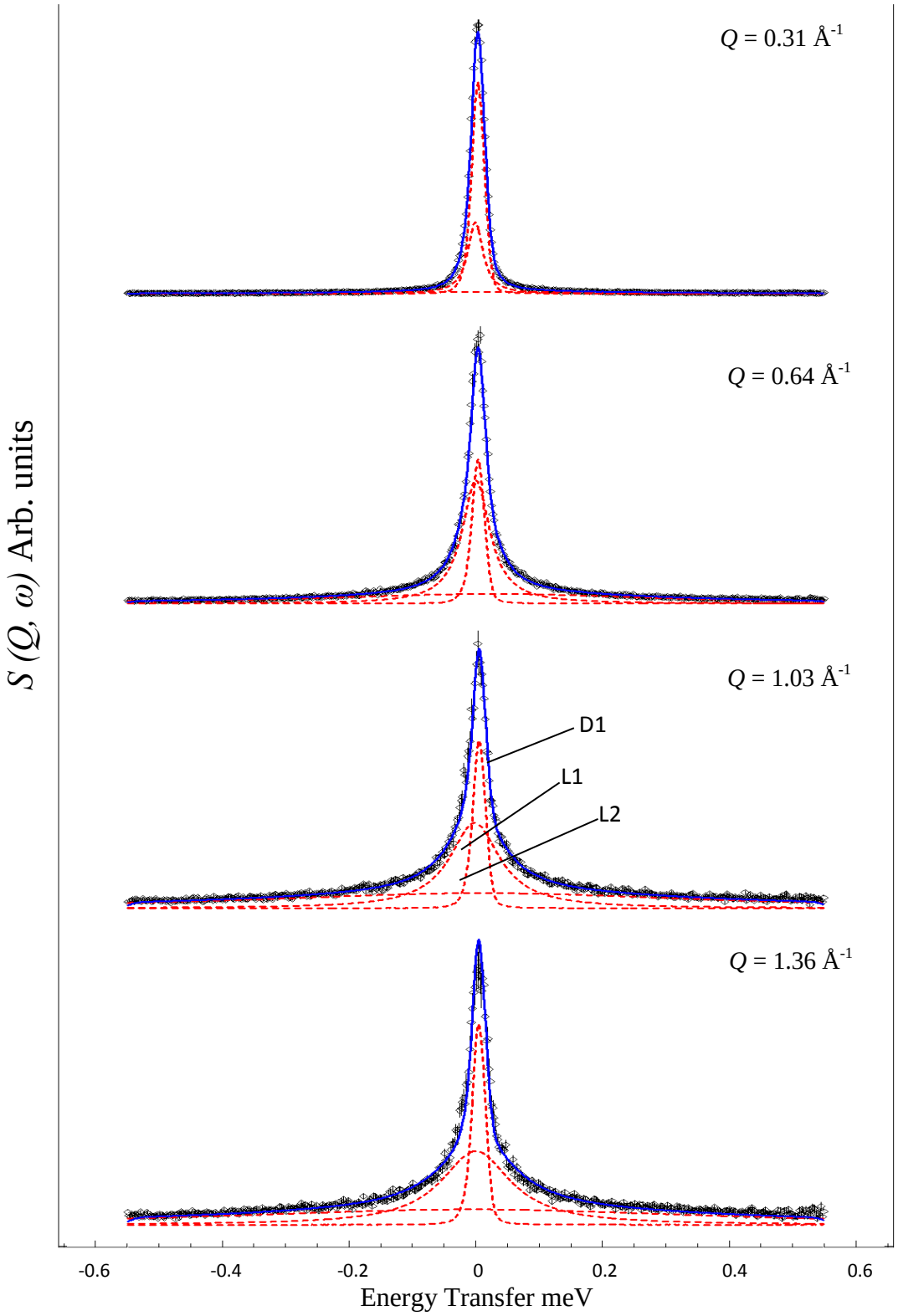

Fig. 5.4. QENS spectra at 4 *Q* values for *n*-octane at 300 K. Two Lorentzian functions are observed.

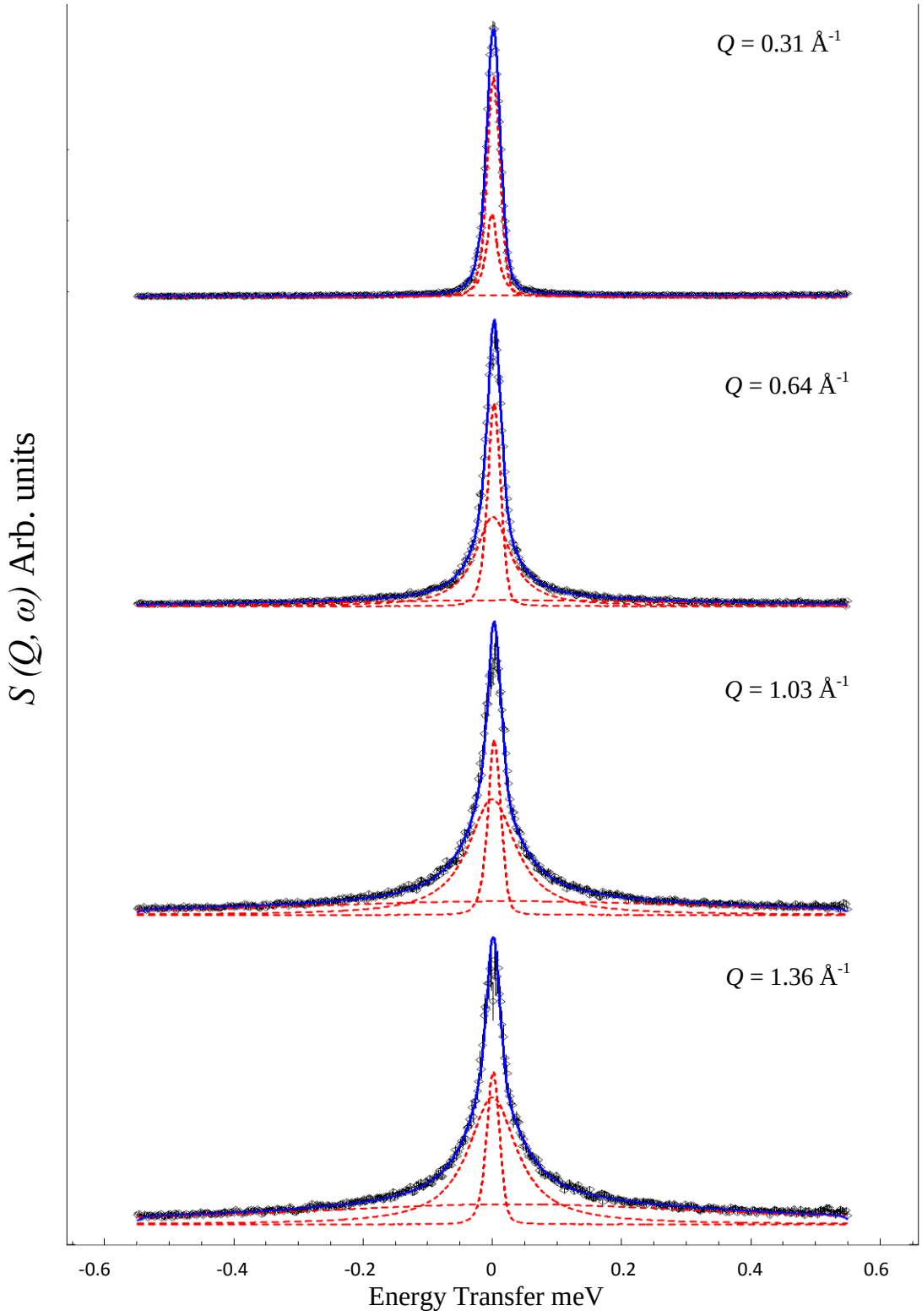

Fig. 5.5. QENS spectra at 4 *Q* values for 2,5-dimethylhexane at 300 K. Two Lorentzian functions are observed.

The broadenings of the HWHM of L1 as a function of Q are plotted for all temperatures for *n*-octane in figure 5.6 and for 2,5-dimethylhexane in figure 5.7. The Q dependence fits to the Chudley-Elliott[54] jump diffusion model outlined in section 2.5.1.2, where the molecule is stationary in a location for a residence time, and then jumps a specified distance to the next location. The model assumes jump diffusion with a fixed jump distance and a jump time which is negligible compared to the residence time. For *n*-octane in figure 5.6, a close agreement with the jump diffusion model is shown, the jump distance remains consistent with temperature, and the residence time is shown to decrease with temperature from 28 to 15 ps between 300 and 400 K. The jump distances are similar to that observed for benzene in NaY [23] (3 Å) where it was concluded that jump diffusion within the cage was being observed, on the grounds that cage centre to cage centre diffusion is a much longer distance than was observed. However, we consider that movement from one side of the 7.5 Å diameter window region to the other side could be this length, though further work and in depth simulation would be necessary to verify that these residence times are feasible.

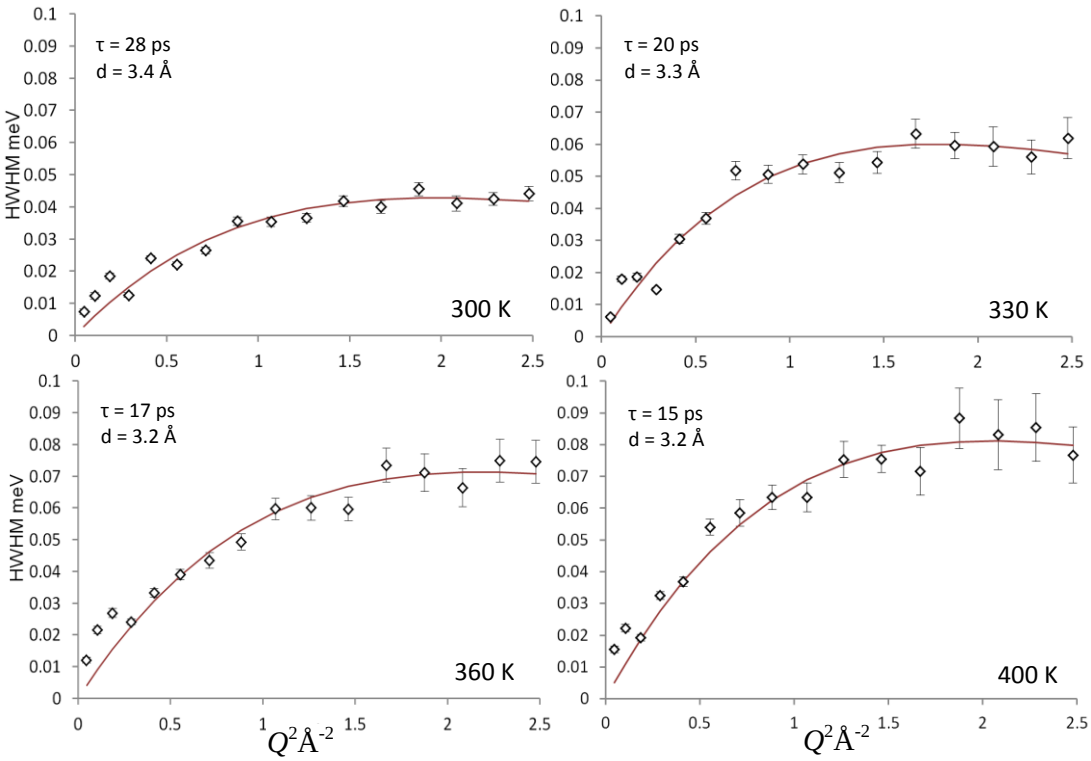

Fig. 5.6. Q dependence of HWHM for L1 of the QENS spectra at all temperatures for *n*-octane in zeolite HY at all temperatures. ◇ are the experimental points and ---- is the dependence calculated from the jump diffusion model with the d and τ parameters listed in each plot.

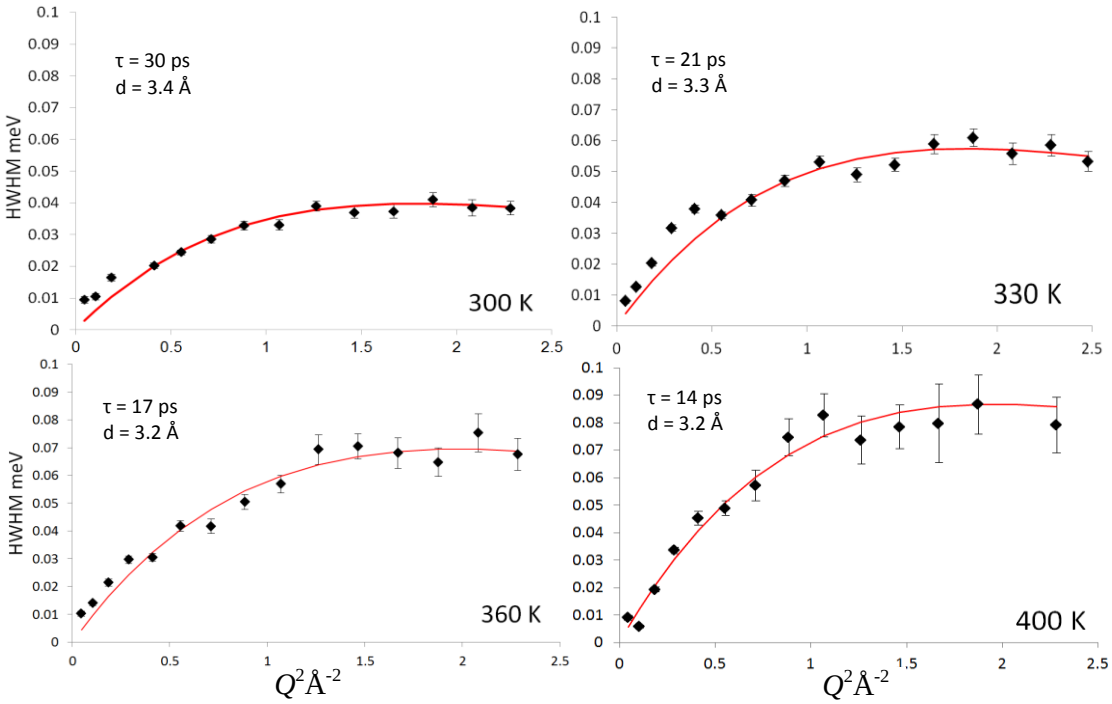

Fig. 5.7. *Q* dependence of HWHM for L1 of the QENS spectra at all temperatures for 2,5-dimethylhexane in zeolite HY at all temperatures. ◆ are the experimental points and ---- is the dependence calculated from the jump diffusion model with the d and τ parameters for each plot.

The *Q*-dependencies for L1 of 2,5-dimethylhexane in HY are plotted in figure 5.7. We note that the residence times are in the range of 30 – 14 ps between 300 to 400 K, very similar to that of dimethylhexane suggesting that the effect of branching on the jump process is negligible. If one considers the possibility of the jump distance measuring movement between the window regions, then this result suggests, that the branching does not have a significant effect on the diffusion of 2,5-dimethylhexane through these windows despite the branching, compared to n-octane. DFT calculations[55] have shown that the kinetic diameter of 2,5-dimethylhexane is ~5.5 Å, compared to 4.1 Å for *n*-octane. Given that the diameter of the window region is 7.5 Å, there is a possibility that either this 1.5 Å difference makes little difference to the mobilities involved, or other factors such as the additional torsional and flexibility characteristics associated with *n*-octane make a contribution to a mobility reduction through this window. This is of course speculation, and an in depth study of the configurational geometries upon passing through this window region would be necessary.

One may also consider the implications for the levitation effect proposed by Yashonath,[34,56,57] where the diffusion of molecules with molecular widths close to that of the channel increase in diffusivity due to the mutual cancellation of forces between the channel wall and the sorbates. If the levitation effect were to play a role in our observations one might expect to see a significant increase in diffusivity upon movement of the wider molecule through the 7.5 Å windows, which is not the case. However, given the width difference of 2 Å between the window and the kinetic diameter of 2,5-dimethylhexane we can conclude the levitation effect would not be applicable to this result. The so-called 'window effect' [58,59] may also be discounted from our observations as the mobilities are very similar (when the residence times are taken into account). The increased length of octane and ability of the chain to protrude through the window of the faujasite cage does not appear to increase its mobility significantly. This differing observation from that of Jobic *et al*. [60] studying *n*-alkanes can be rationalised due both the smaller cages present in their zeolite 5A sample compared to zeolite Y, and the longer alkanes involved (C_{12} compared to C_8 for *n*-octane).

We now consider the broadening of the second Lorentzian (L2) as a function of Q for both alkanes in HY at all temperatures. The Q dependence of L2 for *n*-octane is plotted in figure 5.8. As mentioned before, at low Q values the intensity of this Lorentzian is close to zero. Figure 5.8 shows that at values of $Q^2 \leq 0.42$ Å^{-2} the width is constant; after this value the broadening shows a DQ^2 dependence. As outlined in section 2.5.1.3, this dependence is indicative of Fickian diffusion in a confined spherical volume,[61] where the constant width below this particular Q value is due to the suppression of trajectories over the distances corresponding to these Q values (where the diameter of the confining sphere is $d = 2\pi/Q$). Unfortunately, due to the grouping of detectors of the instrument to decrease the statistical error of the Lorentzian HWHM at each Q value, it is difficult to determine the exact Q^2 value where the broadening plateaus. However, the range as shown by the vertical black lines suggest that the *n*-octane molecules are diffusing in a confined spherical volume of diameter 8.5 to 10 Å. The upper limit of these values would correspond to free diffusion confined in the faujasite supercages 12.5 Å in diameter.

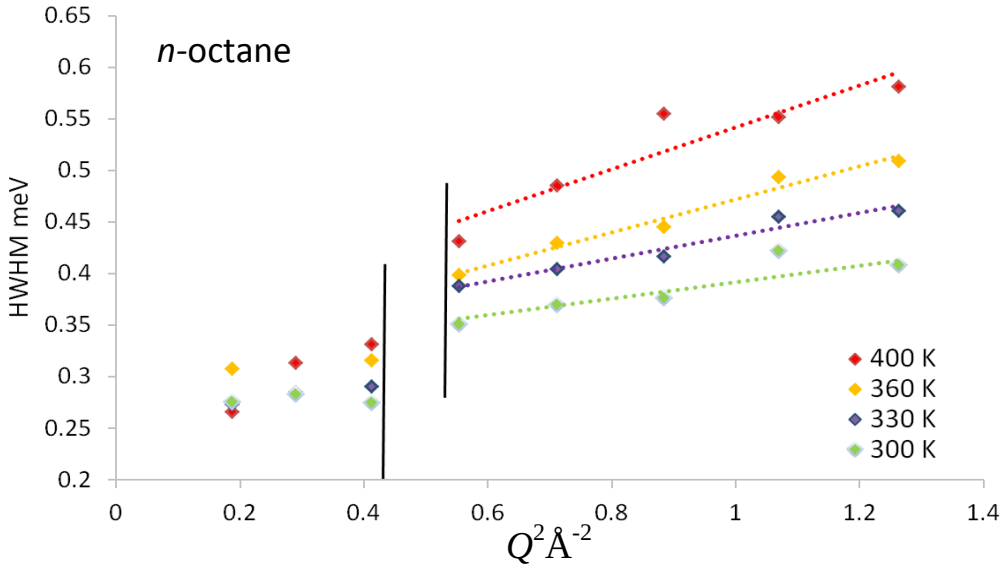

Fig. 5.8. Q dependence of HWHM for L2 of the QENS spectra at all temperatures for *n*-octane in zeolite HY at all temperatures. The vertical black lines indicate where the plateauing in the Q-dependence takes place.

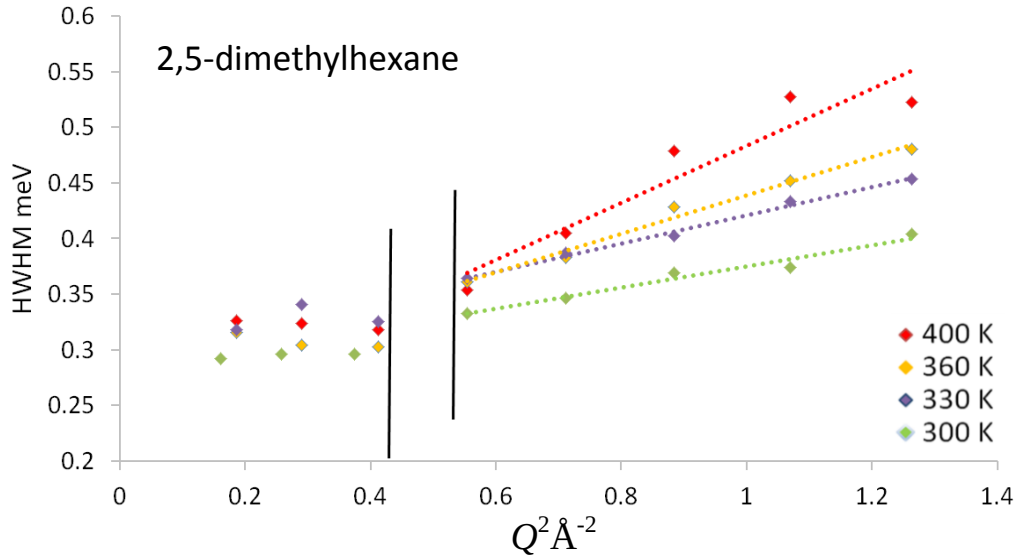

Fig. 5.9. Q dependence of HWHM for L2 of the QENS spectra at all temperatures for 2,5-dimethylhexane in zeolite HY at all temperatures.

The same Q-dependence is plotted for 2,5-dimethylhexane at all temperatures in figure 5.9 which shows the same confined diffusion behaviour as 2,5-dimethylhexane suggesting that at least qualitatively, the behaviours observed by each hydrocarbon do not differ with branching. The Fickian diffusion coefficients were then calculated from the broadenings obtained between Q = 0.7 – 1.22 Å^{-1}. Broadenings above these values were discounted as at higher temperatures; the

width of the Lorentzian HWHM was outside the instrumental resolution of 0.6 meV. The diffusion coefficients obtained are listed in table 5.3 and plotted in figure 5.10. The diffusion coefficients were measured as consistently higher for 2,5-dimethylhexane than for *n*-octane. The diffusivities for *n*-octane were in the range of 5.2 - 14 x 10^{-10} m^2 s^{-1}, and the diffusivities for 2,5-dimethylhexane in the range of 7.2 - 17 x 10^{-10} m^2 s^{-1}). This observation contrasts with that for the ZSM-5 system, where the larger molecular width of the branched alkane caused significant slowing of the diffusion compared to straight chain analogues in reference 43.

	***n*-octane**		**2,5-dimethylhexane**	
***T* (K)**	***Ds* (QENS)**	***Ds* (MD)**	***Ds* (QENS)**	***Ds* (MD)**
300	5.17 x 10^{-10} ±0.8 x10^{-10}	5.87 x 10^{-10}	7.2 x 10^{-10} ±0.9 x10^{-10}	7.09 x 10^{-10}
330	7.95 x 10^{-10} ±1.15 x10^{-10}	6.27 x 10^{-10}	10.9 x 10^{-10} ±1.4 x10^{-10}	9.18 x 10^{-10}
360	9.75 x 10^{-10} ±1.4 x10^{-10}	8.68 x 10^{-10}	11.4 x 10^{-10} ±1.6 x10^{-10}	13.40 x 10^{-10}
400	14 x 10^{-10} ±2 x10^{-10}	12.90 x 10^{-10}	17 x 10^{-10} ±2.3 x10^{-10}	15.39 x 10^{-10}
E_a (kJ mol^{-1})	9.6	8.0	8.3	7.1

Table 5.3. The measured diffusion coefficients and calculated activation energies of diffusion for *n*-octane and 2,5-dimethylhexane obtained from QENS and MD simulations. All diffusion coefficient values in units of m^2s^{-1}.

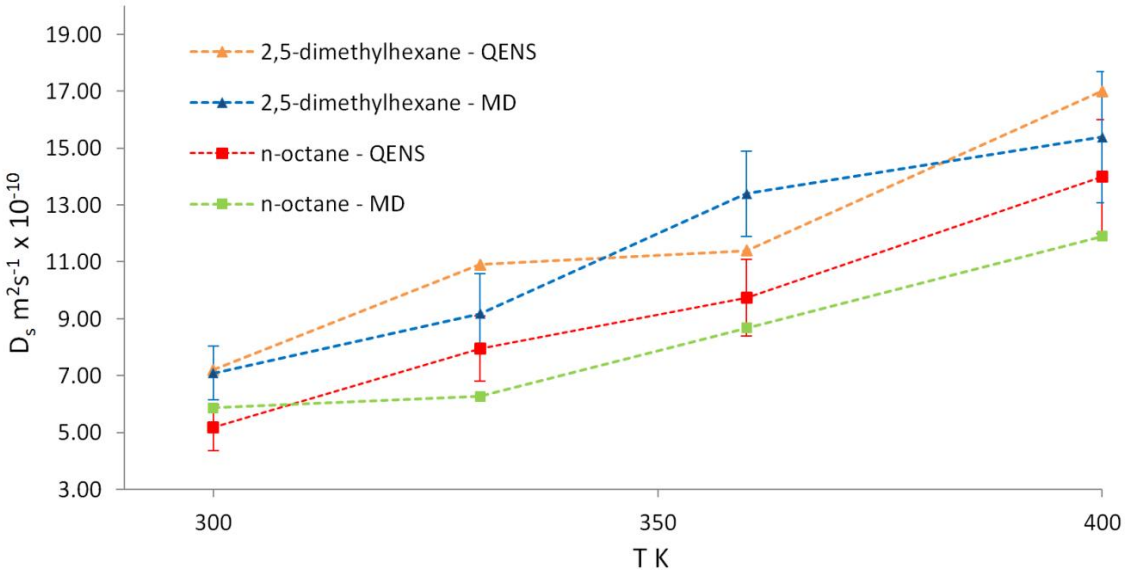

Fig. 5.10. Calculated diffusion coefficients as a function of temperature for *n*-octane and 2,5-dimethylhexane in zeolite HY as measured by both QENS and MD simulations.

The activation energies were derived from the Arrhenius plot in figure 5.11 and are listed in table 5.3; they give a lower activation energy of diffusion for 2,5-dimethylhexane than for *n*-octane (8.3 and 9.6 $kJmol^{-1}$ respectively) suggesting less hindered diffusion of 2,5-dimethylhexane. The probable cause for the difference in observation between the HY system and the aforementioned ZSM-5 is that ZSM-5 has a network of straight and sinusoidal channels with a width of 5.5 Å so the kinetic diameter of a branched alkane would become significant and hinder diffusion in this smaller diameter pore. The zeolite HY faujasite structure consists of 12 Å supercages connected by 7.5 Å window regions. This larger pore size would decrease the effect of molecular branching on the diffusivity. However, it does not account for the increased diffusivity of the branched alkane, which is revealed by the analysis of the molecular dynamics simulations presented in the next section.

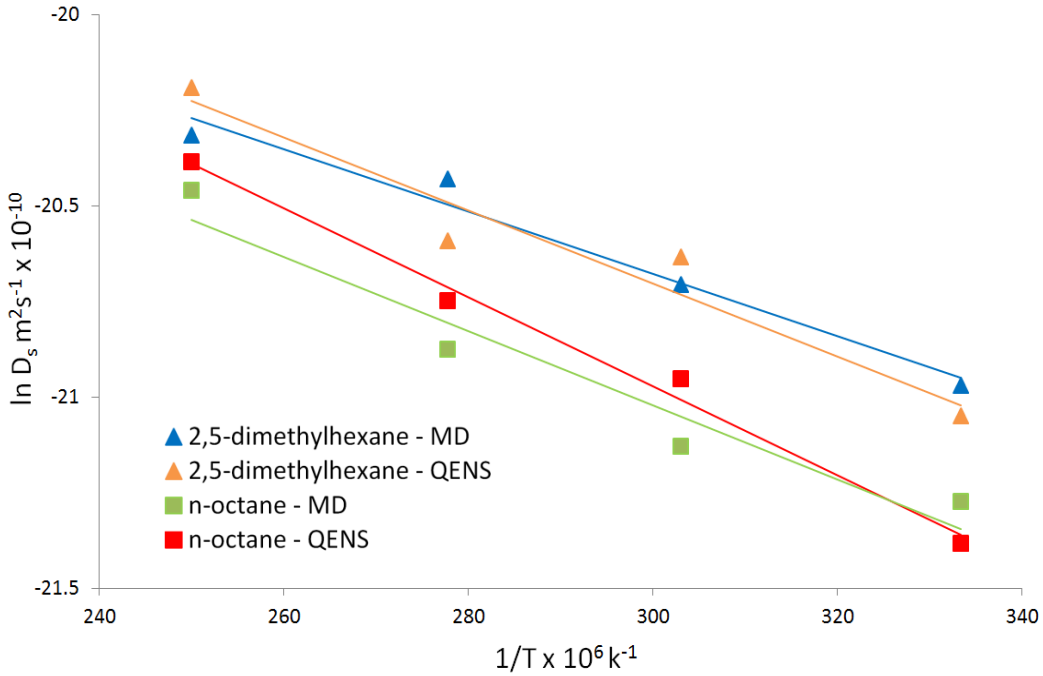

Fig 5.11. Arrhenius plots for 2,5-dimethylhexane and *n*-octane in zeolite HY from diffusion coefficients measured by both QENS and MD simulations.

All QENS spectra relevant to this chapter can be found at the following webpage: https://www.dropbox.com/sh/y4zshxt818f7jzt/AADxXYfgVLpBpXfxVAbLlNpwa?dl=0

5.3.2 Molecular Dynamics Simulations

The diffusion coefficients obtained from the simulations are listed in Table 5.3 and plotted in figure 5.10. They are in the range of 5.8 -12.9 x10^{-10} m^2 s^{-1} for octane and 7.1 -15.4 x 10^{-10} m^2 s^{-1} for 2,5-dimethylhexane. Counterintuitively, and in agreement with the QENS measurements, the simulated diffusion coefficients are higher for 2,5-dimethylhexane than those measured for octane. It is difficult to calculate the statistical errors of these values; however the very linear nature of the calculated MSD plots, an example of which is shown in figure 5.12, suggest these errors are low. It is noted that the unlike most diffusion studies of these systems such as those in chapter 4, the calculated diffusion coefficients are not consistently higher than those obtained by experiment (usually attributed to the use of a perfect zeolite crystal, free from defects and grain boundaries that would hinder diffusion

of sorbates in the real material). The agreement between simulation and experiment is very close, within experimental error for all measurements. However, this agreement must be treated with caution, as the diffusion coefficients measured by experiments only measure intracage diffusion. The average mean square displacement plot also takes into account cage to cage diffusion. The activation energies of diffusion were derived from the Arrhenius plots in figure 5.11 and are listed in table 5.3, with values of 8 kJ mol^{-1} for octane and 7.1 kJ mol^{-1} for 2,5-dimethylhexane. There is close agreement with experiment (both within 2 kJ mol^{-1}), and activation energy of octane is higher than that of 2,5-dimethylhexane, consistent with experiment.

Insight into the unexpected observation that 2,5-dimethylhexane has a higher diffusion coefficient than octane can be obtained from the MSD plots in figure 5.12 of the average MSD of both octane and 2,5-dimethylhexane at 300 K.

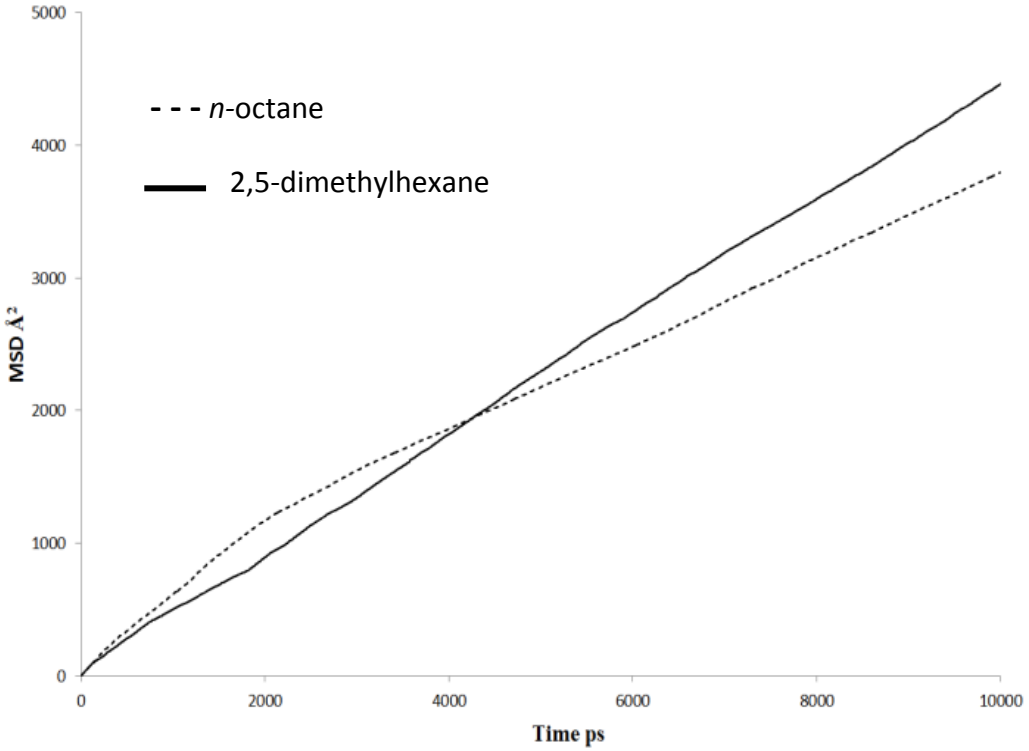

Fig. 5.12 MSD plots obtained for *n*-octane and 2,5-dimethylhexane from MD simulations in zeolite HY at 300 K at loading 2 mol/uc.

The gradient of the MSD for *n*-octane is higher than that of 2,5-dimethylhexane for the first 2 nanoseconds of the simulation, consistent with the increase in molecular width hindering diffusion through the 7.5 Å window region. An important point, however, is that this is not observed in the QENS experiments, if the jump diffusion observed in experiment is indeed due to movement through the window region. A decrease in gradient is observed as the simulation progresses, with a crossover in the MSD of 2,5-dimethylhexane at roughly 4 ns. Both the gradient decrease for *n*-octane and the MSD crossover were observed at *ca.* 4 ns for all measured temperatures. We can understand why the diffusivity of *n*-octane decreases by examining the trajectory analysis of these runs, shown in figure 5.13 for both *n*-octane and 2,5-dimethylhexane at 4 ns at 300 K. Clustering of the alkanes is seen to take place in the faujasite supercages at all temperatures for both alkanes. These clusters are maintained for the duration of the 10 ns simulation, highlighting the energetic favourability and strength of sorbate-sorbate interactions in these systems.

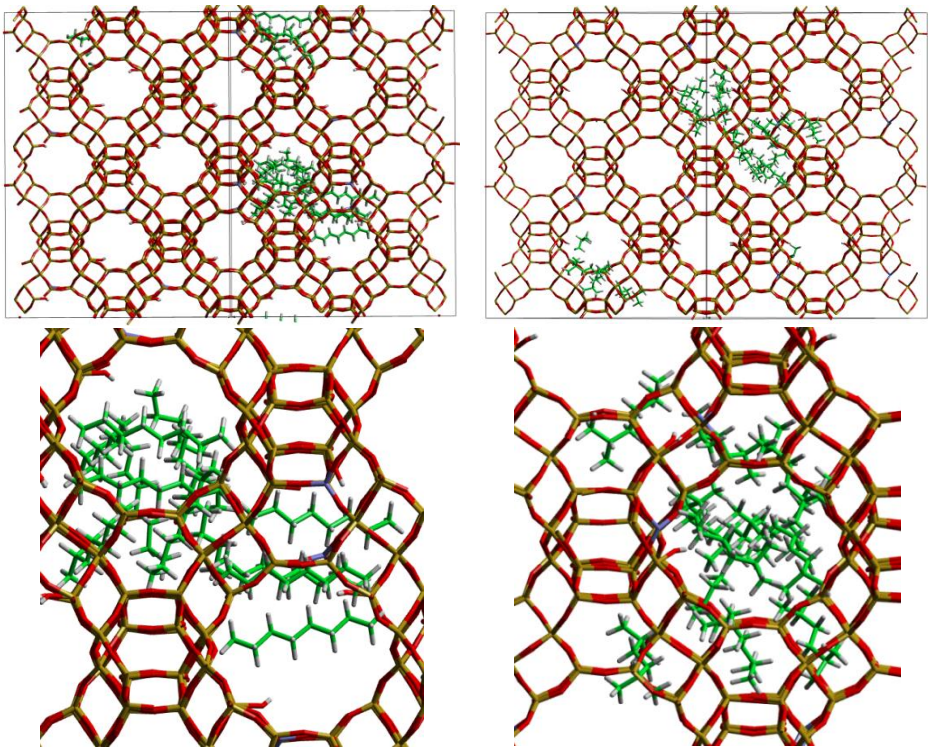

Fig. 5.13. Snapshots of the MD simulations of n-octane (left) and 2,5-dimethylhexane (right) in zeolite HY after 4 ns of simulated time, illustrating the extent of alkane clustering.

The observation that the MSDs and therefore diffusion coefficients at all temperatures of *n*-octane are significantly more affected upon this clustering than 2,5-dimethylhexane is consistent with stronger intermolecular forces of the straight chain alkanes than those of branched isomers (illustrated by higher boiling point and lower vapour pressure of octane than 2,5-dimethylhexane). These stronger sorbate-sorbate interactions will restrict diffusion more after clustering, providing a potential explanation as to why the observed diffusion coefficients of *n*-octane were measured as lower than those of 2,5-dimethylhexane from the QENS experiments. In the experiment, the system has equilibrated, so the self-diffusivity of the alkanes will be that for the system after the clustering has occurred. If this is the reason for the slowing of the diffusion then it would appear that the experimental diffusion coefficients of hydrocarbons of this size and shape in faujasite systems are influenced more by the strength of sorbate-sorbate interactions than the restrictions of the pore/channel width, which dictate the diffusion differences in ZSM-5 as found in reference 43.

We consider again the application of the levitation effect to these systems, where the increase in diffusivity has been shown to be a result of clustering extent and sorbate-sorbate interactions (as illustrated by the MSD in figure 5.12, where the switch in diffusivity is not observed until the clustering has taken place). If one were observing the levitation effect, we note that the increased diffusivity for the branched isomer would be observed from the start of the simulation before the sorbate-sorbate interactions become significant. For the majority of the simulation the dominant diffusive behaviour is that of intracage diffusion as part of the alkane cluster, rather than individual molecules diffusing between the cages through the windows closer in size to the molecular width. For this reason we can conclude that the levitation effect plays no role in our observation of accelerated diffusion for the branched isomer.

Clearly there is a balance between the effects of pore dimensions on the diffusion of hydrocarbons in microporous catalysts and those of sorbate-sorbate interactions. There is only an increase of 2 Å between the channel dimensions of the MFI structure and the 7.5 Å window regions between the 12 Å supercages in

zeolite HY. In ZSM-5, the effect of branching slows sorbate diffusion due to an increase in molecular width, whereas in HY the effect of branching may have the opposite effect due to the more open cage structure allowing weaker sorbate-sorbate interactions to become the controlling factor, permitting more free diffusion of the branched isomer.

5.4 Summary and Conclusions

Quasielastic neutron scattering and molecular dynamics simulations were used in tandem to study the effect of molecular shape on the diffusion of isomers *n*-octane and 2,5-dimethylhexane in zeolite HY between 300 and 400 K. The QENS measurements showed 2 modes of motion of both hydrocarbons in the zeolite, that of jump diffusion, potentially through the window regions between faujasite cages, and Fickian diffusion in a confined volume, with dimensions corresponding to the faujasite supercage. The jump diffusion had similar jump lengths and residence times for both hydrocarbons; however, the confined volume diffusion was measured to be faster for the branched isomer than for the straight chain *n*-octane.

Diffusion coefficients calculated using MD simulations, perhaps counterintuitively, agreed with the QENS experiments, showing lower diffusivity and increased activation energy for *n*-octane than for 2,5-dimethylhexane. We explain the decrease in diffusivity for *n*-octane by clustering of the alkanes in the faujasite supercages for both alkanes. The fact that this slowing of *n*-octane diffusion only takes place after the alkane clustering suggests that sorbate-sorbate interactions affect *n*-octane more than the branched 2,5-dimethylhexane due to its increased molecular length, and thus a larger surface area for van der Waals interactions. The diffusion coefficients calculated from MD simulations were all within experimental error of the QENS measurements; however this agreement must be treated with caution, as the simulations account for both intra and intercage diffusion.

These results highlight the importance of sorbate-sorbate interactions when considering diffusion of FCC species in the faujasite zeolite structure, where pores are of sufficient dimensions to allow for this clustering to become significant, and the slowing of diffusion for the longer *n*-octane is observed due to these interactions. This behaviour is contrary to that in the MFI structure where the effect of branching hinders diffusion due to constricted pore sizes, illustrating the complex nature of diffusion of common hydrocarbon species in routine zeolite catalysts. A development on this study would be the performance of static energy calculations to quantify energetically this clustering process, along study of the configurational geometries of each hydrocarbon upon passing through the window region between supercages, thus comparing barriers of the intercage diffusion process.

This chapter has highlighted important factors affecting the diffusion behaviour of molecules relevant to the FCC process inside faujasite zeolites. At the same time, the ability of tandem studies of QENS and MD simulations to measure and explain such behaviour is demonstrated. Moreover, the complex nature of such processes is illustrated, highlighting the importance of dynamical studies of these catalytic systems using these complementary experimental and computational techniques.

References

(1) Wilson, S.; van Bekkum, H.; Flanigan, E.; Jansen, J. *Stud. Surf. Sci. Catal* **1991**, *58*, 137.
(2) Schirmer, W. *Zeitschrift für Physikalische Chemie* **1994**, *186*, 269.
(3) Eic, M.; Ruthven, D. *Zeolites* **1988**, *8*, 472.
(4) Cavalcante Jr, C. L.; Silva, N. M.; Souza-Aguiar, E. F.; Sobrinho, E. V. *Adsorption* **2003**, *9*, 205.
(5) Ruthven, D. M. *Principles of Adsorption and Adsorption Processes*; John Wiley & Sons, 1984.
(6) http://turroserver.chem.columbia.edu/images/publications/NJT728.gif.
(7) DeCanio, S. J.; Sohn, J. R.; Fritz, P. O.; Lunsford, J. H. *Journal of Catalysis* **1986**, *101*, 132.
(8) Katada, N.; Kageyama, Y.; Takahara, K.; Kanai, T.; Begum, H. A.; Niwa, M. *Journal of Molecular Catalysis A: Chemical* **2004**, *211*, 119.
(9) Klinowski, J.; Thomas, J.; Fyfe, C.; Gobbi, G. **1982**.
(10) Samoson, A.; Lippmaa, E.; Engelhardt, G.; Lohse, U.; Jerschkewitz, H.-G. *Chemical Physics Letters* **1987**, *134*, 589.

(11) Sanz, J.; Fornés, V.; Corma, A. *Journal of the Chemical Society, Faraday Transactions 1: Physical Chemistry in Condensed Phases* **1988**, *84*, 3113.
(12) Patzelova, V.; Jaeger, N. *Zeolites* **1987**, *7*, 240.
(13) Choifeng, C.; Hall, J.; Huggins, B.; Beyerlein, R. *Journal of Catalysis* **1993**, *140*, 395.
(14) Hopkins, P.; Miller, J.; Meyers, B.; Ray, G.; Roginski, R.; Kuehne, M.; Kung, H. *Applied Catalysis A: General* **1996**, *136*, 29.
(15) Möller, K.; Kojima, M.; O'Connor, C. *The Chemical Engineering Journal and the Biochemical Engineering Journal* **1994**, *54*, 115.
(16) Eic, M.; Ruthven, D. M. *Zeolites* **1988**, *8*, 40.
(17) Goddard, M.; Ruthven, D. *Zeolites* **1986**, *6*, 283.
(18) Goddard, M.; Ruthven, D. *Zeolites* **1986**, *6*, 445.
(19) Germanus, A.; Kärger, J.; Pfeifer, H.; Samulevič, N.; Zďanov, S. *Zeolites* **1985**, *5*, 91.
(20) Kärger, J.; Pfeifer, H.; Rauscher, M.; Walter, A. *Journal of the Chemical Society, Faraday Transactions 1: Physical Chemistry in Condensed Phases* **1980**, *76*, 717.
(21) Klein, H.; Kirschhock, C.; Fuess, H. *The Journal of Physical Chemistry* **1994**, *98*, 12345.
(22) Auerbach, S. M.; Bull, L. M.; Henson, N. J.; Metiu, H. I.; Cheetham, A. K. *The Journal of Physical Chemistry* **1996**, *100*, 5923.
(23) Jobic, H.; Fitch, A. N.; Combet, J. *The Journal of Physical Chemistry B* **2000**, *104*, 8491.
(24) Jobic, H.; Bée, M.; Méthivier, A.; Combet, J. *Microporous and Mesoporous Materials* **2001**, *42*, 135.
(25) Jobic, H. *Microporous and Mesoporous Materials* **2002**, *55*, 159.
(26) Jobic, H. *Physical Chemistry Chemical Physics* **1999**, *1*, 525.
(27) Rajappa, C.; Krause, C.; Borah, B.; Adem, Z.; Galvosas, P.; Kärger, J.; Subramanian, Y. *Microporous and Mesoporous Materials* **2013**, *171*, 58.
(28) Jobic, H.; Borah, B. J.; Yashonath, S. *The Journal of Physical Chemistry B* **2009**, *113*, 12635.
(29) Demontis, P.; Yashonath, S.; Klein, M. L. *The Journal of Physical Chemistry* **1989**, *93*, 5016.
(30) Klein, H.; Fuess, H.; Schrimpf, G. *The Journal of Physical Chemistry* **1996**, *100*, 11101.
(31) Bull, L. M.; Henson, N. J.; Cheetham, A. K.; Newsam, J. M.; Heyes, S. J. *The Journal of Physical Chemistry* **1993**, *97*, 11776.
(32) Yashonath, S.; Demontis, P.; Klein, M. L. *Chemical Physics Letters* **1988**, *153*, 551.
(33) Yashonath, S. *The Journal of Physical Chemistry* **1991**, *95*, 5877.
(34) Yashonath, S.; Santikary, P. *The Journal of Physical Chemistry* **1994**, *98*, 6368.
(35) Clark, L. A.; George, T. Y.; Gupta, A.; Hall, L. L.; Snurr, R. Q. *The Journal of Chemical Physics* **1999**, *111*, 1209.
(36) Chempath, S.; Krishna, R.; Snurr, R. Q. *The Journal of Physical Chemistry B* **2004**, *108*, 13481.
(37) Sanborn, M. J.; Snurr, R. Q. *AIChE journal* **2001**, *47*, 2032.
(38) Sayeed, A.; Mitra, S.; Anil Kumar, A.; Mukhopadhyay, R.; Yashonath, S.; Chaplot, S. *The Journal of Physical Chemistry B* **2003**, *107*, 527.
(39) Mukhopadhyay, R.; Sayeed, A.; Mitra, S.; Kumar, A. A.; Rao, M. N.; Yashonath, S.; Chaplot, S. *Physical Review E* **2002**, *66*, 061201.

(40) Deroche, I.; Maurin, G.; Borah, B.; Yashonath, S.; Jobic, H. *The Journal of Physical Chemistry C* **2010**, *114*, 5027.
(41) O'Malley, A. J.; Catlow, C. R. A. *Physical Chemistry Chemical Physics* **2013**, *15*, 19024.
(42) O'Malley, A.; Catlow, C. *Physical Chemistry Chemical Physics* **2015**, *17*, 1943.
(43) Gergidis, L. N.; Theodorou, D. N.; Jobic, H. *The Journal of Physical Chemistry B* **2000**, *104*, 5541.
(44) Telling, M. T.; Andersen, K. H. *Physical Chemistry Chemical Physics* **2005**, *7*, 1255.
(45) Hriljac, J.; Eddy, M.; Cheetham, A.; Donohue, J.; Ray, G. *Journal of Solid State Chemistry* **1993**, *106*, 66.
(46) Dempsey, E.; Kühl, G.; Olson, D. H. *The Journal of Physical Chemistry* **1969**, *73*, 387.
(47) Schröder, K.-P.; Sauer, J.; Leslie, M.; Richard, C.; Catlow, A.; Thomas, J. M. *Chemical Physics Letters* **1992**, *188*, 320.
(48) Youngs, T. *Journal of Computational Chemistry* **2010**, *31*, 639.
(49) Kiselev, A.; Lopatkin, A.; Shulga, A. *Zeolites* **1985**, *5*, 261.
(50) Titiloye, J.; Parker, S.; Stone, F.; Catlow, C. *The Journal of Physical Chemistry* **1991**, *95*, 4038.
(51) Herzberg, G.; Van Nostrand, New York: 1945.
(52) Berendsen, H. J.; Postma, J. P. M.; van Gunsteren, W. F.; DiNola, A.; Haak, J. *The Journal of Chemical Physics* **1984**, *81*, 3684.
(53) Todorov, I. T.; Smith, W.; Trachenko, K.; Dove, M. T. *Journal of Materials Chemistry* **2006**, *16*, 1911.
(54) Chudley, C.; Elliott, R. *Proceedings of the Physical Society* **1961**, *77*, 353.
(55) Jiménez-Cruz, F.; Laredo, G. C. *Fuel* **2004**, *83*, 2183.
(56) Yashonath, S.; Ghorai, P. K. *The Journal of Physical Chemistry B* **2008**, *112*, 665.
(57) Ghorai, P. K.; Yashonath, S.; Demontis, P.; Suffritti, G. B. *Journal of the American Chemical Society* **2003**, *125*, 7116.
(58) Gorring, R. *Journal of Catalysis* **1973**, *31*, 13.
(59) Ruthven, D. M. *Microporous and Mesoporous Materials* **2006**, *96*, 262.
(60) Jobic, H.; Méthivier, A.; Ehlers, G.; Farago, B.; Haeussler, W. *Angewandte Chemie International Edition* **2004**, *43*, 364.
(61) Volino, F.; Dianoux, A. *Molecular Physics* **1980**, *41*, 271.

Chapter 6

Methanol Dynamics in Zeolites HY and H-ZSM-5

An understanding of the behaviour of methanol in acidic zeolites is of great importance to a number of catalytic processes, such as production of higher hydrocarbons industrially in the methanol-to-hydrocarbons (MTH) and methanol to olefins (MTO) processes. For this reason, the dynamical behaviour of methanol in acidic zeolites is of great interest. In this chapter, quasielastic neutron scattering, inelastic neutron scattering and quantum mechanical calculations are combined to study methanol behaviour in zeolites HY and H-ZSM-5. As an interesting development from the original diffusion studies, room temperature methoxylation is observed in the latter. The QM/MM embedded cluster methodology is then employed to probe the energetics of the methoxylation mechanism, and potential differences between the two zeolite frameworks. The diffusion of methanol in zeolite HY was also quantified, uncovering only one mode of motion contrary to observations in the previous chapter. The diffusion coefficients are compared with previous studies of methanol diffusion in faujasite zeolites.

6.1 Room Temperature Methoxylation in Acidic Zeolites

In this section we report a substantial development from an attempt at measuring the difference in methanol diffusivity in zeolites HY and H-ZSM-5 at room temperature and above. Room temperature methoxylation was observed in H-ZSM-5, which was concluded after quasielastic neutron scattering showed methanol to be immobile on the instrumental timescale, and inelastic neutron scattering gave clear evidence of the condensation reaction through the disappearance of all hydroxyl groups, with persisting bands being assigned to framework methoxy by quantum mechanical calculations. Crucially, no methoxylation was observed in zeolite HY, not used for MTH/MTO catalysis, despite sharing the same Si/Al ratio. The stark contrast in activity may be attributed to the dealumination process involved in high silica HY synthesis, which can lead to terminal hydroxyl defects and silanol nest formation which severely limits catalytic activity. This combined neutron/computational study gives strong evidence that a key step of the MTH/MTO process takes place rapidly under ambient conditions in an active catalyst, with insight into how this activity depends on catalyst preparation.

6.1.1 Introduction

Since the seminal publication of Chang and Silvestri,[1] the zeolite catalyzed conversion of methanol to hydrocarbons (MTH) has been intensively studied, with the first commercialization of the MTH process in New Zealand in 1985.[2] Recent demand for light olefins has also made conversions such as the methanol-to-olefins (MTO) process highly desirable.[3]

One early step in the reaction mechanism is the formation of framework methoxy species after initial physisorption of methanol through H-bonding to the zeolite Brønsted acid site.[4-6] In the MTO process, methoxy groups have been proposed to form ethene directly,[7-9] while other studies also support the methoxy group being

the starting point for initial C-C bond formation, leading to intermediate alcohols and ethers before formation of higher hydrocarbons.[10] However, studying such species is difficult, as under reaction conditions secondary reactions dominate rapidly.[11]

Framework methoxylation at elevated temperatures has been observed by *in situ* FT-IR[12-14] correlating with the onset of hydrocarbon formation. Solid state NMR[15] has shown a variety of surface methoxy groups formed between 493-533 K, with other studies showing their role in dimethyl ether formation.[16] Studies into the stability of framework methoxy species in H-ZSM-5, HY and SAPO-34 (with varying Si/Al ratios and thus different acidic content), concluded that formation was very favourable at 393-473 K upon constant removal of water,[17] but rapid hydrolysis and reformation of methanol occurred under ambient conditions. At ambient temperatures, only partial methoxylation of H-ZSM-5 has been proposed using IR[18] and also in HY[19] (Si/Al =1.86) with maximum methoxylation occurring at ~403 K.

Quantum mechanical simulations have studied framework methoxylation using small silicate clusters,[20-23] with periodic DFT calculations in the ferrierite framework[24] and *ab initio* molecular dynamics used in the chabazite framework.[25] All of these have concluded notable barriers to methoxylation (~200 kJ mol^{-1}), suggesting that elevated temperatures are necessary. The case was further supported by other computational studies highlighting the part played by entropy in forming this intermediate at higher temperatures in H-ZSM-5. [26,27]

Using quasielastic neutron scattering (QENS), inelastic neutron scattering (INS) spectroscopy, and density functional theory (DFT) calculations, we report the complete conversion of methanol and framework hydroxyls to framework methoxy species on adsorption into a commercial H-ZSM-5 sample at room temperature. This was not observed in zeolite HY, not employed for MTH catalysis; where despite the sample having the same composition (Si/Al = 30) the methanol remains intact, in contrast to partial methoxylation previously observed in a low silica (Si/Al = 1.86) HY sample.[19] Unlike H-ZSM-5, to reach Si/Al = 30 the HY sample must be dealuminated by steaming to bring higher heat stability and Brønsted acidity, giving

way to framework defects such as terminal hydroxyls and silanol nests (of lower Brønsted acidity).[28-34] The rapid, complete conversion in H-ZSM-5 shows that elevated temperatures are not required for this step in active catalysts, but also suggests that the dealumination procedure necessary for heat stable faujasite zeolites inhibits this step.

6.1.2 Methodology

6.1.2.1. Sample Preparation

The H-ZSM-5 and HY samples used were commercial catalysts obtained from Zeolyst International, both with Si/Al = 30. The zeolite HY samples were received in the catalytic proton form, already steam dealuminated to this composition. The ZSM-5 samples were received originally in the NH_4 form. These were activated into the catalytic H-ZSM-5 form by heating to 798 K for 4 hours, with a heating rate from room temperature of 5 K/min. The zeolites were then dehydrated at 120˚C under flowing helium for 4 hours. After cooling to room temperature, methanol was then loaded by bubbling He as a carrier gas through the liquid to a loading equating to 4 molecules per unit cell. The samples (4.5 grams in total) were transferred inside a glovebox under argon to thin walled aluminium containers of annular geometry. The same samples were used for both the inelastic neutron scattering and the quasielastic neutron scattering experiments. The powder X-ray diffraction patterns of both zeolites can be found in Appendix B.

6.1.2.2. Quasielastic Neutron Scattering Experiments

As in chapter 5, all measurements were performed using the time-of-flight backscattering neutron spectrometer OSIRIS[35] (detailed in section 2.5.2.2) at the ISIS Pulsed Neutron and Muon Source. The cells were placed in a top-loading closed cycle refrigerator cryostat so that a resolution measurement could be taken at base temperature of 6 K. QENS measurements were then taken at 298 K in a Q range of 0.2–1.5 $Å^{-1}$. Graphite 002 analyser crystals were used to give an energy resolution

of 24.5 μeV with energy transfers measured in a window of ±0.55 meV. The measurement was taken of an empty zeolite sample and then the signal was subtracted from the signal of the loaded zeolite so that only the signal derived from the methanol was measured. All QENS spectra were fitted using the neutron analysis software DAVE.[36]

6.1.2.3. Inelastic Neutron Scattering Experiments

Inelastic neutron scattering (INS) was used in order to probe the species that formed in both the zeolites at room temperature. The INS technique is especially sensitive to the vibrational modes involving hydrogen due to its uniquely high incoherent scattering cross section. It is an ideal vibrational spectroscopy method for these systems, as it allows access to vibrations in the low energy region without limitations due to selection rules or low transmittance of the framework, which inhibit optical spectroscopy.

The experiments were carried out using high-flux INS spectrometer MAPS[37,38] (detailed in section 2.4.2), also at the ISIS Pulsed Neutron and Muon Source, (STFC Rutherford Appleton Laboratory, Oxfordshire, UK). The cans containing the prepared samples were placed in a top-loading closed cycle refrigerator cryostat so that all measurements could be taken at 10 K. Measurements were taken in a range of 500–4000 cm^{-1} with an incident neutron energy of 650 meV, and then in a range of 400–1600 cm^{-1} with an incident neutron energy of 250 meV to give a higher resolution measurement of the lower energy vibrational modes. The spectra obtained are depicted in figure 6.4 for HY, and figure 6.5 in H-ZSM-5.

6.1.2.4. Quantum Mechanical Simulations of Vibrational Spectra

The geometry optimisations and phonon calculations to generate theoretical vibrational neutron spectra were performed by A. Chutia and M. R. Farrow at University College London. The plane-wave density functional theory (DFT) calculations were performed using *ab-initio* plane-wave pseudopotential code CASTEP (version 7.03).[39] The Perdew-Wang 1991 (PW91)[40] Generalised Gradient Approximation (GGA) exchange-correlation functional was chosen for the

calculations due to its reliability over a wide-range of materials. Norm-conserving pseudopotentials were employed at a cut-off energy of 830 eV. Calculations were performed at the gamma point in the Brillouin zone. The quasi-Newtonian Broyden-Fletcher-Goldfarb-Shanno (BFGS)[41] algorithm was used for the geometry optimisation of the system and forces. The optimizations were carried out until the energy, maximum force, maximum stress and maximum displacement were less than 2.0×10^{-6} eV/atom, 0.03 eV/Å, 0.05 GPa and 0.001 Å respectively. On the optimized structures, the phonon vibrational frequencies were calculated by diagonalization of dynamical matrices computed using density functional perturbation theory (DFPT).[42] The calculated INS spectrum was generated from the phonon vibrational modes using the ACLIMAX[43] software designed for modelling INS spectra, thus enabling direct comparison with experimental data (performed by S.F Parker at the ISIS Neutron and Muon Source). ACLIMAX assumes a particular trajectory in (Q,ω) space, which is different from that of MAPS. To enable a direct comparison with the experimental data, an artificial Debye-Waller factor was used. The zeolite HY primitive cell containing 144 atoms was chosen as the host to reduce the computational cost (c.f. 288 atom ZSM-5 unit cell). However, it is expected that the vibrational properties of the methoxy species are not sensitive to the host.

6.1.3 Results and Discussion

6.1.3.1 Quasielastic Neutron Scattering Experiments

We first probe the mobility of the methanol in the two zeolites at 300 K using QENS, which can provide detailed information on both translational and rotational motion, especially in the case of hydrocarbons in porous materials. The diffusivity is measured from the broadening of the QENS peak as a function of neutron momentum transfer vector Q. The QENS spectra for methanol in both zeolites are shown in figure 6.1 at Q = 0.9 $Å^{-1}$. The broadening at 298 K compared to the resolution spectra taken at 6 K in the HY system is consistent with significant movement. However the distinct lack of broadening in H-ZSM-5 system at all Q

values (shown also in figure 6.2) suggests that the methanol molecules are not moving on the instrumental time scale.

Indeed, the close fit to the resolution spectra suggests that virtually all the methanol protons remain static. The lack of mobility could either be due to the constriction of the 5.5 Å pores causing significant slowing of the methanol molecules, or due to conversion of methanol to framework methoxy and thus immobilisation. Detailed analysis of the diffusion behavior of methanol in zeolite HY will be reported in section 6.3. The incoherent scattering functions (S(Q,ω)) measured at 300 K at 4 Q values are depicted in figures 6.2 and 6.3 for H-ZSM-5 and zeolite HY respectively. As mentioned, the red dotted line represents a delta function convoluted with the resolution spectra taken at 6 K. In H-ZSM-5 the broadening of the QENS peak as a function of Q is minimal. This lack of broadening, persistence of the elastic line and close fit to the elastic resolution spectra even at the higher Q-values (in the rotational region) suggest immobility of methanol, certainly on a translational scale.

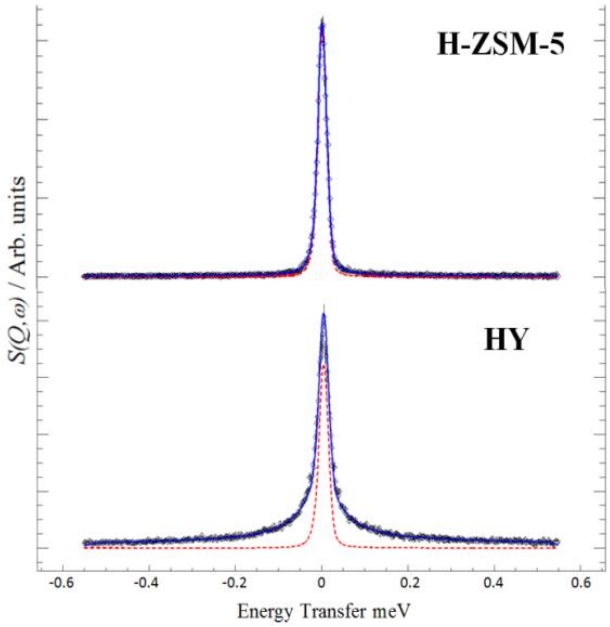

Fig. 6.1. QENS spectra obtained of methanol loaded in zeolites H-ZSM-5 and HY at Q = 0.9 Å at 300 K, (--) represents the resolution data taken at 6 K. The close fit to the resolution function in H-ZSM-5 suggests immobilization, supporting framework methoxylation unlike the significant broadening in HY suggesting intact diffusing methanol.

A Lorentzian component to the overall fit was only present in H-ZSM-5 at higher Q values. This was a very small component and was independent of Q, which is indicative of rotational motion; however it is important to note that due to such a small quasielastic component, the elastic incoherent structure factor (EISF) could not be fitted to models developed previously to describe rotational motions of methanol trapped in H-ZSM-5 (including one developed for a methoxy group).[44,45] However, this problem is probably due to the difference in dynamical time scales sampled by the spectrometer between the present and previous studies.

In contrast, the QENS spectra of methanol in HY are shown in figure 6.3. Significant broadening from the resolution spectra is observed compared to H-ZSM-5 due to a significant quasielastic signal at lower Q values, increasing in width with Q, showing relatively high mobility on a translational timescale. An in depth analysis of the diffusion behaviour of methanol in zeolite HY between 300 K and 400 K is performed in section 6.3.

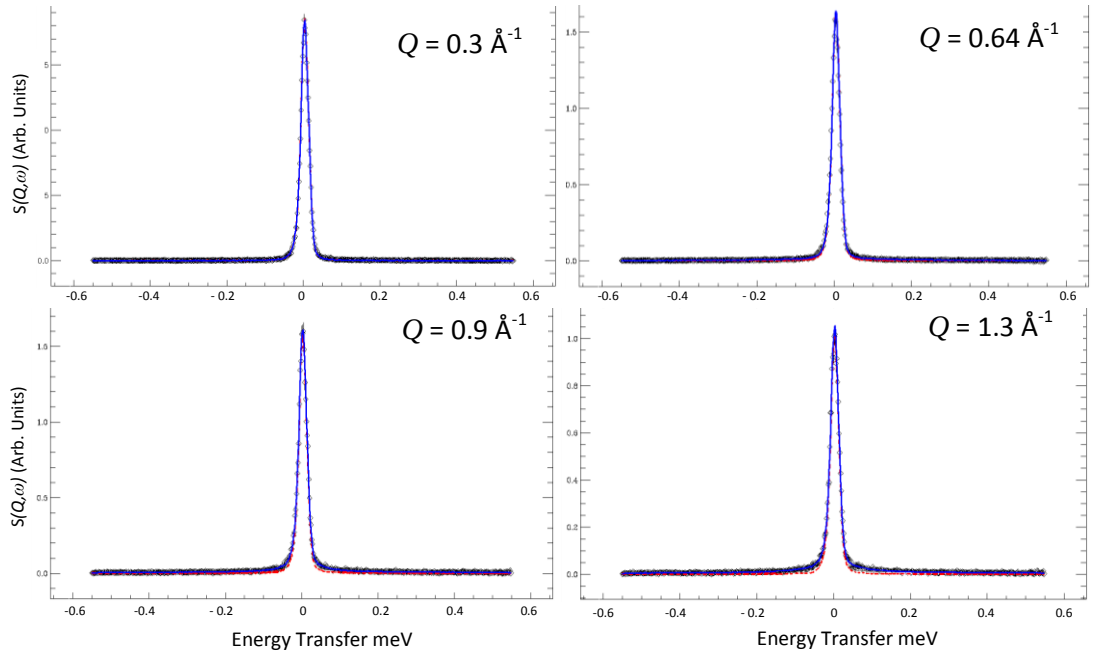

Fig. 6.2. QENS spectra of methanol at 300 K in H-ZSM-5. (--) represents a delta function convoluted with the resolution function (measured at 6 K).

All QENS spectra relevant to this chapter can be found at the following webpage: https://www.dropbox.com/sh/da8cc2xwdz8oip9/AAAke_hGU9nTSR_N-wVE1u8Ca?dl=0.

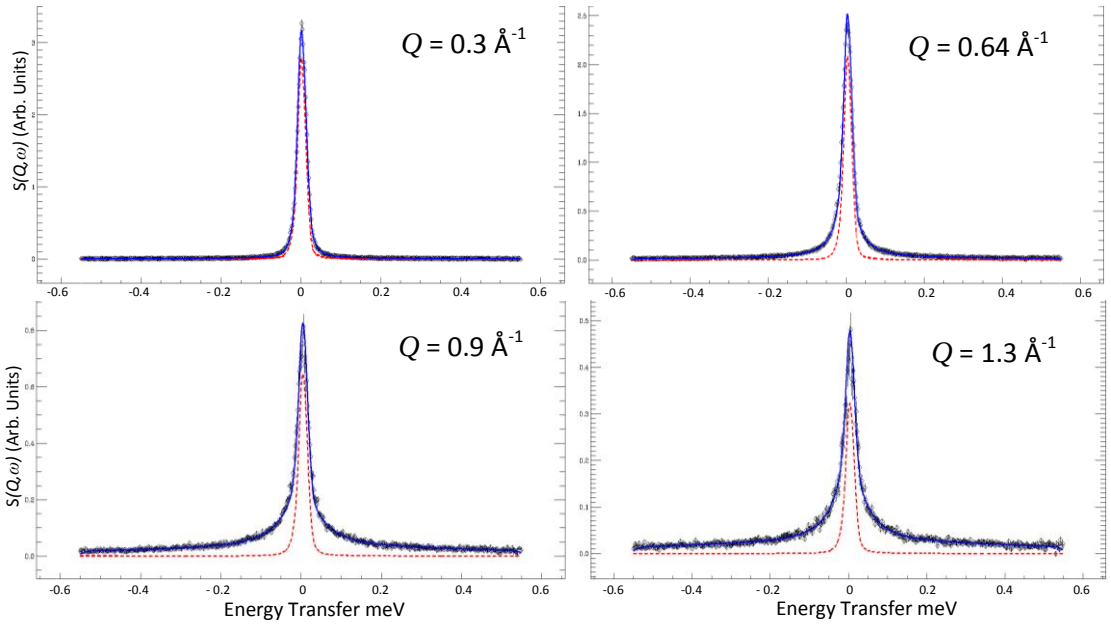

Fig. 6.3. QENS spectra of methanol at 300 K in HY. (--) represents a delta function convoluted with the resolution function (measured at 6 K).

6.1.3.2 Inelastic Neutron Scattering Experiments

INS was then used to probe the species present in both zeolites at 298 K. The vibrational spectra obtained are shown in figures 6.4 and 6.5 for HY and H-ZSM-5 respectively. The high and low energy spectra are plotted for solid methanol, methanol dosed into the zeolite, and the empty zeolite. In the high energy spectrum, the methanol reference spectrum contains bands of the OH deformation at 747 cm^{-1}, the CH_3 rocking mode at 1160 cm^{-1}, the CH bend at 1494 cm^{-1} and the CH and OH stretches at 2988 and 3259 cm^{-1} respectively. In the low energy spectra, the OH deformation of the solid methanol vibrational spectrum is resolved into a doublet with bands at 713 and 777 cm^{-1}. In the bare zeolites, the acidic OH stretching bands are observed at 3660 and 3720 cm^{-1} in H-ZSM-5 and HY respectively. OH deformations are observed at 1095 cm^{-1} in both zeolites. After loading the methanol into HY, the methanol OH deformation then downshifts to 677 cm^{-1} (figure 6.4 (a)) consistent with H-bonding to framework OH groups and other methanol molecules. The downshift is accompanied by a significant broadening observed in the lower energy vibrational spectrum (figure 6.4 (b)). The

methanol OH stretch and the framework OH stretch bands appear combined with the CH stretch due to downshifting, again due to H-bonding of methanol with the framework. In contrast, on loading of methanol into H-ZSM-5, the methanol OH deformation is not present in either the high or low energy spectra. The methanol OH stretch at 3259 cm^{-1} is also not observed after adsorption as shown in figure 6.5 (a); the framework OH stretch is also difficult to observe.

The disappearance of all OH groups upon adsorption into H-ZSM-5, and the persistence of the CH_3 deformation and stretch modes would suggest the complete conversion of methanol to framework methoxy at 300 K. Notably, no absorptions corresponding to water are observed in either system. Upon condensation, a strong OH stretch at 3600 cm^{-1}, bend at 1600 cm^{-1} and broad librational mode around 600 cm^{-1} would be expected to emerge. The absence of water is to be expected for the HY system as the zeolite is dehydrated and then loaded with methanol using a He/methanol gas stream. However the H-ZSM-5 system might be expected to show bands associated with water, the product of the condensation reaction. The absence of these bands suggests that the methoxylation is almost instantaneous on loading of methanol into the dehydrated zeolite, with the He/methanol stream carrying away any water formed, leaving behind the methoxylated zeolite, rather than the process taking place on a longer time scale inside the sealed can. This explanation indicates an unhindered methoxylation step in this catalyst at room temperature.

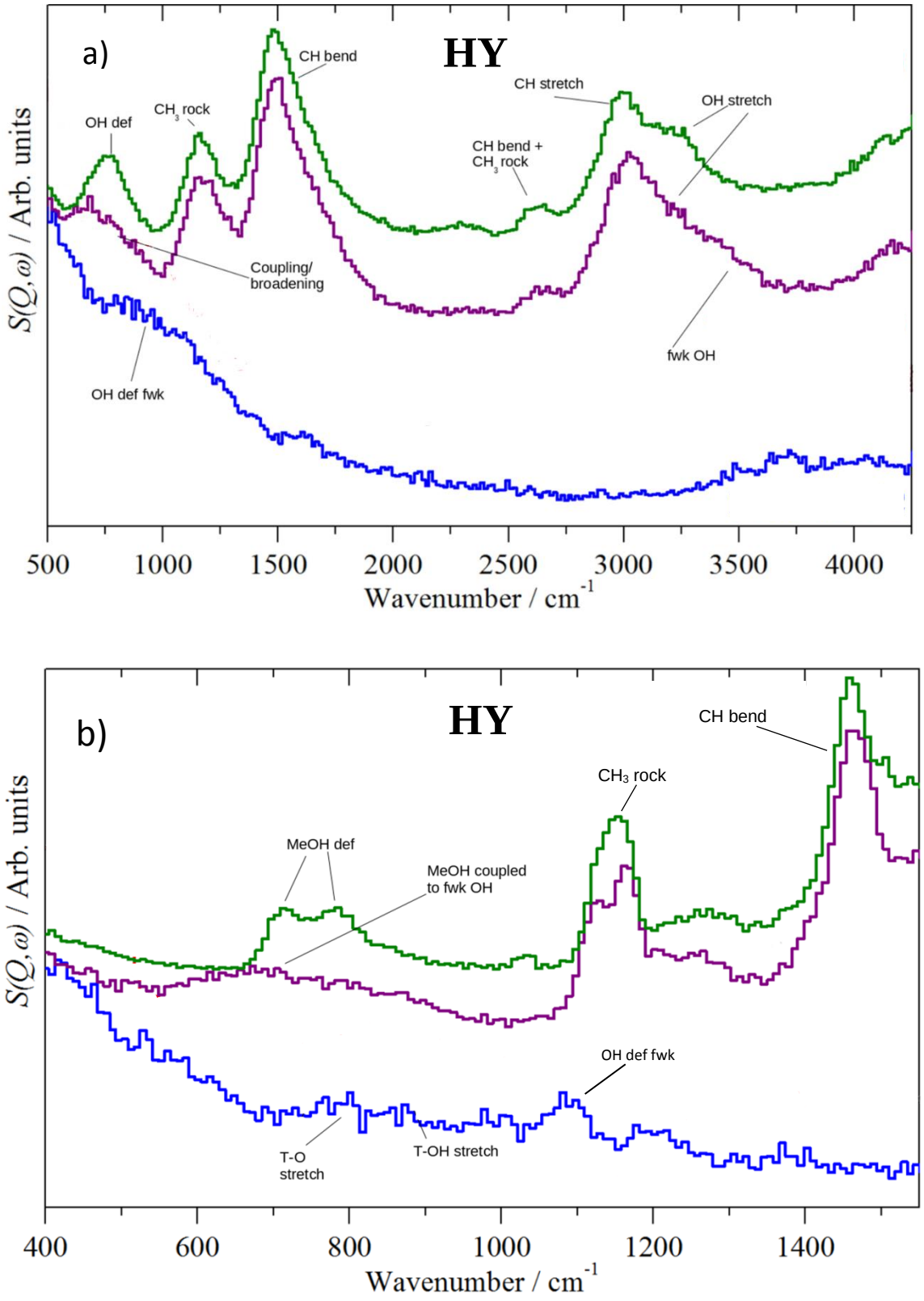

Fig. 6.4. INS spectra obtained of methanol (--), the empty dehydrated zeolite HY (--) and methanol loaded into zeolite HY (--) at incident energies of 650 meV (a) and 250 meV (b). Downshifting and broadening of the methanol OH stretches and deformations are observed due to hydrogen bonding with the HY hydroxyl sites and other methanol molecules.

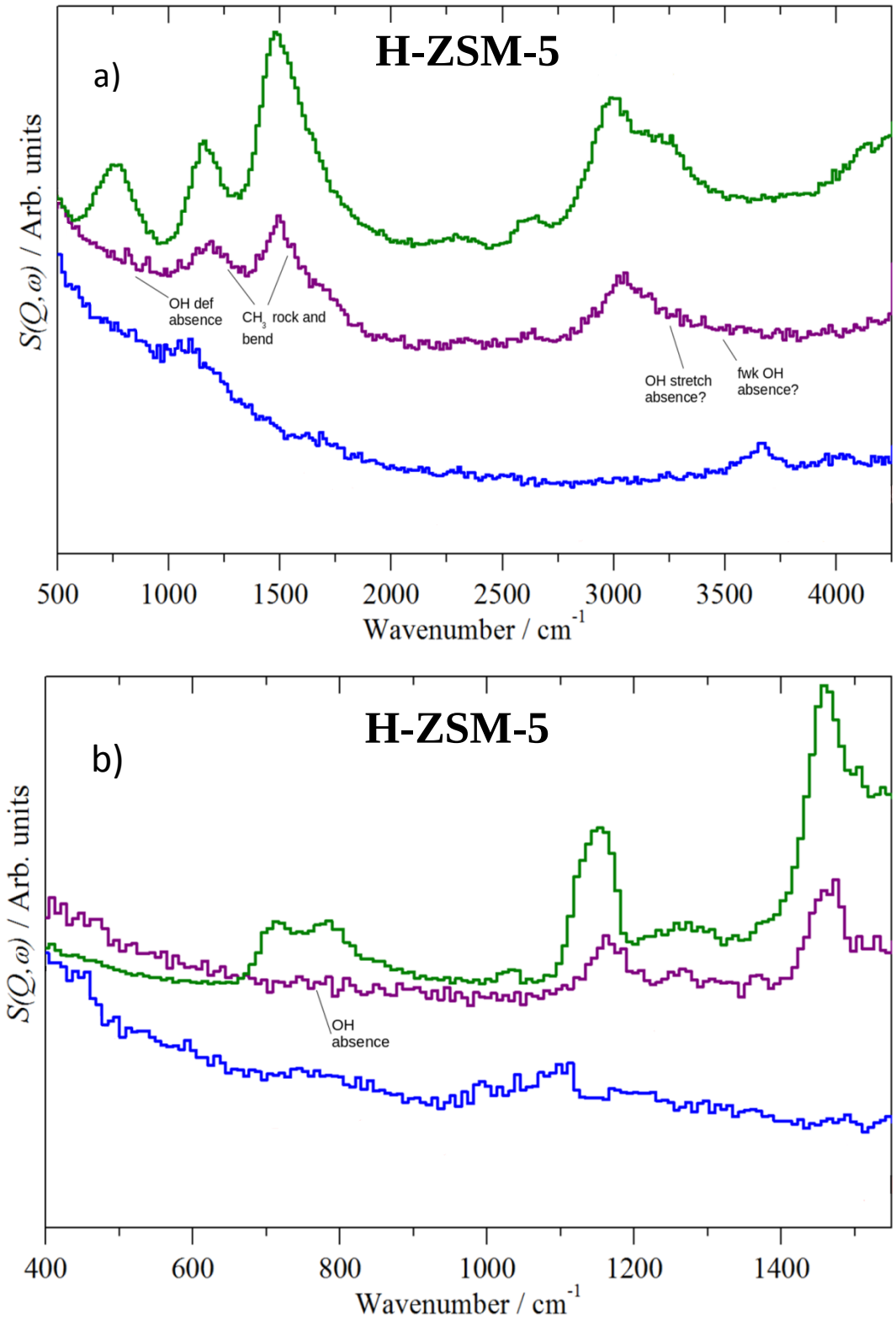

Fig. 6.5. INS spectra obtained of methanol (--), the empty dehydrated H-ZSM-5 (--) and methanol loaded into H-ZSM-5 (--) at incident energies of 650 meV (a) and 250 meV (b). Disappearance of the OH deformation at 747cm^{-1} and stretch at 3259 cm^{-1} is observed upon adsorption of methanol into H-ZSM-5, whereas the CH_3 rocking mode, CH bend and CH stretches persist, suggesting that methoxylation has taken place.

6.1.3.3 Quantum Mechanical Calculations of Vibrational Spectra

To confirm our assignment, DFT calculations were used to calculate the vibrational spectra of the empty protonated zeolite and the framework bound methoxy species. The calculated spectra were weighted for neutron scattering cross section to generate theoretical INS spectra. The flexible section of the empty HY structure is shown in figure 6.6 (a) and the methoxylated HY structure in figure 6.6 (b). Full simulation details are in the supporting information. These sites are part of the HY unit cell shown in 6.6 (c).

Figure 6.7 shows the experimental and theoretical INS spectra. There is very close agreement for both the empty and methoxylated systems with calculated adsorption bands of the OH stretch and deformation in the empty HY system calculated at 3624 and 1117 cm^{-1} respectively. The calculated methoxylated HY spectrum also gives close agreement with experiment, with the CH stretch at 3055 cm^{-1} and the CH bend and CH_3 rocking mode calculated at 1428 and 1126 cm^{-1} respectively. The agreement coupled with the immobilisation in the QENS measurements confirms the room temperature methoxylation in the H-ZSM-5 framework, in contrast to the intact methanol observed in HY.

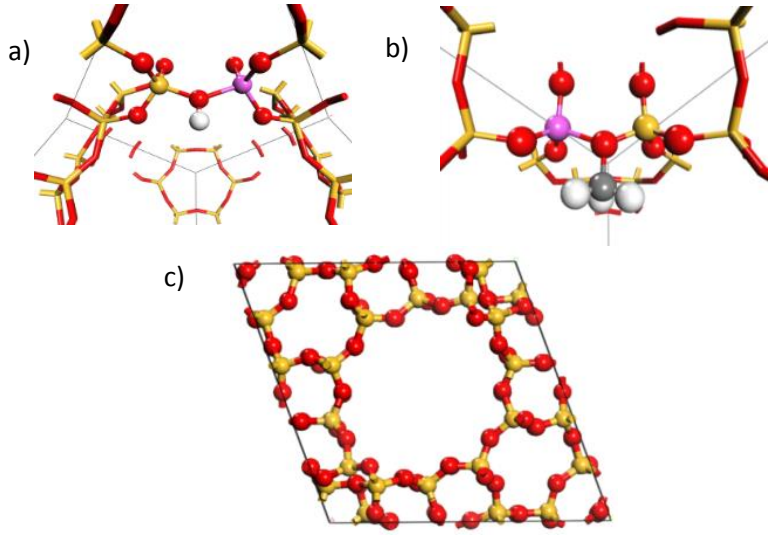

Fig. 6.6. Active site configurations of the DFT calculation used of the protonated zeolite (a) and the methoxylated framework (b) in the primitive unit cell of HY (c).

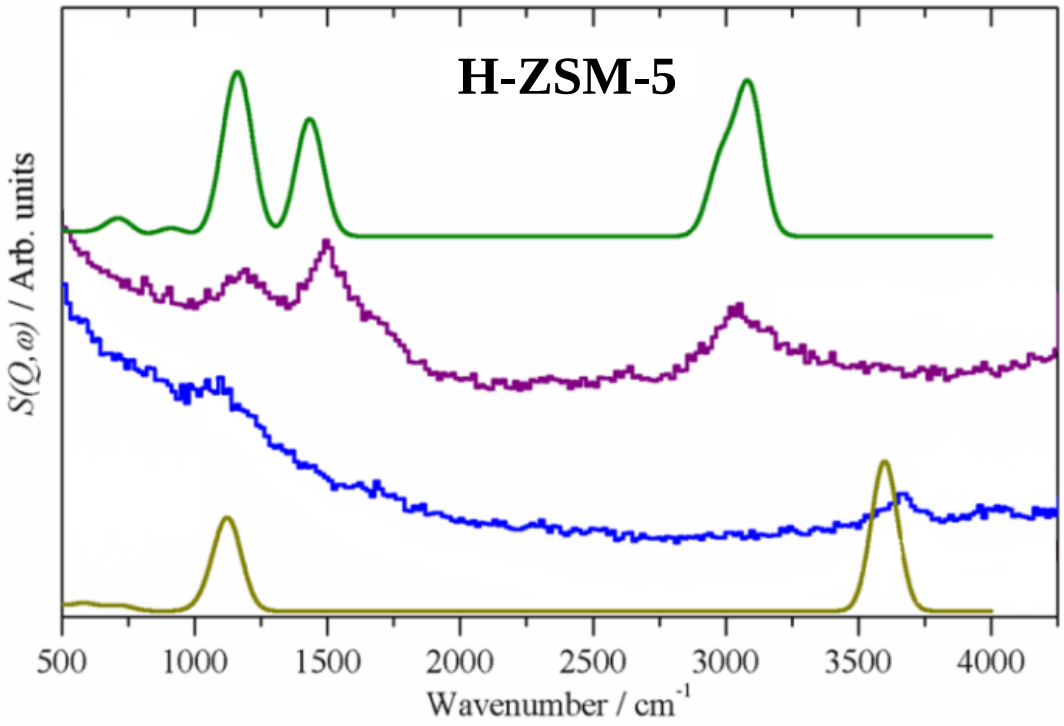

Fig. 6.7. Spectra of the experimental methoxylated ZSM-5 system (--), and the experimental empty H-ZSM-5 system (--), with the calculated spectra of the methoxylated zeolite (--) and the empty zeolite (--). Close agreement between the calculated experimental spectra support the case for ambient framework methoxylation.

6.1.4 Summary and Conclusion

Using QENS, INS and DFT vibrational spectra calculations, we observe the total conversion of methanol and framework hydroxyls to framework methoxy, and therefore completion of an early step of the MTH/MTO reaction in a commercial H-ZSM-5 sample at room temperature. This conclusion was supported through the observed immobilization of methanol upon adsorption into H-ZSM-5 using QENS and the absence of hydroxyl related absorptions from the INS spectra. These spectra show agreement with DFT calculations of vibrational spectra generated of the methoxylated zeolite. Room temperature methoxylation was not observed in the catalytically less applicable zeolite HY of the same Si/Al ratio (brought to this composition through steam dealumination), where methanol was observed to be highly mobile upon adsorption, with hydroxyl bands persisting in the INS spectrum. The absence of water in the H-ZSM-5 system suggests very rapid methoxylation of

the framework, with water removal in the He/methanol gas stream during dosing, as opposed to methoxylation over an extended period in the sealed system.

These observations provide strong evidence that the initial framework methoxylation step of the MTH/MTO process takes place rapidly at ambient temperatures in an active catalyst. They also suggest that despite sharing the same Si/Al ratio, the defects produced through the necessary dealumination process to create high silica faujasites can diminish this methoxylation capability, especially as previous studies have shown ambient methoxlation in an as synthesized HY sample of low Si/Al ratio. Our results also illustrate the power of the combination of QENS, vibrational spectroscopy and quantum mechanical modelling techniques in probing dynamical and mechanistic aspects of catalytic processes.

The work in this section has been published in the following paper:

O'Malley, A. J.; Parker, S. F.; Chutia, A.; Farrow, M. R.; Silverwood, I. P.; García-Sakai, V.; Catlow, C. R. A. *Chemical Communications* **2016**, *52*, 2897-2900.

6.2 Embedded Cluster Calculations of Acidity and Methanol Adsorption in HY and H-ZSM-5

The differences in activity between H-ZSM-5 and HY in the previous section suggest a significant barrier to methoxylation in the latter (concurrent with previous computational studies). Though the difference is attributed to the necessary dealumination procedure for high silica HY synthesis (creating defects which decrease the activity), the question of the effect of framework topology on a reaction barrier is still an important one. In this section we begin a larger study into the reactivity of zeolites as a function of framework topology using the QM/MM embedded cluster methodology. We compare the energetics of deprotonation and methanol adsorption in H-ZSM-5 and HY. These calculations make developments on previous simulations taking into account the different electrostatic potential at the active site of both zeolite frameworks. We find trends in the acidity counter to

experimental observations in the previous section, and uncover interesting factors which affect the trend in methanol adsorption energies between HY and different sites in the H-ZSM-5 framework.

6.2.1. Introduction

Though the MTG/MTO process has received a significant amount of attention from a theoretical perspective,[46,47] even the early stages (the adsorption of methanol to the Brønsted acidic site and subsequent methoxylation) of this are not understood in detail. *Ab initio* studies into the adsorption began with small aluminosilicalite clusters.[48,49] Numerous studies using three tetrahedral site clusters have concluded the exothermic hydrogen bonding of the methanol oxygen with the Brønsted acid hydroxyl, generally concluding adsorption energies of between 50 – 100 kJ mol^{-1}. [5,6,20,22,50] It has also been found that there is an energetic difference between 'side-on' and 'end-on' adsorption, with the end-on geometry (where the methyl group protrudes almost perpendicular from the aluminosilicate cluster) more favourable by 8 to 22 kJ mol^{-1}, [20,21] with reference 21 showing a barrier to geometry switching of 6 kJ mol^{-1} . However, it was also shown in reference 21 that the methoxylation process necessitates a side-on adsorption geometry. All studies into the methoxylation process using clusters conclude a barrier to methoxylation with values of ~180-225 kJ mol^{-1}.[5,6,20-22] Methoxylation and adsorption has also been studied in periodic zeolite structures, with static calculations showing endothermic methoxylation in chabazite (with a barrier of 56 kJ mol^{-1}),[51] and DFT-MD giving an adsorption energy of -94 kJ mol^{-1}.[25] Andzelm and Govind[24] studied the methoxylation process in a periodic ferrierite structure, finding a methoxylation barrier of 226 kJ mol^{-1}. However, it was found that when a second methanol molecule was added to the system, the barrier to methoxylation was then lowered by 42 kJ mol^{-1} due to formation of hydrogen bonding networks spanning the width of the channel, significantly stabilising the methoxylation transition states.

We note that the use of a discrete cluster model is less accurate than the use of a periodic zeolite structure, due to the lack of any long-range electrostatic potential influencing the system energetics. However, in addition to being computationally

expensive in calculations involving large unit cells (illustrated in section 6.1 where the spectral calculation of the MFI structure was not possible) the use of periodic boundary conditions can bring problems when calculating reaction barriers and adsorption energetics, such as incomplete relaxation of the system or the influence of sorbate mirror images interacting with each other. This can be especially significant when comparing the effect of framework structure on sorbate behaviour. A large zeolite unit cell would minimise the effect of these sorbate-sorbate interactions on the methoxylation process compared to say, chabazite where they may become significant. These complications can be bypassed using the quantum mechanical/molecular mechanical (QM/MM) embedded cluster technique [52,53] outlined in section 3.4. The technique allows for isolated processes to be studied at a quantum mechanical level, while incorporating the electrostatic potential of the entire zeolite framework through embedding the QM cluster in a large classical cluster surrounded by point charges. We present a comparison of the deprotonation and methanol adsorption energies in H-ZSM-5 and HY zeolite frameworks, in an attempt to elaborate on the observations of room temperature methoxylation in H-ZSM-5 in the previous section. The deprotonation energy is first investigated to consider the Brønsted acidity of the differing frameworks, including a comparison of three different sites in the ZSM-5 structure. The adsorption energy of methanol at these sites is then compared to quantify the difference in interaction strength between methanol and the differing acidic hydroxyl sites.

6.2.2 Methodology

6.2.2.1 Generation of Embedded Clusters

We first discuss the construction of the embedded cluster models for the HY and H-ZSM-5 structures, performed by A. J. Logsdail at University College London. We begin with the purely siliceous spherical structure generated from the periodic experimental unit cells of the silicalite[54] and siliceous faujasite.[55] The use of the experimental unit cell is assumed to have minimal effects on the geometric and electronic structure. Each spherical cluster centres on a tetrahedral Si T-site. Only

1 cluster is generated for the HY structure as the tetrahedral sites are equivalent, however this is not the case for H-ZSM-5. Three embedded clusters are generated based on three sites in the ZSM-5 structure, [56] a T-site at the straight channel (M7-T1), the sinusoidal channel (Z6-T4) and the channel intersections (I2-T12). The clusters, including their locations in the MFI structure are shown in figure 6.8.

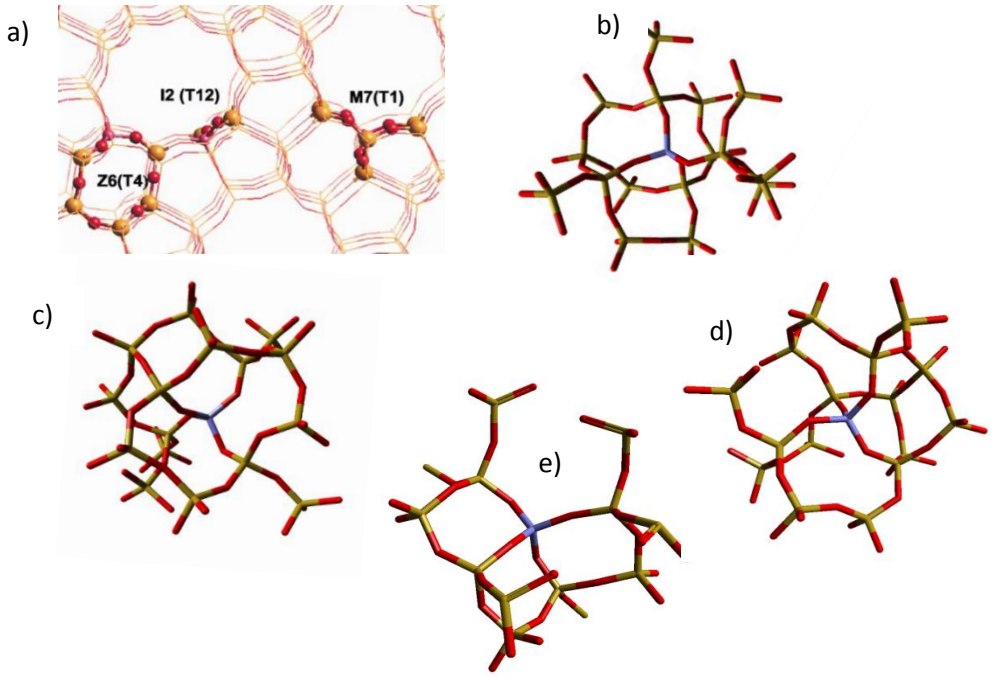

Fig. 6.8. a) The locations of the I2, Z6 and M7 clusters in the MFI framework (figure from reference 57), and the optimised QM clusters for the b) I2, c) M7, d) Z6 sections of the MFI framework, along with the optimised QM cluster in the zeolite Y calculations e). The central T-site is coloured purple.

The QM region is expanded from the central atom to include the fifth neighbour, the third oxygen atom away from the T-site as shown in figure 6.8. The cluster is then terminated with hydrogen atoms. We then add two concentric regions of molecular mechanics (MM) atoms spherically around this QM cluster. The first concentric region allows the MM atoms to relax during the energy calculation, this region reaches a 10.58 Å radius (20 bohrs) from the central atom. Beyond this region, the next concentric region fixes the framework atoms, reaching a 21.17 Å radius (40 bohrs) from the central T-site. The combined number of atoms in each cluster was 1653 for HY, 2165 for H-ZSM-5 (I2), 2180 for H-ZSM-5 (M7) and 2155 for H-ZSM-5 (Z6). Due to the termination of the incomplete bonds in the QM cluster

by hydrogen atoms upon embedding into the MM region, a bond-dipole correction must be added to the boundaries of the MM region.[58] At the QM/MM boundary where the Si-O bond is terminated to form a Si^{+}- - H-O system, the positive charge of the MM silicon may affect the electronic structure of the QM atoms nearby. The unrealistic electrostatic interaction between the MM silicon and the QM termination is overcome by redistributing the charge of the Si among the adjacent MM sites. The dipole of these charge shifts is corrected by adding a point dipole, implemented by a pair of point charges at said adjacent MM sites. The MM interactions are represented using the forcefield of Hill and Sauer[59], and the QM atoms are treated using the Ahlrichs and Taylor TZVP Gaussian basis sets.[60] Three exchange correlation functionals are used during the studies, the GGA functional of Perdew and Wang (PW91)[40], and the hybrid functionals of Becke, Lee , Yang and Parr (B3LYP)[61-64] and Wilson, Bradley and Tozer (B97-2). [65]

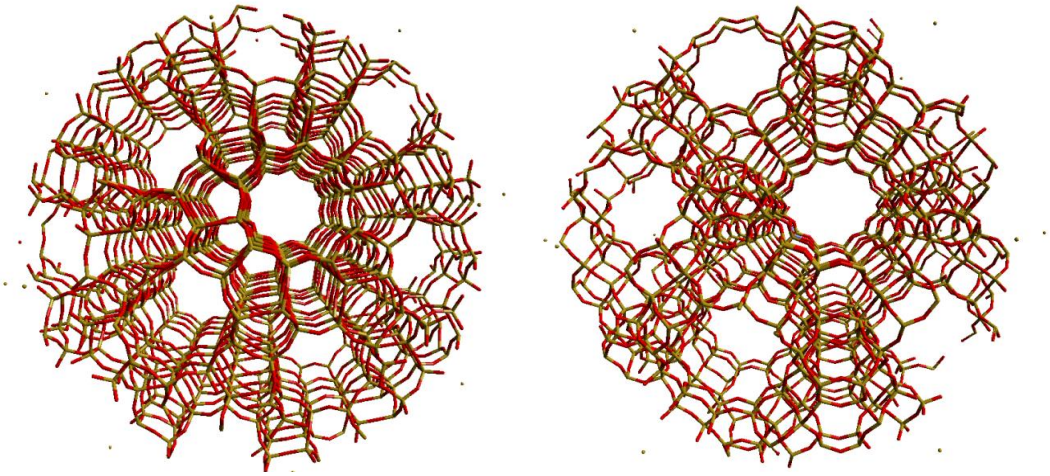

Fig. 6.9. Spherical embedded cluster models of the I2-T12 centred H-ZSM-5 system (left) and the zeolite Y system (right).

The optimisation of the QM region was carried out using the Gamess-UK package[66], and the optimisation of the MM region was carried out using the DL_POLY package.[67] The QM and MM calculations were coupled in the ChemShell environment.[56] The electronic structures for each system were energy minimised until convergence of 2.72 x 10^{-6} eV was achieved (1 x 10^{-7} Hartrees). The geometries were optimised using the Limited-Memory Broyden-Fletcher-Goldfarb-Shanno (L-BFGS)[68-71] algorithm until convergence of 0.015 eV/Å These convergence criteria are standard for the Gamess-UK package.

6.2.3 Calculation of Deprotonation Energies

In our first comparison of HY and H-ZSM-5 activity, we investigate the deprotonation energy differences between the structures. The deprotonation energy may be used as a measure of acidity[72-74] as the lower deprotonation energy equates to a more favourable protonation of the sorbate. We begin by determining the oxygen site around the central aluminium T-site which will deliver the most acidic zeolite structure (with the lowest deprotonation energy). The most acidic site will then be used for further studies into the methanol adsorption, and later methoxylation studies. We define the deprotonation energy as

$$E_{dp} = (E_{zeoH}) - \left(E_{zeo}^{-} + E_{Jost}\right) \quad (6.2.1)$$

Here, E_{zeoH} is the energy of the protonated zeolite, E_{zeo}^{-} is the energy of the deprotonated zeolite and E_{Jost} is the Jost correction,[53,75] which accounts for the truncation of the MM polarisation at the end of the first (flexible) MM region. Upon the creation of charge in the structure due to the deprotonation in the QM region, the atoms in the fixed MM region would also move to a slightly lower energy position in response to the localised electron on the QM O^- . The Jost correction takes account of this by calculating the energy gained at this distance based on the dielectric constant of the material. It has the form:

$$E_{Jost} = \frac{Q^2}{2R}\left(1 - \frac{1}{\varepsilon}\right) \quad (6.2.2)$$

Q is the charge defect, R is the radius of the total cluster and ε is the dielectric constant of the material, taken as 2.65 for FAU zeolites and 3.38 for MFI, calculated using classical shell model methods.[76] Figures 6.10 – 6.13 show geometries of the four protonated systems around the central Al T-site in each zeolite system, labelled O1-O4.

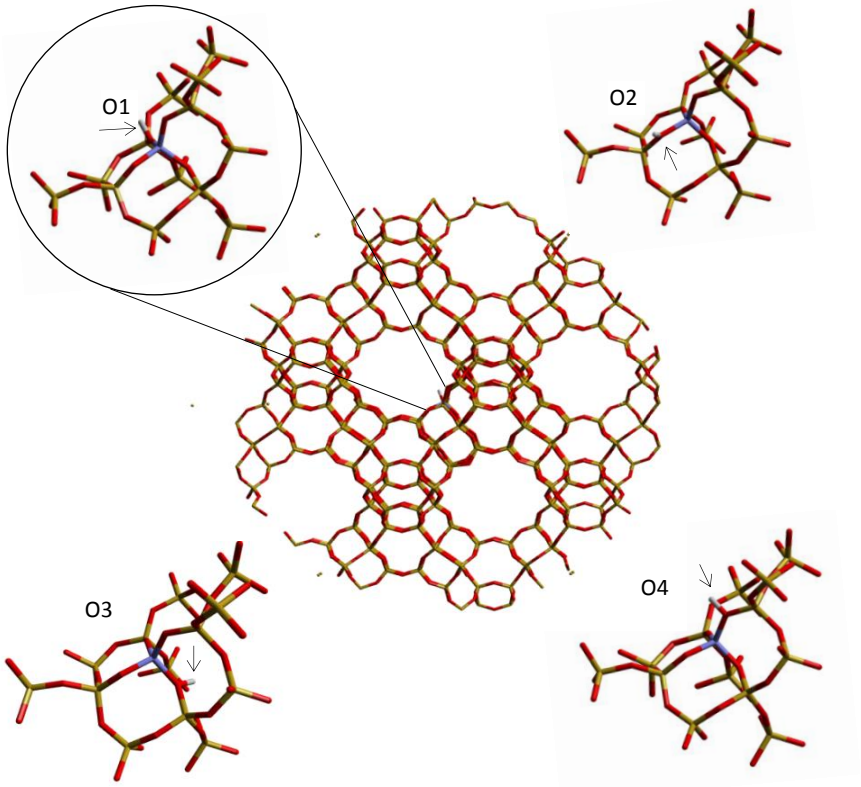

Fig. 6.10. Oxygen sites from which the deprotonation energy is calculated around the aluminium substitution in the HY cluster.

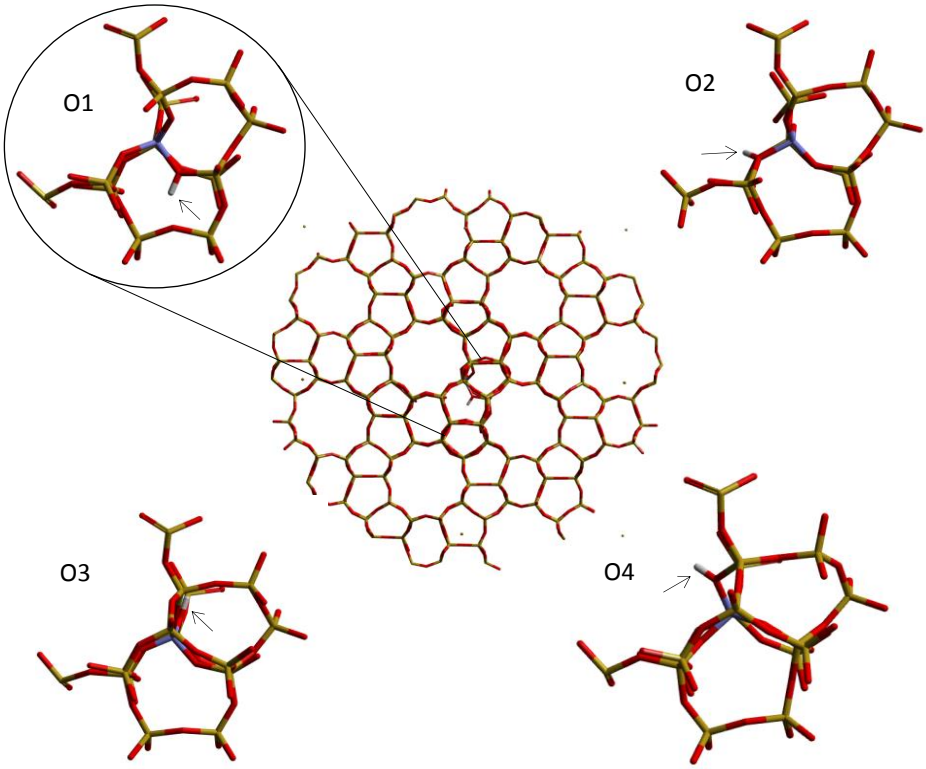

Fig. 6.11. Oxygen sites from which the deprotonation energy is calculated around the aluminium substitution in the H-ZSM-5 (I2-T12) cluster.

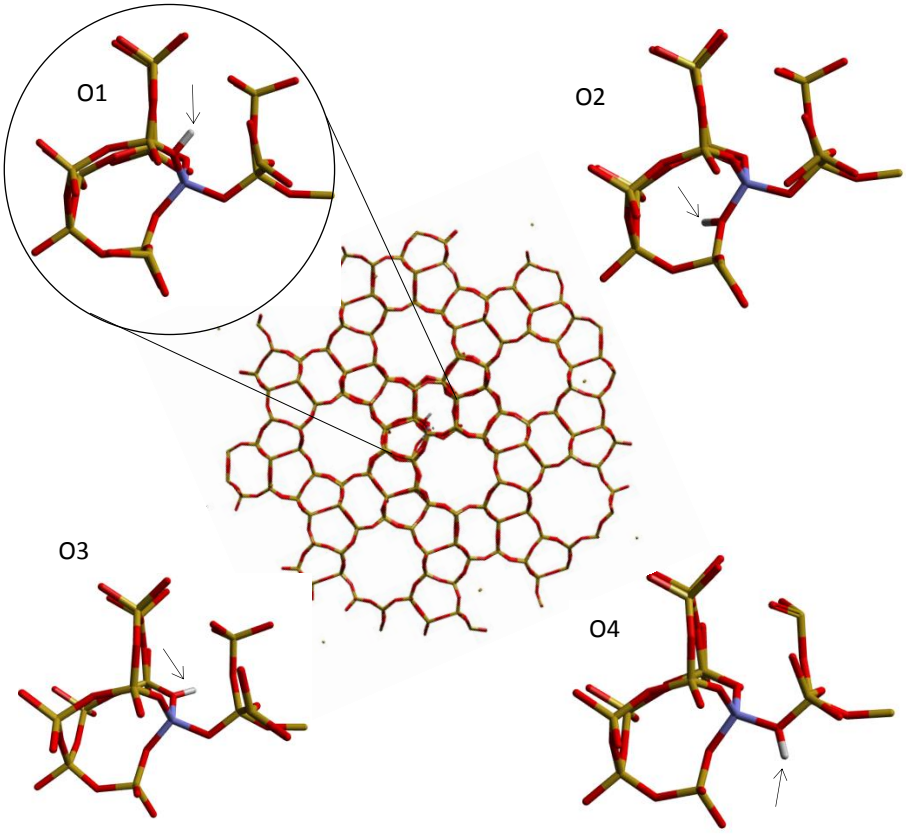

Fig. 6.12. Oxygen sites from which the deprotonation energy is calculated around the aluminium substitution in the H-ZSM-5 (M7-T1) cluster.

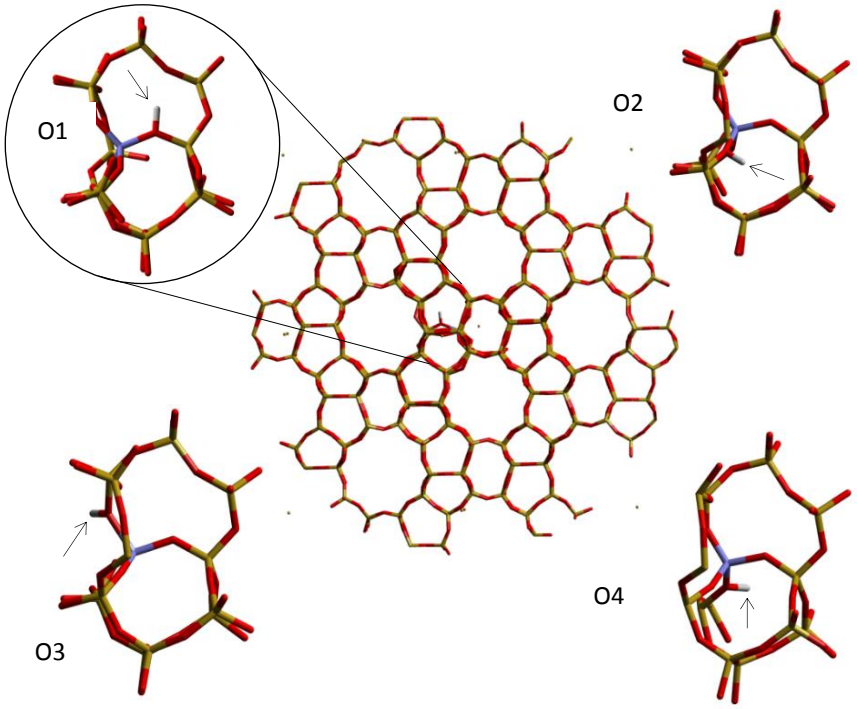

Fig. 6.13. Oxygen sites from which the deprotonation energy is calculated around the aluminium substitution in the H-ZSM-5 (Z6-T4) cluster.

The deprotonation energies of each oxygen site were calculated using the PW91 exchange correlation functional and are listed in table 6.1. Absolute values of the protonated and deprotonated structures can be found in appendix A, table A.1.

	E_{dp} kJ mol^{-1}			
Cluster	**O1**	**O2**	**O3**	**O4**
HY	**1013.4**	1041.0	1031.8	1023.0
H-ZSM-5 (I2)	1099.2	1106.3	**1093.4**	1122.0
H-ZSM-5 (M7)	1123.6	1114.7	**1103.6**	1109.5
H-ZSM-5 (Z6)	1059.5	**1020.9**	1042.9	1061.0

Table 6.1. Calculated deprotonation energies of each zeolite structure, with the most acidic oxygen atoms highlighted.

Using the PW91 functional, the most acidic oxygen sites are O1 for HY, O3 for H-ZSM-5 (I2), O3 for H-ZSM-5 (M7) and O2 for H-ZSM-5 (Z6). The difference between lowest and highest deprotonation energies (HY and H-ZSM-5 (M6) respectively) is 90.2 kJ mol^{-1}. We note preliminarily that HY has the lowest deprotonation energy of the series, followed by ZSM-5 (Z6) which is located in the sinusoidal channel, ZSM-5 (I2) in the intersections and the least acidic site is in the straight channel (M7).

We now explore the deprotonation energies of the most acidic sites in each structure using the B3LYP and B97-2 hybrid exchange correlation functionals. These are listed in table 6.2. The absolute values of the aluminated and protonated structures can be found in appendix A, table A.2.

	E_{dp} kJ mol^{-1}		
Cluster	**PW91**	**B3LYP**	**B-972**
HY	1013.4	1065.9	1081.3
H-ZSM-5 (I2)	1093.4	1100.4	1114.1
H-ZSM-5 (M7)	1103.6	1155.9	1166.1
H-ZSM-5 (Z6)	1020.9	1084.7	1101.9

Table 6.2. Calculated deprotonation energies of each zeolite structure, with three different functionals.

The deprotonation energies calculated using the B3LYP functional, were higher than when using the PW91 functional, and higher still using the B97-2 functional. This can be attributed to the superior representation of the localised electrons in the zeolite, due to the exact exchange interaction from Hartree-Fock methods incorporated into the hybrid functionals. However, the ranking of deprotonation energy is maintained through use of all functionals as HY < H-ZSM-5 (Z6) < H-ZSM-5 (I2) < H-ZSM-5 (M7). The deprotonation energy calculated in ZSM-5 (I2) is 122 kJ mol^{-1} lower than that obtained by *ab initio* molecular dynamics in the MFI structure using plane wave DFT [74] using the same PW91 functional. Other potential reasons for this difference could be the aforementioned sorbate-sorbate interactions, the lack of total structural relaxation afforded using the QM/MM method, or the charge compensation parameter needed for periodic DFT calculations. However, we also note that reference 74 used a different intersectional T-site (T7) to ours (T12).

Our results suggest that HY has the most acidic Brønsted sites between the two zeolites even when the different oxygen environments are taken into account, disagreeing with our observation of room temperature methoxylation in H-ZSM-5 rather than HY. It is possible that acidic strength (especially with differences on the order 20 kJ mol^{-1}) is not the significant factor in this methoxylation process, compared to the interaction of the framework with the methanol molecule which is investigated next. The most acidic oxygen sites for each cluster will be used for the methanol adsorption energy calculations.

6.2.4 Calculation of Methanol Adsorption Energies

The interaction of methanol with the active site is investigated through measurement of the adsorption energies of methanol in HY and H-ZSM-5. Though the acidity of a zeolite is a typical indicator of the activity in a catalytic process, the favourability of the sorbate interaction with the active site may also be a deciding factor in our observed methoxylation process. We note however that in terms of the methoxylation barrier, a favourable adsorption energy can facilitate the

process, or indeed hinder the methoxylation through increasing the barrier to reaction. The adsorption energy of methanol is calculated as

$$E_{ads} = (E_{MeOH+ZeoH} - E_{BSSE}) - (E_{MeOH} + E_{ZeoH}) \ , \qquad (6.2.3)$$

Where E_{MeOH} is the calculated energy of a methanol molecule in a vacuum. E_{ZeoH} is the energy of the protonated embedded zeolite cluster, $E_{MeOH+ZeoH}$ is the calculated energy of the methanol adsorbed onto the protonated embedded zeolite cluster and E_{BSSE} is the basis set superposition error explained in this section. The geometry of the adsorbed methanol for each cluster is shown in figures 6.14–6.17 (upon geometry optimisation using the B3LYP functional).

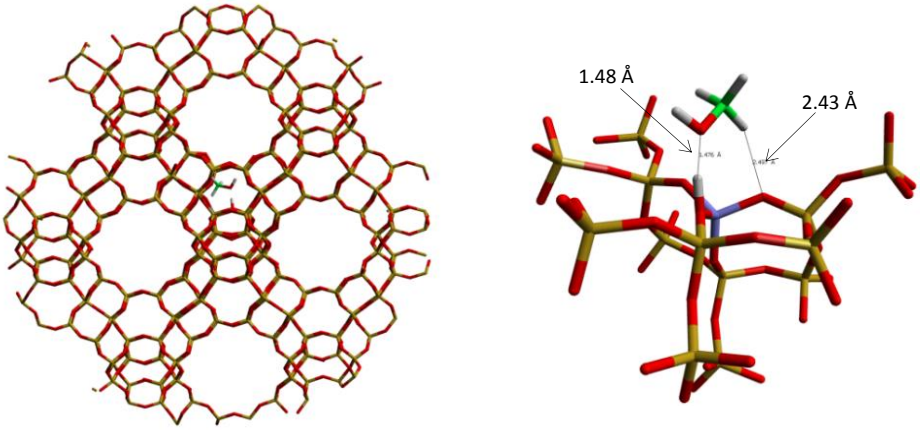

Fig. 6.14. Optimised adsorbed geometry of methanol in the HY structure.

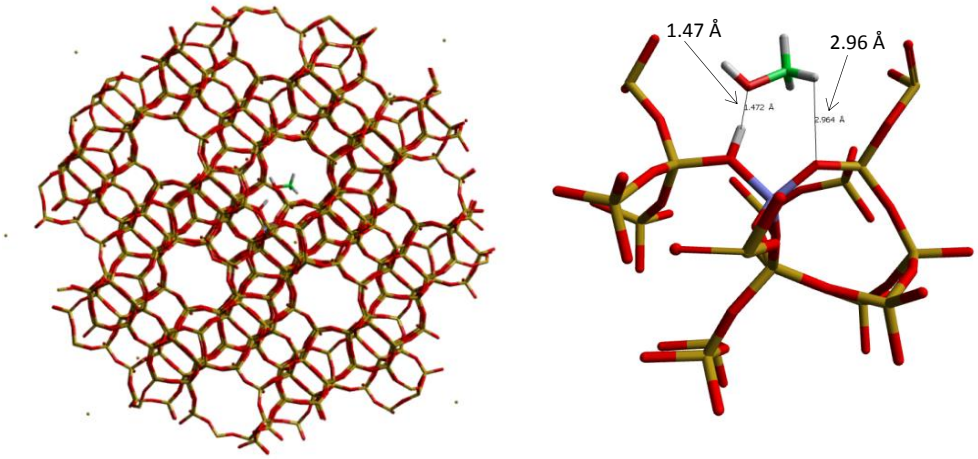

Fig. 6.15. Optimised adsorbed geometry of methanol in the H-ZSM-5 (I2-T12) structure.

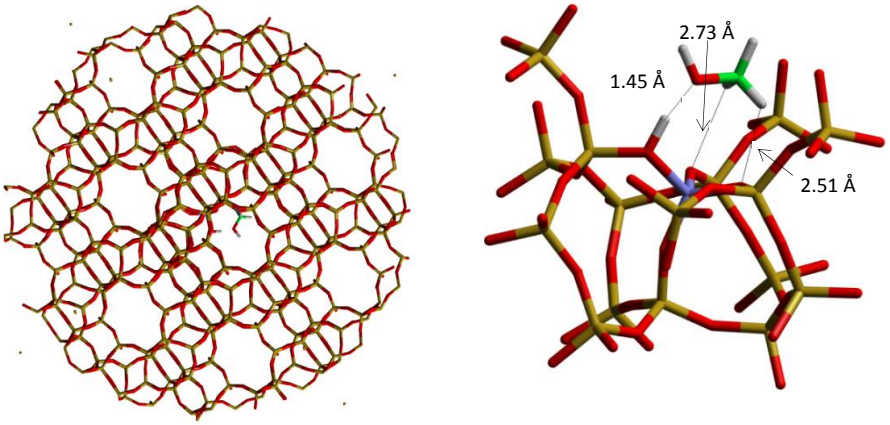

Fig 6.16. Optimised adsorbed geometry of methanol in the H-ZSM-5 (M7-T1) structure.

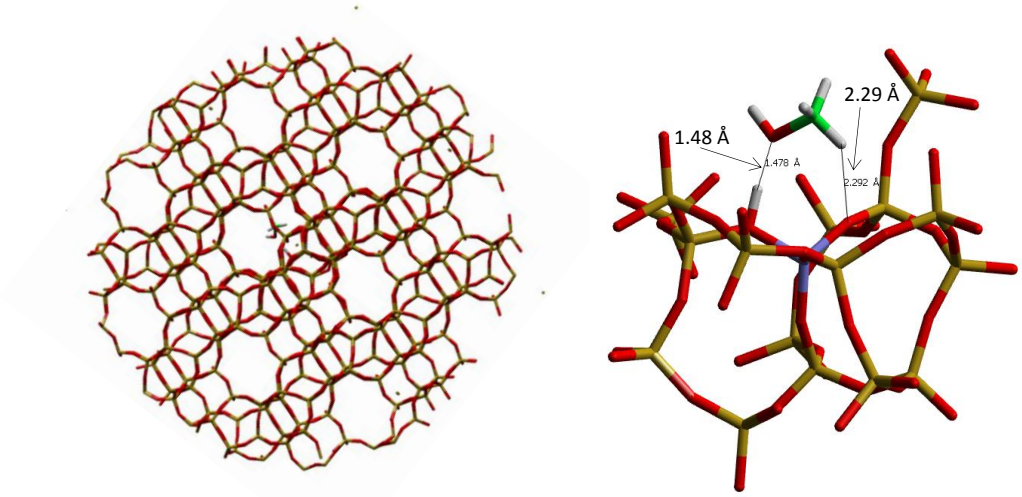

Fig. 6.17. Optimised adsorbed geometry of methanol in the H-ZSM-5 (Z6-T4) structure.

We study the 'side-on' adsorption in all zeolite systems. Though we note in previous studies 'end-on' adsorption is preferred,[20,21] the side-on adsorption is more conducive to methoxylation which is the emphasis of this study, and the very low barriers previously calculated for this switch in orientation in reference 21 are feasibly overcome under experimental conditions. From figures 6.14-6.17, it is observed that the H-bond length between the hydroxyl site and the methanol hydroxyl is 1.476 Å for the HY cluster, and 1.452 – 1.478 Å for the H-ZSM-5 clusters, with the shortest H-bond being in the M7-T1 cluster. Interestingly, the M7 cluster exhibits the shortest H-bond despite having the highest deprotonation energy.

However, we note that the difference of 0.026 Å in this range is small enough that a comparison with deprotonation energies is not necessarily valid. Before a discussion of the adsorption energies calculated, a description of the basis set superposition error (BSSE) and the values which correct our adsorption energies will be outlined.

In calculating adsorption using quantum mechanical methods, one may observe an artificial stabilisation as one molecule utilises the extra basis functions from the other molecule to adjust for the inadequacies in describing its electron distribution (in our case, the methanol interacting with the zeolite framework). At shorter intermolecular distances, the electron density of both molecules may access additional functions from each other. The artificial strengthening of the intermolecular interactions due to this 'borrowing' of functions from nearby components is termed the basis set superposition error.[77] The magnitude of this error may be calculated and subtracted from the original uncorrected adsorption energy. The method of choice for this section is termed the counterpoise correction method.[78]

The adsorption energy is calculated conventionally as:

$$E_{ads} = (E_{MeOH+ZeoH}) - (E_{MeOH} + E_{ZeoH}) \qquad (6.2.4)$$

The extent of the 'mixing' of zeolite and methanol orbitals may be quantified using so called 'ghost atoms'. This is where the basis functions of a molecule are placed on the atomic centres of that molecule, however the electrons and nuclear charges are neglected. In our example, one may take the complete zeolite structure (in the optimised adsorbed geometry) and calculate the energy in the presence of the adsorbed empty methanol basis functions ($E_{Zeo\_ads+MeOH\_ads(ghost)}$), and then subtract the energy value of the adsorbed geometry zeolite structure without the presence of the empty methanol basis functions (E_{Zeo_ads}). Any energy difference is attributed to the empty methanol orbitals borrowing basis functions from the

zeolite structure. The same must then be carried out in the reverse case, where the energy of an adsorbed geometry methanol molecule (E_{MeOH_ads}) is subtracted from the energy of an adsorbed geometry methanol molecule in the presence of the adsorbed geometry empty zeolite basis functions ($E_{MeOH\_ads+Zeo\_ads(ghost)}$). The total BSSE is then calculated as:

$$E_{BSSE} = \left(E_{Zeo_{ads}+MeOH_{ads(ghost)}} - E_{Zeo_{ads}}\right) + \left(E_{MeOH_{ads}+Zeo_{ads(ghost)}} - E_{MeOH_{ads}}\right) \quad (6.2.5)$$

The BSSE is then incorporated into the adsorption energy calculation as in equation 6.2.3. The BSSE values and the percentage error they contribute to the total adsorption energies are listed in table 6.3 and noted as being relatively small. The absolute values of the methanol molecule, the protonated zeolites and the corrected adsorbed structures can be found in Appendix A.

System	BSSE kJ mol^{-1}	%
HY + MeOH	-5.32	2.8
H-ZSM-5 (I2 T12) +MeOH	-5.72	3.2
H-ZSM-5 (M7 T1) +MeOH	-4.20	2.2
H-ZSM-5 (Z6 T4) +MeOH	-7.63	5.2

Table 6.3. Calculated basis set superposition errors using the B3LYP functional for each methanol adsorbed system.

An important point to make is that these BSSE values were calculated with the B3LYP functional only. As an approximation we have then taken the percentage error that these values contribute to each system (table 6.4) and applied it to the adsorption energy calculations using the PW91 and B97-2 functionals. The calculated adsorption energies are listed in table 6.4 after subtraction of this percentage error.

	E_{ads} kJ mol^{-1}		
Cluster	**PW91**	**B3LYP**	**B97-2**
HY	-180.2	-179.6	-180.4
H-ZSM-5 (I2)	-186.8	-177.5	-168.9
H-ZSM-5 (M7)	-215.1	-194.8	-206.9
H-ZSM-5 (Z6)	-147.24	-136.6	-136.7

Table 6.4. Corrected adsorption energies of methanol in each structure using three different functionals.

For all functionals the order of methanol adsorption energy is H-ZSM-5 (M7) < HY < H-ZSM-5 (I2) < H-ZSM-5 (Z6). We note that the difference in adsorption between the most favourable site (H-ZSM-5 (M7)) and the least favourable site (H-ZSM-5 (Z6)) is between 60-70 kJ mol^{-1} depending on the functional used. We also note that the H-ZSM-5 (M7) system is H-bonded to two framework oxygens by two C-H hydrogens (depicted in figure 6.16), suggesting that this geometry is more favourable than a short, single C-H - - - O bond, demonstrated by the higher adsorption energy in the H-ZSM-5 (Z6) system. An important point is also that the most favourable adsorption process also occurs at the site with the highest deprotonation energy (the least acidic site), however the most acidic site (HY) has the second lowest adsorption energy. A possibility is that there is a correlation between acidity and the adsorption energy (the HY < ZSM-5 (I2) < ZSM-5 (Z6) trend is preserved in the adsorption energies as for the acidities) and the ZSM-5 (M7) structure is an anomaly to this trend due to its differing adsorption geometry. This significant reduction in adsorption energy for ZSM—5 (M7) may suggest that the adsorption energy is dominated by the H-bonding capability of the methyl group of the methanol. We are however, neglecting the propensity of methanol to adsorb in the end-on geometry which may have a completely different trend in adsorption energies. If this is the case, the adsorption energy in the end-on geometry combined with the barrier of end-on/side-on switching would be desirable to calculate.

We have obtained an interesting insight into the interaction of methanol with the acidic sites and how this can change with framework structure and location. However, this is an ongoing study which will use the embedded cluster models developed for these two frameworks to investigate the energetics of methoxylation in zeolites. The difference between end-on and side-on methanol adsorption will be studied in all locations, as this barrier may affect the energetics of further processes as studied in references 20 and 21. Currently running are nudged elastic band (NEB) calculations of the methoxylation process at each location, where the barrier may be calculated at steps between the adsorbed methanol and the methoxylated structure with the water molecule by-product. The formation of water will affect the energy of the system due to its H-bonding with the framework methoxy group and the zeolite framework. The effect was illustrated by Andzelm and Govind[24] in the FER framework, who also showed that the presence of a second methanol molecule can lower the total methoxylation barrier by 42 kJ mol^{-1}. The lowering was attributed to the formation of a H-bonded network spanning the width of the ferrierite channel. An important point is that the maximum width of the ferrierite channel is 5.4 Å, similar to the MFI structure of H-ZSM-5. A significant possibility is that the constricted width of the H-ZSM-5 pore could facilitate the formation of the favourable H-bonding network spanning the channel (so the entire network may interact favourably with the channel walls in all directions). The capability for the network to span the channel is in contrast to the 12 Å supercage in HY, where this large volume is not a suitable environment for this H-bonding network, resulting in a less stabilised environment for methoxylation to take place. On this premise, NEB calculations involving two methanol molecules will be carried out to assess the effect of the different framework structures on the methoxylation energetics and the networks formed which may stabilise the process.

6.2.5 Summary and Conclusions

To investigate the acidity and energetics of methanol interaction with the two acidic zeolite catalysts, QM/MM embedded cluster systems have been set up for zeolites HY, and H-ZSM-5 with acidic sites centred in the straight channel, sinusoidal

channel and intersection region. The deprotonation energies were calculated as a measure of acidity giving a trend of HY < H-ZSM-5 (Z6) < H-ZSM-5 (I2) < H-ZSM-5 (M7) suggesting the HY structure is the most acidic, contrary to our experimental observation of no methoxylation activity. The side-on adsorption energy of methanol in each structure was also calculated, giving a trend of H-ZSM-5 (M7) < HY < H-ZSM-5 (I2) < H-ZSM-5 (Z6), the most favourable adsorption site (H-ZSM-5 (M7)) exhibited an adsorption geometry where two methyl hydrogens were able to hydrogen bond to framework oxygen atoms, suggesting that the H-bonding behaviour of the methyl group is dominant in dictating the adsorption energy (the same order is otherwise obtained for adsorption energy as with acidity). Studies are currently taking place into the methoxylation mechanism and the H-bonded networks of multiple methanol molecules and the methoxylation by-product, water.

The work in this section has been published in the following paper:

O'Malley, A.J.; Logsdail, A.J.; Sokol, A.A; Catlow, C.R.A. *Faraday Discussions*. **2016 -** DOI: 10.1039/C6FD00010J.

6.3 Methanol Diffusion in Zeolite HY

The aim of the section 6.1 was to quantify methanol diffusivity in H-ZSM-5 and HY, comparing the effect of the differing FAU and MFI structures on its mobility. The observed room temperature methoxylation in H-ZSM-5 made quantifying the diffusion in this zeolite impossible. However QENS studies of methanol in HY were possible due to this lack of activity. We report the use of QENS to perform the first microscopic measurement of methanol diffusion in HY. Measurements were carried out in a temperature range of 300 – 400 K. Unlike the octane isomers in chapter 5, only one mode of motion was observed, that of unconfined Fickian diffusion, interestingly with significantly higher diffusion coefficients than calculated previously by experiment and MD simulations in NaX.

6.3.1 Methanol Diffusion in Zeolite HY: Introduction

Experimentally, diffusion of methanol in faujasite has been performed only using NaX, as the methods used necessitated larger crystal sizes (up to 100 μm). A comparison of zero-length column (ZLC) and PFG-NMR methods showed good agreement in the activation energy (11 kJ mol^{-1}) upon extrapolation to zero loading.[79] The PFG-NMR measurements showed a maximum in diffusivity at loading of 8 molecules per faujasite cage. Comparison between the two techniques is difficult, as traditional ZLC measurements are only suited to low concentrations. However, the tracer ZLC method allowed direct comparison at 100°C, agreeing with this trend in the variation with loading. [80]

Molecular dynamics simulations have also investigated methanol diffusion in faujasites, without the constraint of needing to use zeolite X for the larger crystal size. Comparison between NaY (Si/Al = 2.4) and siliceous Y was made,[81] showing that the presence of counterions can significantly inhibit the diffusion (by up to a factor of 7 at higher temperatures) with an activation energy higher than a factor of 4 with the counterions present. The increase was attributed to a strong interaction between methanol oxygen and the Na^+ counterion. Longer MD simulations[82] of this system found that activation energies for long range (intercage) motion decrease with loading, and that at lower loadings surface-mediated (intracage) diffusion dominates. Cation behaviour upon methanol adsorption was also studied,[83] showing that the extra-framework Na^+ in certain crystallographic sites can move to the centre of the supercage (probably hindering methanol motion) upon interaction with the methanol. The cation mobility is also limited at higher methanol loadings. Later MD simulations incorporated this cation mobility, giving qualitative agreement with the experimentally observed diffusivity maximum at lower concentrations.[84]

To our knowledge, no research has taken place measuring the diffusion of methanol in zeolite HY, though this zeolite has been studied for activity in methanol dehydration[85] and methanol-to-olefin transformations[86] post dealumination. Study of higher silica faujasites is not feasible for the aforementioned experimental

methods as they necessitate larger crystals, which are not available for these zeolites. QENS does not suffer from this limitation, allowing intracrystalline diffusion in powders to be studied. We report the first microscopic measurement of methanol diffusivity in a commercial sample of zeolite HY (Si/Al = 30) using QENS. We are able to quantify Fickian diffusion coefficients of the methanol between 300 – 400 K, giving activation energies lower than those measured in NaY/X, but higher than in simulations of the siliceous zeolite.The experimental procedure was that of section 6.1.2, QENS measurements were carried out at 300, 330, 360 and 400 K.

6.3.2 Results and Discussion

A selection of QENS spectra at each temperature are shown at 4 Q values in figures 6.18–6.21. The spectra are fitted to a delta function convoluted with the resolution measurement taken at 6 K, a flat background function and a single Lorentzian function. The fitting of a single Lorentzian is in contrast to the octane isomers in chapter 5, where two Lorentzians were fitted to the spectra signifying two quantifiable modes of motion. One can see that the Lorentzian component is consistently broadening with Q at all temperatures, suggesting free translational motion.

The Q dependencies of the HWHM of the Lorentzian component are plotted for all temperatures in figure 6.22. A linear dependence of the HWHM with Q^2 is adhered to at all 4 temperatures, indicative of Fickian diffusion. The measured diffusion coefficients are in a range of 2–5 x 10^{-10} m^2s^{-1}. The activation energy of diffusion was measured from the Arrhenius plot in figure 6.23, of 8.8 kJ mol^{-1}. The diffusion coefficients are listed with those obtained from other methods in table 6.5 and plotted in figure 6.24. We note that those obtained by QENS are higher by an order of magnitude than all experimental diffusion coefficients meaured of methanol in NaX and MD studies in NaY (Si/Al = 2.4). This observation could be attributed to the high concentration of counterions throughout the structure of NaX/low silica NaY, hindering diffusion. These extra framework counterions are not present in HY, which instead has bridging hydroxyls attached to the framework.

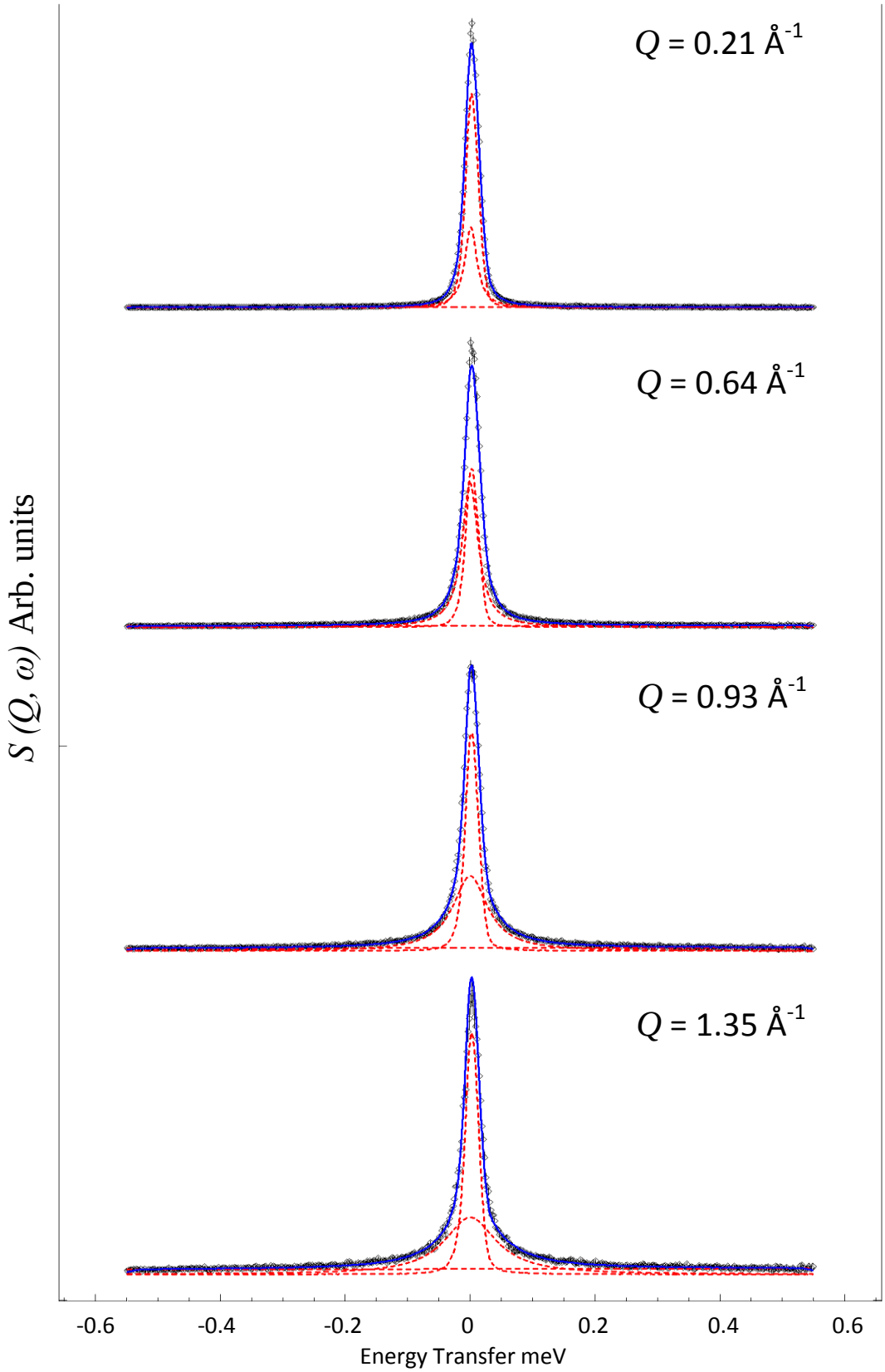

Fig. 6.18. S(Q,ω) at 4 Q values for methanol in HY at 300 K. 1 Lorentzian quasielastic component is observable.

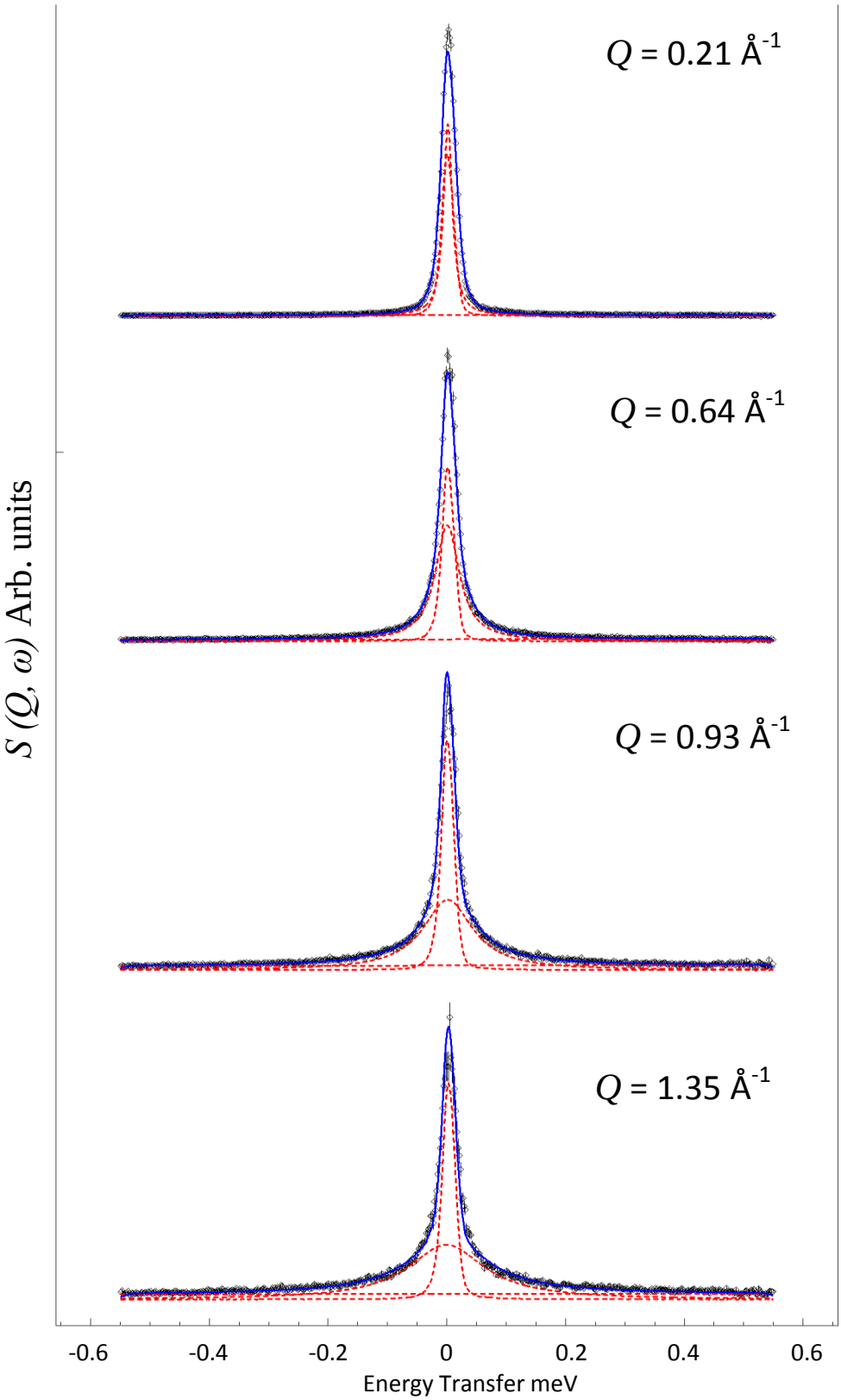

Fig 6.19. S(Q,ω) at 4 Q values for methanol in HY at 330 K. 1 Lorentzian quasielastic component is observable.

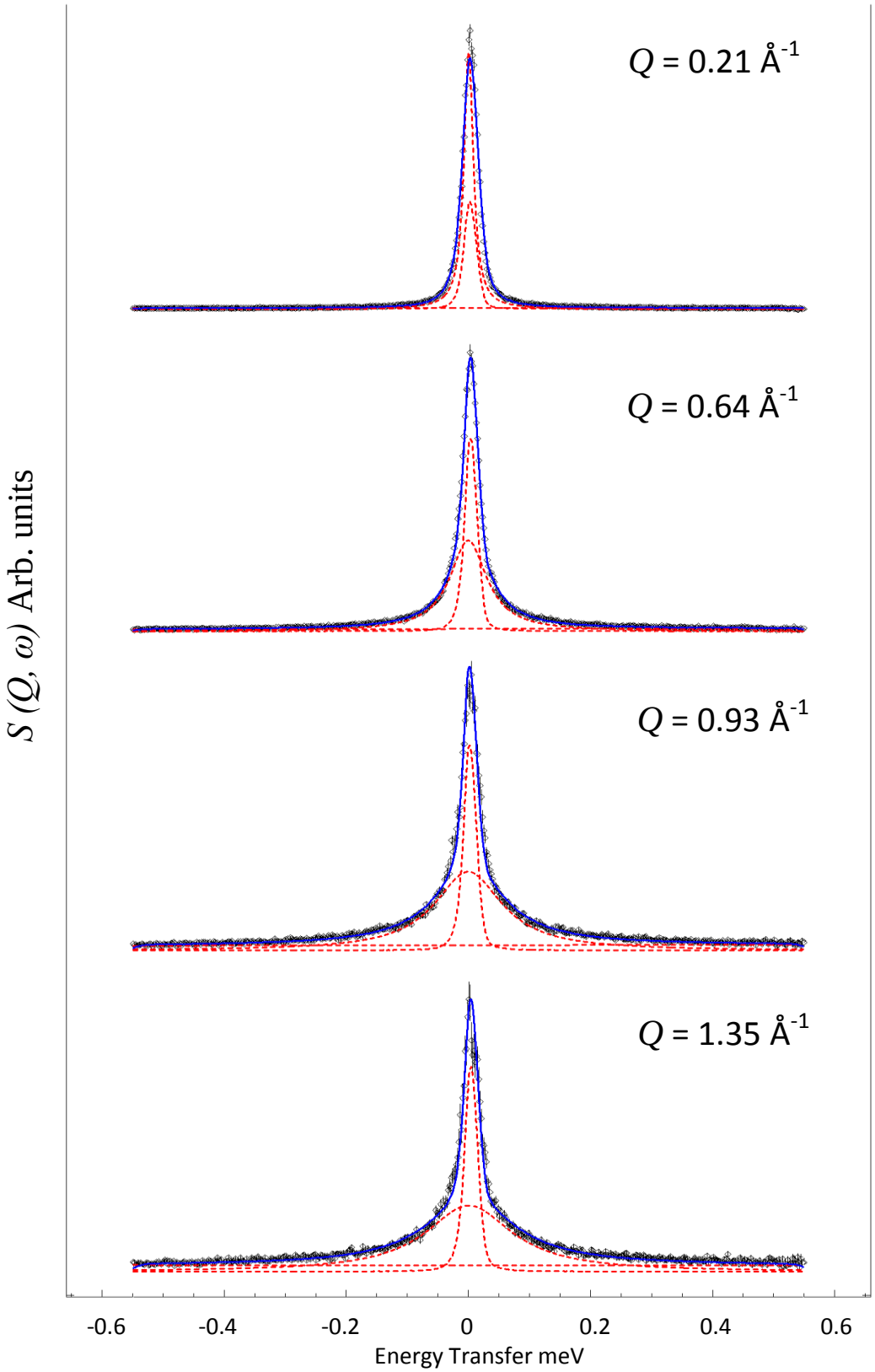

Fig. 6.20. S(Q,ω) at 4 Q values for methanol in HY at 360 K. 1 Lorentzian quasielastic component is observable.

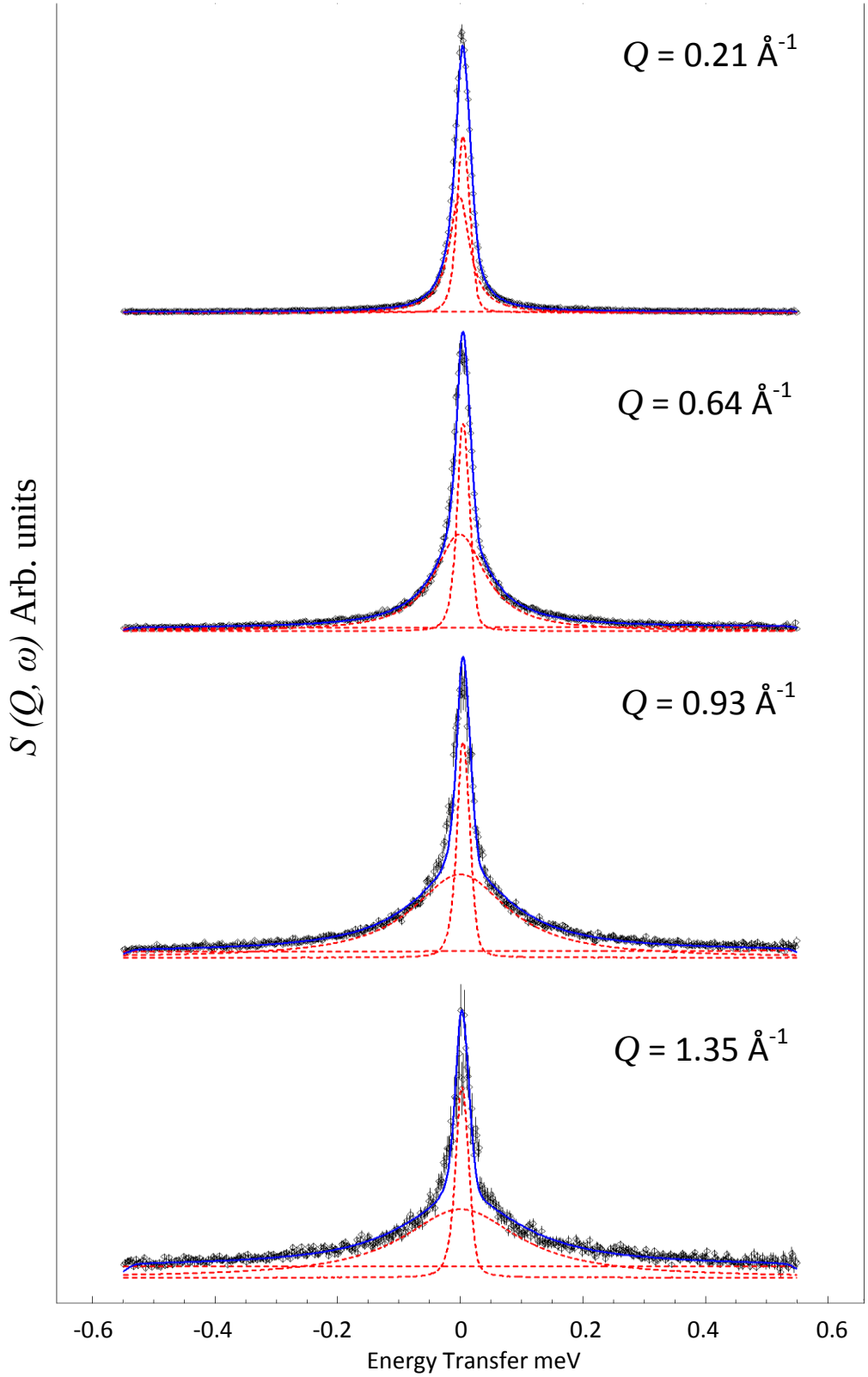

Fig. 6.21. S(Q,ω) at 4 Q values for methanol in HY at 400 K. 1 Lorentzian quasielastic component is observable.

All QENS spectra obtained in this chapter can be found at the following webpage: https://www.dropbox.com/sh/da8cc2xwdz8oip9/AAAke_hGU9nTSR_N-wVE1u8Ca?dl=0.

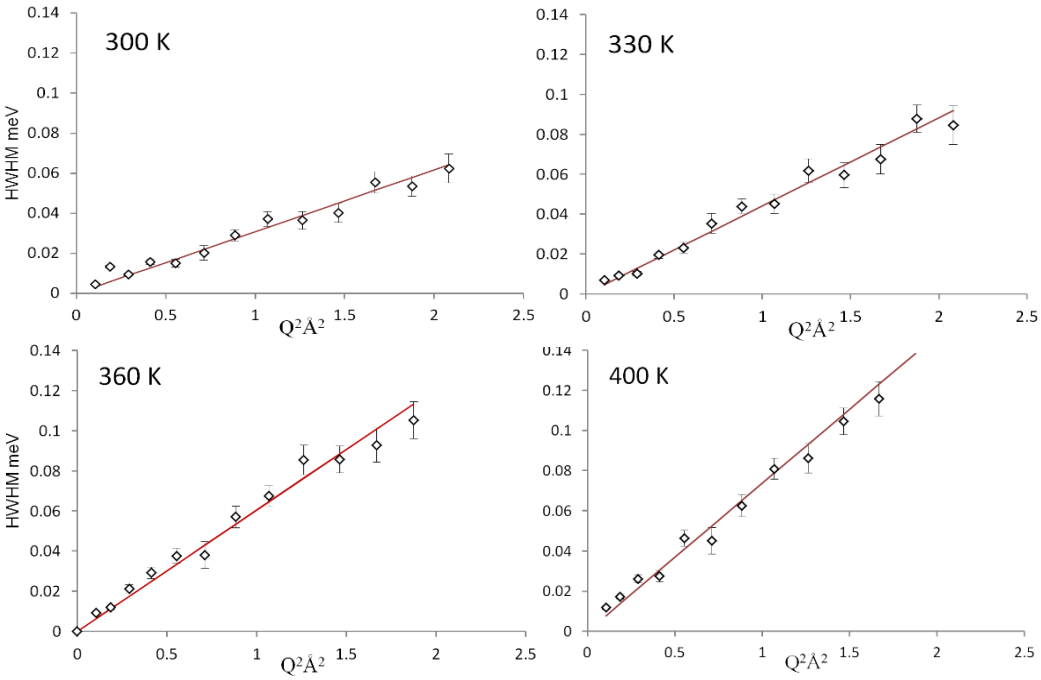

Fig 6.22. Q dependencies of the HWHM of the Lorentzian component of each QENS spectrum for methanol in HY at all 4 temperatures. The linear dependence with Q^2 suggests Fickian diffusion.

T K	QENS (present work)	MD in siliceous Y (ref 48)	MD in NaY (ref 48)	PFG-NMR NaX (ref 46)	Tracer ZLC in NaX (ref 47)
300	2.05×10^{-10} $\pm 0.32 \times 10^{-10}$	-	-	-	-
330	2.9×10^{-10} $\pm 0.56 \times 10^{-10}$	-	-	-	-
350	-	8×10^{-9}	-	-	-
360	4×10^{-10} $\pm 0.93 \times 10^{-10}$	-	-	-	-
373	-	-	-	6×10^{-11}	7×10^{-11}
400	4.9×10^{-10} $\pm 1.2 \times 10^{-10}$	1×10^{-8}	4.7×10^{-11}	-	-
Ea kJ mol^{-1}	8.8	5.8	24	14	-

Table 6.5. Diffusion coefficients and activation energies of diffusion between 300 – 400 K measured by different methods including the QENS measurements in the current study. All diffusion coefficients in units of m^2s^{-1} .

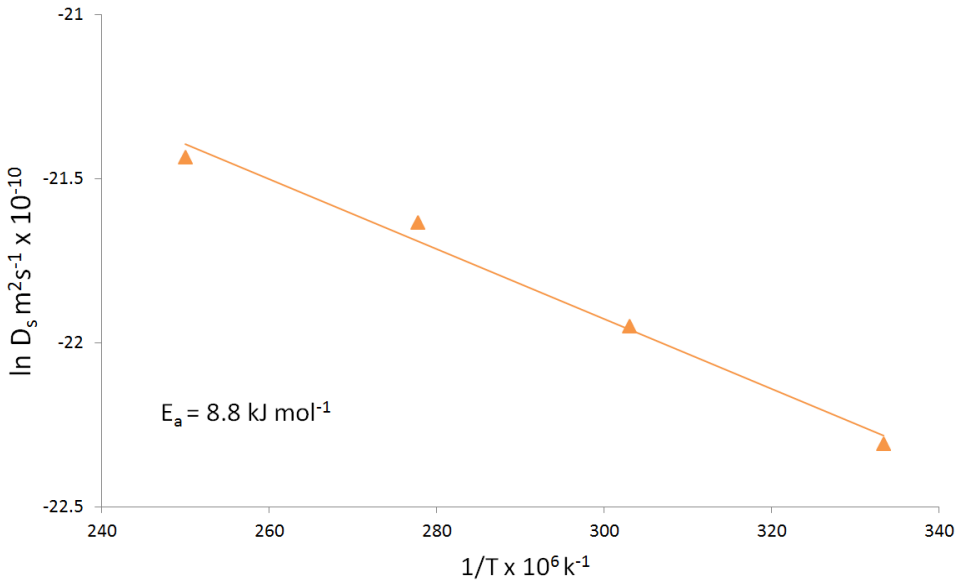

Fig. 6.23. Arrhenius plot for methanol in HY from diffusion coefficients measured by QENS.

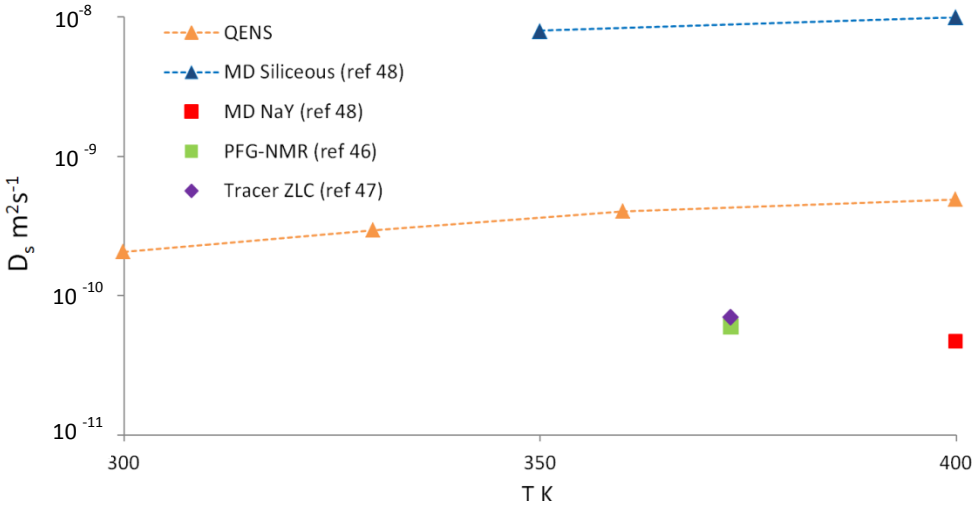

Fig. 6.24. Plot of diffusion coefficients between 300 – 400 K measured by different methods including the QENS measurements in the current study.

The less hindered diffusion in HY is also illustrated by the lower activation energy of diffusion from our QENS studies than the experimental studies in NaX and simulations in low silica NaY. We note also that our QENS measurements result in diffusion coefficients lower than previous MD simulations in siliceous faujasite by a factor of 20 at ~360 K and 400 K. This discrepancy is reasonable given the lack of

proton sites in the siliceous MD simulation, removing the potential for favorable H-bonding between the methanol OH groups and the Brønsted acid sites (or terminal hydroxyls) present in the aluminated structure. When the removal of this H-bonding potential is combined with the use of a perfect zeolite crystal in the simulations, where defects and grain boundaries on the scale of a few nanometres would hinder diffusion in a real sample, the discrepancy appears to be of an expected magnitude. Importantly, the methanol loading is not the same between our QENS studies and the previous MD simulations (4 molecules per unit cell and 8 molecules per unit cell respectively).

Future work will involve MD simulations, using matching loadings and Si/Al ratio to the experimental sample. The simulations will be performed in HY (Si/Al = 30) and siliceous faujasite so that the effect of framework hydroxyls on diffusivity can be quantified with consistent loadings. However, we note that defects such as silanol nests will be present in the experimental sample.

6.3.3 Summary and Conclusions

We report the first microscopic measurement of methanol diffusion in zeolite HY using quasielastic neutron scattering. Measurements between 300 – 400 K gave diffusion coefficients between 2–5 x 10^{-10} m^2s^{-1} giving an activation energy of 8.8 kJ mol^{-1}. The diffusion coefficients measured were higher by a factor of ~ 20 than previous PFG-NMR and ZLC measurements in zeolite NaX (and lower activation energies than PFG-NMR experiments and MD simulations in low silica NaY), attributable to the high density of Na^+ counterions which hinder diffusion, not present in a high silica HY sample. The QENS measurements also gave diffusion coefficients that are higher by a factor of 5 (and a lower activation energy) than MD simulations performed previously in siliceous faujasite, which we expect is due to the potential for favourable H-bonding between the methanol and framework hydroxyls in the experimental sample. It is also noted that the loadings between this study and the previous studies are not consistent. For this reason future MD

simulations will complement our QENS studies with consistent loadings, comparing diffusivity in HY and siliceous faujasite.

The work in this section is currently under review for publication in Physical Chemistry and Chemical Physics.

References

(1) Chang, C. D.; Silvestri, A. J. *Journal of Catalysis* **1977**, *47*, 249.
(2) Maiden, C. *Studies in Surface Science and Catalysis* **1988**, *36*, 1.
(3) Olsbye, U.; Svelle, S.; Bjørgen, M.; Beato, P.; Janssens, T. V.; Joensen, F.; Bordiga, S.; Lillerud, K. P. *Angewandte Chemie International Edition* **2012**, *51*, 5810.
(4) Shah, R.; Gale, J. D.; Payne, M. C. *The Journal of Physical Chemistry* **1996**, *100*, 11688.
(5) Blaszkowski, S. R.; van Santen, R. A. *The Journal of Physical Chemistry B* **1997**, *101*, 2292.
(6) Sinclair, P. E.; Catlow, C. R. A. *Journal of the Chemical Society, Faraday Transactions* **1997**, *93*, 333.
(7) Jiang, Y.; Hunger, M.; Wang, W. *Journal of the American Chemical Society* **2006**, *128*, 11679.
(8) Wang, W.; Jiang, Y.; Hunger, M. *Catalysis Today* **2006**, *113*, 102.
(9) Jiang, Y.; Wang, W.; Marthala, V. R.; Huang, J.; Sulikowski, B.; Hunger, M. *Journal of Catalysis* **2006**, *238*, 21.
(10) Blaszkowski, S. R.; van Santen, R. A. *Journal of the American Chemical Society* **1997**, *119*, 5020.
(11) Cui, Z.-M.; Liu, Q.; Bain, S.-W.; Ma, Z.; Song, W.-G. *The Journal of Physical Chemistry C* **2008**, *112*, 2685.
(12) Forester, T. R.; Wong, S.-T.; Howe, R. F. *J. Chem. Soc., Chem. Commun.* **1986**, 1611.
(13) Forester, T.; Howe, R. *Journal of the American Chemical Society* **1987**, *109*, 5076.
(14) Kubelková, L.; Nováková, J.; Nedomová, K. *Journal of Catalysis* **1990**, *124*, 441.
(15) Salehirad, F.; Anderson, M. W. *Journal of Catalysis* **1998**, *177*, 189.
(16) Tsiao, C.; Corbin, D. R.; Dybowski, C. *Journal of the American Chemical Society* **1990**, *112*, 7140.
(17) Wang, W.; Buchholz, A.; Seiler, M.; Hunger, M. *Journal of the American Chemical Society* **2003**, *125*, 15260.
(18) Ono, Y.; Mori, T. *Journal of the Chemical Society, Faraday Transactions 1: Physical Chemistry in Condensed Phases* **1981**, *77*, 2209.
(19) Salvador, P.; Kladnig, W. *Journal of the Chemical Society, Faraday Transactions 1: Physical Chemistry in Condensed Phases* **1977**, *73*, 1153.
(20) Zicovich-Wilson, C.; Viruela, P.; Corma, A. *The Journal of Physical Chemistry* **1995**, *99*, 13224.
(21) Blaszkowski, S.; Van Santen, R. *The Journal of Physical Chemistry* **1995**, *99*, 11728.
(22) Blaszkowski, S. R.; van Santen, R. A. *Journal of the American Chemical Society* **1996**, *118*, 5152.
(23) Tajima, N.; Tsuneda, T.; Toyama, F.; Hirao, K. *Journal of the American Chemical Society* **1998**, *120*, 8222.

(24) Andzelm, J.; Govind, N.; Fitzgerald, G.; Maiti, A. *International Journal of Quantum Chemistry* **2003**, *91*, 467.
(25) Haase, F.; Sauer, J.; Hutter, J. *Chemical Physics Letters* **1997**, *266*, 397.
(26) Jones, A. J.; Iglesia, E. *Angewandte Chemie International Edition* **2014**, *53*, 12177.
(27) Brogaard, R. Y.; Henry, R.; Schuurman, Y.; Medford, A. J.; Moses, P. G.; Beato, P.; Svelle, S.; Nørskov, J. K.; Olsbye, U. *Journal of Catalysis* **2014**, *314*, 159.
(28) Cairon, O. *ChemPhysChem* **2013**, *14*, 244.
(29) Cairon, O.; Lavalley, J.-C. *Journal of the Chemical Society, Faraday Transactions* **1998**, *94*, 3039.
(30) Cairon, O.; Thomas, K.; Chevreau, T. *Microporous and Mesoporous Materials* **2001**, *46*, 327.
(31) Li, S.; Huang, S.-J.; Shen, W.; Zhang, H.; Fang, H.; Zheng, A.; Liu, S.-B.; Deng, F. *The Journal of Physical Chemistry C* **2008**, *112*, 14486.
(32) Silaghi, M.-C.; Chizallet, C.; Raybaud, P. *Microporous and Mesoporous Materials* **2014**, *191*, 82.
(33) Janin, A.; Maache, M.; Lavalley, J.; Joly, J.; Raatz, F.; Szydlowski, N. *Zeolites* **1991**, *11*, 391.
(34) Menezes, S.; Camorim, V.; Lam, Y.; San Gil, R.; Bailly, A.; Amoureux, J. *Applied Catalysis A: General* **2001**, *207*, 367.
(35) Telling, M. T.; Andersen, K. H. *Physical Chemistry Chemical Physics* **2005**, *7*, 1255.
(36) Azuah, R. T.; Kneller, L. R.; Qiu, Y.; Tregenna-Piggott, P. L.; Brown, C. M.; Copley, J. R.; Dimeo, R. M. *Journal of Research of the National Institute of Standards and Technology* **2009**, *114*, 341.
(37) http://www.isis.stfc.ac.uk/instruments/maps/maps4739.html
(38) Parker, S. F.; Lennon, D.; Albers, P. W. *Applied Spectroscopy* **2011**, *65*, 1325.
(39) Segall, M.; Lindan, P. J.; Probert, M. A.; Pickard, C.; Hasnip, P.; Clark, S.; Payne, M. *Journal of Physics: Condensed Matter* **2002**, *14*, 2717.
(40) Perdew, J. P.; Wang, Y. *Physical Review B* **1992**, *45*, 13244.
(41) Pfrommer, B. G.; Côté, M.; Louie, S. G.; Cohen, M. L. *Journal of Computational Physics* **1997**, *131*, 233.
(42) Refson, K.; Tulip, P. R.; Clark, S. J. *Physical Review B* **2006**, *73*, 155114.
(43) Ramirez-Cuesta, A. *Computer Physics Communications* **2004**, *157*, 226.
(44) Volino, F.; Dianoux, A.; Hervet, H. *Le Journal de Physique Colloques* **1976**, *37*, C3.
(45) Jobic, H.; Renouprez, A.; Bee, M.; Poinsignon, C. *The Journal of Physical Chemistry* **1986**, *90*, 1059.
(46) Lesthaeghe, D.; Van Speybroeck, V.; Marin, G. B.; Waroquier, M. *Industrial & Engineering Chemistry Research* **2007**, *46*, 8832.
(47) Hemelsoet, K.; Van der Mynsbrugge, J.; De Wispelaere, K.; Waroquier, M.; Van Speybroeck, V. *ChemPhysChem* **2013**, *14*, 1526.
(48) Vetrivel, R.; Catlow, C.; Colbourn, E. *The Journal of Physical Chemistry* **1989**, *93*, 4594.
(49) Gale, J.; Catlow, C.; Carruthers, J. *Chemical PhysicsLletters* **1993**, *216*, 155.
(50) Sinclair, P.; Catlow, C. *Journal of the Chemical Society, Faraday Transactions* **1996**, *92*, 2099.
(51) Gale, J.; Shah, R.; Payne, M.; Stich, I.; Terakura, K. *Catalysis Today* **1999**, *50*, 525.
(52) Berger, D.; Logsdail, A. J.; Oberhofer, H.; Farrow, M. R.; Catlow, C. R. A.; Sherwood, P.; Sokol, A. A.; Blum, V.; Reuter, K. *The Journal of Chemical Physics* **2014**, *141*, 024105.
(53) Sokol, A. A.; Bromley, S. T.; French, S. A.; Catlow, C. R. A.; Sherwood, P. *International Journal of Quantum Chemistry* **2004**, *99*, 695.

(54) Artioli, G.; Lamberti, C.; Marra, G. *Acta Crystallographica Section B: Structural Science* **2000**, *56*, 2.
(55) Hriljac, J.; Eddy, M.; Cheetham, A.; Donohue, J.; Ray, G. *Journal of Solid State Chemistry* **1993**, *106*, 66.
(56) Sherwood, P.; de Vries, A. H.; Guest, M. F.; Schreckenbach, G.; Catlow, C. R. A.; French, S. A.; Sokol, A. A.; Bromley, S. T.; Thiel, W.; Turner, A. J. *Journal of Molecular Structure: THEOCHEM* **2003**, *632*, 1.
(57) Nachtigallova, D.; Nachtigall, P.; Bludský, O. *Physical Chemistry Chemical Physics* **2004**, *6*, 5580.
(58) Sherwood, P.; de Vries, A. H.; Collins, S. J.; Greatbanks, S. P.; Burton, N. A.; Vincent, M. A.; Hillier, I. H. *Faraday Discussions* **1997**, *106*, 79.
(59) Hill, J.-R.; Sauer, J. *The Journal of Physical Chemistry* **1995**, *99*, 9536.
(60) Ahlrichs, R.; Taylor, P. *Journal De Chimie Physique Et De Physico-Chimie Biologique* **1981**, *78*, 315.
(61) Becke, A. D. *The Journal of Chemical Physics* **1993**, *98*, 5648.
(62) Lee, C.; Yang, W.; Parr, R. G. *Physical Review B* **1988**, *37*, 785.
(63) Vosko, S.; Wilk, L.; Nusair, M. *Canadian Journal of Physics* **1980**, *58*, 1200.
(64) Stephens, P.; Devlin, F.; Chabalowski, C.; Frisch, M. J. *The Journal of Physical Chemistry* **1994**, *98*, 11623.
(65) Wilson, P. J.; Bradley, T. J.; Tozer, D. J. *The Journal of Chemical Physics* **2001**, *115*, 9233.
(66) Guest*, M. F.; Bush, I. J.; Van Dam, H. J.; Sherwood, P.; Thomas, J. M.; Van Lenthe, J. H.; Havenith, R. W.; Kendrick, J. *Molecular physics* **2005**, *103*, 719.
(67) Smith, W.; Yong, C.; Rodger, P. *Molecular Simulation* **2002**, *28*, 385.
(68) Broyden, C. *Mathematics of Computation* **1970**, *24*, 365.
(69) Fletcher, R. *The Computer Journal* **1970**, *13*, 317.
(70) Goldfarb, D. *Mathematics of Computation* **1970**, *24*, 23.
(71) Shanno, D. F. *Mathematics of Computation* **1970**, *24*, 647.
(72) Mortier, W.; Sauer, J.; Lercher, J.; Noller, H. *The Journal of Physical Chemistry* **1984**, *88*, 905.
(73) Sauer, J. *Journal of Molecular Catalysis* **1989**, *54*, 312.
(74) Haase, F.; Sauer, J. *Microporous and Mesoporous Materials* **2000**, *35*, 379.
(75) Jost, W. *The Journal of Chemical Physics* **1933**, *1*, 466.
(76) Poloni, R.; Kim, J. *J. Mater. Chem. C* **2014**, *2*, 2298.
(77) http://vergil.chemistry.gatech.edu/notes/cp.pdf.
(78) Boys, S. F.; Bernardi, F. d. *Molecular Physics* **1970**, *19*, 553.
(79) Meunier, F.; Gray, P.; Kärger, J.; Xu, Z.; Ruthven, D. *Zeolites* **1994**, *14*, 242.
(80) Brandani, S.; Ruthven, D. M. *Zeolites* **1995**, *15*, 494.
(81) Plant, D.; Maurin, G.; Bell, R. *The Journal of Physical Chemistry B* **2006**, *110*, 15926.
(82) Plant, D. F.; Maurin, G.; Bell, R. G. *The Journal of Physical Chemistry B* **2007**, *111*, 2836.
(83) Maurin, G.; Plant, D.; Henn, F.; Bell, R. G. *The Journal of Physical Chemistry B* **2006**, *110*, 18447.
(84) Nanok, T.; Vasenkov, S.; Keil, F. J.; Fritzsche, S. *Microporous and Mesoporous Materials* **2010**, *127*, 176.
(85) DeCanio, S. J.; Sohn, J. R.; Fritz, P. O.; Lunsford, J. H. *Journal of Catalysis* **1986**, *101*, 132.
(86) Nováková, J.; Kubelková, L.; Dolejšek, Z. *Journal of Catalysis* **1987**, *108*, 208.

Chapter 7

Diffusion of Cyclohexanone Oxime in Microporous Acidic Catalysts

Though quantitative diffusion studies of reaction species inside microporous catalysts have received attention for commercial processes, incorporation of these studies into the design of microporous catalytic processes is rare. In this chapter we present a contribution to a larger project designing sustainable nylon production processes through the Beckmann rearrangement of cyclohexanone oxime to ε-caprolactam (the precursor to polymer nylon 6), using acidic microporous catalysts. The diffusion behaviour of cyclohexanone oxime is studied using quasielastic neutron scattering in microporous catalysts H-ZSM-5, HY and recently developed SAPO-37. We find very interesting differences in the diffusion behaviour of the oxime between HY and SAPO-37, despite their sharing the same faujasite framework topology, potentially connected to their very different catalytic capabilities.

7.1 Introduction

The work in this thesis so far has focused on systems relevant to the petrochemical industry such as fluid catalytic cracking and the methanol-to-hydrocarbons processes. However, the use of solid-acid catalysts is desirable for industries such as nylon production. The precursor to nylon 6 is ε-caprolactam, which is formed by via the Beckmann rearrangement of cyclohexanone oxime, shown below. Conventional routes to nylon production suffer from drawbacks such as the use of mineral and Friedel Crafts acids (bringing safety and disposal concerns), side and waste product formation, leading to environmental issues and a large number of reaction steps in the process, all of which have contributed to interest in the use of solid acid catalysts.[1]

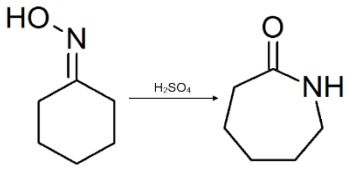

Fig. 7.1. The Beckmann rearrangement forming ε-caprolactam from cyclohexanone oxime.

The Beckmann rearrangement was carried out using MFI zeolites in the vapour phase at 300 °C.[2-4] However, use of the liquid phase has been recently patented, with a reaction temperature 130 °C in the faujasite silicoaluminophosphate SAPO-37, giving yields of 98 mol% at this temperature.[5] Studies into the behaviour of the active sites and their interaction with the reactants have taken place in MFI,[6] with one concluding that the steric hindrance of the smaller pore of ZSM-5 causes the formation of ε-caprolactam to take place on the external surface of the crystal.[7] To understand better the dynamics associated with the vapour-phase Beckmann rearrangement, the diffusion of the reactant cyclohexanone oxime is measured in H-ZSM-5, and to understand the dynamics associated with the liquid-phase Beckmann rearrangement, diffusion measurements are carried out in zeolite HY and SAPO-37. No catalytic activity is observed in zeolite HY compared to the high activity in the structurally analogous SAPO-37, suggesting that activity should not be

diffusion limited. However we observe marked differences in the diffusion behaviour of the oxime between the two faujasite catalysts.

7.2 Methodology

7.2.1. Sample Preparation

The SAPO-37 samples were synthesised by M.E. Potter and S. H. Newland at the University of Southampton. The synthesis procedure was that used in reference 5. Pseudo-boehmite was added to the mixture of phosphoric acid and water (85% phosphoric acid). The mixture was then stirred for 7 h. Fumed silica was slowly added to a stirred solution of TPAOH and TMAOH · $5H_2O$, and was stirred for 2 h before adding to the Pseudo-boehmite/phosphoric acid mixture. The gel was stirred for 68 h before it was transferred to a Teflon-lined tube, sealed inside a stainless-steel autoclave that was put in an oven at 200 °C for 24 h. The contents were then centrifuged, filtered and washed with deionized water. The material was dried overnight at room temperature. For activation, the white solid was then calcined at 550 °C for 8 h and stored under an inert atmosphere. The HY samples were obtained from Zeolyst International (Si/Al = 30) and received originally in the acidic HY form, steam dealuminated to this composition. The ZSM-5 samples were also obtained from Zeolyst International (Si/Al = 30) and received originally in the NH_4 – ZSM-5 form. These were activated to the catalytic H-ZSM-5 form by heating to 798 K for 4 hours, with a heating rate from room temperature of 5 K/min. The powder X-ray diffraction pattern of all zeolites can be found in Appendix B.

The zeolite and SAPO-37 samples were then dehydrated at 120˚C under flowing helium for 4 hours. After cooling to room temperature, a homogenous physical mixture of the oxime and each catalyst was made in a glovebox under argon of 1:10 weight ratio of oxime to catalyst. The samples (4.5 grams in total) were transferred inside a glovebox under argon to thin walled aluminium containers of annular geometry.

7.2.2. Quasielastic Neutron Scattering Experiments

As in the previous two chapters, all measurements were performed using the time-of-flight backscattering neutron spectrometer OSIRIS[8] detailed in section 2.5.5.2 at the ISIS Pulsed Neutron and Muon Source. The cells were placed in a top-loading closed cycle refrigerator cryostat so that a resolution measurement could be taken at a base temperature of 6 K. QENS measurements were then taken at 373, 383 and 393 K in a Q range of 0.2 – 1.6 $Å^{-1}$. Graphite (002) analyser crystals were used to give an energy resolution of 24.5 μeV with energy transfers measured in a window of ±0.55 meV. The signal taken from an empty zeolite was taken pre-loading and then subtracted from the signal of the loaded zeolite so that only the signal from the oxime was measured. All QENS spectra were fitted using the neutron analysis software DAVE.[9]

7.3 Results and Discussion

It is important first to note that a very narrow temperature range of 373-393 K is measured, because 363 K is the melting temperature of the cyclic oxime, and 403 K is the observed reaction temperature of the oxime to ε-caprolactam. The narrow temperature range means that any activation energies calculated must be treated with caution.

The QENS spectra of the cyclic oxime in H-ZSM-5 at 373 K are shown in figure 7.2, at 4 Q values between 0.43 and 1.53 $Å^{-1}$. A very close fit to the resolution function at lower Q values is observed with no observable quasielastic component. This suggests that no diffusion is observable over the time and length scales accessible to the spectrometer at these temperatures. A minimal Lorentzian component can be fitted at higher Q values, the HWHM of which is independent of Q, possibly indicative of rotational motion. However, the magnitude of this component is too small for reliable analysis. The most probable reason is that the channel dimensions (5.5 Å) are too small to allow diffusion of the bulky cyclic oxime, even at elevated temperatures.

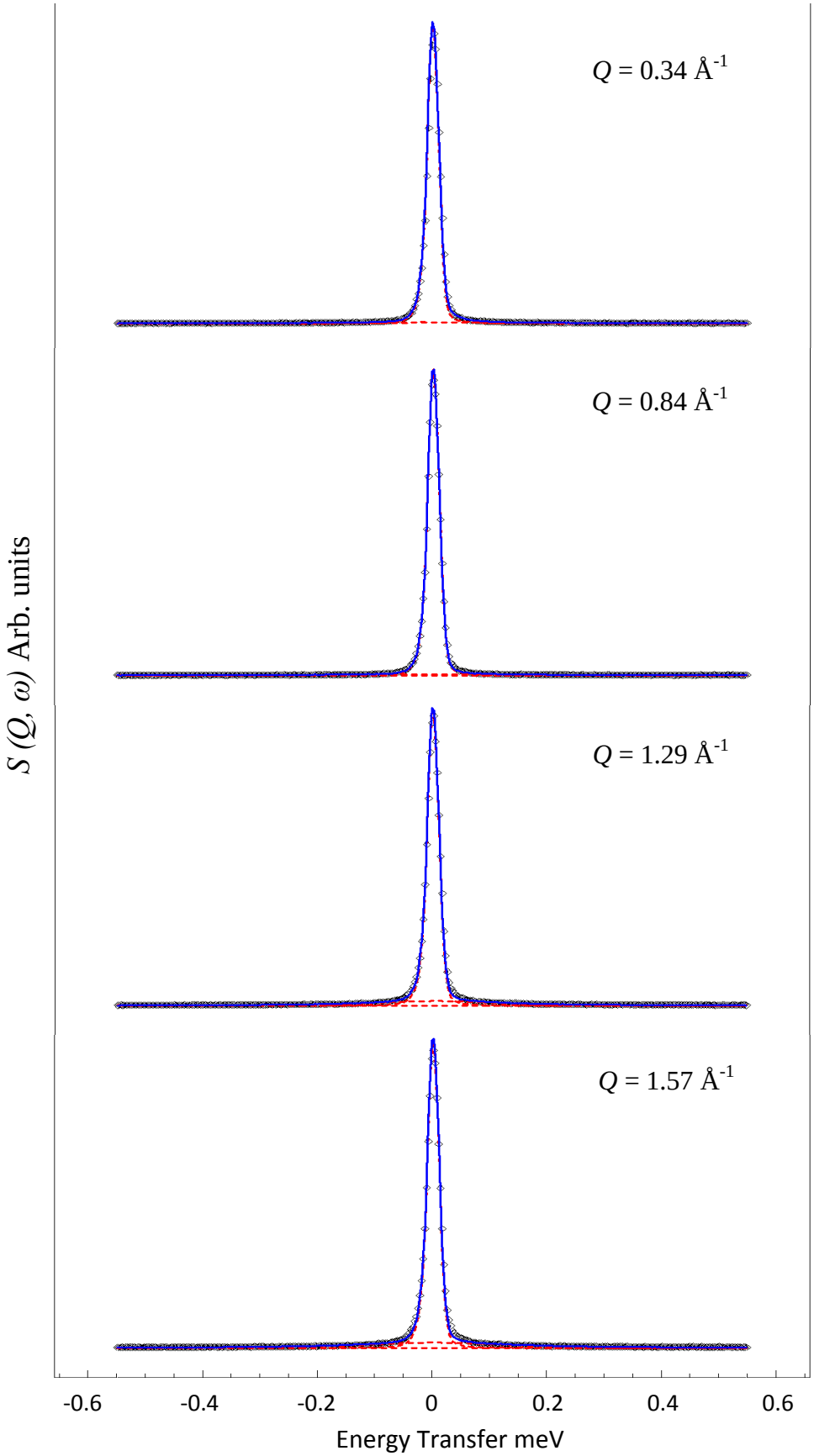

Fig 7.2. QENS spectra obtained for the cyclic oxime diffusing in H-ZSM-5 at 4 different *Q* values at 373 K. (--) is the total fit. 1 very small Lorentzian component is observed at higher *Q* values.

The lack of movement could correlate with the lack of catalytic activity in the liquid phase Beckmann rearrangement in H-ZSM-5, corresponding to a potentially diffusion limited reaction. This adherence to the resolution function was observed at all temperatures.

Spectra obtained for the cyclic oxime in both zeolite HY and SAPO-37 for 4 Q values between 0.43 - 1.53 $Å^{-1}$ at 373 K are depicted in figure 7.3 and 7.4 respectively. All spectra could be fitted with a resolution function, a single Lorentzian function describing the quasielastic component and a flat background. As shown in figure 7.3, the Lorentzian component of the spectra obtained for zeolite HY showed continuous broadening, consistent with a DQ^2 dependence associated with free Fickian diffusion, unlike SAPO-37 which showed broadening up until a Q value of ~1.2 $Å^{-1}$ followed by a deviation from the linear increase in HWHM with Q^2. This deviation is consistent with a jump diffusion mechanism illustrated by the Q dependence of HWHM plotted in figure 7.5. The Q dependences of the HWHM are shown for the cyclic oxime in both HY and SAPO-37 at all temperatures in figure 7.5. We observe that at 373 K, the HWHM broadening in zeolite HY shows a DQ^2 dependence, consistent with free Fickian diffusion; the diffusion coefficient was calculated at 2 x 10^{-10} m^2s^{-1} shown in table 7.1, whereas in SAPO-37 at 373 K the Q dependence fits with the Chudley-Elliot model for jump diffusion (used previously to describe diffusion of benzene in NaY)[10] with a jump distance of 4.5 Å and a residence time of 50 ps. Though 4.5 Å seems like a small distance, it matches the length of a window region within the faujasite structure, it is possible therefore that the oxime is residing in one supercage before jumping into a neighbouring cage. The diffusion coefficient rises between 373-393 K in HY to 3 x 10^{-10} m^2/s^{-1}. This leads to an Arrhenius plot giving an activation energy of 24.7 kJ mol^{-1}. The difference in diffusion behaviour at 373 K between HY and SAPO-37, may be related to the difference in catalytic activity. The tendency of the oxime to reside for longer periods in certain areas of the framework in the more active SAPO-37 catalyst may yield a higher chance of conversion than the inferior HY catalyst, which allows free diffusion of the reactant and no detectable residence time.

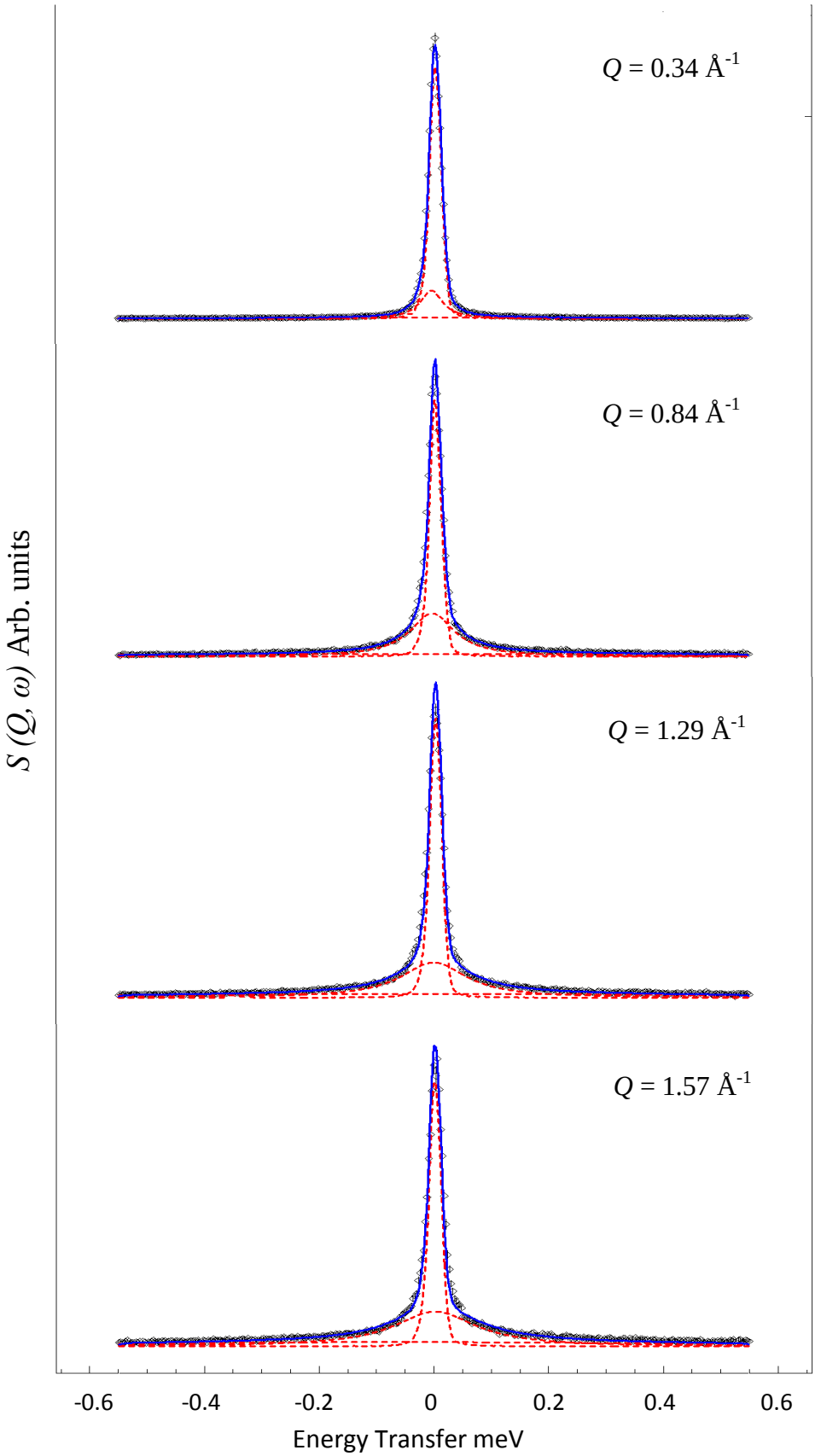

Fig 7.3. QENS spectra obtained for the cyclic oxime diffusing in zeolite HY at 4 different *Q* values at 373 K. (**--**) represents the total fit. A single Lorentzian component is observed at all *Q* values.

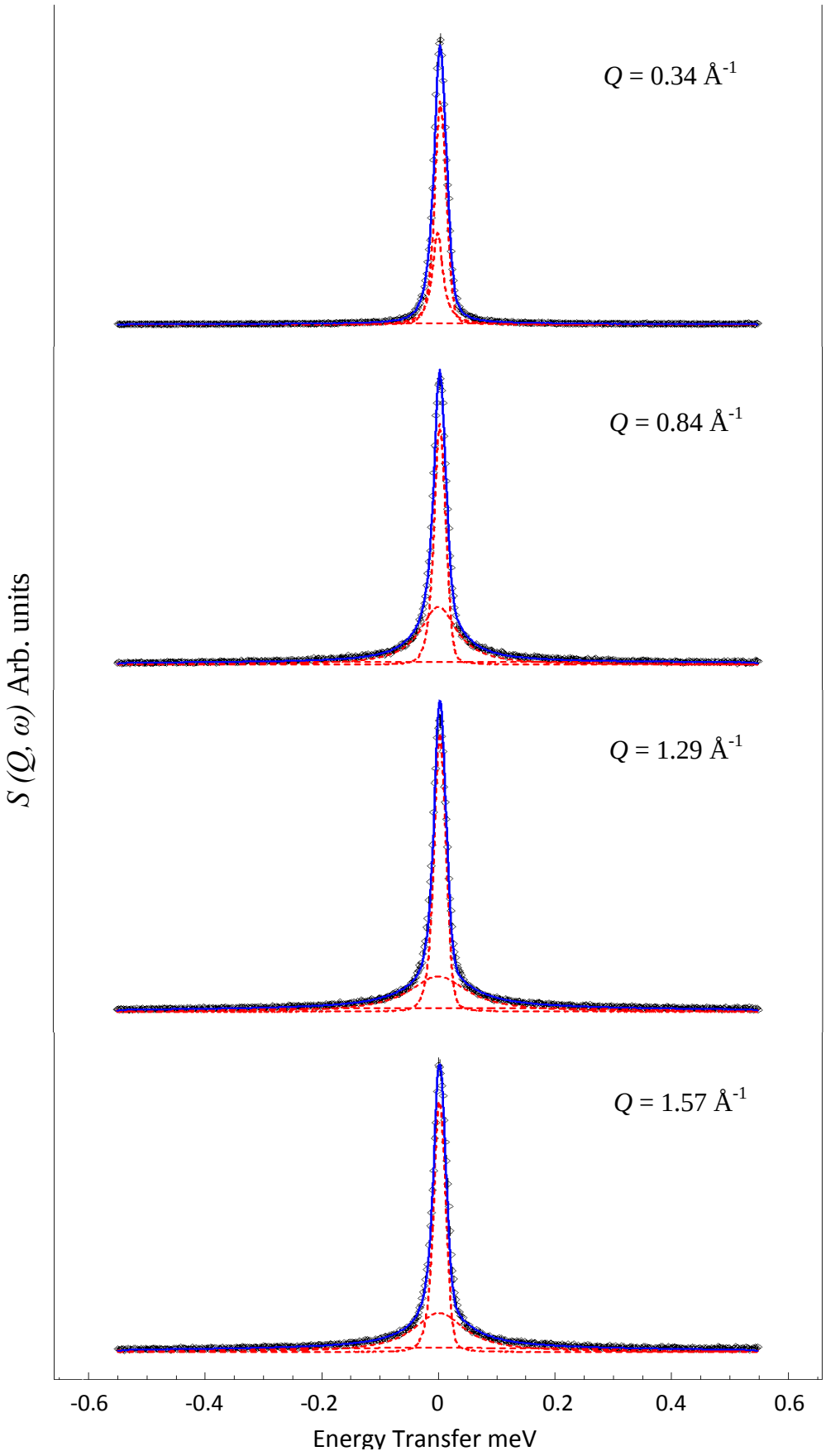

Fig 7.4. QENS spectra obtained for the cyclic oxime diffusing in SAPO-37 at 4 different *Q* values at 373 K. (**--**) represents the total fit, a single Lorentzian component is observed at all *Q* values.

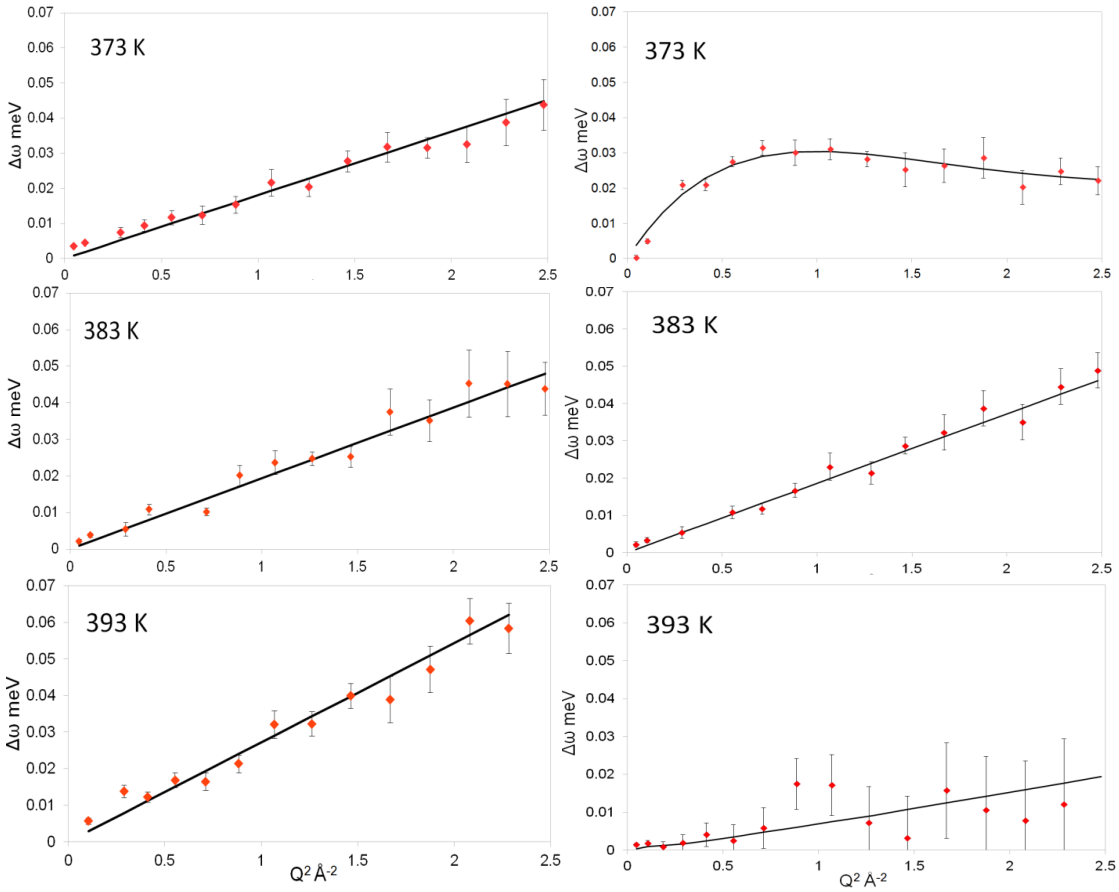

Fig. 7.5. The Q dependence of the HWHM of the Lorentzian for zeolite HY (left) and SAPO-37 (right) at 373, 383 and 393 K.

In SAPO-37 at 383 K, Fickian diffusion is observed, with measured a diffusion coefficient of 2.05 x 10^{-10} m^2s^{-1}, which is very similar to the value in zeolite HY of 2.14 x 10^{-10} m^2s^{-1}. However at 393 K a very poor fit to the theoretical Fickian DQ^2 dependence is observed. An attempt at a DQ^2 dependence gives a significant slowing in the average diffusion coefficient. However due to the large errors, the fit and therefore the D_s value in table 7.1 is not reliable. A possible explanation for any reduction in the observed diffusion coefficient is that the temperature is close to the reaction temperature, with the formation of ε-caprolactam observed at 403 K. Another possibility is that a significant number of cyclic oxime molecules could be immobilised having formed a bound state as a stable intermediate, requiring further activation to undergo product formation. Observing any immobilisation of the reactant at 393 K in the superior catalyst may also give an insight into the energetics of the reaction, and an observation of any bound species could give insight into the nature of the reaction mechanism itself.

T	373 K	383 K	393 K	E_a kJ mol^{-1}
Zeolite Y	1.9×10^{-10} $\pm 0.26 \times 10^{-10}$	2.14×10^{-10} $\pm 0.35 \times 10^{-10}$	3.00×10^{-10} $\pm 0.6 \times 10^{-10}$	24.7
SAPO-37	-	2.05×10^{-10} $\pm 0.32 \times 10^{-10}$	0.84×10^{-10} $\pm 0.7 \times 10^{-10}$	-

Table 7.1. Fickian diffusion coefficients of cyclohexanone oxime at all temperatures in zeolite HY and SAPO-37, all diffusion coefficients in units of m^2s^{-1}.

Future work to understand the mechanism necessitates studying the vibrational spectra of these systems to observe any changes at the temperature of interest mainly in the OH vibrational region, to observe a protonated or bound cyclic oxime, or the formation of ε-caprolactam. An important distinction would be the difference in the OH vibrations of the catalysts themselves at all temperatures. Changes observed in this region could give further insight into framework/sorbate interactions, perhaps justifying the residence times observed, illustrating further possible reasons for enhanced catalytic activity in SAPO–37 despite sharing the same framework topology with zeolite HY.

All QENS spectra relevant to this chapter can be found at the following webpage: https://www.dropbox.com/sh/9jutpj396h3vz5y/AAAUcUdUr5c1DWIv0fkRy68ca?dl=0

7.3 Summary and Conclusions

The diffusion of cyclohexanone oxime in zeolites H-ZSM-5, H-Y and SAPO-37 was studied using quasielastic neutron scattering at temperatures between 373 and 393 K. No observable diffusion was found at any temperature in H-ZSM-5, consistent with a lack of catalytic activity in the liquid-phase Beckmann rearrangement due to diffusion limitations. Zeolite HY showed free Fickian diffusion at all temperatures between 373 and 393 K with self-diffusivities between 2-3 x 10^{-10} m^2s^{-1} giving an activation energy of 24.7 kJ mol^{-1} (though this narrow temperature range of measurements means that the activation energy value should be treated with

caution). However, in SAPO-37, jump diffusion was observed at 373 K, with a residence time of 50 ps and a jump distance of 4.5 Å. Fickian diffusion was observed at 383 K with a diffusion coefficient almost identical to that in zeolite HY, and at 393 K the diffusion was very difficult to characterise, with a very poor fit to a DQ^2 dependence. This possible dependence indicated a significant slowing of diffusion, probably caused by ε-caprolactam formation at this temperature, or immobilisation of a large amount of the oxime. The immobilisation is perhaps due to binding to the zeolite framework, or the formation of the bulkier ε-caprolactam consistent with observation of high catalytic activity in SAPO-37. The observation of jump diffusion at 373 K in SAPO-37 could also be linked to the superior catalytic activity, where the tendency of the oxime to reside for longer periods may yield a higher chance of conversion than the inferior HY catalyst. Vibrational spectroscopy experiments have been proposed to investigate which species are present at different temperatures, and understand interactions of the oxime with the hydroxyl groups in each zeolite.

References

(1) Bellussi, G.; Perego, C. *Cattech* **2000**, *4*, 4.
(2) Heitmann, G.; Dahlhoff, G.; Hölderich, W. *Journal of Catalysis* **1999**, *186*, 12.
(3) Izumi, Y.; Ichihashi, H.; Shimazu, Y.; Kitamura, M.; Sato, H. *Bulletin of the Chemical Society of Japan* **2007**, *80*, 1280.
(4) Forni, L.; Fornasari, G.; Giordano, G.; Lucarelli, C.; Katovic, A.; Trifiro, F.; Perri, C.; Nagy, J. *Physical Chemistry Chemical Physics* **2004**, *6*, 1842.
(5) A. B. Levy, R. R., M. E. Potter, WO Patent, WO 2013063244 A1. .
(6) Flego, C.; Dalloro, L. *Microporous and Mesoporous Materials* **2003**, *60*, 263.
(7) Yashima, T.; Miura, K.; Komatsu, T. *Studies in Surface Science and Catalysis* **1994**, *84*, 1897.
(8) Telling, M. T.; Andersen, K. H. *Physical Chemistry Chemical Physics* **2005**, *7*, 1255.
(9) Azuah, R. T.; Kneller, L. R.; Qiu, Y.; Tregenna-Piggott, P. L.; Brown, C. M.; Copley, J. R.; Dimeo, R. M. *Journal of Research of the National Institute of Standards and Technology* **2009**, *114*, 341.
(10) Jobic, H.; Fitch, A. N.; Combet, J. *The Journal of Physical Chemistry B* **2000**, *104*, 8491.

Chapter 8

Summary, Conclusions and Future Work

The work in this thesis has highlighted the potential of complementary microscopic experimental and simulation studies into the dynamics of hydrocarbons in microporous catalysts, uncovering detailed quantitative and qualitative information about sorbate behaviour in the catalyst of interest. As mentioned, the majority of this work has studied established catalytic systems, while the incorporation of these studies into the catalyst design process is lacking. After summarising the work in this thesis, the present chapter will deal with proposed studies where the techniques mentioned are applied to catalyst development in an attempt to understand molecular behaviour in these systems. These include investigating the diffusion component of the ammonia selective catalytic reduction process in metal doped zeolite chabazite, and benzene hydrogenation in Pt/MCM-41. Other proposed studies utilise the capability of neutrons to study hydrocarbon counter diffusion, through deuteration of certain mixture components. Additional to other diffusion measurements, extension of work carried out in previous chapters involving static energy calculations, and vibrational spectroscopy experiments aiming to explain previously observed dynamical phenomena are proposed.

8.1 Thesis Summary and Conclusions

We have presented the complementary use of neutron scattering techniques and molecular simulations to obtain detailed insight into dynamical behaviour of hydrocarbons in well-established microporous zeolite catalysts. Alkane diffusion in ZSM-5 analogue silicalite was studied using molecular dynamics (MD) simulations and compared with neutron spin echo (NSE) and previous quasielastic neutron scattering (QENS) experiments. Measured diffusion coefficients showed far improved agreement between theory and experiment from previous studies, due to the more accurate framework and hydrocarbon models used. We also uncovered qualitative differences to previous studies in the behaviour of isobutane, and its preferred siting locations in the MFI structure.

The effect of molecular shape on the diffusion of octane isomers in a commercial HY sample was studied using QENS and MD in tandem, owing to its relevance to the fluid catalytic cracking (FCC) process. We observed counterintuitive differences in diffusivity, with the branched isomer 2,5-dimethylhexane diffusing more quickly than *n*-octane. This observation was found to be due to the stronger sorbate-sorbate interactions between *n*-octane upon clustering in the faujasite supercage. This observation highlights the complex relationship between molecular shape, framework structure and sorbate diffusion in microporous catalysts, as it was assumed that branched isomers diffuse more slowly due to increased molecular width as observed in MFI zeolites.

The behaviour of methanol was also studied in zeolites HY and H-ZSM-5, to understand the effect of framework structure on sorbate dynamics relevant to methanol-to-hydrocarbons catalysts. QENS studies showed a lack of methanol mobility in H-ZSM-5, compared to free diffusion in HY. This immobility was found to be due to methoxylation taking place at room temperature in H-ZSM-5, after study with inelastic neutron scattering (INS) and quantum mechanical calculations of vibrational spectra. The observations not only contradict the general assumption that heating is necessary to complete this step, but highlight the strength of complementary neutron scattering studies and quantum mechanical calculations in

deciphering reactive processes in zeolite frameworks. State-of-the art QM/MM embedded cluster calculations were also performed, as part of an ongoing project to quantify energetic differences of the methoxylation process between the two frameworks. So far, the zeolite acidities and adsorption energies of methanol have been measured, suggesting a more acidic HY structure, and detailing favourable methanol adsorption geometries in H-ZSM-5.

We reported the first quantitative microscopic diffusion study to be incorporated into the design of a microporous catalytic process, with QENS measurements investigating the diffusion component of the SAPO-37 catalysed Beckmann rearrangement. It was found that cyclohexanone oxime exhibits differing diffusion behaviour between structural analogues HY and SAPO-37, showing jump diffusion in the active catalyst. This observed residence time may assist the reaction process, giving an insight into how differences in the dynamics of cyclohexanone oxime may correlate with the activity of the faujasite catalyst.

To conclude, neutron scattering methods and molecular simulations have proven to be a very powerful tool for the quantitative and qualitative study of hydrocarbon dynamics in microporous catalysts. With improved models able to simulate diffusion accurately, readily paired with quasielastic neutron scattering methods, and quantum mechanical calculations paired with inelastic vibrational neutron spectroscopy, crucial dynamic processes can be understood in great detail. These advances show the great potential of these methods to benefit well established catalytic processes, and assist in the design of new microporous catalysts.

8.2 Extension of Present Work

Before a discussion of proposed experiments expanding the scope of neutron scattering studies of dynamic processes in catalysis design, the proposed extension of the studies in each chapter will be summarised, although we note that these points are mentioned at the end of each relevant section.

8.2.1 Energetics Governing *n*- and Isoalkane Behaviour

The work in chapter 4 showed some interesting behaviour of longer *n*- alkanes and isobutane in silicalite, such as channel switching of *n*-octane at higher temperatures (in the presence of another *n*-octane molecule in the same channel), and the siting preference of isobutane in the sinusoidal channel system. An energetic understanding for these behaviours is desirable for a reliable explanation, and can be obtained using static energy calculations. Programs such as GULP[1] may be used to create a potential energy profile of the channel switching process, and comparing the potential energies of isobutane sitings in different channel sections. These static energy calculations are also necessary to explain the phenomenon observed in chapter 5 of decreased *n*-octane diffusion compared to 2,5-dimethylhexane in zeolite HY. The favourability of the sorbate-sorbate interactions governing the clustering process can be probed by comparing the difference in energy between the isolated octane isomers and that after clustering. A significant difference between the two isomers could be expected to dictate the mobility difference.

8.2.2 Energetics of Methoxylation in Zeolites

The methoxylation behaviour observed in H-ZSM-5 in chapter 6 can be expanded upon (spectroscopically) predominantly in two ways. One could first probe the development of this system as a function of temperature. At elevated temperatures one would observe carbon-carbon bond formation allowing probing of the 'hydrocarbon pool' present in MTH/MTO catalysis.[2] One could also probe the methoxylation process, and the energetics thereof inside differing zeolite frameworks such as mordenite, ferrierite, beta or chabazite, allowing for a valid comparison of framework topology effects on methoxylation energetics in zeolites. Another interesting development would be to assess the methoxylation capability as a function of Si/Al ratio in H-ZSM-5, giving an insight into the activity as a function of zeolite composition. The variation of framework topology can also be investigated in the embedded cluster simulations comparing energetics directly. It was mentioned at the end of section 6.2 that the mechanism of methoxylation

investigated using embedded cluster calculations must be probed with two methanol molecules in the zeolite pore. Previous simulations have shown that the barrier to methoxylation is significantly reduced in the presence of another methanol molecule. [3]

8.2.3 Methanol Diffusion in HY

Molecular dynamics simulations would be desirable to complement the QENS experiments studying methanol diffusion in HY in section 6.3. MD simulations will be performed of methanol in a HY supercell of Si/Al = 30, aiming to measure the diffusivity, and explore the hydrogen bonding characteristics with the acidic hydroxyl site and their effect on methanol mobility. Simulations are also planned for a fully siliceous supercell to quantify directly the effect of acidic hydroxyl presence on methanol diffusion.

8.2.4 Characterisation of Intermediates in the Production of ε-Caprolactam

The interesting differences in diffusion behaviour of cyclohexanone oxime between SAPO-37 and HY (despite sharing the same faujasite framework structure) in chapter 7, are possibly related to the much higher catalytic activity in SAPO-37. Any changes in the species present when observing jump diffusion, and lack of observable diffusion 10 ˚C below the product formation temperature may be observed to explain these differences. Vibrational spectroscopy is the technique of choice to investigate adsorbed species. However, studies using infrared spectroscopy performed at the University of Southampton have been inconclusive. INS spectroscopy would only be sensitive to the SAPO-37 hydroxyls and the adsorbates, particularly so in the diagnostic region below ~1400 cm^{-1}. These characteristics would allow for detailed study of the species present as a function of temperature, and a reliable correlation with the mobility observations.

8.3 Investigating Competitive Diffusion of Reactants, Products and By-products in a Microporous Catalyst

Dimethyl ether (DME) is quickly emerging as an important component in green technology, be it an alternative fuel for vehicle engines, a fuel additive, cooking gas, an environmentally friendly aerosol spray or green refrigerant.[4] For these reasons, the production and application of DME has received a large amount of attention in the face of declining fossil fuel reserves and the need for environmental protection.

DME is traditionally produced via methanol dehydration as in eq. 8.1, catalysed by sulphuric acid and more frequently solid acid catalysts such as zeolites.[5] Moreover, in specially prepared rare earth metal modified zeolite Y samples, this synthesis can be carried out at temperatures as low as 245 ˚C.[6]

$$2CH_3OH \rightarrow CH_3OCH_3 + H_2O \quad (\Delta = -12.1 \text{ kJ}, 250^{\circ}C) \tag{8.1}$$

QENS experiments have been proposed to study the diffusion of dimethyl ether, dimethyl ether/methanol mixtures, and dimethyl ether/water mixtures in zeolite HY. To probe the motion of one of the components, one can turn off the signal from another component through deuteration, as deuterium has a much smaller incoherent scattering cross section than hydrogen. This procedure is ideal for studying a system including methanol, dimethyl ether and water, as selective deuteration would allow the study of competitive diffusion within the catalyst. For example, how is the diffusion of the reactant affected by the presence of the product and vice versa? And is the diffusion of either component hindered by the presence of the by-product?

We now have the opportunity to measure the diffusivity of components at different stages of the reaction, e.g. when both the product and by-product are present together (at the end of the reaction), when the reactant and product are present (during the reaction), and in a scenario where by-product removal is employed, so solely the product is present at the end of the reaction. These studies will be

combined with the study of methanol diffusion in chapter 6.3, where solely the diffusion of the reactant, methanol is measured.

8.4 Probing the Diffusion Component of the Ammonia SCR Process in Automotive Catalysts

NO_x emissions from the energy and transport sectors present a major hazard to human health and has been the focus of significant industrial and academic research. One important process available to combat NO_x is the selective catalytic reduction reaction (SCR), in which a reductant such as ammonia, urea or hydrocarbon fuel, is injected into the exhaust to reduce the NO and NO_2 (NO_x) to harmless nitrogen.

Typical catalysts used for ammonia SCR include those based on vanadium oxide, and copper supported on zeolites (Cu/zeo). The Cu/zeo materials such as Cu-chabazite (Cu-CHA) have proven to be extremely active for SCR, and demonstrate long term stability.[7-9] Research projects carried out at Johnson Matthey, have highlighted the excellent performance of small pore zeolites, such as Cu/chabazite for the SCR reaction. With such small pore systems it is very important to understand not only the intrinsic NH_3-NO reaction kinetics and the chemistry of the active sites, but also the diffusion processes that might be important in the design of an optimum SCR catalyst.

QENS experiments have been proposed to characterise the diffusion of ammonia in chabazite with and without the Cu counterion, and also to measure ammonia diffusion in zeolite levynite, comparing the mobility difference between a 3D zeolite (CHA) and a 2D zeolite (LEV). MD simulations have been performed at Johnson Matthey to calculate diffusion coefficients of small molecules (e.g. NO, NH_3, H_2O) in zeolite structures with varying dimensionality and pore sizes. The experiments will also help to validate these simulations. The proposed QENS studies would also complement PFG-NMR studies at the University of Cambridge, where the diffusion

coefficients for intracrystalline diffusion in these small pore zeolites are at the limit of the PFG-NMR technique.

8.5 Investigating the Diffusion of C_6 Cyclic and Aromatic Hydrocarbons in Pt/MCM-41

Mesoporous materials such as MCM-41, have wide ranging applications from catalysis and separation (particularly important to the petrochemical industry) to gas adsorption. MCM-41 has significantly wider pores than zeolite structures (in the range of 30 to 50 Å) allowing bulky guest molecules to diffuse more freely. The physicochemical properties of a fluid are altered significantly upon confinement in pores even of these dimensions, influencing the heat of adsorption and transport properties of the guest molecule. These property changes have an influence on the catalytic characteristics of mesoporous systems.

The impregnation of Pt metal into the MCM-41 framework allows for the catalysed hydrogenation of benzene to cyclohexane,[10] a reaction of significant commercial interest due to the use of cyclohexane as a precursor in the production of nylon, as well as environmental applications such as the removal of benzene from fuels. Understanding the dynamics of aromatic guest molecules is of key importance for these applications.

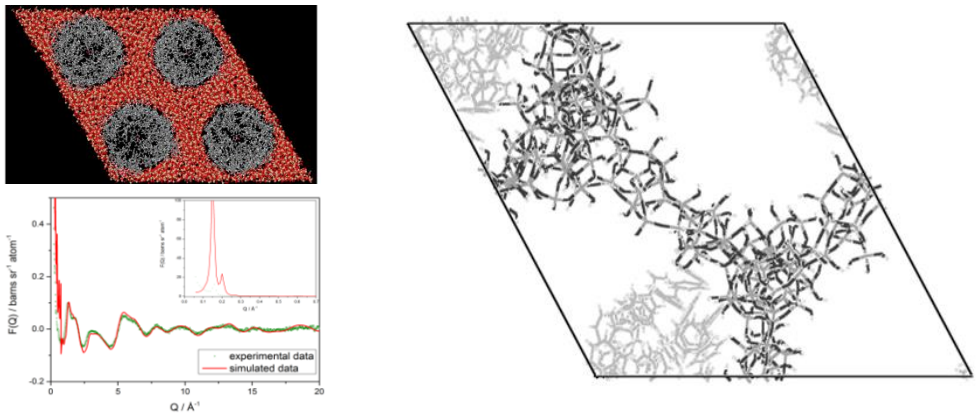

Fig 8.1. CBMC simulations of the structure of benzene confined in MCM-41, with the calculated system structure (top, left) and the calculated structure factor in comparison with experiment (bottom, left). (right) Benzene clusters formed during current MD simulations.

Though diffusion may be quantified through a typical Fickian coefficient within the pore structure, of equal interest may be jump diffusion characteristics, where residence times at (potentially) active sites on the pore wall may determine characteristics such as catalytic turnover.

Neutron total scattering experiments performed on these systems have shown that neutrons are a highly effective probe of the reaction kinetics of Pt/MCM-41 catalysed benzene hydrogenation,[10] concluding that mass transport played a very significant role. It was suggested that increasing the rate of diffusion may have a promoting effect on catalyst performance, providing guidance on future catalyst design and development. For this reason the diffusion of the cyclic C_6 species present during this reaction (namely benzene, cyclohexane and cyclohexene) is of great interest.

Recent neutron diffraction experiments performed by Hardacre et al are currently being interpreted with configurational bias Monte Carlo (CBMC) simulations by M. Falkowska at Queens University Belfast (figure 8.1), giving an insight into the local ordering of benzene-d_6 confined in MCM-41 pores. However, the sorbate dynamics are yet to be quantitatively investigated. QENS experiments have been proposed to investigate the diffusion of benzene, cyclohexene and cyclohexane in Pt/MCM-41 to measure experimentally the effect of confinement on these species and the dynamical aspects potentially dictating the benzene hydrogenation reaction. The experiments will be compared with MD simulations currently being performed by D. Dervin at Univeristy College London, which so far have uncovered the extent of benzene clustering shown in figure 8.1. We may then determine the effect of differing sorbate-sorbate, and guest-host interactions due to the presence of aromaticity, pi-bonding or lack thereof in these cyclic C_6 hydrocarbons. Principally though, we aim to provide the necessary information on the mass transport which appeared so pivotal in the referenced kinetic study.

8.6 The Effect of Framework Composition on the Diffusion of Octane in H-ZSM-5

In chapters 4 and 5, the effect of molecular shape and framework topology on alkane diffusion in zeolites was studied by microscopic experimental and simulation methods. However, another important variable to consider in terms of both catalysis and diffusion is the composition (Si/Al ratio) of the zeolite sample, where a low ratio sample has more acidic proton sites and vice versa. In the case of the acidic zeolite catalysts, having too few sites can lead to low activity and low yield, whereas having too many sites will lead to over-activity, coking and eventually deactivation of the catalyst. Thus an optimum Si/Al ratio is necessary. There is also a crucial diffusion component, as the diffusion of *n*-alkanes has been shown to be faster by a factor of 4 in silicalite, than in Na-ZSM5 samples.[11] This could have implications for the catalyst performance, given that too higher concentration of catalytic sites could impede the diffusion of reactants throughout the zeolite crystal, resulting in inefficient use of the catalyst.

Preliminary molecular dynamics simulations currently being performed on H-ZSM-5 frameworks (of Si/Al = 30) show that *n*-octane molecules slow their diffusion upon encountering a potential barrier in the form of a bridging hydroxyl. QENS studies have been proposed to investigate for the first time, the effect of Si/Al ratio on the diffusion behaviour of *n*-octane in commercial samples of acidic H-ZSM5 catalysts of Si/Al = 30 and 280. Results from these studies will be compared to further molecular dynamics simulations, giving a detailed insight into the effect of catalyst composition on the dynamics of the sorbate.

References

(1) Gale, J. D.; Rohl, A. L. *Molecular Simulation* **2003**, *29*, 291.

(2) Haw, J. F.; Song, W.; Marcus, D. M.; Nicholas, J. B. *Accounts of Chemical Research* **2003**, *36*, 317.

(3) Andzelm, J.; Govind, N.; Fitzgerald, G.; Maiti, A. *International Journal of Quantum Chemistry* **2003**, *91*, 467.

(4) Arkharov, A.; Glukhov, S.; Grekhov, L.; Zherdev, A.; Ivashchenko, N.; Kalinin, D.; Sharaburin, A.; Aleksandrov, A. *Chemical and Petroleum Engineering* **2003**, *39*, 330.
(5) Jin, D.; Zhu, B.; Hou, Z.; Fei, J.; Lou, H.; Zheng, X. *Fuel* **2007**, *86*, 2707.
(6) Vishwanathan, V.; Jun, K.-W.; Kim, J.-W.; Roh, H.-S. *Applied Catalysis A: General* **2004**, *276*, 251.
(7) Deka, U.; Lezcano-Gonzalez, I.; Weckhuysen, B. M.; Beale, A. M. *ACS catalysis* **2013**, *3*, 413.
(8) Beale, A. M.; Gao, F.; Lezcano-Gonzalez, I.; Peden, C. H.; Szanyi, J. *Chemical Society Reviews* **2015**, *44*, 7371.
(9) Brandenberger, S.; Kröcher, O.; Tissler, A.; Althoff, R. *Catalysis Reviews* **2008**, *50*, 492.
(10) Youngs, T. G.; Manyar, H.; Bowron, D. T.; Gladden, L. F.; Hardacre, C. *Chemical Science* **2013**, *4*, 3484.
(11) Jobic, H.; Theodorou, D. N. *The Journal of Physical Chemistry B* **2006**, *110*, 1964.

Appendix A

Absolute Values of QM/MM Embedded Cluster Calculations

We present in this appendix the absolute values used to calculate the deprotonation energies and methanol adsorption energies in each zeolite structure from the embedded cluster calculations in section 6.2.

Protonated/deprotonated Zeolite Structures with PW91 functional				
Cluster	**HY**	**H-ZSM-5 (I2)**	**H-ZSM-5 (M7)**	**H-ZSM-5 (Z6)**
Zeo^-	-694437.643875931	-845900.696256	-834187.733671932	-826797.981563349
ZeoH (O1)	-694475.060265537	-841446.248640129	-834229.220097486	-826837.103335592
ZeoH (O2)	-694476.082536073	-841446.510332353	-834228.893003617	-826835.676062597
ZeoH (O3)	-694475.742921125	-841446.817911452	-834228.481990115	-826836.488670478
ZeoH (O4)	-694475.419810946	-841443.357937019	-8689.882301258250	-826837.161721475

Table A.1 Absolute energies of the (Jost corrected) deprotonated zeolite structure for all four systems (Zeo^-), and the absolute energy value of the zeolite structure when protonated on each of the 4 neighbouring oxygens (O1, O2, O3, O4). Calculated using the PW91 functional, all values in units of eV.

Protonated Structures (ZeoH)				
System/functional	**HY**	**H-ZSM-5 (I2)**	**H-ZSM-5 (M7)**	**H-ZSM-5 (Z6)**
B3LYP ZeoH	-694607.236670069	-841880.410517247	-834658.184160576	-827260.022834133
B3LYP Zeo^-	-694567.880643936	-841839.778753724	-834615.506398087	-827219.973335854
B97-2 ZeoH	-694485.862814519	-841735.05959523	-834513.48420897	-827120.505929385
B97-2 Zeo-	-694445.93891397	-841693.922577653	-834472.346700498	-827079.82047064

Table A.2 Absolute energies of the aluminated, deprotonated zeolite structure for all four systems (Zeo^-), and the absolute energy value of the zeolite structure when protonated on the most acidic oxygen site (ZeoH) using the B3LYP and B97-2 functionals, all values in units of eV.

Functional	**PW91**	**B3LYP**	**B972**
MeOH	-11104.8223713845	-11109.9174359049	-11105.2565857189

Table A.3 Absolute energies of a methanol molecule in a vacuum, using the PW91, B3LYP and B97-2 functionals, all values in eV.

BSSE Corrected Energy of Methanol Adsorbed Structures				
Functional	**HY**	**H-ZSM-5 (I2)**	**H-ZSM-5 (M7)**	**H-ZSM-5 (Z6)**
PW91	-705352.581557389	-852831.241824756	-845610.422493668	-838214.569516905
B3LYP	-705723.915824696	-852997.091980091	-845775.448176289	-838375.69615062
B97-2	-705597.975630637	-852846.759914423	-845626.54570513	-838231.711052437

Table A.4 Absolute energies of the methanol adsorbed zeolite structures, using the PW91, B3LYP and B97-2 functionals, all values in units of eV.

Appendix B

Characterisation of HY, H-ZSM-5 and SAPO-37

We present in this appendix the X-ray diffraction characterisation of the zeolite samples used for the experimental work in this thesis.

Characterisation of the commercial HY (Si/Al = 30), commercial H-ZSM-5 (Si/Al = 30) and synthesised SAPO-37 samples were carried out by M. E. Potter at the University of Southampton. Powder X-Ray diffraction patterns were obtained using a Siemens D5000 diffractometer using Cu $K_{\alpha 1}$ radiation, where $\lambda = 1.54056$ Å. Rietveld refinement was performed using the appropriate space group.

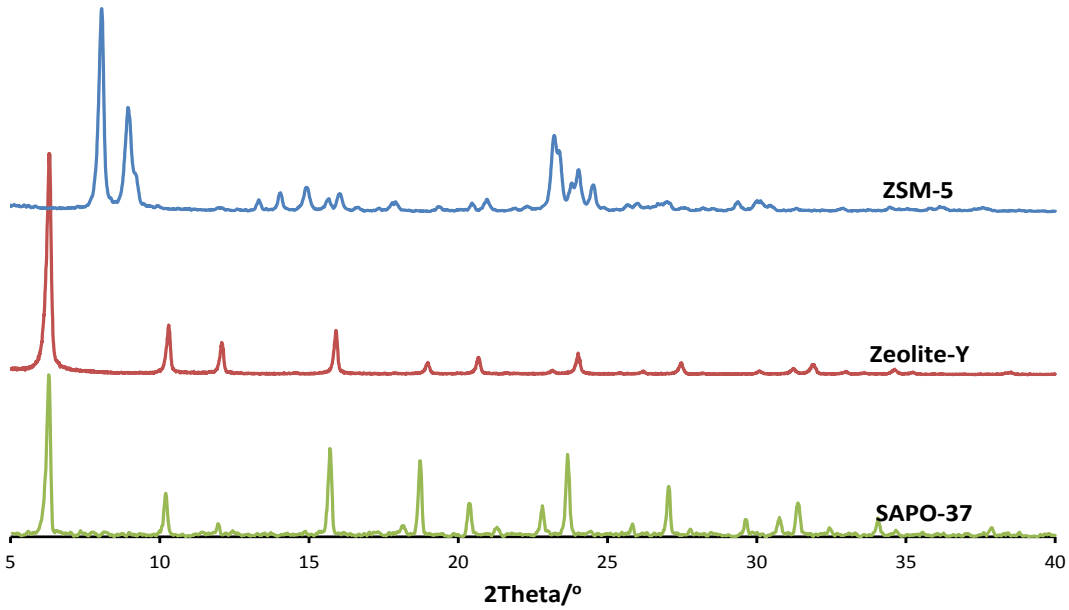

Figure B1: Powder XRD patterns of ZSM-5 (top), Zeolite-Y (middle) and SAPO-37 (bottom) showing phase pure MFI, FAU and FAU topologies respectively.